REFERENCE ONLY

UNIVERSITY OF LONDON THESIS

Degree	Year	Name of Author
PhD	2005	GARROD, ROBIN TRISTAN

The Chemistry of Transient Dense Cores in Interstellar Clouds

Robin Tristan Garrod

Thesis submitted for the Degree of Doctor of Philosophy
of the University of London

Department of Physics & Astronomy
UNIVERSITY COLLEGE LONDON

February 2005

ProQuest LLC
789 East Eisenhower Parkway
P.O. Box 1346
Ann Arbor, MI 48106-1346

Abstract

I model the chemical effects on dark clouds of their being composed of small (<0.1 pc), transient (order of 1 Myr), dense cores (which are only observed with high-resolution interferometry) within which most of the clouds' mass resides, surrounded by a diffuse background gas. I investigate the chemical evolution of the cores, and the resultant chemical enhancement of the background gas by cyclical processing through core formation and dissipation. I approximate the MHD mechanism of Falle & Hartquist (2002), by which large transient density inhomogeneities may be produced by slow-mode waves in a cold plasma, into a multi-point 1-D chemical code. Molecular freeze-out onto dust grains and subsequent re-injection into the gas phase are switched on or off according to the attainment of a critical visual extinction at individual points. I explore a grid of parameter space in five physical and chemical variables. Among a number of conclusions, I find firstly that multi-point chemical codes are highly necessary for modelling dark cloud regions, due to the large chemical variation over time and space. I find that the core chemistry is young at all times, in keeping with observations, and that the abundance and spatial extent of several important species is significantly enhanced by the cycling process. Further to this, I construct (non-interacting) assemblies of such cores, producing convolved maps mimicking observational constraints, and present evidence that such collections of transient dense cores may reproduce the morphologies observed in both low- and high-resolution molecular line studies of dark clouds. I further modify the convolution method in a number of ways, using this mapping procedure to test hypotheses derived from the chemical analysis. Hence I obtain observational diagnostics for the determination of physical and chemical conditions in dark clouds.

Acknowledgements

I would like to take this opportunity to thank Jonathan Rawlings and David Williams for their help, encouragement, and enthusiasm for the subject. When trying to find a suitable field of PhD study, it was an unexpected conversation with David which convinced me that astrochemistry would be as exciting as it has proved to be.

I also thank my wife Joann for her patience and understanding during the writing-up stage, when her tasks were more than equal to mine.

Contents

List of Figures

List of Tables

CHAPTER 1

Introduction

1.1 Modelling Astrochemistry

The physical and chemical processes which take place in the interstellar medium are closely bound together. Whilst the vast majority of material in interstellar space is composed of molecular hydrogen, chemical interactions involving other less abundant species are crucial to a number of processes: the regulation of temperature, the level of absorption and emission of electromagnetic radiation, and the degree of ionisation, to name a few. Whilst the behaviour of these processes feeds back directly into the chemical behaviour of the interstellar medium, it also has a direct impact on the gas dynamics, making them inter-dependent and, in some cases, highly non-linear. Because of this fact, a simplistic estimate of the chemical abundances present in observed regions will not suffice. In order to understand the chemistry, and therefore understand how it influences and is influenced by the physical state of the gas, we must model it in a time-dependent way.

The mechanics of astrochemical modelling is the numerical integration of large numbers of time-dependent, simultaneous, ordinary differential equations. These are rate equations governing the formation and destruction of chemical species. For a two-body gas phase chemical reaction of the type:

$$\mathrm{A} + \mathrm{B} \xrightarrow{k} \mathrm{C} + \mathrm{D}$$

the rate of destruction of A or B is equal to the rate of formation of C or D due to the reaction. So, concentrating on formation, the rate of formation of species C is:

$$\frac{\mathrm{d}n[\mathrm{C}]}{\mathrm{d}t} = k.n[\mathrm{A}].n[\mathrm{B}] \tag{1.1}$$

where $n[i]$ is the number density of species i, and k is the reaction rate coefficient. Generally, the abundances of species are expressed in terms of a fraction of the total hydrogen nucleon number density, n_H. The fractional abundance of species i is then $X[i] = n[i]/n_H$. This leaves equation (1.1) in the form:

$$\frac{\mathrm{d}X[\mathrm{C}]}{\mathrm{d}t} = k.X[\mathrm{A}].X[\mathrm{B}].n_H \tag{1.2}$$

From equation (1.2) it can be seen how the rate of formation or destruction of species A, B, C or D is dependent on the gas density. The total loss or gain over an infinitesimal time period is the sum of the contributions from each such rate equation as (1.2). Obviously, the type of reaction determines the form the rate equation takes.

The rate coefficients for the equations governing the reactions of a network of chemical species are determined using a number of methods: theoretical (quantum mechanical) analysis, laboratory experiment, Monte Carlo techniques, or by inference using observational evidence in conjunction with chemical modelling. In all of the work presented in this thesis, the rate equations and rate coefficients are obtained from the UMIST ratefile (see Millar *et al.* 1997), a long-standing, continually updated database for astrochemistry.

Generally, the starting point of a simulation is that all material is in atomic, or atomic ion form, although hydrogen may sometimes be assumed to be all in the molecular form. From this starting point, the simultaneous differential equations are solved numerically, usually up to the point where they reach equilibrium values, if they are able – in models where freeze out is activated, and without corresponding desorption from the grain surfaces, an equilibrium would ultimately be reached where all material except H, H_2 and He (and their corresponding ions) would be frozen out. Those species remain, due to their low vapour pressures.

A number of gas phase chemical reactions are included in models. Cosmic ray ionisation, which is usually assumed to be isotropic, takes a canonical rate value of 3×10^{-17} s^{-1}. The rate of cosmic ray ionisation of a particular species is therefore only dependent on the abundance of that one species, hence it is independent of density. This ionisation mechanism is weak, and therefore only becomes dominant in regions of high visual extinction, where photoionisation is blocked.

Photodestruction processes are usually characterised with a generic reaction rate coefficient of the form:

$$k = \alpha \exp\left(-\gamma A_V\right) \tag{1.3}$$

where α and γ are constants specific to the reaction in question, A_V is visual extinction (due to dust), and T_K is the gas kinetic temperature. These rates are specified for a Habing type interstellar radiation field (see Habing 1968). The value of γ is dependent on the relative importance of ultraviolet and visual wavelengths in these photoprocesses, since the level of attenuation in the radiation field is measured in terms of the visual waveband. The interstellar radiation field does not include photons of energy above 13.6 eV, since these are effectively absorbed much nearer to the sources of the radiation, by atomic hydrogen.

Other reactions are usually characterised by a temperature dependent reaction rate of the form:

$$k = \alpha \left(\frac{T_K}{300}\right)^{\beta} \exp\left(-\frac{\gamma}{T_K}\right) \tag{1.4}$$

Such reactions could be: neutral-neutral, ion-atom, ion-molecule, or radiative or dissociative recombination. The temperature term takes account of the temperature-dependent collision cross-section and reaction probability. The final term represents those cases where an activation energy barrier is present. This term gives the classical statistical proportion of collisions which breach the energy barrier and therefore go on to chemically react. Note that three-body collisions are not considered: at the low densities attained in the interstellar medium, the likelihood of these reactions taking place is negligible.

In many situations it is the cosmic ray or photon ionisation that provides the ionisation which drives the (mainly) ion-molecule chemistry in the gas phase.

Table 1.1 shows typical reaction rate values for a number of different reaction types, obtained from Duley & Williams (1984).

Aside from the gas phase chemistry, the other important factor is chemistry on the surface of dust grains. Knowledge of these processes is more limited due to the location of the participant species. In some cases, dust grain reactions involve the sticking of a reactant onto the surface of a grain for long enough to react with a localised H atom, the product of which is then realeased back into the gas phase due to the binding energy released in the reaction. The most important example of this process is the formation of molecular hydrogen, H_2. Analysis of reaction rates shows that it is impossible to achieve the high levels which are attained purely by gas phase mechanisms, over realistic time scales.

In other cases, sticking occurs, and the release of any energy resulting from a surface

Table 1.1: Representative values of rates or rate coefficients for reactions of interstellar interest, from Duley & Williams (1984)

Reaction Type	Representative rate or rate coefficient
Cosmic Ray Ionisation	10^{-17} s^{-1}
Ion-Molecule Reaction	10^{-9} cm ^{3} s^{-1}
Charge Transfer Reaction	10^{-9} cm ^{3} s^{-1}
Radiative Association - diatomic - large polyatomic	10^{-17} cm ^{3} s^{-1} 10^{-9} cm ^{3} s^{-1}
Neutral Exchange	10^{-11} cm ^{3} s^{-1}
Radiative Recombination	10^{-12} cm ^{3} s^{-1}
Dissociative Recombination	10^{-6} cm ^{3} s^{-1}
Negative Ion Reaction	10^{-9} cm ^{3} s^{-1}

reaction is not strong enough to overcome the sticking energy. This process is often referred to as "freeze out", and is most important in regions where gas densities are high and visual extinctions are at least moderately high. Often the sticking of species to grain surfaces is assumed to be followed by the hydrogenation of those species.

Because the rates of sticking and subsequent grain surface reactions are not well constrained, the treatment of freeze-out reactions in this work and in most other models uses a free parameter, fr, as a generic freeze out rate for all species which stick.

This summary of the basic approach to modelling astrochemistry shows how the physical conditions (density, temperature, visual extinction due to dust) in the interstellar medium influence chemical behaviour.

In the following two sections I present two examples of this approach applied to particular problems.

1.2 Chemical Effects of H_2 Formation Excitation[1]

1.2.1 Introduction

It is widely accepted that most interstellar H_2 is formed on the surface of dust grains (*e.g.* Duley & Williams 1984). However, the fundamental issue of the nature of the interaction between an H-atom and a dust grain remains poorly understood. Recently, a combined

[1]The work of this section is published in Astrophysics and Space Science (Garrod *et al.* 2003)

theoretical and laboratory study of this process (see Williams *et al.* 1999) has addressed such issues as the nature and efficiency of the absorption, the surface mobility of H-atoms, and the energy budget of the H_2 formation reaction. Simple equipartition arguments would suggest that the net H_2 formation energy ($\sim$ 2.9 eV) may be distributed between grain heating and the excitation of translational and ro-vibrational states of H_2. The detailed quantum mechanical calculations have indeed shown that much of the H_2 should be produced in an excited state, with ro-vibrational and translational energy of the order of 1 eV (Farebrother *et al.* 2000, Meijer *et al.* 2001). These calculations are based on the assumption that H_2 formation on grain surfaces occurs via the Eley-Rideal (prompt) mechanism. This assumes that H atoms are abundant on the surface of dust grains - as would be the case in regions with a low H_2:H ratio; a colliding H atom from the gas phase will instantaneously encounter a physisorbed H atom to form an H_2 molecule (without the need for any surface migration of H-atoms) which then immediately leaves the surface. Reaction thus occurs following a single collision. The recent experimental work of Perry *et al.* (2002) has confirmed the theoretical predictions; H_2 molecules formed on a graphite surface at low temperatures ($T < 20$ K) and low densities, are found to exist in a range of ro-vibrationally excited states (with $v'' = 0 - 5$) and with significant kinetic energies.

Until now, the observational and chemical consequences of the distribution of the energy excess have not been addressed in any detailed form. Possible indicators and chemical/physical effects in the context of the interstellar medium (ISM) include; a significant contribution to the infrared emission as a result of the radiative relaxation of the excited states, the possibility that the internal energy (particularly for $v'' > 3$) may overcome chemical barriers and endothermicities (*e.g.* Stecher & Williams 1972), a contribution to the ionization of the ISM - $H_2(v'' > 3)$ can be ionized by photons with energies < 13.6 eV, and a heating source for the ISM through collisional relaxation.

The observational implications were addressed by Tiné *et al.* (2003) who made predictions for the H_2 ro-vibrational emission line intensities for diffuse and dark interstellar clouds, assuming that the H_2 is formed by the Eley-Rideal process. Their model, which included both formation excitation as well as the more usual radiative and collisional pumping of H_2 rotational and vibrational states, suggested that there should be a clear spectral signature of H_2 formation excitation in both diffuse and (particularly) dark clouds.

H_2 plays a crucial role in interstellar chemistry and takes part in many gas-phase reactions. However, some of these are endothermic or have an activation energy barrier. At low

Table 1.2: Parameter values for models 1 and 2. Note that n_H is the total hydrogen nucleon number density

Model:	1. Diffuse cloud	1. Dark cloud	2. Pre-collapse	2. Post-collapse
Density, n_H (cm^{-3})	10^2	10^4	10^2	10^5
Visual extinction, A_V	1	10	1	100
Temperature, T (K)	100	20	100	100

gas temperatures, appropriate to the conditions within interstellar clouds, these reactions are therefore heavily suppressed. We propose that the internal and translational excitation energy of the nascent H_2 may act to overcome the barriers or reaction endothermicities of certain key reactions.

To test this hypothesis we have included excited molecular hydrogen, H_2^*, as a separate species whose chemistry is limited to formation on grain surfaces, radiative and collisional relaxation to the ground state, and the two gas-phase reactions which produce the radicals, OH and CH^+;

$$H_2^* + O \longrightarrow OH + H \tag{1.5}$$

$$H_2^* + C^+ \longrightarrow CH^+ + H \tag{1.6}$$

In the case of ground state H_2, these reactions have activation energy barriers of 3160 K and 4640 K respectively (corresponding to single particle energies of 0.41 eV and 0.60 eV). For H_2^* we simply estimate the rate coefficient for these reactions to be the same as for ground state H_2, but without the presence of the activation energy barriers. This suggests (upper-limit) temperature-independent values of the rate-coefficients for reactions (1.5) and (1.6) of $k_1 = 10^{-11}$ cm^{-3} s^{-1} and $k_2 = 10^{-9}$ cm^{-3} s^{-1} respectively.

These reactions may initiate a rich chemistry and are particularly pertinent to the inclusion of H_2^* since a correlation has been observed between the column densities of CH^+ and H_2 in highly rotationally excited states (Frisch & Jura 1980, Lambert & Danks 1986). Reaction (1.5) may be important in both dark and diffuse cloud environments where large abundances of atomic oxygen are present, whilst reaction (1.6) may be particularly significant in diffuse cloud environments where C^+ abundances are high.

1.2.2 Models

In order to test the hypothesis, we have included this representative chemistry of excited H_2 (H_2^*) in a simple one-point model of the time-dependent chemistry of interstellar clouds. The model follows the evolution of the abundances of some 83 chemical species, linked through a network of 1071 (gas-phase) reactions. The chemistry is similar to that employed by Rawlings & Yates (2001) and Rawlings *et al.* (2002); it is limited to simple species containing the elements, H, He, C, N, O, S and a representative low ionization potential metal, Na. Most of the reaction network and the rate coefficients are drawn from the UMIST rate file databases (Millar *et al.* 1991, Millar *et al.* 1997) and are broadly representative of the chemistry of small species in molecular clouds.

The cosmic ray induced ionisation rate is taken to be 1.3×10^{-17} s^{-1} in all of the models. H_2 is assumed to be efficiently self-shielded against photodissociation by the interstellar radiation field. In all of our model runs we only consider a gas-phase chemistry, with the obvious exception of grain surface H_2 (or H_2^*) formation. The initial conditions assume a purely atomic gas, so that the initial H_2:H ratio is zero.

We have approximated the abundance of H_2^* in two ways;

- by setting it to a fixed, steady-state value *relative to* H_2
- by allowing it to change in a time-dependent way, governed by the associated formation and destruction reactions.

1.2.2.1 Model 1: Steady state approximation for H_2^*

Our first approximation is to assume that the H_2^* maintains a constant abundance relative to H_2. To find this abundance, we first assume that *all* of the H_2 formed on dust grains is in a generic excited state (an assumption that is used throughout this study). The rate for the surface formation of H_2 (or H_2^*) is given by $Rn(\mathrm{H}).n_H$, where n_H is the total hydrogen nucleon density and R is of the order of 10^{-17} cm^3 s^{-1}. We then assume that the principal formation route for (ground-state) H_2 is via radiative de-excitation of H_2^* and that its principal destruction route is photodissociation. This implies that in steady-state ($\mathrm{d}n(\mathrm{H}_2)/\mathrm{d}t = 0$), $An(\mathrm{H}_2^*) = \beta n(\mathrm{H}_2)$ where A is an assumed average Einstein A-coefficient for radiative transitions of H_2^* over all the excited levels, and β is the rate-coefficient for (unshielded) photodissociation. Adopting values of $A = 10^{-6}$ s^{-1} and $\beta = 10^{-11}$ s^{-1} implies a fractional abundance ratio of $X(\mathrm{H}_2^*)/X(\mathrm{H}_2)= 10^{-5}$. However, the value of β may

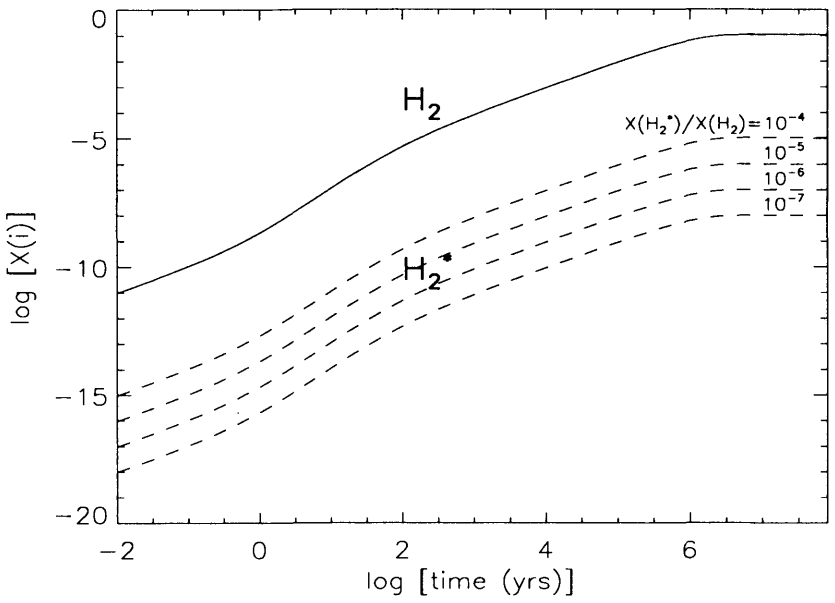

Figure 1.1: Model 1 [diffuse cloud] Fractional abundances of H_2 and H_2^*

be lower by as much as 4 orders of magnitude, dependent on the level of self-shielding, and A may also vary somewhat depending on the ro-vibrational excitation state of the H_2^* on formation. Hence, model calculations were performed for several values of $X(H_2^*)/X(H_2)$; 10^{-4},10^{-5},10^{-6} and 10^{-7}. The abundance ratio remains strictly fixed at all times in each model run.

We ran the model for the two cases; representative of diffuse cloud and dark cloud environments. Values of the parameters employed in all of our model runs are given in table 1.2, above.

Results from Model 1 are shown in figures 1.1 – 1.3 (diffuse cloud) and 1.4 – 1.5 (dark cloud). Figure 1.1 shows the development of the fractional abundances of H_2 and H_2^*, [$X(H_2)$ & $X(H_2^*)$], as functions of time, for different values of the $X(H_2^*)/X(H_2)$ abundance ratio. The behaviour of $X(H_2^*)$ rigidly tracks that of $X(H_2)$ at all times and the timescale to convert ~10% of the hydrogen to H_2 (~10^6 years) is approximately equal to $0.1(R.n_H)^{-1}$. From figure 1.2 it can be seen that $X(CH^+)$ is strongly enhanced in the diffuse cloud model once $X(H_2^*) \geq 10^{-8}$, which typically occurs at times of $\geq 10^4$ years. However, the enhancement is not sufficient to account for the high CH^+ abundances ($X(CH^+) \simeq 10^{-8}$) observed in diffuse clouds. Thus, under our steady-state approximation, excited $X(H_2^*)$ cannot be the main factor in accounting for the over-abundance of CH^+ in diffuse clouds.

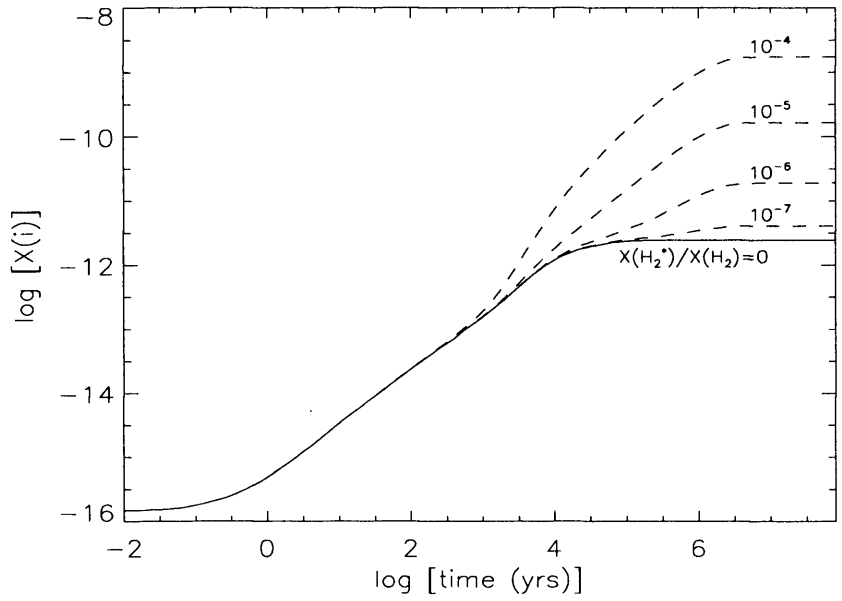

Figure 1.2: Model 1 [diffuse cloud] Fractional abundances of CH^+

The OH abundance is enhanced to a much lesser degree (figure 1.3), once $X(H_2^*) \geq 10^{-6}$, which only occurs for the case of $X(H_2^*)/X(H_2) = 10^{-4}$ at late times ($t > 10^5$ years).

The CH^+ and OH abundances in the dark cloud model are shown in figures 1.4 and 1.5 respectively. The time dependence of $X(CH^+)$ is complex and merits some discussion; the early decline in $X(CH^+)$ is a consequence of a gradual fall in ionization and hence suppression of CH^+ formation. $X(CH^+)$ recovers after about 100 years as the H_2^* abundance rises and reaction (1.6) becomes significant. A double peak structure is evident between 10^2 - 10^6 years: Higher H_2^* abundances result in faster OH (see figure 1.5), and hence CO production rates. This promotes C^+ formation through the reaction $He^+ + CO \rightarrow C^+ + O + He$ and the peak in the CH^+ abundance (formed from C^+ via reaction (1.6)) is pushed to earlier times. This is clearly visible in figure 1.4. As the He^+ abundance falls, $X(CH^+)$ declines, until H_3^+ rises and a second peak develops; driven by the reaction $H_3^+ + C \rightarrow CH^+ + H_2$. Eventually, most carbon is converted to CO and CH^+ abundance falls, but to an equilibrium value that is significantly elevated as compared to the case where reaction (1.6) is not included. However, we again note that the CH^+ abundances are not sufficiently enhanced in any of the model runs to be observationally significant; although the formation rates are faster, the rapid ion-neutral destruction channels dictate that $X(CH^+)$ remains low at dark cloud densities.

The abundances of OH (figure 1.5) are much more strongly enhanced compared to the

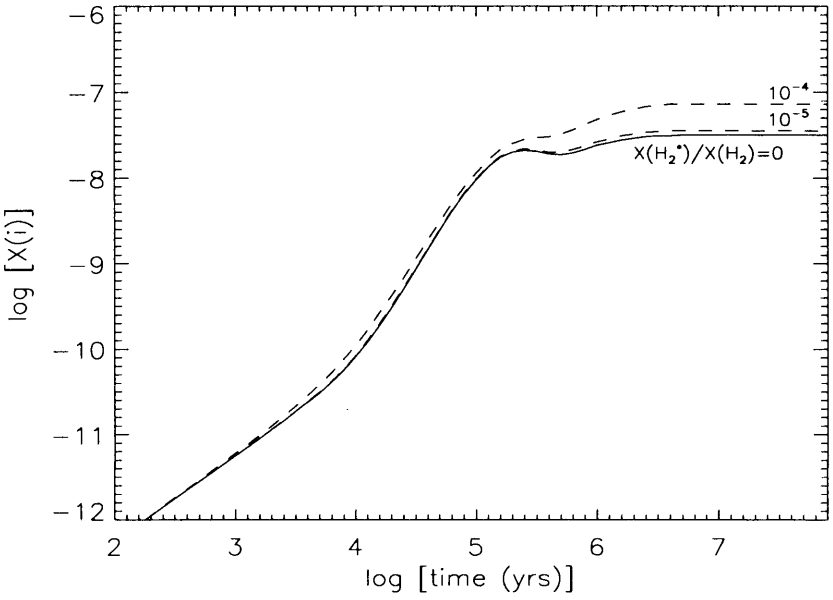

Figure 1.3: Model 1 [diffuse cloud] Fractional abundances of OH

diffuse cloud case (figure 1.3). This is largely a consequence of the reduction in efficiency of the OH destruction channels due to the partial suppression of photodissociation reactions and the lower fractional ionization.

1.2.2.2 Model 2: Time dependent H_2^*

Non-equilibrium time-dependent chemical effects may yield higher values of $X(H_2^*)$ and hence $X(OH)$ and $X(CH^+)$. In order to implement a full time-dependence for $X(H_2^*)$, we therefore introduced a formation rate for H_2^* which is equal to the H_2 formation rate on grains (consistent with our assumption that all H_2 formed on grains is in an excited state). The primary loss channels for H_2^* are radiative relaxation and collisional de-excitation (through collisions with H_2 and H atoms) to the ground state of H_2. Other, chemical, loss routes are less significant. The photodissociation rate for H_2^* is small compared to its radiative decay rate and can safely be ignored. The other main destruction routes open to H_2^* are via reactions (1.5) and (1.6). In addition to these reactions, the chemistry of H_2^* is thus limited to:

$$H + H/\text{grain} \longrightarrow H_2^* + \text{grain}$$

$$H_2^* \longrightarrow H_2 + h\nu$$

$$H_2^* + H_2 \longrightarrow H_2 + H_2 + \text{K.E.}$$

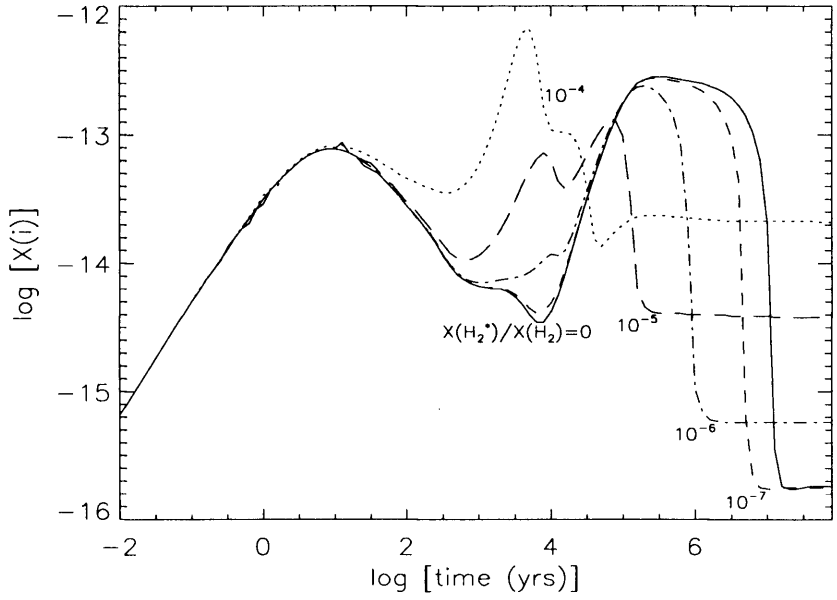

Figure 1.4: Model 1 [dark cloud] Fractional abundances of CH^+

$H_2^* + H \longrightarrow H_2 + H + K.E.$

The rate coefficient for collisional de-excitation is assumed to be the same for both reactions. We can estimate its approximate value, k_{coll} from

$k_{coll} = \langle\sigma\rangle \langle v\rangle$

where $\langle\sigma\rangle$ and $\langle v\rangle$ are the expectation values of the reaction cross-section and the velocity of the H_2^* molecule, respectively. Adopting approximate values of $\langle\sigma\rangle = 10^{-16}$ cm^2 and $\langle v\rangle = 10^5$ cm s^{-1}, we obtain $k_{coll} = 10^{-11}$ cm^{-3} s^{-1}.

We ran the diffuse cloud model with these extra reactions included (and using the same parameters as for our first model - see table 1.2). In figure 1.6 we can see that the abundance of H_2^* rises to a quasi-equilibrium on a timescale that is essentially determined by the rapid (radiative de-excitation) destruction channel; $\tau \sim (1/A) \sim 0.03$ years. However, this abundance ($\sim 2 - 3 \times 10^{-9}$) is less than the threshold ($\sim 10^{-8}$) noted in the previous section and consequently the enhancement on $X(CH^+)$ and $X(OH)$ is barely noticeable.

Higher densities and H:H_2 ratios would result in faster continuous H_2^* formation rates and higher H_2^* abundances, but this implies that the conversion timescale for H to H_2 and hence the period of H_2^* abundance enhancement would be shorter.

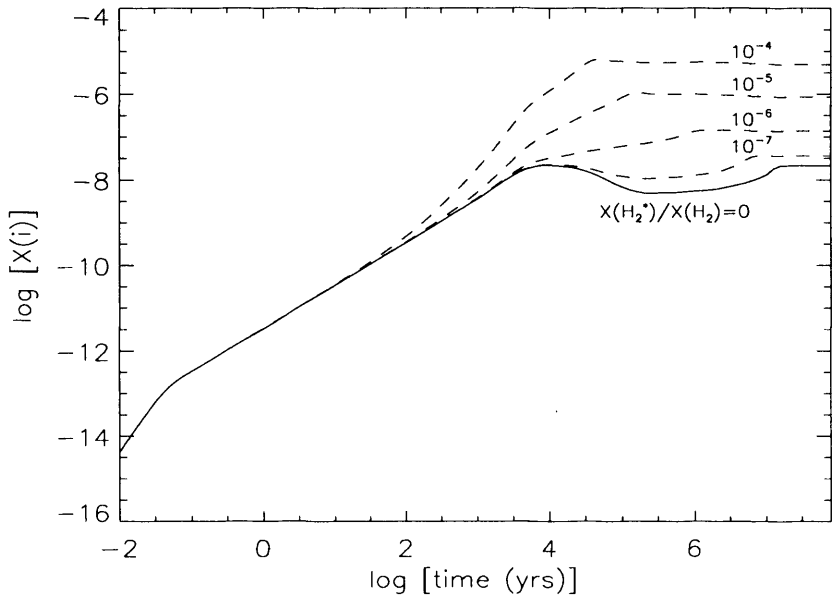

Figure 1.5: Model 1 [dark cloud] Fractional abundances of OH

1.2.2.3 Application to a model of shock-induced collapse of a diffuse cloud

Clearly, the optimal conditions for the formation of large fractional abundances of H_2^* and enhanced OH and CH^+ abundances are obtained in a high density gas with a high transient H:H_2 ratio.

Such conditions may pertain following the passage of a fast shock that dissociates H_2 but which cools rapidly enough for the shock to be considered isothermal. Since the re-formation of H_2 is slow, then the immediate result of the shock will be to generate a dense, cool environment that is primarily composed of hydrogen atoms. Since the density contrast across an isothermal shock is M^2, where M is the Mach number, the post-shock densities and H-atom abundances may be propitious for the formation of H_2^*.

The specific situation that we have modelled is the shock-induced compression of a diffuse cloud, to a darker and denser state. We allow a plane shock-wave to engulf a spherically symmetric cloud, and merely assume that the cloud is homogeneously compressed following the passage of the isothermal shock. The initial chemical conditions were obtained from the diffuse cloud model (as before), run to steady state. The cloud is then assumed to be compressed by a factor of 10 in radius, R. For a spherical, homogeneous compression, the density $n_H \propto R^{-3}$ and the extinction $A_V \propto R^{-2}$. The pre- and post-collapse values of n_H and A_V are given in table 1.2. We assume that the H_2 is fully

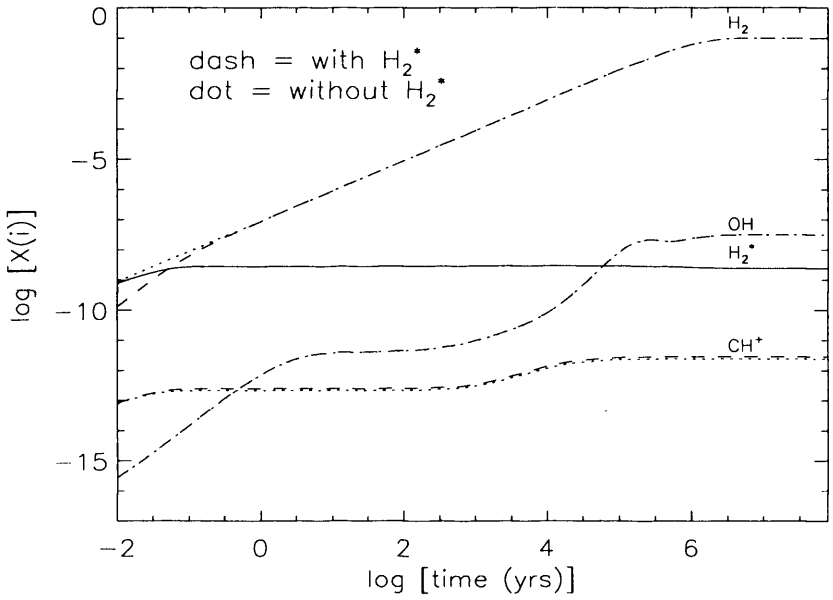

Figure 1.6: Model 2 [diffuse cloud - with time-dependent $X(H_2^*)$] Fractional abundances of H_2, H_2^*, OH, CH^+

dissociated following the passage of the shock and then model the chemical evolution of the post-shock gas.

The results are shown in figure 1.7 where we present the time-evolution of the fractional abundances of CH^+ and OH, together with C^+ and O and H_2^*, from which they are formed through reactions (1.5) and (1.6).

As before, the abundance of H_2^* rapidly rises to a (now much higher) quasi-equilibrium value. However, this enhancement is a direct result of the non-equilibrium chemical conditions that exist in the post-shock gas, and in particular, the high H-atom abundance. This only lasts for approximately 10^4 years, being the approximate re-formation timescale for H_2. During this period (only) $X(OH)$ is enhanced by a factor of $\sim$10. The enhancement of $X(CH^+)$ is more significant ($\sim$ 2 orders of magnitude), but only lasts for as long as $X(C^+)$ remains high ($\sim 10^3$ years, being the approximate timescale for $X(C^+)$ to relax to equilibrium dark cloud values).

1.2.3 Conclusions

We find that the effects of excited H_2, produced via grain-surface formation, on the chemistry of interstellar clouds are in general small, and for denser clouds, short-lived. Whilst our first, "steady-state", model shows that abundances of OH and CH^+ may be augmented

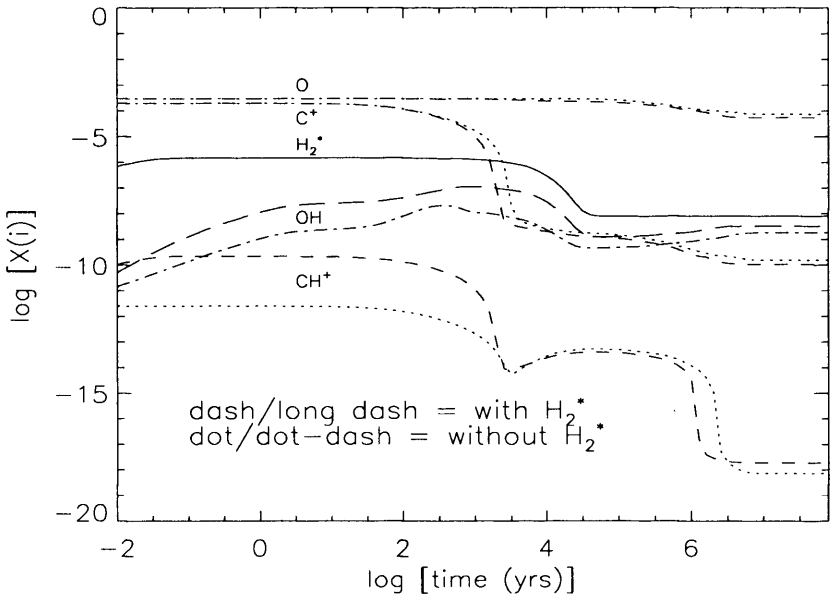

Figure 1.7: Model 2 [with time-dependent $X(H_2^*)$] Fractional abundances of H_2^*, C^+, CH^+, O and OH for shock-induced compression

by taking a large ratio of H_2^*:H_2, this large ratio is not produced when full time-dependency for H_2^* is implemented, and only marginal abundance enhancements are predicted.

However, in the extreme case of diffuse gas that is subjected to a dissociative , isothermal shock, significant enhancements of OH and CH^+ may be generated. These enhancements would be short-lived, only lasting as long as the time that it takes H_2 to re-form. Of course, if the dust grains are disrupted following the passage of the shock, then that timescale may be significantly greater than the $\sim 10^4$ years that the model predicts, although the abundance of H_2^* and its products would be reduced. In any case, it would seem likely that observable enhancements of OH and CH^+ may be produced in immediate post-shock boundary layers.

The rates for reactions (1.5) and (1.6) are strict upper limits in that they assume that the H_2^* excitation energy is sufficiently large to completely overcome the activation energy barriers. In reality any observable effects on $X(CH^+)$ and $X(OH)$ are therefore likely to be less extreme than those seen in the models. The value taken for the Einstein A-coefficient is also an approximate value, since it represents a summation of relaxational radiative transitions from the nominal excited level to the ground state. We have not attempted to model individual, specific transitions.

Ultimately, we are left with the conclusion that, even with the optimistic assumption

that all of the H_2 that is formed on the surface of grains is in an excited state, and with sufficient energy to overcome the activation energy barriers of key chemical reactions, the chemistry of the interstellar medium is only modified in extreme situations, and even then only for a short period of time.

The fact that possible energy excesses in the most abundant non-stellar form of baryonic matter in the Universe has only marginal effects on the chemistry of the interstellar medium is perhaps rather surprising. It is, however, somewhat re-assuring to know that existing models of the chemistry of the interstellar medium do not need to be revised radically in the light of the recent theoretical and experimental studies of the H_2 formation process.

1.3 Chemical effects of X-rays on a quiescent dense clump ahead of object HH 2 [2]

HH2 is a Herbig-Haro object lying in the constellation of Orion, at a distance of ~460 pc from the Sun. HH2 and its companion HH1 are regions of shocked gas situated at the heads of two jets emanating from a proto-star. These jets impact into the surrounding molecular cloud at supersonic speeds, causing bow-shocks at the interfaces. In the regions behind the shocks, high temperatures are attained, producing radiation in the optical, UV and radio. Chandra observations also indicate associated X-ray radiation (Pravdo *et al.* 2001).

Outwards from HH2, at a distance of ~0.1 pc, has been observed a quiescent dense clump of molecular gas. Recent observations (Girart *et al.* 2002) have detected 14 chemical species in the clump, and comparison with other similar environments shows enhancement in fractional abundances of some of these species. For example, HCO^+, CH_3OH and H_2CO are strongly enhanced, whilst SO and SO_2 are weakly enhanced. SO 3_2-2_1 emission-line contours suggest a radius for the clump of ~0.01 pc. The enhanced chemistry of the clump is what facilitates its detection, and its proximity to HH2 makes it very likely that it is the radiation from this object which is causing that enhancement; firstly by the evaporation of grain-depleted species back into the gas-phase, and secondly by the enhanced radiation fields causing photodissociation and photoionisation, stimulating and fuelling the chemistry. Previous modelling (Viti & Williams 1999) has suggested a hydrogen number

[2]The work of this section is part of a publication in Astronomy and Astrophysics (Viti *et al.* 2003)

Table 1.3: HH2 model parameter values for steps 1 and 2

Parameter	Step 1	Step 2
Initial density (cm^{-3})	3×10^3	3×10^5
Final density (cm^{-3})	3×10^5	3×10^5
Temperature, T (K)	10.0	10.0
Collapse period (years)	1 M	N/A
Total evolution period (years)	2 M	10000
Radiation field at near edge/Habing	1	20
C-R ionisation rate/ζ_0	1	1, 100, 1000

density of $n_H \simeq 10^5$ cm^{-3}, with a maximum visual extinction of 5 – 7; this range agrees with results for a number of observed species. The temperature of the clump is estimated from observational data to be ~10 K.

As a part of the study by Viti *et al.* (2003), I have attempted to model the chemistry of the clump, to investigate the effects of an enhanced X-ray field. Other variables tested in this body of work are the gas density, clump size, UV radiation field strength, and level of freeze-out. With this information we may construct a grid of models in all the variables in order to diagnose the most likely physical conditions in the clump. We have used parameter values (or ranges) concordant with the observations of Girart *et al.* (2002).

1.3.1 The model

The model used is a multi-point chemical model, and is a progression from the model of Viti & Williams (1999). The model uses 221 chemical species, and 3194 reactions, which includes deuterium chemistry, since two of the 14 species detected in the clump are the deuterated molecules DCN and DCO^+. Ten individual points were used, spaced equally along a line into the cloud away from the radiation source (object HH2). The model uses a single density and temperature for the whole cloud at any one time.

The complete model consists of two steps; the first step allows a more diffuse medium to isothermally collapse into a dense clump, and traces the chemical evolution of the object as it does so, and for a period afterwards, up to a time at which the enhanced radiation fields are assumed to start up. An important parameter in this collapse stage is

the amount of depletion, or freeze-out, onto grains. This parameter is not well constrained by observation, and the model was run to provide various depletion factors (15%, 40%, 60% and 80%) for the end of the collapse stage, although for my part of the study I have used only one value (see table 1.3 for parameter values used in the model). Depletion will obviously lower chemical abundances available for gas-phase reactions, and certain species which stick to the grains may be singly or multiply hydrogenated on the grain surfaces.

Through both stages, hydrogen and deuterium atoms were allowed to form H_2 and HD on the grain surfaces by reactions with hydrogen and deuterium atoms on the grains. Here the Eley-Rideal mechanism was used, i.e. instant formation and release of H_2 or HD upon a successful contact of the reactant with the grain surface. Deuterium atoms on grain surfaces are less abundant than hydrogen atoms, and so to take account of this, the rate of grain-situated deuterium reactions with incoming hydrogen was set lower than that of the equivalent H-H reaction. The reducing factor applied to the former was an estimate of the comparative abundance of deuterium to hydrogen on the grain surfaces, which we took to be the same as that of the gas phase: 10^{-5}. Hydrogen and deuterium were *not* allowed to stick to the grains.

The clump was set to collapse over a period of $\sim$1 million years, according to the modified free-fall collapse model of Rawlings *et al.* (1992), and then allowed to evolve for a further 1 million years. The timescales of both the collapse of the clump and the point in time at which it is affected by the radiation from HH2 are not accurately known, and so these could be sources of error.

In the second step, the enhanced UV radiation field is "switched on", and all grain-depleted species are instantaneously returned to the gas phase. Because some of these returning species will have been modified on the grain surfaces, this makes the level of freeze-out very important to this stage. The release of H_2O from grain surfaces, having been formed via hydrogenation of O and O^+ on grain surfaces, is called upon to explain the enhancement of HCO^+, which may be formed by the reaction $C^+ + H_2O \rightarrow HCO^+ + H$ in the gas-phase. The radiation field used for the second step was just the (Habing) radiation field used for the normal interstellar radiation field, multiplied (in this case) by a factor of 20. It is attenuated via an inverse-square law, dependent on depth into the cloud.

Also in the second step, an X-ray field is switched on. This X-ray field is approximated by an augmentation of the cosmic ray ionisation rate, ζ. This may be justified by observing

that whilst X-rays preferentially ionise heavier atoms, secondary electrons released in the de-excitation of these atoms are responsible for the majority of ionisations caused by X-rays. The ionising electrons preferentially ionise atomic and molecular hydrogen, thus mimicking cosmic ray ionisation (Lepp & Tiné 1998). This treatment takes no account of the absorption of X-rays in particular atomic lines, and disregards geometric attenuation effects, assuming a constant value of ζ throughout the cloud.

The irradiated clump was allowed to evolve at a fixed temperature and density for a period of 10,000 years - the clump would be unlikely to survive for a period any longer than this due to the encroachment of the shocked region. Three runs of the model were made using different values for the cosmic ray ionisation rate for step two: 1, 100 and 1000 times the canonical value, $\zeta_0 = 1.3 \times 10^{-17}$ s^{-1}. Values of the visual extinction at the ten depth points ranged from 1.1 to 6.3.

1.3.2 Results

Figures 1.8 – 1.10 show fractional abundances of selected species versus visual extinction, at times of 3 and 1000 years, using the three values of ζ = 1, 100 and 1000.

After three years, fractional abundances of neutral species are generally unaffected by the radiation field or the cosmic-ray/X-ray field at all visual extinctions. However the abundances of many ions are greater at lower A_V and are quite drastically increased by the augmentation of ζ; this is most obviously true for ionised atomic and molecular hydrogen and carbon. The plateau effect seen for some ions, e.g. C^+, at high A_V shows where ζ becomes important, and there $X(C^+)$ is visibly higher for higher ζ.

After 1000 years, fractional abundances of almost all neutral species have dropped considerably at low visual extinctions. At large visual extinctions, X(CO) is increased for greater ζ, particularly with ζ = 1000, and considering the absolute abundance of CO in this region, this counts for a great deal of carbon and oxygen. Here, molecules H_2O, NH_3, CH_4, H_2S and CH_3OH are appreciably reduced for increased ζ, with NH_3 and H_2S falling dramatically (2 - 3 orders of magnitude) for ζ = 1000, compared to the ζ = 1 case. Formaldehyde abundance stays fairly stable for different ζ-values, whilst the deuterated HDCO is heavily suppressed with increasing ζ.

Figure 1.8: Fractional abundances across the clump, $\zeta = 1$

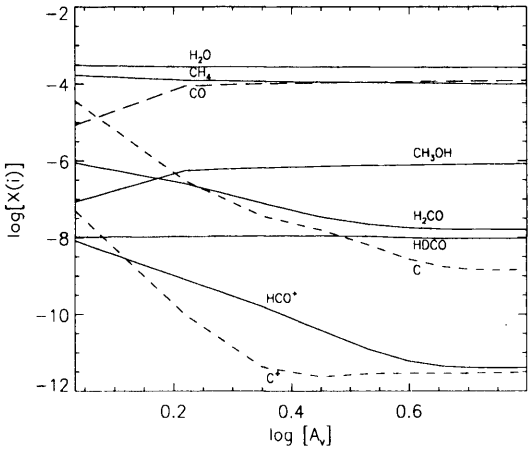

a: Species set 1, $t = 3$ yrs

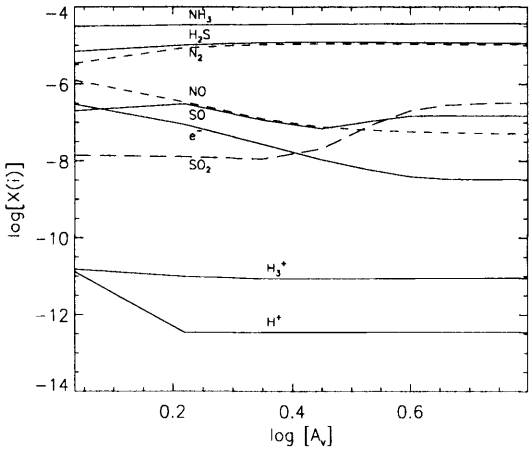

b: Species set 2, $t = 3$ yrs

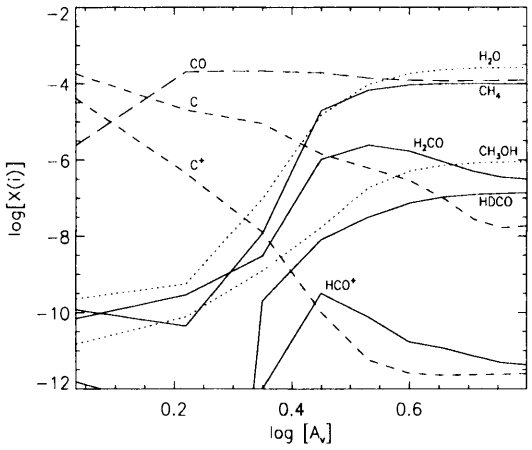

c: Species set 1, $t = 1000$ yrs

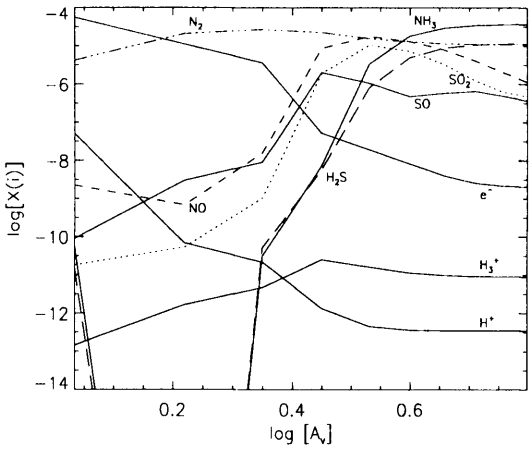

d: Species set 2, $t = 1000$ yrs

1.3.3 Discussion

The primary effect of the increase in ζ is to raise the abundances of various ionised species (mostly single atoms) compared to their neutral abundances. This effect is most obvious at high A_V, where the cosmic-ray/X-ray mechanism is the only significant contributor to ionisation, since the radiation field is heavily suppressed. The increase in ζ also causes more photodissociation of molecules. This is due to a secondary radiation field which results from the relaxation of H_2 molecules excited by the secondary electrons of cosmic-ray/X-ray interactions (see *e.g.* Gredel *et al.* 1987,). This increased (cosmic-ray/X-ray) dissociation of CO causes a significant increase in C at high A_V, where the abundance of

Figure 1.9: Fractional abundances across the clump, $\zeta = 100$

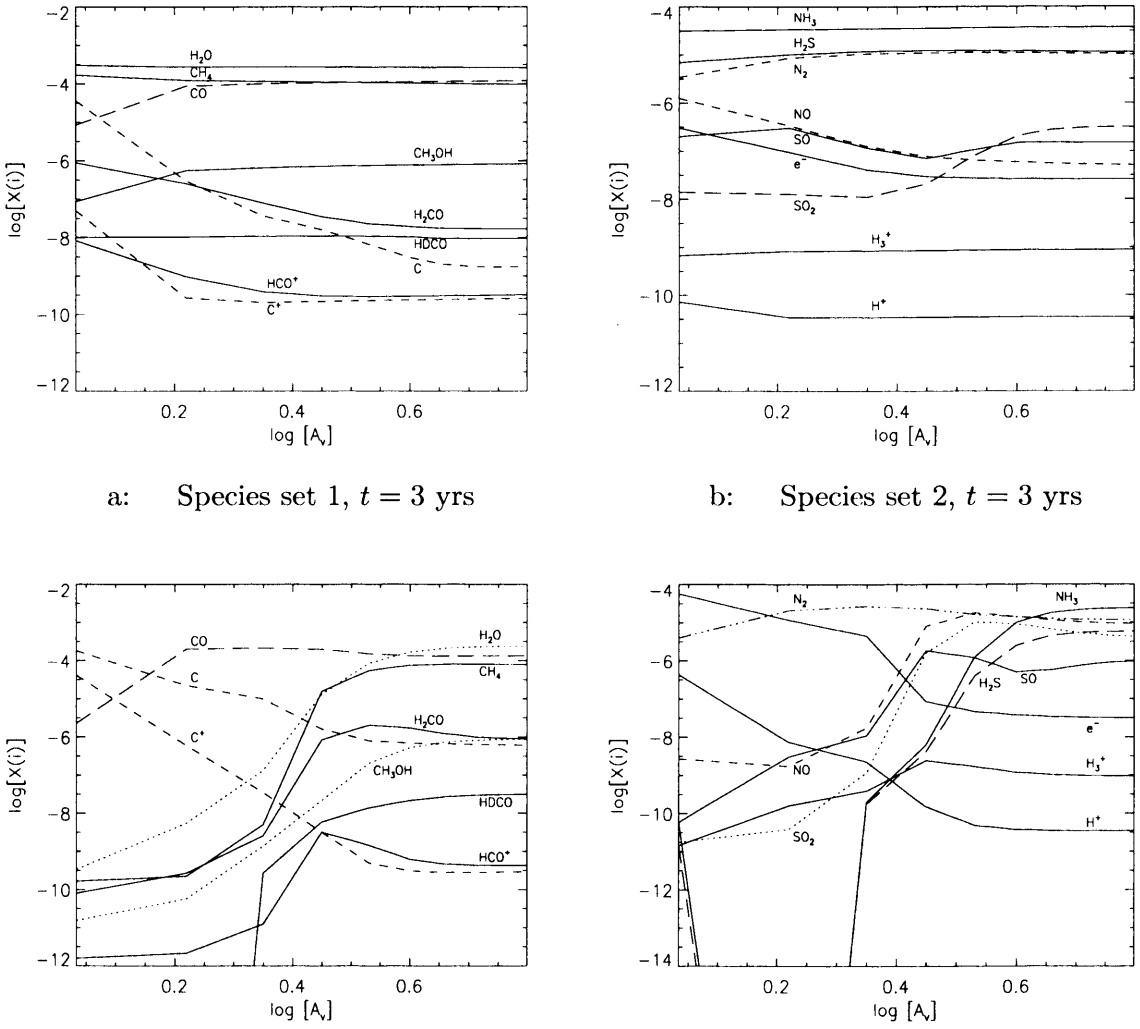

a: Species set 1, $t = 3$ yrs

b: Species set 2, $t = 3$ yrs

c: Species set 1, $t = 1000$ yrs

d: Species set 2, $t = 1000$ yrs

C is lowest. This in turn allows higher values of C^+ via cosmic-ray/X-ray ionisation of C. The C^+ may then readily react with H_2O, which at early times is abundant at all depths due to evaporation of icy mantles, enhancing HCO^+.

After 1000 years, ion-neutral reactions and photodissociation have greatly reduced abundances of most molecules at lower A_V, for all ζ-values. In the case where $\zeta = 100$, at high A_V the increased ionisation degree (quantified by $X(e^-)$ in the figures) causes the considerable losses in the most abundant molecules, like H_2O, NH_3, CH_4 and H_2S. CO, which is already very abundant, is the main beneficiary of the destruction of H_2O and CH_4.

Figure 1.10: Fractional abundances across the clump, $\zeta = 1000$

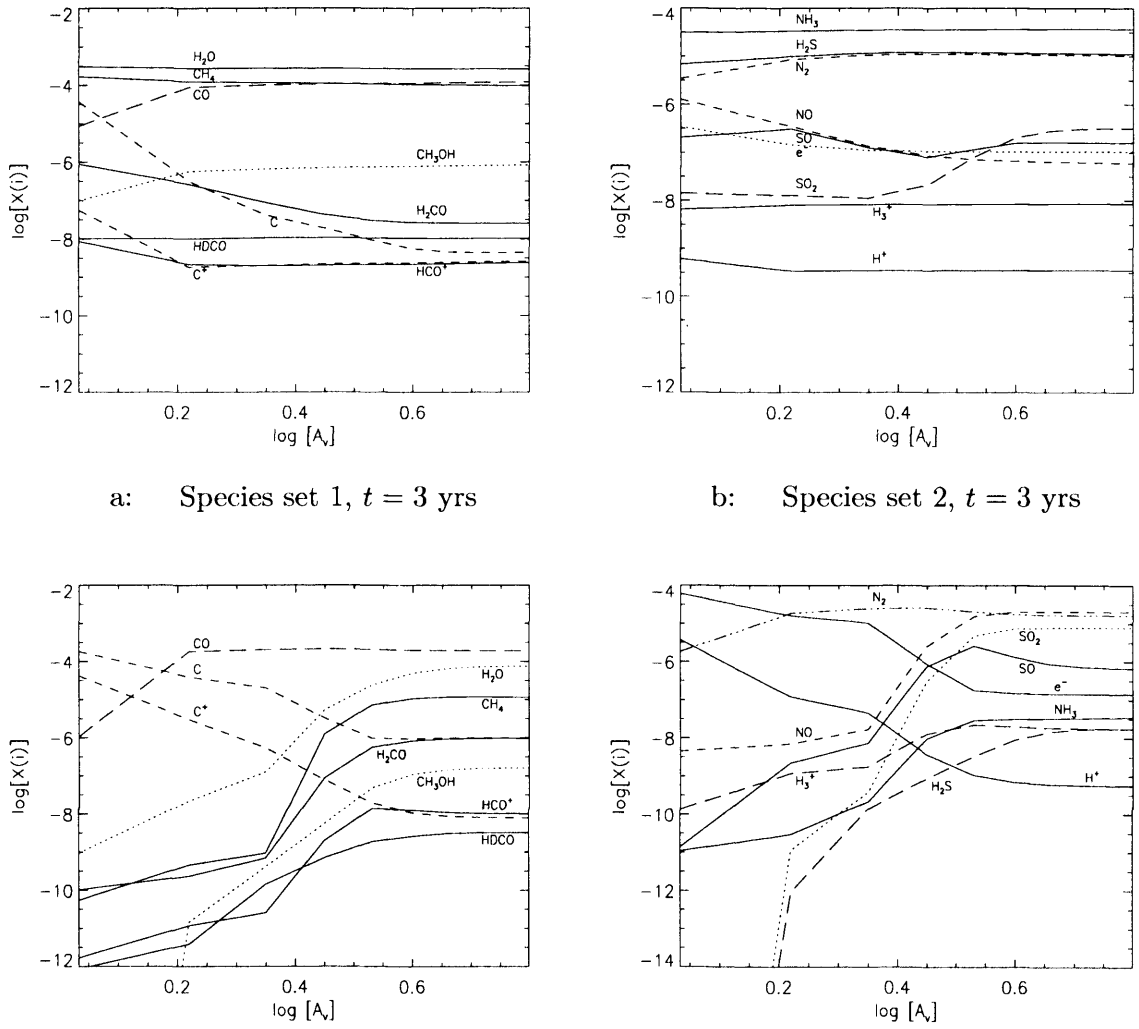

a: Species set 1, $t = 3$ yrs

b: Species set 2, $t = 3$ yrs

c: Species set 1, $t = 1000$ yrs

d: Species set 2, $t = 1000$ yrs

The enhanced ionisation degree causes ion-neutral reactions to destroy CH_4 to form ions like CH_3^+, which through further such reactions (many of which destroy H_2O), act to enhance HCO^+ and H_2CO (which may also be destroyed in ion-neutral reactions to form more HCO^+). This HCO^+ can then react with any of the more abundant molecules to produce more CO.

HCO^+ is seen to be strongly enhanced with the augmented X-ray field at large A_V (compare $X(HCO^+) \simeq 10^{-12}$ for $\zeta = 1$ to $X(HCO^+) \simeq 10^{-8}$ for $\zeta = 1000$). Methanol is not strongly affected for $\zeta = 100$, however for $\zeta = 1000$, the increased cosmic-ray/X-ray-induced photodissociation and ion-neutral reactions destroy it more noticeably. At

$\zeta = 1000$, cosmic-ray/X-ray photodissociation reactions will have become comparable to ion-neutral reactions in their influence, for many molecules.

The destroyed H_2S contributes to an increase in other sulphur-bearing molecules, particularly SO_2 at high A_V. SO is not similarly enhanced at these A_V values, causing an increased SO_2/SO ratio. CS is also enhanced at high A_V, strongly for $\zeta = 1000$.

NH_3 is destroyed via ion-neutral reactions, forming NH_2^+ and NH_3^+. This may react with O and O_2 to form HNO^+ or with N to form N_2H^+, both of which may react with many of the more abundant molecules (further depleting them) to form NO or N_2 respectively. These two species are the main beneficiaries of the destruction of NH_3.

1.3.4 Conclusions

This work has demonstrated the trends in the chemistry of the clump ahead of object HH2 for different values of the incident X-ray field. This alone cannot provide a perfect match for the physical conditions present in this particular environment, but combined with the trends observed, through similar models, for changes in other variables, we may find a combination which agrees well with observations.

Uncertainties do exist in many of the parameters used for this model; the collapse period and point at which irradiation should commence, the amount of freeze-out, the size of the clump, and the amount and composition of material residing along our field of view, in front of the clump, contributing to observed column densities.

I have made a run allowing the X-ray field to be attenuated with distance from the source; however this actually has little effect on the chemistry. A fuller, more accurate representation of the X-ray field (rather than the cosmic-ray approximation made here) might yield some noticeably different results, particularly if the absorption in lines were taken into account.

CHAPTER 2

Chemical Modelling of Transient Dense Cores[3]

2.1 Introduction

A number of studies have identified small-scale density inhomogeneities in dark clouds, e.g. Morata *et al.* (2003), Girart *et al.* (2002). Morata *et al.* (2003) used the BIMA interferometer array to make observations of a dense condensation in the L673 region, in the molecular transitions of CS ($J = 2 \rightarrow 1$), N_2H^+ ($J = 1 \rightarrow 0$) and HCO^+ ($J = 1 \rightarrow 0$). The greater resolution provided by this instrument revealed a smaller-scale structure than previously seen with a single dish. Several cores of gas of size $\leq$0.08 pc were detected in each molecular line, most with the molecular line maxima displaced from each other. This suggested a heterogeneous medium of cores, of various densities and at various stages of chemical evolution.

Girart *et al.* (2002) carried out a molecular line survey of a dense quiescent core (scale of $\sim$ 0.1 pc) ahead of the Herbig-Haro object HH2 which showed an enhanced chemistry. The illumination of the core with a UV field emanating from the shocked region HH2, and the subsequent chemical enhancement, aided in its detection. Follow-up modelling work (Viti *et al.* 2003) suggested that only a short period of time had passed since irradiation had commenced ($\sim$100 yr), implying that the core's formation was not a result of the dynamical action of HH2. The models also indicated that the core had spent only a moderate period

[3]The work of this chapter is published in Monthly Notices of the Royal Astronomical Society (Garrod *et al.* 2005)

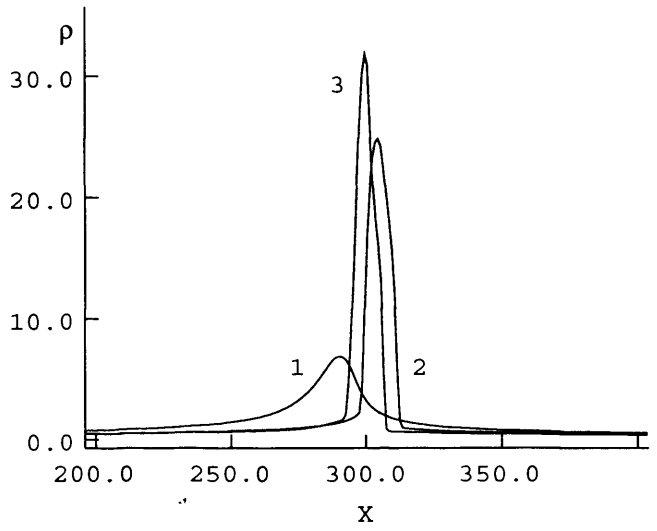

Figure 2.1: Density profiles at three different times in collapse phase, from FH02, figure 6a

at high-density (<2 Myr) before irradiation, which could indicate a transient nature for such objects.

In this chapter, we postulate that molecular clouds are largely made up of assemblies of transient cores surrounded by a more diffuse medium from which they condense. Obviously the relationship between star formation and cores implies that self-gravity is important in some cores; cores bound by their self-gravity will not be transient in the sense that we are considering at least some of the cores to be transient.

Traditionally, core formation has been attributed to the effects of self-gravity (*e.g.* Fiedler & Mouschovias 1992, Ciolek & Mouschovias 1995). Self-gravity can induce core formation even in regions where the thermal and magnetic pressures are initially comparable (*e.g.* Balsara *et al.* 2001).

However, since the publication of the paper by Arons & Max (1975), many authors have considered the material from which molecular cores form to have initially low values of the thermal pressure to magnetic pressure ratio, β. As discussed by Falle & Hartquist (2002) (hereafter, FH02), when this ratio is initially small the presence of waves with magnetically dominated amplitudes within the translucent clumps of Giant Molecular Clouds leads to high density, transient structures on many scales including those in which self-gravity is unimportant. The formation of high density constrast transient structure involves the excitation of slow-mode waves as a consequence of the nonlinear steepening of fast-mode waves. The mechanism does not lead to much larger density contrasts than initially present

unless the initial magnetic pressure is much larger than the initial thermal pressure. The numerical results in FH02 are for plane-parallel, time-dependent MHD models, designed to gain an understanding of the nonlinear mechanism leading to the formation of structure with density constrasts in excess of ten. They are currently extending the work to more dimensions, and the mechanism that they have identified is no doubt important in existing multi-dimensional studies of core formation in magnetized media in which self-gravity has been included (*e.g.* Gammie *et al.* 2003). However, the inclusion of the self-gravity and the way in which the simulations have been analyzed do not facilitate an examination of the importance of the mechanism discussed by FH02.

With the possibility in mind that at least some cores are not bound by their self-gravity and are transient, we attempt to simulate the chemistry of one of these cores as it evolves physically, over a characteristic time-scale of approximately 1 million years, with the main purpose of finding tracers for its evolution. This requires a description of the way in which cores form, evolve, and eventually disperse, from the point of view of a parcel (or parcels) of gas within a core. FH02 conducted simulations of plane-parallel magneto-hydrodynamic waves passing through a cold plasma, and found that modest density perturbations could lead to the growth of significant density inhomogeneities. They produced a number of spatial density profiles, which, very broadly, showed an initially shallow-peaked function evolving into a sharp, strongly peaked function, gradually dying away again. Our figure 2.1 shows figure 6a from FH02: spatial density profiles for three different times in the growth stage, $t = 3, 3.5, 3.6 \times 10^3$. Units are determined according to parametrization of variables in FH02. Plots of the time-evolution of the *peak density* showed another similarly peaked function.

In order to obtain a chemical description of the dense cores, we are required to make qualitative approximations to the density profiles of FH02, and use these in independent chemical codes. This is necessary since the construction of a coupled MHD-chemical code with which detailed chemical observations of dense structures can be explained is at present a long way off. Whilst in the FH02 simulations only one spatial variable is considered, this is the only work to address specifically the generation of structure in a low-β environment by the mechanism of slow-mode excitation in fast-mode shocks. Many multi-dimensional MHD simulations exist. However, almost all have been performed with codes based on non-conservative schemes; Falle (2002) has pointed out the difficulties with such codes for even very simple problems. Moreover, almost all such calculations have either followed

the decay of artificially imposed velocity and density spectra or have included distributed source terms to drive "turbulent" motions in a totally unphysical manner. In reality, the internal motions are driven by perturbations at the boundaries. Even in simple geometries, the construction of the boundaries and boundary conditions requires serious thought.

Hence, because the FH02 results are presently the most relevant to the picture that we are exploring, and because of the simulations' plane-parallel character and the non-linear, non-Alfvénic nature of the perturbations, we are restricted to a qualitative approach to the incorporation of their density profiles into a chemical model.

To do this, we here approximate them as Gaussians in space and time, which they resemble. We model the spatial density profile as a Gaussian whose scale varies with time. The central density of the core (to which the densities at all other points are referred) also follows a time-dependent Gaussian. The resulting space- and time-dependent Gaussian is constrained by the conservation of mass. No other hydrodynamic conservation equations (i.e. energy, momentum) are included. Rather, realistic time-scales and distances adopted for the collapse and expansion are specified. The space- and time-dependent visual extinction through the core is calculated as a function of density.

By simulating the chemistry of a core in this way, and focusing on a number of parcels of gas at positions from centre to edge, we attempt to build up a picture of the entire core, to find chemical tracers of its evolution, and to describe the spatial behaviour of these tracers. This study may then provide a means by which to put some constraints on the ages and the evolution of physical and chemical conditions of actual cores. Further, we may illuminate the connection between the cores and the surrounding diffuse medium, and see how the transient cores act to enhance the overall chemical composition of a dark cloud. In this chapter we test the hypothesis that cores are in a continual state of dynamical evolution and we identify potential chemical diagnostics of such activity. In future work we will consider a cloud to be an assembly of such transient dense cores.

2.2 Density and Visual Extinction as Functions of Position and Time

We take the spatial density profile to be a Gaussian, whose amplitude also varies as a time-dependent Gaussian:

$$\rho(z,t) = \rho(0,t_m)\exp\left[-\left(\frac{z}{\Delta z(t)}\right)^2\right]\exp\left[-\left(\frac{t-t_m}{\tau}\right)^2\right] \tag{2.1}$$

where $\rho(z,t)$ is the gas density, z is position in the core from the centre outwards, t is time, $\rho(0,t_m)$ is the peak central density, t_m is the time at which peak central density occurs, $\Delta z(t)$ is the core's length scale, and τ is a time-scale. The time-dependence of the length scale allows for a mass-conservation condition to be imposed.

t_m is the time-scale for the collapse of the core down from its most diffuse (initial) state to its most condensed state. Because of the condition of the conservation of mass, the length scale must be determined in a time-dependent way. Mass-conservation also requires the z-position of a chemical reference point to vary as the collapse and expansion take place, in order to represent the same parcel of gas at all times. A fluid element should move such that the mass interior to its position stays constant. In order to implement this condition, a mass element has to be constructed. The mass element was set up to allow for a multi-dimensional collapse, using one principal axis:

$$\mathrm{d}M = C_k\ \rho(z,t)\ z^{k-1}\ \mathrm{d}z \tag{2.2}$$

This, of course, still uses the 1-D density profile $\rho(z,t)$, but provides a way to take account of the effects of a higher than one-dimensional collapse and expansion, which is likely. k represents the "dimensionality" of the collapse – the number of dimensions along which collapse occurs. C_k is a geometrical constant; in a three-dimensional case, if collapse occurs at the same rate along each axis, $C_3 = 4\pi$. (C_k may be assumed to incorporate length constants when $k \neq 3$, however C_k is not actually needed for any of the programme calculations, and is included here merely for completeness). We may use non-integer values of k and integer values of k other than 3 to represent unequal rates of collapse along different axes. Substituting equation (2.1) into equation (2.2) and integrating from $z = 0$ (core's centre) out to some $z = a$ gives the following integral in z:

$$M_{int}(z=a,t) = C_k\ \rho(0,t_m)\ f(t)\ \int_0^{z=a}\exp\left[-\left(\frac{z}{\Delta z(t)}\right)^2\right] z^{k-1}\mathrm{d}z \tag{2.3}$$

where $M_{int}(z=a,t)$ is the mass internal to the boundary defined by the point $z = a$ and the dimensionality of collapse, k, and $f(t)$ represents the second exponential in equation (2.1). When $k = 1$, the integral is just a multiple of the complimentary error function. When $k \neq 1$, the solution takes the form of a convergent series in z and $\Delta z(t)$. This

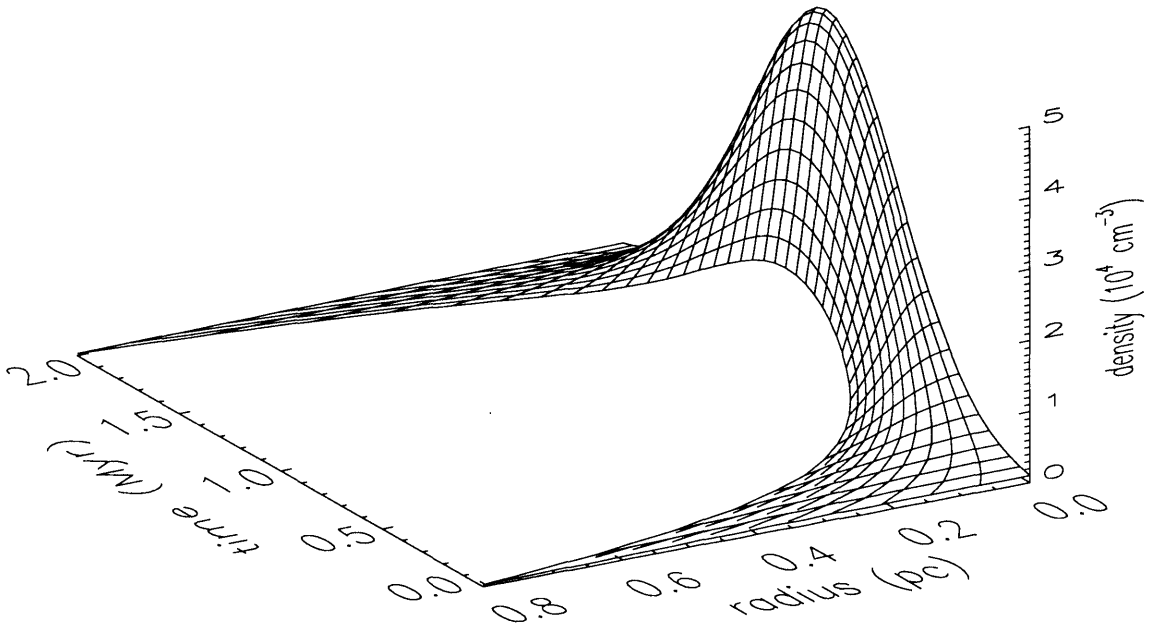

Figure 2.2: Density profile as a function of time

solution may be simplified by parametrizing such that:

$$z(t) = \alpha \Delta z(t) \tag{2.4}$$

For equation (2.4) to hold true, and hence for α to be time-independent and to represent the same parcel of gas at all times, we require that $M_{int}(\alpha \Delta z(t_1), t_1) = M_{int}(\alpha \Delta z(t_2), t_2)$. This condition is true if we assume that the mass enclosed within $\alpha \rightarrow \infty$ (i.e. the total mass) is conserved.

This parametrization leaves a convergent series in α only:

$$M_{int}(\alpha \Delta z, t) = C_k \; \rho(0, t_m) \; f(t) \; [\Delta z(t)]^k \sum_{n=0}^{\infty} \frac{(-1)^n \alpha^{(2n+k)}}{n!(2n+k)} \tag{2.5}$$

which requires the sum to be calculated only once for all time values. Mass-conservation relates equation (2.5) for two different times, hence:

$$\Delta z(t) = \left[\frac{\rho(0, t_m)}{\rho(0, t)} \right]^{\frac{1}{k}} \Delta z(t_m) \tag{2.6}$$

The parameterisation of z reduces the density expression to:

$$\rho(\alpha, t) = \rho(0, t_m) \exp\left[-\alpha^2\right] \exp\left[- \left(\frac{t - t_m}{\tau} \right)^2 \right] \tag{2.7}$$

$\Delta z(t)$ is still required for the calculation of the visual extinction (and the computation of instantaneous column densities, so that line self-shielding may be taken into account in the H_2 and CO photo-dissociation rates). We set:

$$A_V(\alpha,t) = k_A \int_{\alpha\Delta z(t)}^{\infty} \rho(z,t)\,\mathrm{d}z$$

$$A_V(\alpha,t) = k_A \int_{\alpha\Delta z(t)}^{\infty} \rho(z,t)\,\mathrm{d}z \exp\left[-\left(\frac{z}{\Delta z(t)}\right)^2\right]\mathrm{d}z \qquad (2.8)$$

This integral is a multiple of the complimentary error function. Retaining the form used for equation (2.5), and substituting for $\Delta z(t)$, we have:

$$A_V(\alpha,t) = k_A\,[\rho(0,t_m)]^{\frac{1}{k}}\,[\rho(0,t)]^{(1-\frac{1}{k})}\,\Delta z(t_m)\left[\frac{\sqrt{\pi}}{2} - \sum_{n=0}^{\infty}\frac{(-1)^n\alpha^{(2n+1)}}{n!(2n+1)}\right] \qquad (2.9)$$

Since α is time-independent, the above sum need be evaluated only once in the program (per α-value).

The physical free parameters available with this method of modelling are:

- k = dimensionality of collapse
- $\Delta z(t_m) \Rightarrow$ defines width of core
- $\rho(0,0)$ = initial central density
- $\rho(0,t_m)$ = peak central density
- t_m = time at which peak density is reached
- τ = time-scale over which core density changes

The density profile is constrained to be a Gaussian, so only three of the last four parameters are independent. In this study we use the first five parameters in the above list.

2.3 Chemical model

The chemical model (see Viti & Williams 1999) is a code describing the chemistry of a set of 221 species, including dust grain mantle-bound species and deuterated species, interacting via 3288 reactions. Reaction rates are obtained from the UMIST database

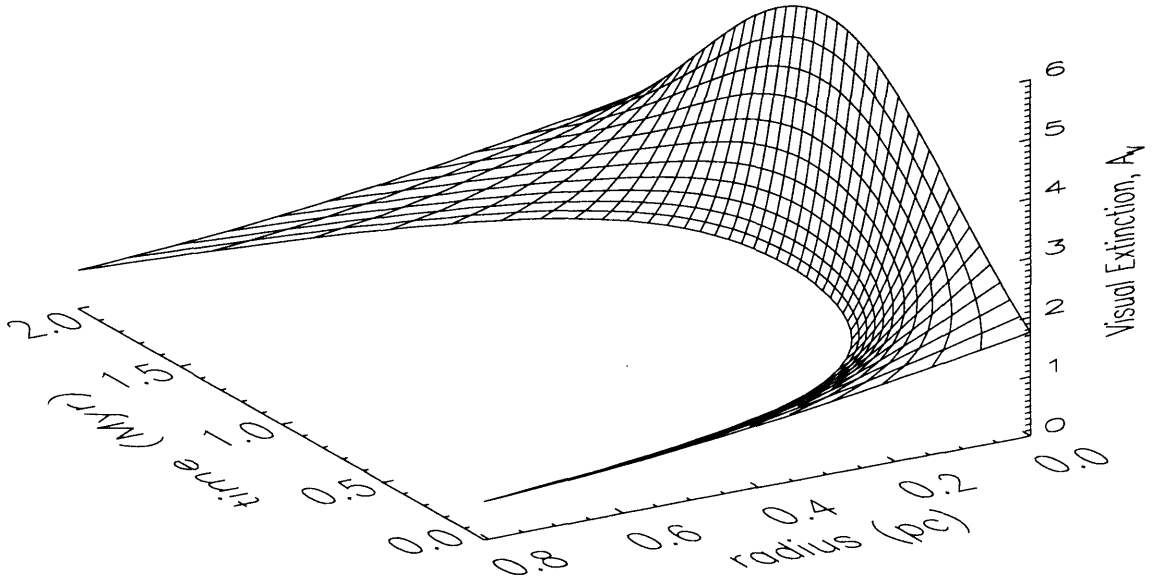

Figure 2.3: Visual extinction profile as a function of time

(Millar *et al.* 1997). We take 12 points, whose positions through the core are defined by their assigned α-values and the scale-width of the core via equations (2.4) & (2.6), and whose density and A_V vary according to equations (2.7) & (2.9). Since distance is parameterised, the only dependence of the chemistry on the *actual* positions of the points is in the calculation of A_V and of column densities of H_2 and CO for their photodissociation rates. Calculation of these column densities is done by a step-wise integration of absolute abundances through every chemical reference point external to the point in question.

The model is run in two stages: in the first stage the chemistry is run to equilibrium (without freeze-out), to obtain values for a chemically evolved diffuse background from which the dense core forms. For this we use a static Gaussian density profile identical to the initial profile for stage two. As may be seen from figure 2.2, this initial density profile is quite shallow compared to that for $t = t_m$. The second stage is the collapse/expansion stage, and includes freeze-out reactions – the sticking and retention of gas-phase species on collision with dust grains, and their subsequent grain-surface reactions.

Freeze-out in stage two is selectively applied according to the visual extinction at each point; this represents the sharp change-over in the retention of dust grain mantles as the penetration of the interstellar radiation field varies in the transition from diffuse medium to dense core and back. Initially only those points with A_V above a critical value, here

assumed to be 2, have freeze-out (Whittet 2003, p.176); however as the core collapses, freeze-out is switched on in more points as they fulfil this criterion. After reaching peak time, the core expands and disperses; as points gradually fall below the critical A_V again, their freeze-out reactions are switched off and the frozen-out species are instantly returned to the gas phase. The critical value of 2 is chosen as representative of the threshold between diffuse and dark conditions, in accordance with the range of observationally determined values of between approximately 2 and 3 shown in Whittet (2003). This lower limit was chosen to ensure that those points which would pass above the critical visual extinction should have time to accrue significant mantles for re-injection into the gas phase.

Some of the freeze-out reactions simply convert gas phase species into mantle-bound species, representing sticking only, for those species which do no more. Other freeze-out reactions represent both sticking and subsequent grain-surface chemistry, which is accounted for in a time-independent way. Those species which may react are simply attributed different mantle-bound products. In this way, they instantly reach their final chemical state.

Almost all species are assumed to freeze out, the main exceptions being the hydrogen species, H, H^+, H_2, H_2^+ and H_3^+, and helium atoms and ions. H forms H_2 on dust grain surfaces which is ejected directly to the gas-phase, and is dealt with completely separately in the code; references to freeze-out exclude this reaction which is assumed to take place at all visual extinctions. The grain-surface reactions (as opposed to just sticking) are mostly hydrogenation reactions. Freeze-out of ions onto grain surfaces results in a recombination of the reactant with a grain-based electron. For the dark cloud conditions which we model, grains are expected to carry a charge of -1, due to electron collisions (see Umebayashi & Nakano 1980). Some of the recombinations are dissociative, leading to the ejection of a hydrogen atom into the gas-phase. We assume no branching in the grain-surface reactions except in the case of carbon monoxide, which either sticks without reaction (99 per cent), or is hydrogenated to form methanol (1 per cent). This represents the maximum amount of CO conversion to methanol (Viti & Williams 1999). The sticking efficiencies of all species are assumed to be essentially the same; however, a differentiation is made between ions and neutrals in their freeze-out rates (see Rawlings *et al.* 1992). At a temperature of 10 K, positive ions freeze out approximately 18 times faster than neutrals; this is again due to the -1 grain-charge which we expect in those regions we model here.

The rate of freeze-out is a free parameter, and is controlled in the chemical code via

Table 2.1: Initial elemental fractional abundances (stage 1)

Species i	$n_{init}(i)/n_H$
H	0.33
He	0.07
C	1.0×10^{-4}
O	2.0×10^{-4}
N	2.0×10^{-5}
S	3.0×10^{-6}
D	1.0×10^{-5}
Mg	2.0×10^{-7}

the quantity *fr*. The freeze-out parameter *fr* is the product of the sticking coefficient, S (which may range from 0 - 1), and the average grain surface area in units of the canonical value (hence normally taking a value of 1). The canonical value of grain cross-section per hydrogen nucleon, $\langle d_g \pi a^2 \rangle$, adopted here (for $Q_{ext} = 1$) is 6.9×10^{-22} cm^2 (Rawlings *et al.* 1992).

Above the critical A_V, the freeze-out parameter is set to $fr = 0.1$ (in the particular computational results which we exhibit in this chapter). This value of *fr* was chosen as a typical value, and in later work will be subject to change, as an important free-parameter. Below the critical A_V, the freeze-out parameter is set to $fr = 0$ to inhibit sticking to grain-surfaces, effectively setting all grain-surface reaction rates to zero (excluding H_2 formation). The side effect of this is to inhibit grain surface reactions which could take place when A_V is too low for the products to be retained on the surfaces in the long-term, but which could result in gas phase products instead. However, the presence of such an unattenuated radiation field would also affect whether and for how long the reactants stick to grain surfaces. When only considering grain surface reactions at above the critical A_V, the reaction products we cite in our ratefiles represent the end points of the surface chemistry, and so time-dependence is not an issue (although the sticking efficiencies and rates adopted for the surface chemistry are still highly imprecise due to the current poverty of information). In a low-A_V environment, many more grain surface "reaction pathways" would open up to an incoming reactant, as it could potentially be released in any of a number of states of hydrogenation. Also, the grain surface hydrogen atom population may

Table 2.2: Model parameter values (stage 2)

Initial central density, $\rho(0,0)$ (cm^{-3})	1000
Maximum central density, $\rho(0,t_m)$ (cm^{-3})	50,000
t_m (Myr)	1
Total evolution time, t_t (Myr)	2
$\Delta z(t_m)$ (pc)	0.045
Dimensionality of collapse, k	1.5
Maximum central A_V	5.1
Temperature, T (K)	10
Freeze-out parameter, fr	0.1

be different in the low A_V environment. This is a complex issue (which is by no means comprehensively dealt with even above the critical A_V in this model), however below the critical A_V, grain surface reactions are still likely to be very much less important than at high visual extinction, due to the very much reduced chances of sticking at all, and the likelihood that any resultant small increases in gas-phase abundance of the products would be quickly swallowed up in other reaction pathways, rather than large abundances being injected into the gas-phase in bulk. This scenario is something which we may investigate further in future.

The diffuse gas surrounding the core is factored into the core model through the choice of a representative visual extinction (0.5) to add to the calculated values for points inside the core, and a representative uniform density of 300 cm^{-3}. This density is not directly applied in any way in the code but guides the choice of free parameters and α-points by serving as a minimum density value.

Each point in the core is assigned an α-value ranging from 0 (core centre) to 1.1, in increments of 0.1. The outer value of $\alpha = 1.1$ is chosen so that the gas density does not drop below 300 cm^{-3} over the time-scale of evolution, when assigning a minimum central density of 1000 cm^{-3}. The peak central density is 5×10^4 cm^{-3}, a factor of 50 difference between initial and peak times, implemented by the choice of τ in equation (2.7).

Due to magnetic field lines pervading the cloud from which the core forms, collapse is likely to take place preferentially along one dimension, whilst much less vigorous collapse takes place along the other two. This would imply a dimensionality of collapse greater

Figure 2.4: Fractional abundances across the core

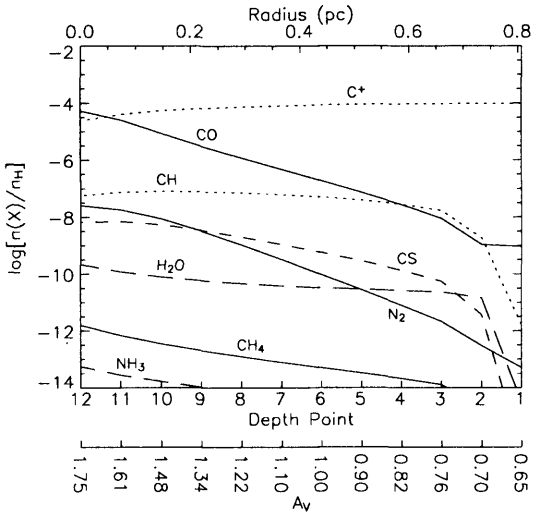

a: $t = 0$ Myr

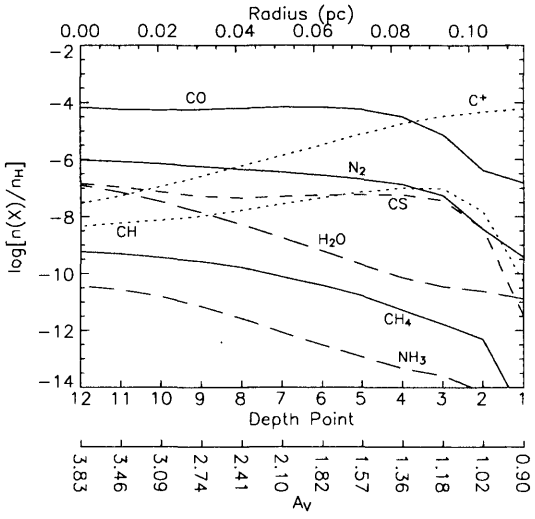

b: $t = 0.5$ Myr

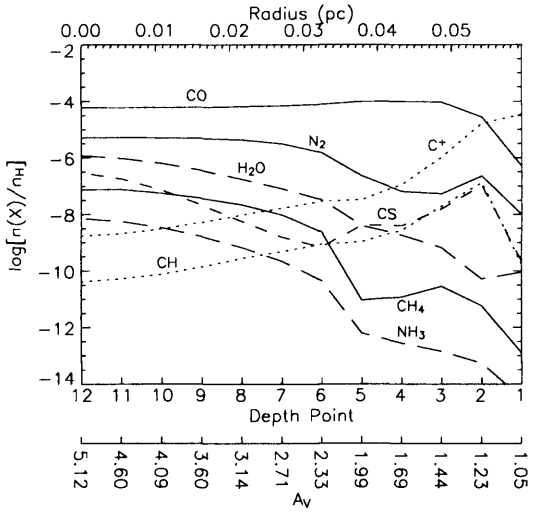

c: $t = 1$ Myr (peak time)

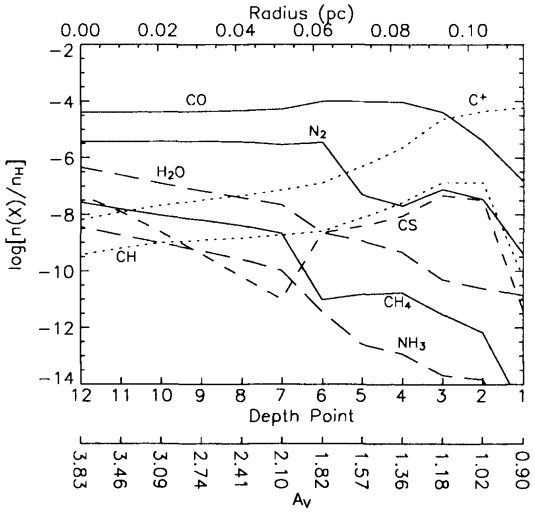

d: $t = 1.5$ Myr

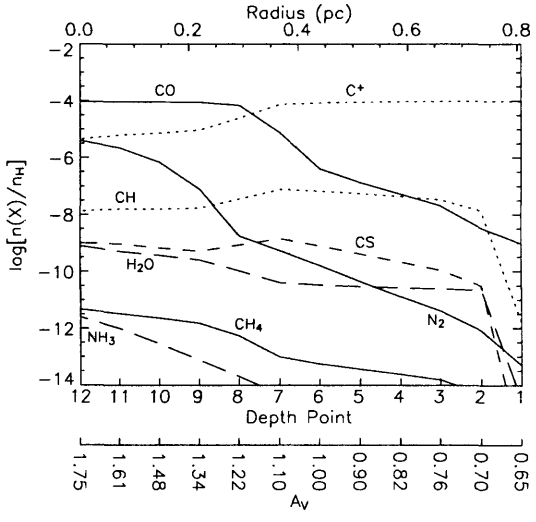

e: $t = 2$ Myr

than 1, but less than 2, since full collapse along two dimensions is not taking place. Hence a value of $k = 1.5$ was chosen for this run. As a consequence $A_V \propto \rho^{\frac{1}{3}}$ for a constant value of α.

Table 2.1 gives initial elemental abundances with respect to hydrogen nuclei, used at the beginning of stage 1, for a representative case. All values except the last two were taken from Ruffle *et al.* (1999). Magnesium, the representative metal, was adjusted to provide a fractional ionisation of $\leq 10^{-8}$ for the central regions of the clump (i.e. where ionisation is caused solely by cosmic ray ionisation), at peak time, consistent with the formula of McKee (1989), $x_e \simeq 10^{-5} n(\mathrm{H_2})^{-1/2}$. The abundance of deuterium is an order of magnitude value obtained from Linsky *et al.* (1995).

Table 2.2 shows the parameters employed for stage 2, the results of which are explored in the next section.

2.4 Results and discussion

Figure 2.2 shows the changing density profile. Each curve at a particular time represents a spatial density profile. To more easily convey their shapes, profiles are shown at intervals of 5×10^4 years. The twelve depth points are plotted along each line of constant time. As the profiles become steeper, the depth points move inwards, due to the collapse. Figure 2.3 similarly shows the visual extinction profiles.

Figures 2.4a - e show chemical abundances with respect to total hydrogen density, for five time values through the core's evolution in stage 2; $t = 0$, $t = 0.5$ Myr, $t = 1$ Myr (peak time), $t = 1.5$ Myr, $t = 2$ Myr (end-time). Note the three horizontal scales; depth point, radius of that point from the core centre, and visual extinction. The radius and A_V scales are time-dependent, while symmetric about the peak time (see figures 2.2 & 2.3). Note that A_V is not a linear scale; it is defined according to equation (2.9). The species whose fractional abundances are shown in the figures are mostly commonly observed molecules, and were chosen also to exemplify the chemical behaviour within the transient cores.

As the density and A_V increase, (larger) molecules become more abundant. Note in particular the increases in the abundances of CO and N_2, for which the enhancements are by far the most significant. The larger molecular abundances which form in the higher density/A_V conditions around $t = t_m$ are able to survive for some time, as the core disperses. This allows transportation of these molecules out into more diffuse regions.

Compare the *spatial* extent of CO, N_2, H_2O and NH_3 at peak-time with that much later; they have been transported out to distances of approximately ten times the extent of the fully condensed core. For example, at $t = t_m$, CO maintains a high value out to a core radius of about 0.05 pc (figure 2.4c) while at $t = t_t$ this same high fractional abundance extends to a core radius of about 0.3 pc (figure 2.4e). This result may be important for the molecular content of a cloud, depending on the number density and filling factor of the transient cores within it. For a sufficiently high number density of cores (as suggested by the observations of L673 by Morata *et al.* 2003) the overlapping regions of re-expanded cores could dominate the chemistry in the inter-core medium. Note also the relative extents of NH_3 and CS. They display broad agreement with observations of molecular rotational line emission in dense cores (*e.g.* Myers *et al.* 1991) which have shown CS emission to be more spatially extended than that of NH_3, despite expectations of the converse, based on the lower critical density for emission of NH_3 (see *e.g.* Rawlings 1996, and references therein).

The freeze-out has the effect of on one hand hydrogenating certain species to form larger molecules, e.g. a fraction of carbon monoxide to methanol, but on the other hand of protecting molecules formed on grains or acquired from the gas-phase from destruction pathways, until the mantles are later re-injected into the gas-phase. The removal of molecules from the gas-phase therefore results in much larger abundances of many molecules, when considering the combined grain-surface and gas-phase abundances, as destruction reactions may no longer affect the grain-depleted fractions.

The effect is large; the inner seven points pass through the critical A_V by the time that the peak density is reached (all points are initially below the critical A_V). At $t = 2$ Myr at depth points 7 - 12, CO is significantly enhanced (in absolute terms) above the levels seen at $t = 0$ Myr. Some of this increase is directly due to the return of grain-depleted material back into the gas-phase; the rest is just a consequence of the high density, high A_V environment reached near the peak time. The CO survives long after the peak time until the visual extinction reaches around 1, at which point line-shielding from photodissociation is no longer effective.

The CS abundance is governed according to two chemistries; one dominated by gas-grain interactions (freeze-out) and one dominated by the gas phase chemistry. This leads to the double peak features prominent in figures 2.4c and 2.4d, at 1 and 1.5 Myr.

The main formation mechanism for CS at 1 Myr is recombination of HCS^+, and at

depth points 7 and 8, recombination of H_3CS^+. At the points where freeze-out does not occur (i.e. $A_V < A_{V,crit.}$), the abundance of CS follows the evolution of CH and C_2, through the following sequence. Initially, CS^+ is formed:

$$S^+ + CH \longrightarrow CS^+ + H$$
$$S^+ + C_2 \longrightarrow CS^+ + C$$

where the C_2 reaction is dominant at the edge of the core, and the CH reaction is dominant from depth point 2 inwards (to depth point 6). S^+ stays high at points 1 - 5 because freeze-out is not occurring. The following two reactions then dominate (at all depth points) CS^+ and HCS^+ destruction, respectively, to produce CS

$$CS^+ + H_2 \longrightarrow HCS^+ + H$$

$$HCS^+ + e^- \longrightarrow CS + H$$

At the inner freeze-out points, large fractions of CS are cycled into CS^+ and back again. Most new CS^+ is brought into the system via

$$C^+ + SO \longrightarrow CS^+ + O$$

At depth points 7 and 8, CH and C_2 abundances have dropped very low, and SO only becomes very large further in, so that little HCS^+ is formed and H_3CS^+ is left as the main contributor to CS levels, through the sequence

$$S^+ + CH_4 \longrightarrow H_3CS^+ + H$$

followed by

$$H_3CS^+ + e^- \longrightarrow CS + H_2 + H$$

Or

$$H_3CS^+ + e^- \longrightarrow H_2CS + H$$
$$H_2CS + h\nu \longrightarrow CS + H_2$$

At the inner points, where freeze-out is taking place, all S-bearing species show a decline in abundance moving away from the core centre to the lower density, lower A_V points, until reaching the outer freeze-out point. Because ions freeze out approximately 18 times faster than neutrals, the larger ionisation level of S at the points further from the core centre allows sulphur to be removed from the gas phase more quickly at these points. This is mitigated slightly by the decreased density away from the core centre leading to slower freeze-out rates, however this decrease is only around 22 per cent of the central value, at

Table 2.3: Selected column densities through the core, fractional abundances computed from column densities, and raw central fractional abundances †

	$t = 0$			$t = 1$ Myr			$t = 2$ Myr		
Species i	$N[i]$ (cm^{-2})	$X_N[i]$ ‡	$X_{12}[i]$ §	$N[i]$	$X_N[i]$	$X_{12}[i]$	$N[i]$	$X_N[i]$	$X_{12}[i]$
H_2	1.7(21)	4.8(−1)	5.0(−1)	6.4(21)	5.0(−1)	5.0(−1)	1.7(21)	4.9(−1)	5.0(−1)
CO	2.7(16)	7.9(−6)	5.3(−5)	8.7(17)	6.8(−5)	5.6(−5)	1.6(17)	4.7(−5)	9.3(−5)
O_2	1.4(10)	4.1(−12)	1.9(−11)	8.8(15)	6.8(−7)	2.6(−6)	6.1(10)	1.8(−11)	9.2(−11)
H_2O	2.2(11)	6.3(−11)	2.2(−17)	4.4(15)	3.5(−7)	1.2(−6)	7.4(11)	2.1(−10)	7.8(−10)
CH_4	9.7(8)	2.8(−13)	1.6(−12)	3.7(14)	2.9(−8)	7.5(−8)	4.3(9)	1.2(−12)	4.7(−12)
OH	9.0(11)	2.6(−10)	5.8(−10)	2.8(14)	2.2(−8)	3.8(−8)	2.6(12)	7.4(−10)	2.5(−9)
CH	2.0(14)	5.7(−8)	5.7(−8)	6.3(13)	4.9(−9)	4.1(−11)	1.2(14)	3.4(−8)	1.3(−8)
HCO^+	1.5(9)	4.2(−13)	9.9(−13)	1.1(13)	8.3(−10)	2.0(−9)	6.3(9)	1.8(−12)	5.9(−12)
H_2CO	2.7(10)	7.9(−12)	2.7(−11)	4.2(13)	3.3(−9)	5.3(−9)	4.8(10)	1.4(−11)	4.4(−11)
CH_3OH	3.7(5)	1.1(−16)	6.5(−16)	1.8(12)	1.4(−10)	6.5(−10)	2.0(6)	5.7(−16)	2.7(−15)
NH_3	4.3(7)	1.2(−14)	5.6(−14)	2.4(13)	1.8(−9)	7.1(−9)	1.1(9)	3.1(−13)	2.5(−12)
N_2H^+	1.1(6)	3.1(−16)	9.3(−16)	3.8(11)	3.0(−11)	6.6(−11)	1.9(8)	5.6(−14)	4.5(−13)
CN	2.2(12)	6.3(−10)	1.3(−9)	5.8(12)	4.5(−10)	1.0(−10)	4.7(11)	1.4(−10)	2.1(−10)
NO	2.7(10)	7.7(−12)	3.8(−11)	7.9(14)	6.2(−8)	1.3(−7)	1.3(11)	3.9(−11)	1.9(−10)
CS	9.7(12)	2.8(−9)	6.6(−9)	7.2(14)	5.6(−8)	3.0(−7)	2.4(12)	6.8(−10)	1.0(−9)
SO	1.9(10)	5.4(−12)	2.0(−11)	1.2(14)	9.0(−9)	3.8(−8)	2.2(10)	6.4(−12)	2.5(−11)

† $a(b) = a \times 10^b$

‡ $X_N[i] = N[i]/(2N[H_2] + N[H])$

§ $X_{12}[i] = n_{12}[i]/n_{H,12}$

depth point 6, and the combination of increased photoionisation rates (approximately 13 times higher at depth point 6 than at the centre, at 1 Myr, due to the visual extinction decrease) and the 18 times faster freeze-out of the resultant ions far outweighs this effect.

For the dark parts of the cores where $A_V > A_{(V,crit.)}$, the pathway

$$\mathrm{S} \xrightarrow{\mathrm{OH}} \mathrm{HS} \xrightarrow{\mathrm{O}} \mathrm{SO} \xrightarrow{\mathrm{C^+}} \mathrm{CS^+} \xrightarrow{\mathrm{H_2}} \mathrm{HCS^+} \xrightarrow{\mathrm{e^-}} \mathrm{CS}$$
$$\mathrm{S} \nearrow \mathrm{OH}$$

converts much of the sulphur into CS molecules, and the freeze-out of S/S^+, C/C+ and other intermediaries, as well as CS itself, depletes CS abundances.

The CS destruction is mostly via photodissociation, however at depth points 11 and 12 this process has decreased sufficiently to allow reactions with ions to take over as the major destruction mechanisms. These processes are lessened towards the core centre due to the higher A_V and the lower fractional ionisation and electron abundance.

After the peak density is reached and re-expansion takes place, the inner points move out of the freeze-out zone, and the CS formation follows the CH and C_2 abundances. The A_V drops and becomes less dependent on position, leaving CS destruction primarily dependent on photodissociation. The lower CS levels in the central regions at $t = t_t$, compared to $t = 0$, are due to lower levels of CH and C_2. Carbon has been locked into

CO via grain surface reactions and re-injection whilst the core is at high density, and this cannot be rectified unless and until those points drop below a visual extinction of around 1 when photodissociation again takes hold.

Table 2.3 shows column densities calculated in a step-wise integration of the computed chemical abundances, for $t = 0$, $t = t_m$, and $t = t_t$, doubled to provide values through the entire core, assuming symmetrical abundances. The selected species represent the most heavily enhanced (or depleted) of those with abundances high enough for detection. Fractional abundances are calculated as the ratio of column density to total hydrogen column density.

The enhancement of the CO abundance at $t = 2$ Myr is the observationally most significant enhancement of a fractional abundance relative to that at $t = 0$. Such an increase would most likely be detectable in data for CO emission and extinction at the outer boundaries of a translucent clump in a molecular cloud.

For most species there is a definite enhancement of the chemistry from the original state of the core compared to values on return to diffuse physical conditions. This could present a way of discerning whether an observed core is in its collapse or expansion phase.

The dependence of the strength of this hysteresis on the free parameters is something which is being investigated further.

Table 2.3 also shows fractional abundances for the central depth point, point 12. Comparison of the variation in these values over time with those of the column densities through the core clearly demonstrates the need for this kind of multi-point code. The variations in the central fractional abundances over time are not always in the same sense or of the same magnitude as those computed from column densities. So measured column densities from observations are unlikely to agree well with central fractional abundances obtained from single point-models; we need to take account of the chemical behaviour of those regions further from the core centre, as these obviously make significant contributions.

2.5 Extended peak time chemistry

An important application of this research would be to diagnose not only whether a core were in an expansion or a contraction phase, but whether it were gravitationally bound, i.e. in a state such that star formation should take place. Here we apply the stricture that a gravitationally bound core would lie dynamically dormant for a period of approximately

Table 2.4: Fractional abundances with respect to H_2, calculated from column densities through the core †

	Extended peak time	Standard run		
	$t = 1.39$ Myr	$t = 1.20$ Myr	$t = 1.39$ Myr	$t = 1.40$ Myr
Species i	$X_N[i]$ ‡	$X_N[i]$	$X_N[i]$	$X_N[i]$
CO	5.4(−5)	6.0(−5)	5.4(−5)	5.7(−5)
O_2	1.2(−6)	1.0(−6)	5.5(−7)	5.3(−7)
H_2O	2.8(−7)	2.9(−7)	1.7(−7)	1.7(−7)
CH_4	2.4(−8)	2.2(−8)	1.3(−8)	1.2(−8)
OH	4.3(−8)	3.8(−8)	5.5(−8)	5.7(−8)
CH	4.8(−9)	5.8(−9)	1.0(−8)	1.0(−8)
HCO^+	1.3(−9)	1.2(−9)	9.4(−10)	8.6(−10)
H_2CO	2.8(−9)	2.6(−9)	2.7(−9)	2.5(−9)
CH_3OH	7.5(−11)	7.8(−11)	3.6(−11)	3.4(−11)
NH_3	2.4(−9)	2.0(−9)	1.2(−9)	1.2(−9)
N_2H^+	5.6(−11)	4.8(−11)	5.1(−11)	4.9(−11)
CN	3.3(−10)	4.0(−10)	6.3(−10)	8.1(−10)
NO	5.5(−8)	5.7(−8)	3.6(−8)	4.1(−8)
CS	2.2(−8)	3.0(−8)	1.5(−8)	1.5(−8)
SO	1.6(−8)	1.4(−8)	9.3(−9)	9.1(−9)

† $a(b) = a \times 10^b$

‡ $X_N[i] = N[i]/(2N[H_2] + N[H])$

0.4 Myr before further collapse and star formation took place, which is consistent with our understanding of dynamical time-scales. Hence we have run a version of the same model with the difference that the peak time physical conditions are maintained for another 0.4 Myr after peak time, at which point the chemical model was stopped since our physical model would no longer accurately describe the dynamics of the core. We compare the chemical abundance values of this "extended peak time" run with those obtained from the "standard" run of the previous section.

The general difference between the two runs is that the standard run core expands again so that density and visual extinction drop with time, and periodically as depth points pass below the critical A_V, re-injection of frozen out species occurs.

At $t = 1.4$ Myr, the visual extinction at depth point 6 in the standard run has just dropped below the critical value of 2, hence there is a large re-injection of depleted material into the gas phase from the dust grains. Figure 2.6a shows standard run abundances at $t = 1.39$ Myr, just before re-injection (which occurs at $t = 1.395$ Myr); figure 2.5 shows extended peak time run abundances for the same time value. Figure 2.6b shows standard run abundances at $t = 1.4$ Myr, approximately 10,000 years after re-injection.

The differences between the two runs at $t = 1.39$ Myr are slight - the general shapes of the abundance profiles are the same. There are small differences comparing those sections that are within the critical visual extinction. But in fact, although the standard

Figure 2.5: Fractional abundances for extended peak time run at t=1.39 Myr

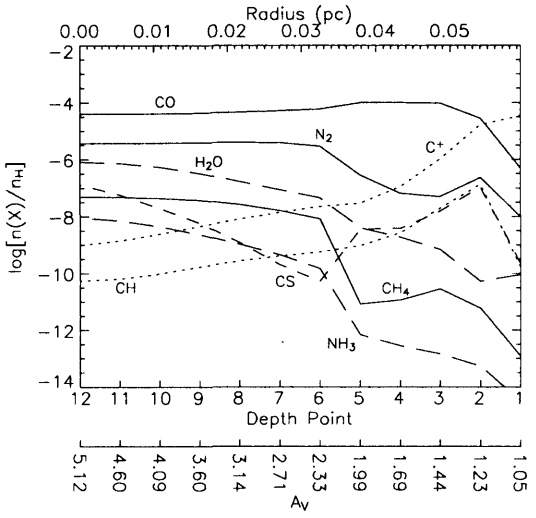

run abundances here are somewhat lower than their extended peak time run equivalents, this does not correspond to higher levels of freeze-out for the standard run (mantle-bound abundances are about the same for both runs). The effect may be explained as follows. As the standard core expands, the visual extinction drops. Although this leads to a slightly larger fractional ionisation level, which would tend to increase freeze-out through the faster depletion of ionic species, the accompanying drop in density makes the freeze-out process slower overall. As the electron density rises with falling A_V, this tends to lead to the destruction of molecules by dissociative recombination, whilst photodissociation of molecules is also increased. These gas phase destruction pathways lead to the drops in molecular abundances, for CS in particular, which are most obvious at points 6 and 7 for the standard run.

Comparing the extended peak time results with those of the standard run at $t = 1.40$ Myr, the re-injection of grain mantle species at depth point 6 clearly has a large impact, but it is fairly short-lived for most species. Ion-molecule reactions, along with photoionisation and photodissociation, are effective at breaking down the comparatively large molecules released. This is because the halting of freeze-out reactions means that ions are no longer being so strongly removed from the gas phase, which drives up the fractional ionisation (and hence the electron density). At this time the core is still in quite a dense state, even at depth point 6, which makes two-body reactions fast. The visual extinction has also dropped to below 2 (by definition) when re-injection takes place so that photoreactions are quite fast for the suddenly high molecular abundances. All of this results in a fast

Figure 2.6: Fractional abundances for standard run at t=1.39 and t=1.40 Myr

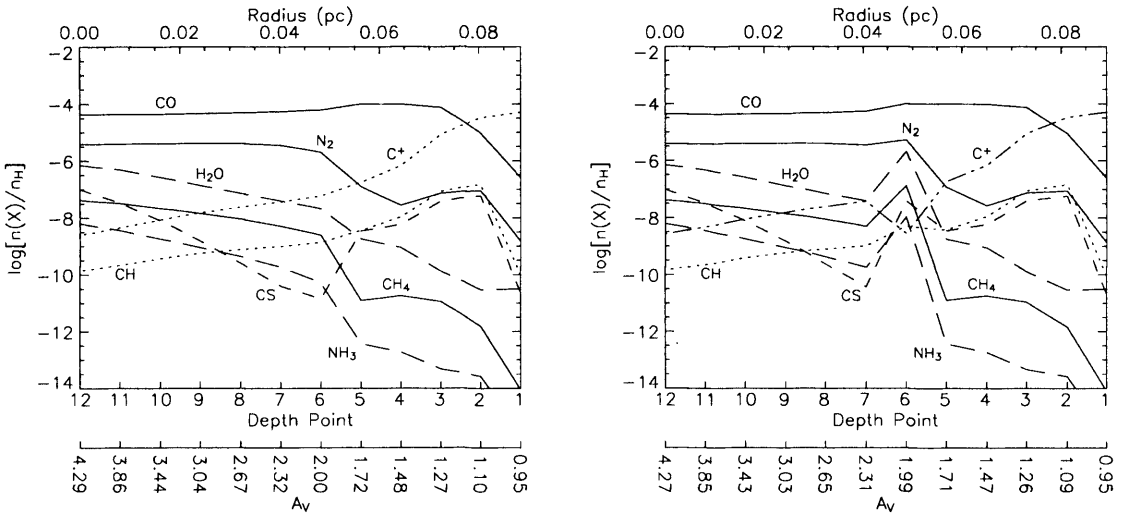

a: $t = 1.39$ Myr b: $t = 1.40$ Myr

chemistry, and in general the species which have been strongly enhanced will very quickly incur large losses. However, since freeze-out is strong (approximately 37 per cent of the total CO is on the grains at depth point 6, just before re-injection), large amounts of the most important carriers of various elements are frozen out, and so when the carriers are re-injected into the gas phase, whether or not those carriers are quickly destroyed, *certain* species are still strongly enhanced in the long term.

This mantle re-injection feature may in fact be the most useful in the diagnosis of self-gravitating versus non-self-gravitating cores; this model only looks at discrete distributions of points through the core, but one would expect that re-injection would be going on at some point in the core all the time that it is in the process of re-expansion, assuming that the inner parts of it have reached the requisite visual extinction. We should be careful in this assumption however, since the mechanism by which we return the mantle species to the gas phase is instantaneous, meaning that the chemistry needs a little time to re-establish quasi-equilibrium values (in many cases, no more than a few 10,000s of years). This mechanism also assumes that different species are re-injected at the same time, which may not be true. Hence we should avoid diagnoses which depend on the short term chemistries which take place after re-injection, and instead concentrate on the chemical enhancements which show some longevity and are therefore more dependent solely on the deposition of the mantle species and not on intricate resultant chemistries. An example might be found in a model employing a larger freeze-out parameter, which

would make the contrast in CO levels larger between regions which had not reached the critical A_V and those which had and had then passed below it again.

Table 2.4 shows fractional abundances with respect to molecular hydrogen, at various times, derived from column densities calculated through the entire core. The raw computed column densities themselves make comparison difficult between the two models, since the standard run column densities are affected by the increasing scale length, and decreasing densities.

The values for the two runs (at either $t = 1.39$ or $t = 1.4$ Myr) do vary, by a factor of as much as $\sim$2.5 for O_2. However, the differences would probably not be significant enough to provide clear parameters by which to judge observational results. Indeed, comparing the extended peak time values at $t = 1.4$ Myr with those for the standard run at $t = 1.2$ Myr, the differences are fairly negligible. Observational results would not provide all of the physical parameters included in this model, so it would be difficult to ascertain the parameters against which an observed core should be compared. Hence, observational results of the sort shown in table 2.4 on their own could potentially correspond to cores in a number of states of evolution, self-gravitating or not. The standard run values at $t = 1.39$ and $t = 1.4$ Myr are not much different for the reason that the large re-injected abundances just do not contribute very much when integrated through all the points in the core. On the other hand, high resolution molecular line surveys *do* yield spatially varying results, and dependent on the line-of-sight, the re-injection bump might show up for those cores which are re-expanding; our simulation here, though one-dimensional in its arrangement of chemical reference points, is not isotropic ($k = 1.5$). This at least would give an indication that those cores were *not* self-gravitating.

2.6 Conclusions

Self-gravity becomes important during at least some phases of the evolution of a core in which a star eventually forms. Self-gravity certainly prevents at least some cores from re-expanding without the input of momentum or energy from a young star. However, in regions in which the magnetic pressure is initially very large compared to the thermal pressure, high density contrast features, in which self-gravity is unimportant, can develop as a consequence of nonlinear MHD processes. Such features are transient and some may be similar to some observed cores. While some cores in molecular clouds are bound by

self-gravity and certainly are not transient in the sense that features in the simulations of FH02 are transient, some cores may be transient.

This is the first study of the chemistry in transient density inhomogeneities in molecular clouds, such as have been observed and are predicted in MHD calculations. The main premise of this work is that dark clouds possess non-uniform density structures, consisting in part of transient localised fluctuations (cores) within a diffuse background medium. Observational and computational evidence suggests that the chemistry of the cores is mostly young, on the order of 1 Myr, implying such a time-scale for their *physical* evolution (and destruction). Due to the action of the interstellar radiation field, which should permeate strongly at least through the diffuse component, freeze-out should be limited to taking place only within the condensations. The importance of freeze-out in dark clouds would therefore be coupled to the cycles over which cores form and disperse, since the characteristic freeze-out time-scale is also of the order of 1 Myr. The cyclic evolution of cores should bring about some degree of transportation of material formed in high density regions into the diffuse background medium. In a case where (at least locally) the evolution time, size of core, etc, are essentially the same, a "limit cycle" may be reached, after which point the chemistry of the core will not change from cycle to cycle (see Nejad *et al.* 1990).

The results of this model also emphasise the need for multi-point chemical codes in modelling dense cores. The central fractional abundances are quite different to those abundances at greater distances from the core centre, particularly with respect to the cross-over between freeze-out and non-freeze-out regions. The column densities that we should expect to observe through dense cores would not be solely dependent on the central fractional abundances, so we should not expect single-point simulations to match observations very well. A limited number of papers (*e.g.* Nejad *et al.* 1990, Nejad & Williams 1992, Charnley *et al.* 1988a, Charnley *et al.* 1988b) considered chemistry in material that passes from lower density to higher density and then back to lower density conditions. However, the dynamical descriptions in those papers were adopted with a view to considering the effects of disruption by the winds of young stars. Furthermore, multipoint calculations allowing the determination of the spatial profiles of chemical abundances at multiple times have been adopted in none of the previous work involving the chemistry of material cycled between lower and higher and back to lower density states. As stated above, the current results demonstrate that multi-point calculations are required.

The results from this study yield a number of specific conclusions:

1. The spatial extent of several key species (CO, N_2, H_2O and NH_3) is significantly enhanced by the cycling process, implying a source of general molecular enrichment of clouds.

2. The relative spatial extents of CS and NH_3 is broadly in agreement with the observed morphologies of star-forming regions.

3. The absolute values of the CO abundance are significantly higher than the values obtained for simple quasi-static collapse models. Such enhancements should be observationally detectable at the outer boundaries of translucent clumps. Many of the time- and space-dependencies of the various chemical species are only detectable at high resolutions and cannot be resolved with single-dish telescopes.

4. Although the re-cycling of material frozen out onto dust grains results in instantaneous chemical enrichment of the gas, the chemical effects are not long-lived, although certain species will be strongly enhanced as a result, when averaged over time.

5. Many species, mostly represented in table 2.3, show enhancements at peak density of their integrated column density-calculated fractional abundances. Of those, the following are expected to be enhanced and remain significantly enhanced even after core re-expansion: CO, N_2, N_2H^+, NH_3, NO, CH_4, O_2, H_2O.

6. The dynamical turnover means that clouds that are ensembles of such transients have a clearly different chemistry from a 'traditional' static cloud. The re-injection of material from solid to gas that occurs as material passes through the $A_{V,crit.}$ zone during re-expansion is crucial for gas-phase chemistry. We have fixed our treatment with reference to observations. But this work shows that the factors determing $A_{V,crit.}$ need to be much better determined than they are now (see Williams *et al.* 1992).

7. Specific differences include the fact that the gas-phase chemistry is "young" at all times if the turnover time is $\sim$1 Myr. A young chemistry is consistent with observations; a turnover time of $\sim$1 Myr is consistent with predictions from MHD. Secondly, freeze-out is important, obviously, but because of the turnover never goes to completion (i.e. 100 per cent freeze-out).

8. Transient clumps that happen to be denser and more massive than the average will have stronger gravitational fields that will dominate the MHD processes that tend to dissipate the clump. The critical case occurs when these tendencies are in near-balance, and the transient inhomogeneity may be expected to be near-static for a period. We have explored the chemistry in such a case; there are some differences from the gravity-free model, although these are probably not observationally significant. Therefore we have been unable to predict a clear signature of a "hung" inhomogeneity. However, features resulting from the re-injection of mantle-bound species back into the gas phase may provide criteria for determining cores which are in a re-expansion phase of evolution, and therefore not in a bound, self-gravitating state. The strength of these features should depend on a number of poorly-defined free parameters in our models.

9. Nevertheless, the model of a molecular cloud presented here has implicit within it the reason why the overall efficiency for low-mass star-formation is rather small: the MHD forces dissipate most of the smaller clumps before collapse can occur. The low efficiency (a few percent) must be related to the mass spectrum of the transient inhomogeneities, to be determined in an extension of the work of Falle & Hartquist (2002) in which three-dimensional structures are considered.

10. A specific prediction of this model is that the background gas in which the inhomogeneities are embedded is fairly diffuse. It is, however, chemically enriched when compared to the chemistry of a canonical isolated static diffuse cloud model. These chemical enhancements may account for the variety of chemistries observed in diffuse clouds; this might occur when the line of sight towards a bright star passes through diffuse regions of a molecular cloud. Thus, this study of dynamical molecular clouds may also give some information about the place of diffuse clouds in the general scheme of interstellar circulation.

CHAPTER 3

Exploring the Parameter Space of the Transient Dense Core Model

3.1 Introduction

The study of the previous chapter looked at the chemistry of a core with a single set of initial physical and chemical conditions, over its evolution from diffuse background gas into a dense core and back to diffuse conditions. Here I explore further the parameter space provided for by the model, in order to test their sensitivity to change and to find potential observable diagnostic features of the resultant chemistry. These parameters are: t_m, the evolution timescale; k, the dimensionality of collapse; $\Delta z(t_m)$, the size of the core; $\rho(0, t_m)$, the peak time central density; and fr, the rate of freeze-out. I do not examine the effects of varying the initial central density, and I leave τ as a dependent variable.

I take a grid of models, starting with one standard set of parameters, similar to those used in the study of chapter 2, varying only one parameter per run. The dynamical parameters chosen for the standard run vary from the model of chapter 2 only in the scale size of the core $\Delta z(t_m)$, which changes the peak central visual extinction. In order to maintain as far as possible the compatibility of the runs with each other and to isolate the effects of individual parameters choices, I parameterise further some of the variables. According to the constraints of the other parameters, the scale size of the core determines the level of visual extinction. Since the visual extinction has a more direct and profound impact upon the core *chemistry*, I use the maximum central visual extinction as a more pertinent and convenient variable, setting $\Delta z(t_m)$ according to the choice. The level of

freeze-out also needs to be standardised in order to compare runs, since the changing of one parameter or another will affect the strength of the freeze-out. For example, lowering the timescale of evolution for the same fr value will intrinsically mean that there is less freeze-out, making the individual effects of the two variables more difficult to isolate.

3.2 The Grid

3.2.1 The Chemical Model

The chemical model is the same as that used for the work in chapter two, but it now consists of 251 species compared to 221, with a resulting increase to the number of reactions, bringing them to approximately 3600. The new chemical species mostly consist of longer chain carbon molecules (up to five carbon atoms compared to three). This change was made in order to treat more fully the formation of larger molecules which might take place whilst visual extinctions are comparatively high.

Parameterisation of freeze-out onto dust grains was necessary to make the runs compatible with each-other. The level of freeze-out is not fixed merely by adopting the same freeze-out rate, fr for each run; this is because the resultant rate of freeze-out also depends on density, and the abundances of material on the grains depends on the period of time over which freeze-out occurs, as well as on the behaviour of the gas phase chemistry, which is affected by all of the physical conditions. Also, unlike some other previous chemical models of similar regions, the physical conditions are evolving constantly whilst freeze-out is taking place. This makes the resultant rate of freeze-out quite variable, and strongly (and non-linearly) dependent on model parameters.

To parameterise the level of freeze-out, I have chosen a depth point at a particular time in the evolution of the core at which to define a reference level. Since depth point 12 is the inner point, and therefore reaches the critical visual extinction for freeze-out earlier than the other depth points, and since depth point 12 also takes the highest density throughout the simulation, this means that it should have the most freeze-out. Therefore it was appropriate to use this depth point to determine the reference level of freeze-out. This level is defined as the percentage of dust grain mantle-bound carbon monoxide to gas phase CO. It was important to use this molecule for reference, since it is uniformly the most strongly frozen-out molecule after H_2O. Not only this, but in a high-density environment with moderate visual extinction, it constitutes the most abundant gas-phase

Table 3.1: Parameters for the Grid of Dense Core Models

Model	Peak Time, t_m (Myr)	Peak Central Visual Extinction, $A_{V,max}$	Dimensionality of Collapse, k	Peak Central Density, $\rho(0,t_m)$ (cm^{-3})	Sticking Coefficient, S
STAN	1	5	1.5	5(4)	1.0
G-T1	**0.5**	5	1.5	5(4)	1.0
G-T2	**2**	5	1.5	5(4)	1.0
G-A1	1	**3**	1.5	5(4)	1.0
G-A2	1	**10**	1.5	5(4)	1.0
G-K1	1	5	**1.2**	5(4)	1.0
G-K2	1	5	**1.8**	5(4)	1.0
G-D	1	5	1.5	**5(5)**	1.0
G-S	1	5	1.5	5(4)	**0.1**

carbon-bearing molecule. Since CO will be formed early on, particularly when the visual extinction is large enough that it is reasonably well shielded, it is important to make sure that the freeze-out level is such that appropriate amounts of gas phase CO are formed, rather than being by-passed by direct C–grain or C^+–grain sticking. Hence CO was deemed the most crucial molecule, and freeze-out determined by reference to it. I set the reference time to be the peak time, t_m. This again was to allow the models to be as compatible as possible. A more accurate determinant of freeze-out might be considered to be the level immediately prior to re-injection into the gas phase, when $A_V \simeq A_{V,crit}$, however this again introduces inconsistencies between models as to the time period for freeze-out, since the reference depth point may reach $A_{V,crit}$ at different times depending on the value of t_m, k, $\rho(0,t_m)$, or $A_{V,max}$. Also, freeze-out will be strongest around the peak time due to high density. Its level at this point in time will be crucial to the chemistry since peak time gas phase chemistry will also be at its most rapid, and hence strongly affected by depletion levels.

I specified a maximal level of freeze-out to be 60% at depth point 12, at $t = t_m$. This level ensured that for all the runs, the final level of freeze out at any depth point, immediately before re-injection, would be $\leq$90%, as determined by trial runs. More than this could result in levels of C/C^+, in particular, becoming unphysically low, and, practically, result in the ODE integrator crashing for this reason.

I identify this maximal level of 60% with a sticking probability of $S = 1.0$. Hence I identify a level of 6% with a sticking probability of $S = 0.1$.

Also, to further minimise the possibility of too much direct C/C^+ freeze-out too early on, I raised $A_{V,crit}$ to 2.5. In the work of chapter two I adopted a value of 2 to ensure that there was sufficient time for significant grain mantles to accrue. However, since this has not proved to be a problem, I may use a value perhaps more in keeping with our estimate from Whittet (2003) of between 2 and 3. This has the effect of limiting freeze-out in the standard model to depth points 7 - 12, rather than points 6 - 12 as for the model of chapter 2.

3.2.2 The Model Parameter Grids

I construct a grid of 9 models centred around one standard run, thus: 3 pairs of models, each with larger or smaller values of the evolution time, maximum visual extinction, or dimensionality of collapse, plus two further runs, one with larger peak density, the other with a lower sticking coefficient for gas-grain reactions. Table 3.1 gives details for the entire grid. As before, all models are isothermal, at 10 K.

Certain runs take different initial physical conditions from the standard model, even when they achieve the same peak time conditions. They therefore require their own stage 1 runs, by which they achieve chemical equilibrium ready for the main evolution of stage 2 (see chapter 2). These runs are: G-A1 & G-A2, which achieve different visual extinctions throughout stage 2; G-K1 & G-K2, whose visual extinctions are the same as that of the standard run, at peak time, but achieve them starting from different initial levels; and G-D, which, due to its being fixed at the same peak time visual extinction as the standard run, whilst achieving a peak density ten times larger, requires a lower initial visual extinction profile. The differences between those runs which share their stage 1 evolution only manifest themselves in stage 2.

3.3 Results

I first present results for the standard model run, and compare these with those obtained for the similar model of chapter 2. In following subsections, I present variations on the standard run, with which I compare them.

Column densities are calculated in the same way as in chapter two. In this method, in

order to obtain fractional abundance levels in between those depth points specified in the code, I interpolate linearly the *logarithms of the fractional abundances*, in keeping with the line graphs of the chemical abundances. I approximate the density variation between points as linear, which over the interval of $\Delta\alpha = 0.1$ is quite reasonable, then integrate the product of density and chemical abundance over the instantaneous core width. I then double the resultant column density to take in both halves of the core. This approach assumes a line of sight along the principal axis. No radiative transfer effects are considered in these calculations. Fractional abundance values are obtained from the column densities by normalising with respect to $2N[H_2] + N[H]$ (where $N[H_2]$ is the column density of H_2, *etc*).

3.3.1 Standard Run

Figures 3.1a – e show chemical abundances for the standard run across the core at five points in its evolution: as before, t=0, $t = 0.5$ Myr, $t = 1$ Myr (peak time), $t = 1.5$ Myr, $t = 2$ Myr. Figures 3.2a – c show abundances of eight more species (which are mostly not abundant at low densities) for times $t = 0.5$ Myr, $t = 1$ Myr, $t = 1.5$ Myr.

There is virtually no difference, at $t = 0$, between this model and that of chapter 2, however, by $t = 0.5$ Myr differences begin to emerge. The higher value of $A_{V,crit}$ means that one fewer depth point is in the freeze-out zone. At the same time, whereas in chapter 2 a typical value of fr was chosen, which corresponded to a peak time CO freeze-out level at depth point 12 of ~34%, here a level of 60% has been set as the standard. Whilst this leads to more depleted CO and H_2O levels, this leads to larger proportions of NH_3, CH_4, and other less abundant carbon-bearing molecules. These enhancements are not only due to, for example, lower levels of water in the gas-phase (diminishing the reaction $C^+ + H_2O \rightarrow HCO^+ + H$, which removes C^+ from the gas phase) but also the lower electron abundance, which in the code is identical to the level of ionisation in the gas-phase, as it is governed by the conservation of electric charge. As ions are strongly frozen-out, so the electron abundance drops, depressing destructive recombination pathways for the carbon-bearing ions which mediate the formation of CH_4 and others.

This effect is more suppressed at the peak time, due to the strong freeze-out of carbon from the chemical network. CS displays the multiple peaking familiar from chapter two, but exhibits greater depletion due to stronger freeze-out of both carbon- and sulphur-bearing species, not least S^+ (see chapter two for details of the chemistry leading to CS

Figure 3.1: Fractional abundances across the core – standard run

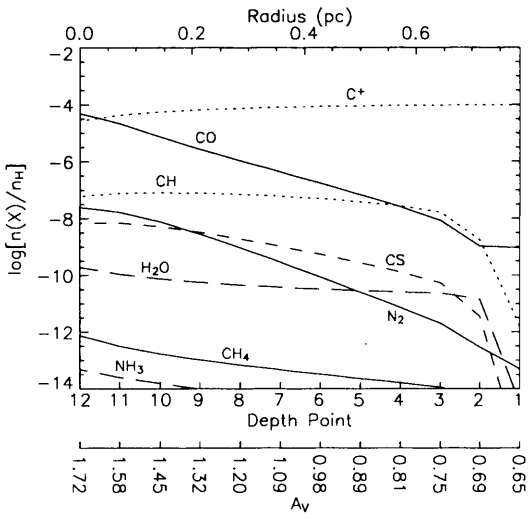

a: $t = 0$ Myr

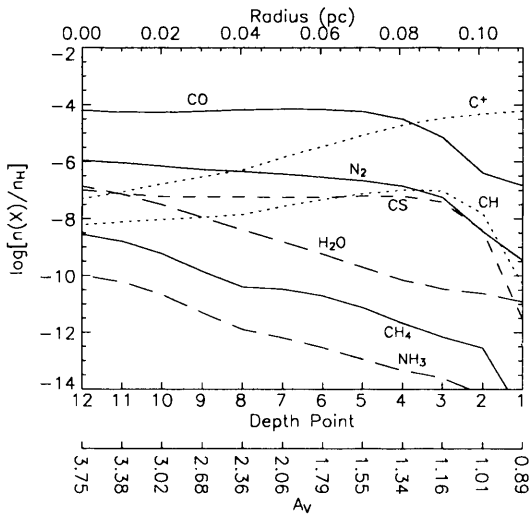

b: $t = 0.5$ Myr

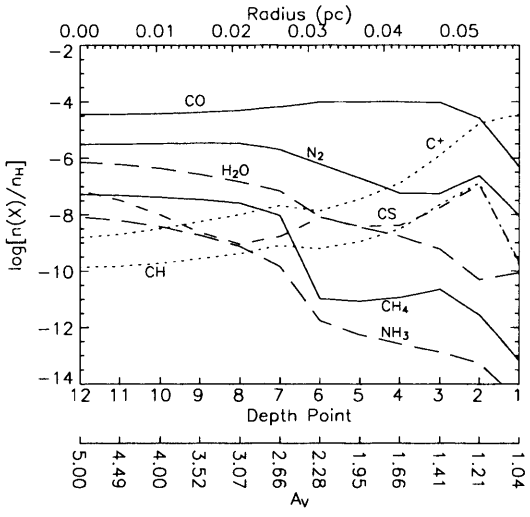

c: $t = 1$ Myr (peak time)

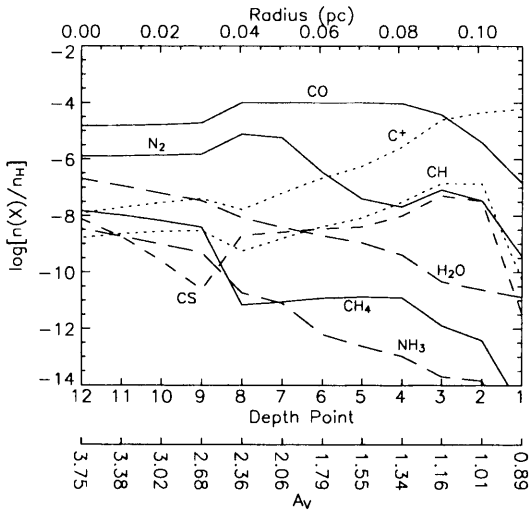

d: $t = 1.5$ Myr

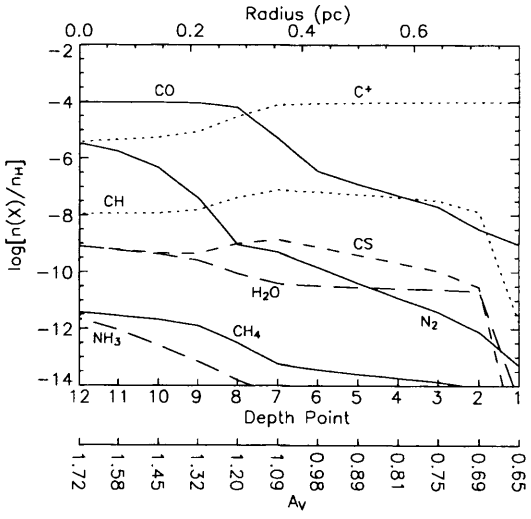

e: $t = 2$ Myr

Figure 3.2: Fractional abundances across the core – standard run

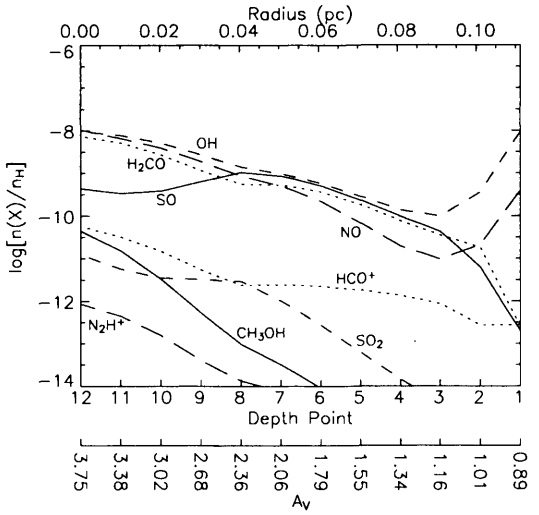

a: $t = 0.5$ Myr

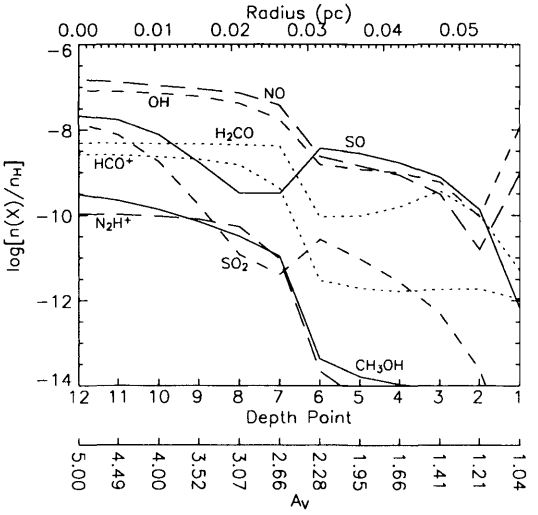

b: $t = 1$ Myr (peak time)

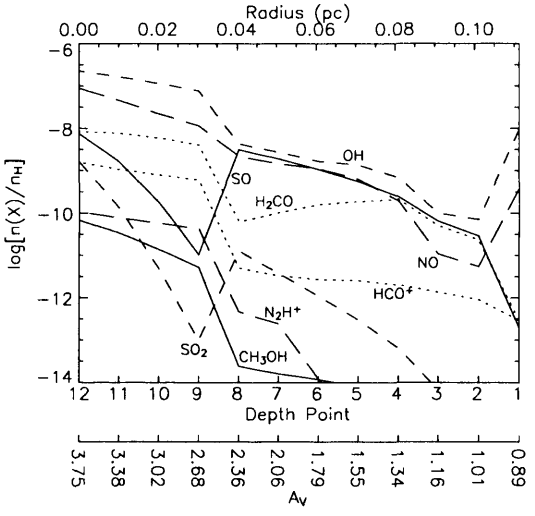

c: $t = 1.5$ Myr

depletion). SO and SO_2 show the effects of depletion of sulphur and oxygen, in particular at the outer edges of the freeze-out zone, where ionisation is strongest and therefore the rate is higher due to the disparity between ion and neutral freeze-out rates.

Species affected by freeze-out may be divided into two categories:

- Those which display differential depletion
- Those which assume a fairly even depletion across those depth points affected

Freeze-out of the former (*e.g.* CS, SO) is mainly governed by the faster rate for ionic species, so that lower visual extinction points show the heaviest losses; the latter (*e.g.* CO,

Figure 3.3: Column densities as functions of time, calculated through the core – standard run

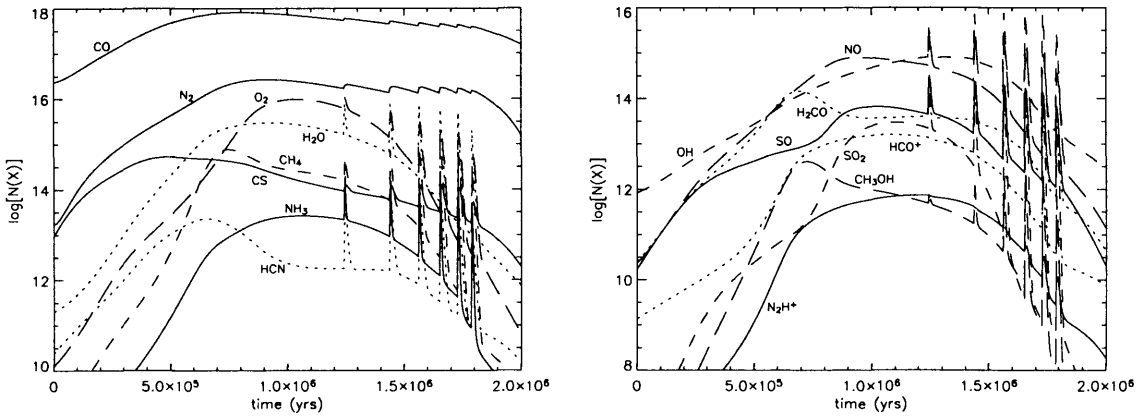

a: Species set 1 b: Species set 2

N_2) are mostly depleted by freeze-out of neutral species, which tends to produce a flat(ter) profile across the freeze-out zone, or in some cases a profile which drops towards the core centre (both due to the sole dependence of category 2 on density and not ionisation). To generalise, sulphur-bearing species tend to fall into the first category, since there is always a significant proportion of S in ionic form, S^+, with either S or S^+ being generally the most abundant sulphur-bearing species. The high fraction of S-ionisation is due to the charge transfer reaction:

$$C^+ + S \longrightarrow C + S^+$$

When freeze-out is in action, C^+ is generally formed via:

$$He^+ + CO \longrightarrow C^+ + O + He$$

because by this time most carbon has been locked up into CO form. The above reaction produces a large amount of ionisation which is transferred to S as above. Most other C^+ neutralising reactions ultimately re-produce CO. Helium is ionised by cosmic rays, whose intensity is constant throughout the core.

Since CO comprises the largest C-bearing species for most of the core, it is also the principal freeze-out candidate, and therefore most carbon depletion depends on the neutral path.

Nitrogen species also fall into the second category, since N^+ reacts with H_2 far more rapidly than it freezes out onto dust grains. This sets in motion the chain of reactions:

$$NH^+ \xrightarrow{H_2} NH_2^+ \xrightarrow{H_2} NH_3^+ \xrightarrow{H_2} NH_4^+ \xrightarrow{e^-} NH_3$$

Figure 3.4: Fractional abundances with respect to total hydrogen as functions of time, calculated from column densities through the core – standard run

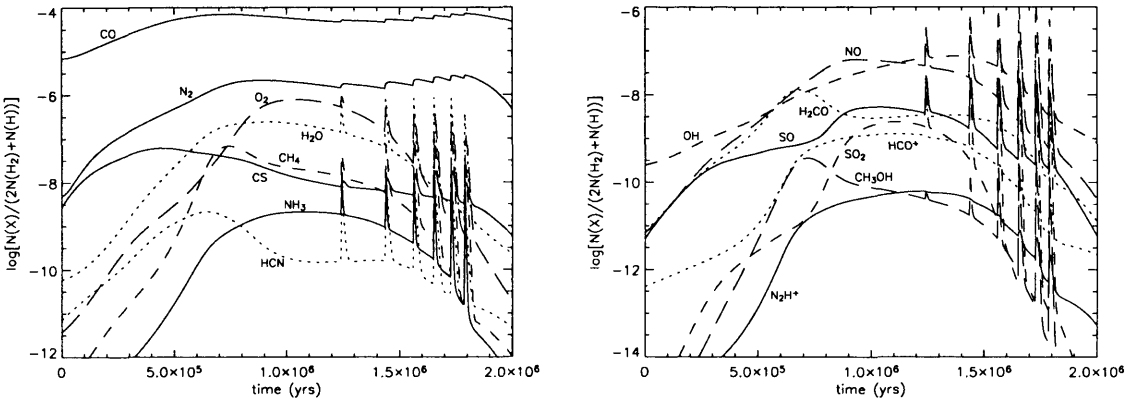

a: Species set 1 b: Species set 2

which occur faster than freeze-out. This leaves N, and N_2, as the principal freeze-out candidates, due to their large abundances.

By $t = 1.5$ Myr, only four depth points remain in the freeze-out zone. Besides this, another difference due to the higher critical visual extinction also becomes apparent. Notwithstanding the higher level of freeze-out in this run, because the density and A_V at which re-injection of grain mantles occurs are both higher than in the previous work, the resultant molecular material may achieve larger abundances for longer, either re-injected directly or as the products of the destruction of re-injected species. At $t = 1.5$ Myr, OH, NO, NH_3, N_2H^+, HCO^+, H_2CO, SO and SO_2, show quite clearly that there is chemical hysteresis in the core, when compared to levels at $t = 0.5$ Myr.

By the end point of the standard run ($t = t_t$), most differences with the previous work have largely disappeared; CO and N_2 are very slightly enhanced at the very centre of the core compared to the study of chapter 2. Since CO and N_2 abundances are large, these small enhancements still correspond to large amounts of C and N atoms locked up in this form.

When comparing the end time values to the initial values for this run, the same hysteresis is observed as for the model of chapter two — CO especially is enhanced due to the high densities attained at peak time, whilst visual extinction (and self-shielding) is still high enough to prevent it being quickly destroyed. N_2, though not self-shielded, is still strongly enhanced due to its being the end-point of many reactions which destroy other nitrogen-bearing species, many of which have been briefly augmented by re-injection of

grain mantles. H_2O is reasonably enhanced, as is CH_4, and NH_3 is verging on a level which is potentially observable, at inner-most central depth points. CS, meanwhile, shows a net drop of around 1 order of magnitude at the core centre, which in observational terms would represent the greatest contribution to the column, due to higher density. At this time, the sulphur which is no longer in the form of CS is to be found in S^+. Since our assumption is that most frozen-out sulphur sticks to the grains to be hydrogenated to H_2S when $A_V > A_{V,crit}$, when this is re-injected into the gas phase it is quickly photodissociated to HS and S, and the atomic sulphur is quickly photoionised to S^+. At end time this ionised sulphur is still in the process of re-building CS abundances.

Note that it is those points which have been within the freeze-out zone which show appreciable chemical hysteresis.

Figures 3.3 and 3.4 show, respectively, column densities calculated through the core, and fractional abundances calculated from those values, for a range of observable and commonly observed species. Note the different scales for column density/fractional abundance between plots a and b.

The hysteresis and general time-variation of the chemistry can easily be seen here. CO gains approximately 1 order of magnitude in both figures, comparing start time with end time. In fractional abundance, once it reaches its peak level it does not deviate far from it, falling a little after the peak time, as freeze-out takes its toll. N_2 is similarly sustained, excepting the final ~200,000 years, however it is enhanced by ~2 orders of magnitude over initial levels. These two molecules demonstrate well the effects of freeze-out and re-injection: the six spikes in the plots after peak time are caused by the instantaneous re-injection of grain mantles into the gas phase. CO and N_2 clearly benefit a great deal from the re-injection, although it is likely that these two molecules would have attained similar levels at these times, if freeze-out had not been turned on. We can see that while other re-injected species are quickly brought back to their previous levels, CO and N_2 take a comparatively long time to fall, only to be boosted again by re-injection when the next depth point falls below $A_{V,crit}$.

It should be noted that the sporadic nature of the enhancements is an artifact of the discrete distribution of points in the chemical model; each spike corresponds to re-injection at a single depth point. A model with sufficient resolution of depth points would produce a continuous enhancement in time, from when the last to the first depth points to have attained critical visual extinction re-injected.

It should also be noted that the strength of any re-injection features observed in real cores would be dependent on the sharpness of the transition between freeze-out and non-freeze-out zones (*i.e.* the range of visual extinctions over which re-injection may take place incrementally, the rate at which this might happen, and the time taken for a parcel of gas to pass through this critical range). If re-injection were to take place on a timescale which could not reasonably be characterised as instantaneous, then the levels seen here would not occur so strongly. If that timescale were approximately equal to that over which the gas phase chemistry could assimilate the re-injected material, there would be no obvious re-injection enhancement at all, except perhaps for those species which ultimately benefitted, *i.e.* CO and N_2.

Hence, the abundances between the first and last re-injections should be treated with caution.

N_2H^+ and HCO^+ are not strongly affected by re-injection, indeed any differences are barely perceptible. This contrasts with most other (neutral) species. The reason is that no electrically charged species are released from the grain mantles. Meanwhile, the existing ionic species are destroyed by reactions with the suddenly more abundant neutral species. This discrepancy between ionic and neutral tracers could be a strong indicator for whether an individual core were in a pre- or post-peak time stage of evolution, if the mechanism for re-injection is such that these large post-peak time abundances are produced.

Note that CS is not strongly enhanced on re-injection and does not reach its pre-peak time level.

An interesting feature in figures 3.3 and 3.4 may be discerned at $t \simeq 7 \times 10^5$ yr, where a "shoulder" appears in many of the carbon-bearing species' profiles. Those which display this feature tend to subsequently drop, as peak time approaches. The rise of this feature is dependent on the speed at which carbon may be converted into CO, and the time of onset of freeze-out at each depth point. At early times in the evolution of the core, CO and other carbon-bearing species are growing. When a point passes into the freeze-out zone, methane, for example, begins to rise more quickly. Freeze-out has the effect of reducing electron abundance, thereby suppressing recombination reactions, and prolonging the survival of C^+, etc, for long enough to produce CH_4 via the chain:

$$C^+,CH^+ \xrightarrow{H_2} CH_2^+ \xrightarrow{H_2} CH_3^+ \xrightarrow{H_2} CH_5^+ \xrightarrow{CO,C} CH_4$$

Similar mechanisms are present for other C-bearing species. After $t \simeq 7 \times 10^5$ yr, carbon

Figure 3.5: Fractional abundances across the core – $t_m = 0.5$ Myr run

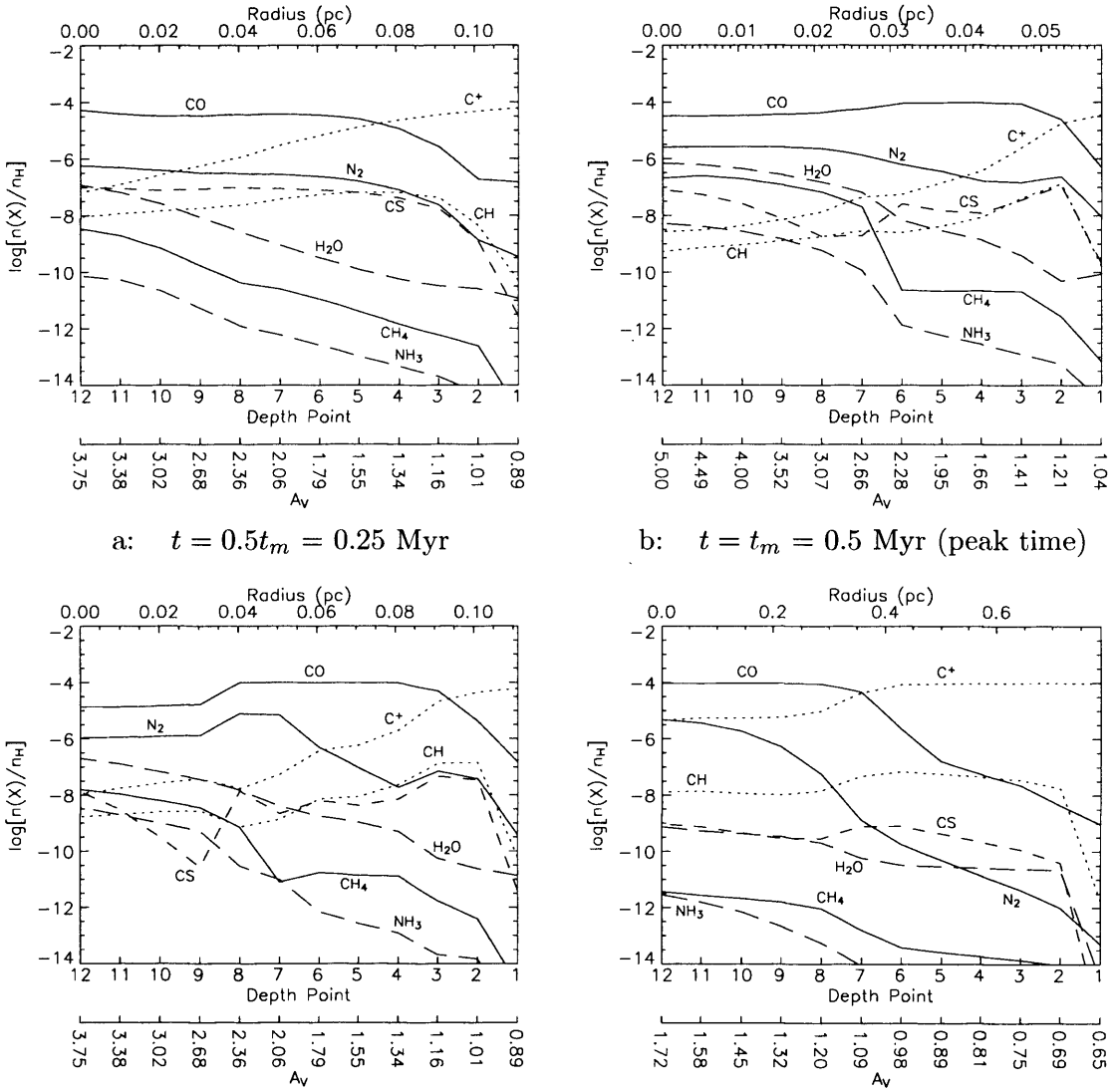

a: $t = 0.5t_m = 0.25$ Myr

b: $t = t_m = 0.5$ Myr (peak time)

c: $t = 1.5t_m = 0.75$ Myr

d: $t = 2t_m = 1$ Myr

begins to run out since most of it has now been locked up in carbon monoxide. By this time, CO itself is also beginning to drop significantly due to freeze-out. This precipitates a fall in C^+, as by now most C^+ is supplied by He^+ reaction with CO, and so formation rates in the CH_4-forming chain drop, whilst destuction rates for CH_4 remain comparatively high. Methane column density turns over when the innermost (highest density) points begin to suffer from very low carbon levels.

Figure 3.6: Fractional abundances across the core – $t_m = 0.5$ Myr run

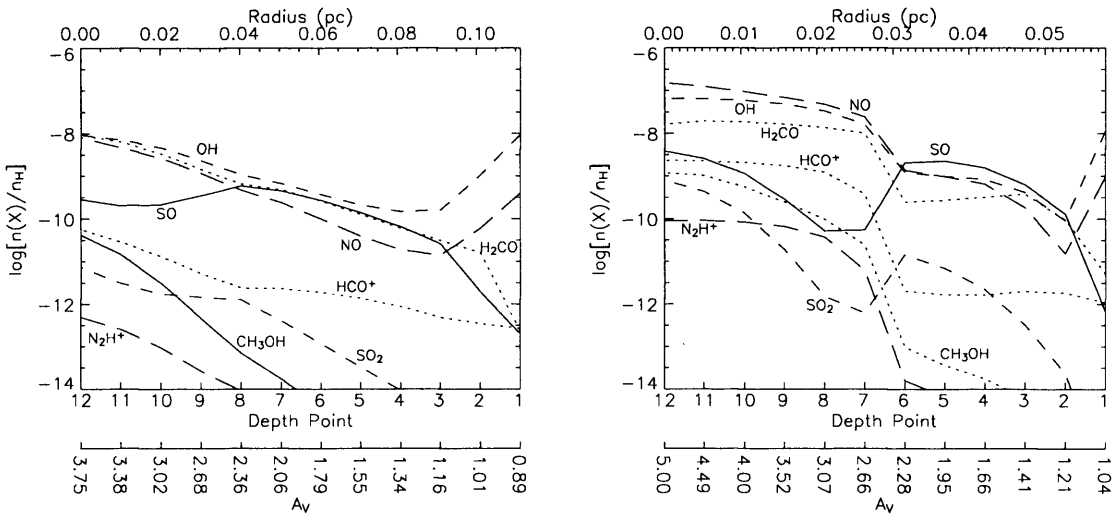

a: $t = 0.5t_m = 0.25$ Myr

b: $t = t_m = 0.5$ Myr (peak time)

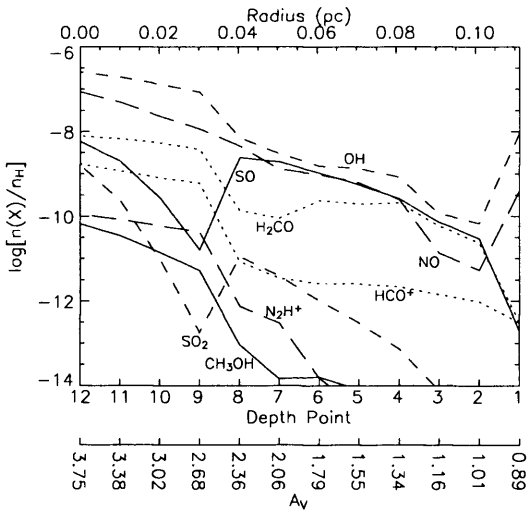

c: $t = 1.5t_m = 0.75$ Myr

3.3.2 Runs G-T1 & G-T2

Both runs G-T1 and G-T2 use the same stage one as the standard case. Hence their chemical profiles at time $t = 0$ in stage two are the same as standard. Because peak times are different between these two runs and the standard case, I compare runs by reference to time as a fraction of peak time, thereby comparing like densities (and visual extinctions).

Figures 3.5 & 3.6 show fractional abundances for model run G-T1, for which $t_m = 0.5$ Myr. At $t = 0.5t_m$ ($t = 0.25$ Myr), differences from the standard case are small, but various species show signs of the shortened timescale, *i.e.* lower abundances for those which build up, and higher for those which feed the growth of others. CO is a little

Figure 3.7: Column densities as functions of time, calculated through the core – $t_m = 0.5$ Myr run

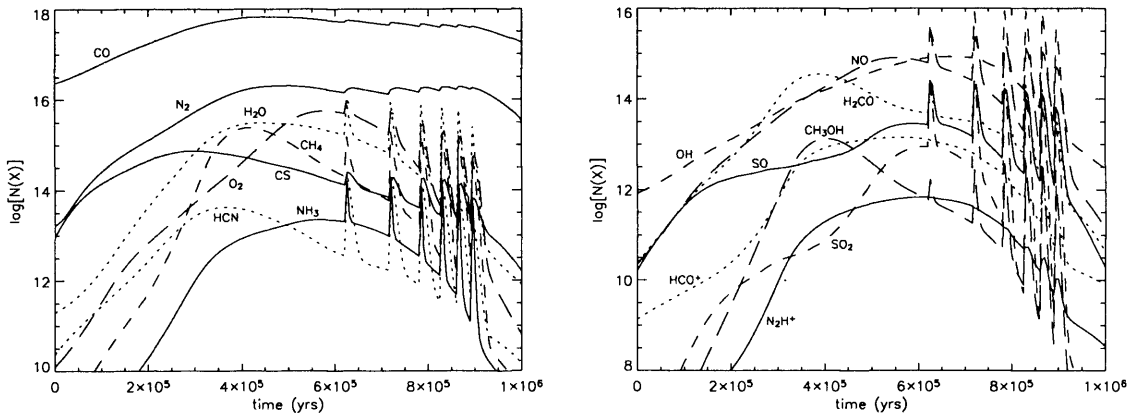

a: Species set 1 b: Species set 2

lower right across the core, which due to the abundance of CO represents large amounts of C and O. N_2 abundance is noticeably smaller. Most other species are to some degree less abundant than at the equivalent time in the standard run. Only certain C-bearing molecules show marginal increases greater than for the standard run, *e.g.* CH_4, H_2CO.

By peak time, many of the symptoms of the shorter timescale are just more pronounced: C^+ is more abundant, as is CH, as they have not been used up to form more complex molecules in the higher density and A_V. N_2 and CO are noticeably lower. Again, this will constitute a lot of N, C, and O, and the differences in N_2 and CO column densities will be more noticeable, since they represent a sum of material through each point. The trough in N_2 abundance at depth points 3 & 4 is shallower for run G-T1 than the standard. This is ultimately due to larger C^+ abundance at these points, which through repetitive H-atom abstraction reactions forms CH_3^+, followed by:

$$CH_3^+ \xrightarrow{e^-} CH \xrightarrow{N} CN \xrightarrow{N} N_2$$

The CS trough around points 7 & 8 is somewhat deeper due to the larger ionisation levels of S for such a high density; freeze-out of S^+ ions is fast and there are many of them due to the larger abundances of C^+, which transfers ionisation effectively.

Profile shapes are not generally altered by the change in timescale.

CH_4, CH_3OH, and H_2CO are substantially larger than for the standard run, right across the core. The reasons for this are slightly different between those points outside, and those inside, the freeze-out zone. Outside, the levels of C/C^+ are still high compared

Figure 3.8: Fractional abundances with respect to total hydrogen as functions of time, calculated from column densities through the core – $t_m = 0.5$ Myr run

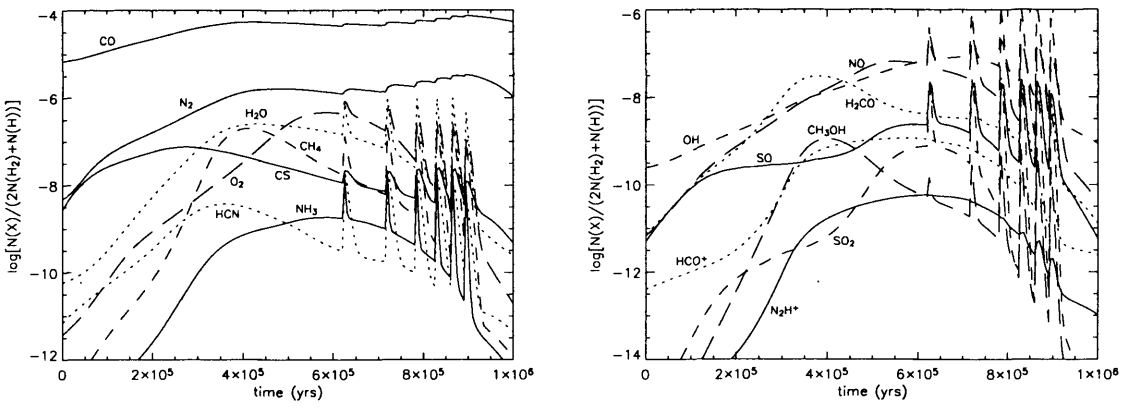

a: Species set 1 b: Species set 2

to the standard run, since there has not been enough time to convert so much into carbon monoxide. Meanwhile, densities and visual extinctions have gone up twice as fast. The excess of C/C^+ in these conditions may be converted into more CH_4 and other more complex carbon bearing molecules. Inside the freeze-out zone, the picture is more complex. Because the onset of freeze-out is coupled to the visual extinction, there is a shorter real-time (rather than comparatively to t_m) period before freeze-out begins. This means that less carbon has been converted into CO in the gas-phase before it starts to be frozen out, and before electron density begins to drop as a consequence of the overall freeze-out process. This, added to the faster onset of high density, high A_V conditions, as experienced inside and outside the freeze-out zone, means that the reactions leading to the production of CH_4 and other larger carbon-bearing molecules proceed more quickly, and with less destructive recombination of the ionic species in the chain. In the standard run, the physical conditions and low fractional ionisation necessary to allow, for example, the abundance of CH_4 to grow were only present at a time when much more carbon had been locked up into CO.

The lower gas phase CO level also affects the rate at which freeze-out needs to take place to achieve 60% by $t = t_m$, at depth point 12. Because model G-T1 has more C/C^+ and less CO, direct C/C^+ freeze-out (the ionic path being faster) is competing with CO production on a more equal basis. In other words, the most effective way to form larger abundances of gas-phase CO is to have a longer period of time before freeze-out begins. To achieve larger mantle-bound CO abundances (at the expense of the gas phase), freeze-

Figure 3.9: Fractional abundances across the core – $t_m = 2$ Myr run

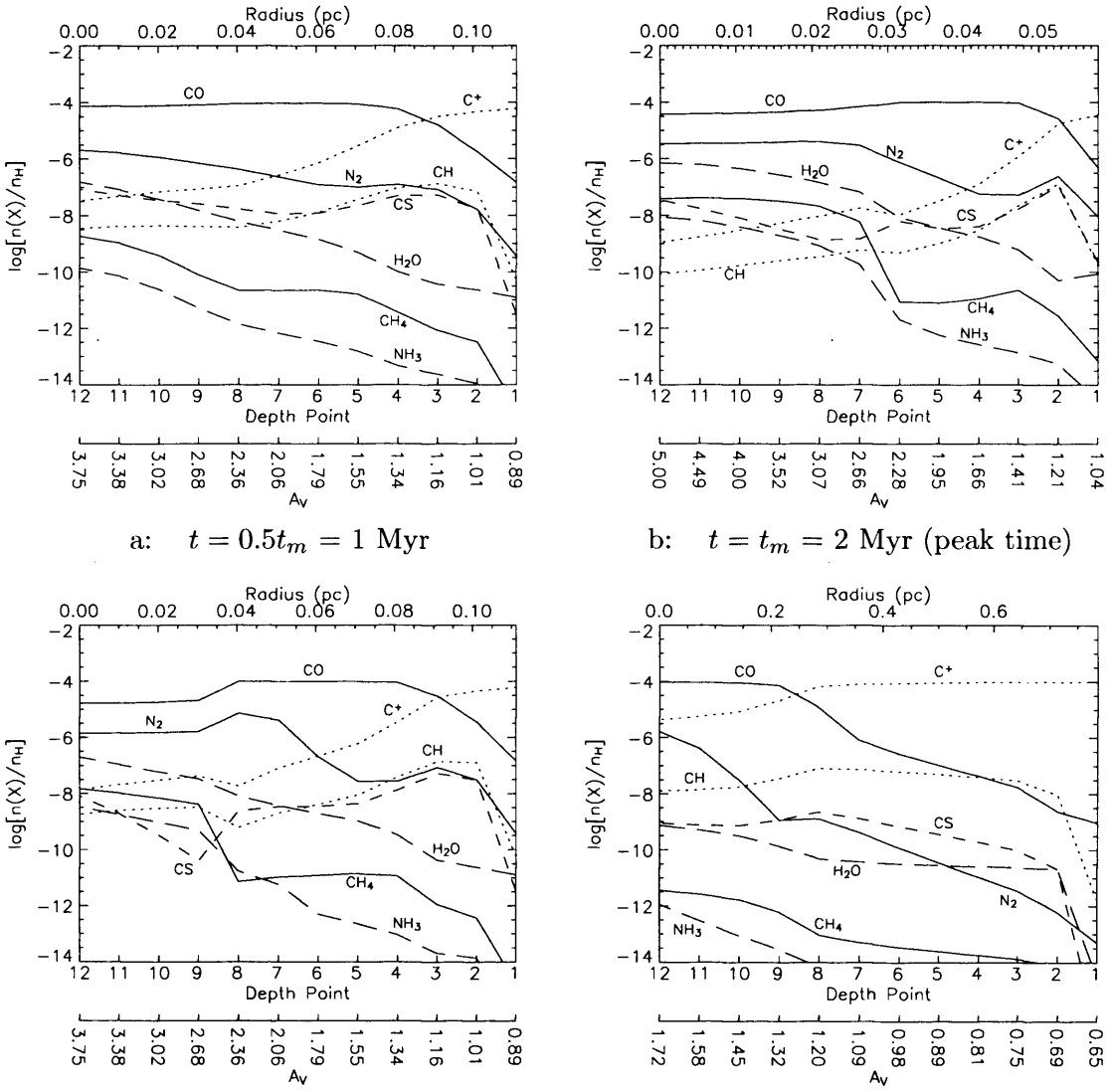

a: $t = 0.5t_m = 1$ Myr

b: $t = t_m = 2$ Myr (peak time)

c: $t = 1.5t_m = 3$ Myr

d: $t = 2t_m = 4$ Myr

out should be switched on quickly, to take advantage of the gas phase carbon before it is converted to CO. This means that the *rate* of freeze-out does not need to be twice as high for G-T1 as for the standard run, since freeze-out levels are made by reference to grain mantle versus gas phase CO abundances.

This lower comparative freeze-out rate does not compensate for the higher ionic abundances in sulphur- and nitrogen-bearing species which in fact causes absolute mantle-bound abundances for such species to be higher in the case of model G-T1 than in the standard run. SO and SO_2 may be seen to be substantially lower within the freeze-out zone, partially due to this, and partially due to the lower levels of OH, which is necessary to form

Figure 3.10: Fractional abundances across the core – $t_m = 2$ Myr run

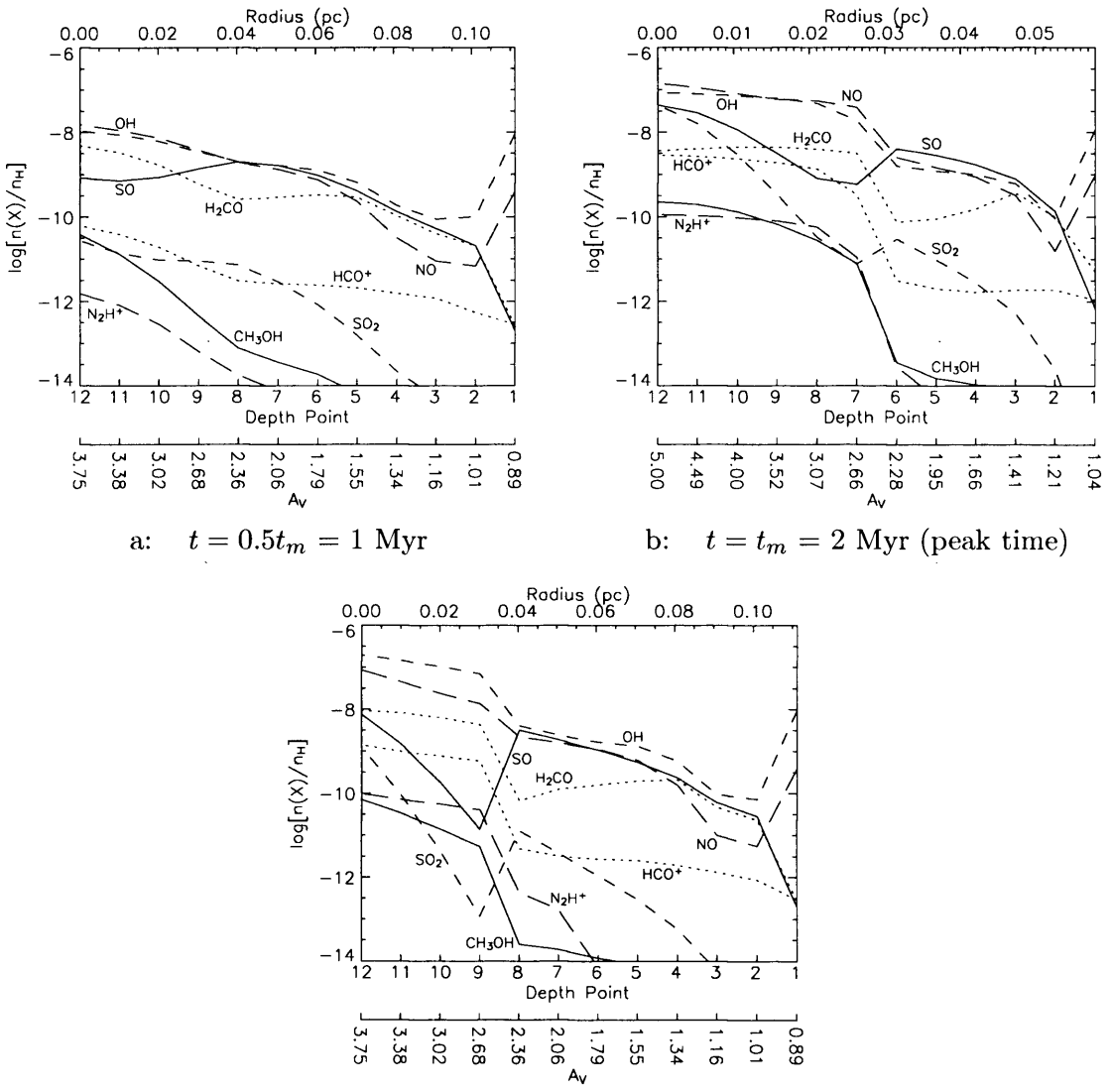

a: $t = 0.5t_m = 1$ Myr

b: $t = t_m = 2$ Myr (peak time)

c: $t = 1.5t_m = 3$ Myr

them. Formation of OH is mainly dependent on the time constraint.

By $t = 1.5t_m$ ($t = 0.75$ Myr), levels are more similar to those of their standard run counterparts. The enhancements in the larger carbon-bearing molecules are now gone, and levels are about the same for both runs.

The main noticeable difference of any interest is that sulphur bearing-species are now very slightly less strongly frozen out than in the standard run at the outer-most freeze-out points, a reversal of pattern compared to $t = 0.5t_m$. This is due to the shorter period the outer points have at high densities *after* peak time, than in the standard run. Inner freeze-out points are less affected because they have already had a long period at high

Figure 3.11: Column densities as functions of time, calculated through the core - t_m = 2 Myr run

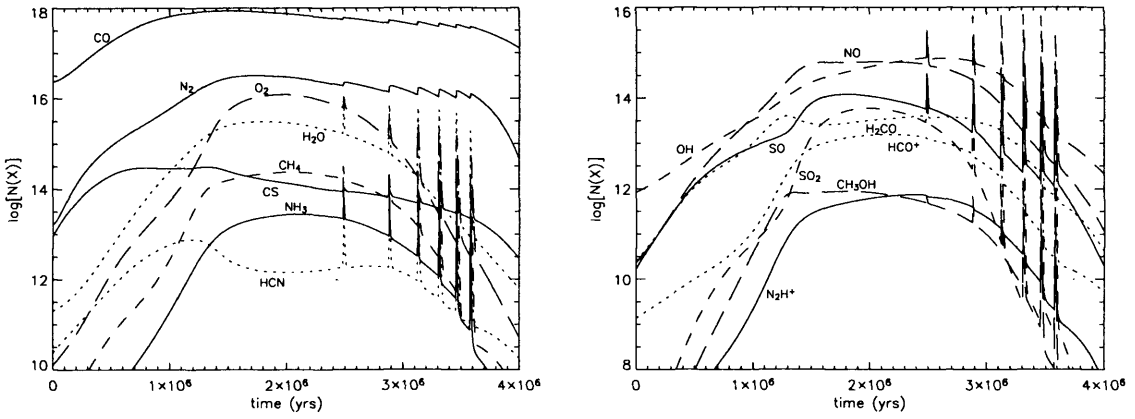

a: Species set 1 b: Species set 2

density, and have removed large amounts of sulphur from the gas phase for the level of ionisation that they have.

The slightly higher CS abundance at depth point 8 is the residue from re-injection, which for G-T1 took place more recently than for the standard run.

By the end time, the most significant differences between models is the physical extent of the molecules, in particular CO, NH_3, and N_2, which have had less time in which to be broken down by the radiation field or ion-molecule reactions.

Figures 3.7 & 3.8 show column densities and resultant fractional abundances through the core's evolution for model G-T1. Differences include the lower CO and N_2 peaks a little before peak time, the much stronger "shoulder" feature at around the same time in CH_4, etc, and the different levels of re-injection, most significantly the higher CS levels. Here, CS is enhanced more strongly due to the greater levels of frozen-out CH_4 which is released and broken down by the radiation field ultimately into CH, which reacts with atomic hydrogen to leave C, which then reacts with SO to form CS. This is supported by reaction of S^+ with CH_4 to form H_3CS^+, which recombines with electrons to produce CS.

SO and SO_2 levels at peak time are lower than for the standard run, due to freeze-out zone depletion.

Note also that the shorter evolution period delays the peaking of O_2 and NO to after the peak time.

The larger physical extents and higher central abundances of certain molecules seen in figure 3.5 at end time show their effects in the column densities and resultant fractional

Figure 3.12: Fractional abundances with respect to total hydrogen as functions of time, calculated from column densities through the core – $t_m = 2$ Myr run

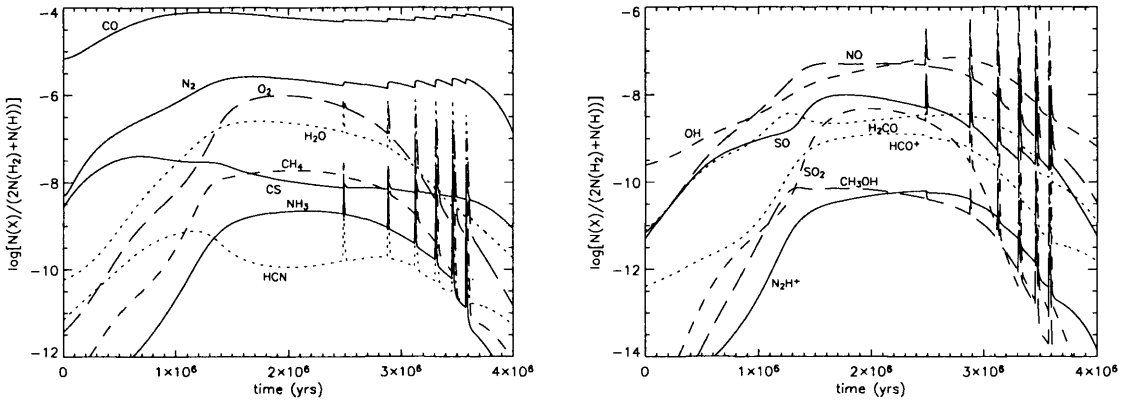

a: Species set 1 b: Species set 2

abundances; N_2 is the most noticeably affected.

Figures 3.9 & 3.10 show fractional abundances for model run G-T2, for which $t_m = 2$ Myr. Peak density and visual extinction are achieved over twice the period taken by the standard run.

Abundances for model G-T2 generally show the reverse effects as for G-T1: CO abundances are generally a little higher than the standard run values, at $t = 0.5t_m$, and similarly for N_2.

By $t = t_m$, most abundances are about the same as the standard case. CH_4 is a little lower, but the lengthening of the time period has a less drastic effect at this point than its shortening in run G-T1.

At the end time there are more obvious differences, again in the slightly lower central abundances, and much lower outer depth point abundances due to the longer period over which the radiation field acts.

The clearest differences with the standard run may be seen at specific times in the column density plots. Figures 3.11 & 3.12 do not display the strong "shoulder" effect before peak time is reached. Indeed, CH_4 does not show any such peaking, only a slight steepness. H_2CO and CH_3OH show only slight peaking at these times. This again is due to the timing of the freeze-out switching on, and the speed at which carbon is converted to CO. Most C/C^+ has been converted to CO by the time freeze-out begins, so that there is little left to form more complex molecules when the conditions are right.

At end time, N_2 is lower than standard for those reasons given already.

Figure 3.13: Column densities as functions of time, calculated through the core - $A_{V,max} = 3$ run

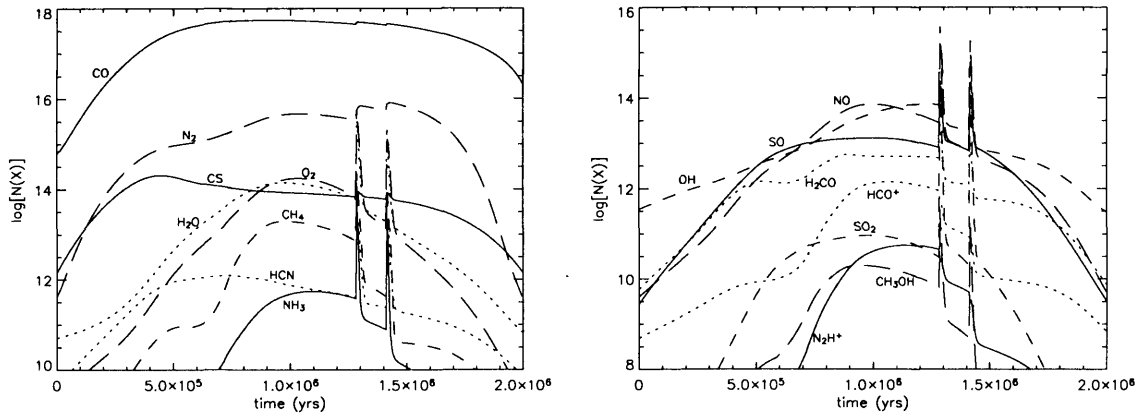

a: Species set 1 b: Species set 2

3.3.3 Runs G-A1 & G-A2

Both runs G-A1 and G-A2 use their own stage ones, rather than the standard one. Hence their chemical profiles at time $t = 0$ in stage two are not the same as standard. Also, since their visual extinctions are controlled by their sizes, this means that column densities are affected in the same sense as the visual extinctions. I here show only column density and resultant fractional abundance plots for models G-A1 & G-A2.

Figures 3.13 & 3.14 show column densities and resultant fractional abundances for model run G-A1, for which $A_{V,max} = 3$. Due to the low A_V, only the two inner-most points reach $A_{V,crit}$. This has the effect of severely limiting the impact of freeze-out zone chemistry on column densities, even considering that this run still uses the same freeze-out level for those which reach $A_{V,crit}$. Hydrocarbon abundances are strongly curtailed, as are many other molecules. Only CO, N_2, CS and SO retain anything like their standard run fractional abundances. Column densities are necessarily lower due to the fixing of $A_{V,max}$. CO does not appear strongly depleted in column density or associated fractional abundance due to the small extent of the freeze-out zone. Meanwhile, N_2 peaks very late due to re-injection. Towards end time it is destroyed because of the low A_V, falling very low, approximately to its initial level. CO is not destroyed so completely, and still retains much of what was formed at the high density stage. This is because the three innermost depth points are still above $A_V = 1$ (1.03, 1.10, 1.18). We may confidently say that the only significant hysteresis in this model is in CO.

Figure 3.14: Fractional abundances with respect to total hydrogen as functions of time, calculated from column densities through the core – $A_{V,max} = 3$ run

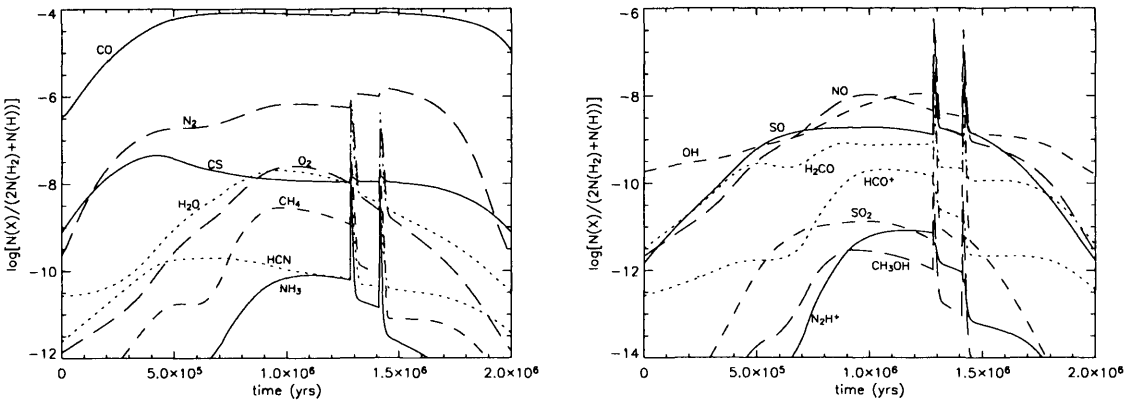

a: Species set 1 b: Species set 2

CS fractional abundances, more than even CO or N_2, remain very close to standard levels, and present a very similar profile over the core's evolution.

Figures 3.15 & 3.16 show column densities and fractional abundances for the slightly more interesting case of G-A2, for which $A_{V,max} = 10$. Here, nine depth points reach the critical extinction — three of them start at this point. However, since the climb to much higher visual extinctions is so fast, and most freeze-out is generally done when densities are higher, this does not make the definition of freeze-out at the inner depth point inconsistent with the other runs for different points through the core. By end time, the three inner points still have yet to return grain mantles to the gas phase.

The enlargement of peak central visual extinction is attained by enlarging the physical extent of the core. This has an obvious effect on column densities; note that the scale of figure 3.15 here goes up to 18.5.

We immediately see that as well as CO having a higher peak column density, it also runs down smoothly to the end time as it has continual re-injection up to this point (as far as is possible with a discrete distribution of depth points). Due to the larger number of points experiencing freeze-out, it also shows stronger depletion in column density. There is, however, little enhancement at end time over initial CO levels — this is because so many points start with high visual extinctions. The physical extent of CO is greater at end time, but still three points are in the freeze-out zone, and their CO abundances are brought low enough by this not to register strongly in column density.

Figure 3.15: Column densities as functions of time, calculated through the core – $A_{V,max} = 10$ run

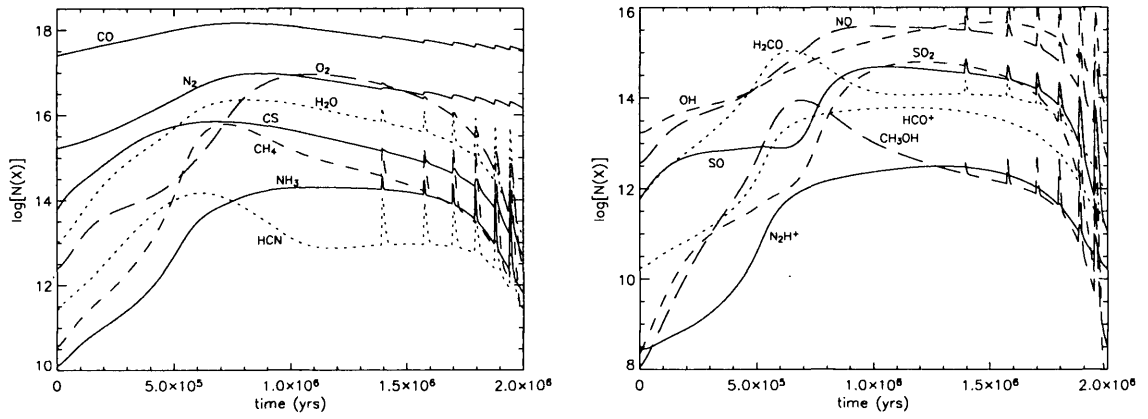

a: Species set 1 b: Species set 2

A general trend for most species which rely on high visual extinction is their much higher abundances, and their much longer survival after peak time. Also note that the pre-peak time shoulder is present, and stronger than for the standard run. Clearly this is due to freeze-out starting very early on for many points, allowing the hydrocarbon species to take advantage by the mechanism discussed in the previous subsection.

Re-injection peaks do not provide such a large contrast in abundances here, compared to other runs, however the peak levels are fairly similar — it is only the underlying values which change between the runs.

3.3.4 Runs G-K1 & G-K2

The dimensionality of collapse parameter, k, represents the number of dimensions along which collapse is taking place (see chapter 2 for a full explanation). Whilst achieving the same peak time visual extinction, with all other parameters remaining the same as standard, the changing of the collapse dimensionality in runs G-K1 & G-K2 results in different visual extinctions and size from the standard values at all times other than $t = t_m$. Hence these two runs start at different visual extinctions and sizes from the standard run, and so they each require their own stage 1. In the same way as for G-A1 & G-A2, the column densities naturally vary in the same sense as the visual extinctions due to the changing size scale.

Run G-K1 takes $k = 1.2$. This means that the increase in visual extinction up to the peak time is less dramatic, therefore the initial level must be higher than for the standard

Figure 3.16: Fractional abundances with respect to total hydrogen as functions of time, calculated from column densities through the core – $A_{V,max} = 10$ run

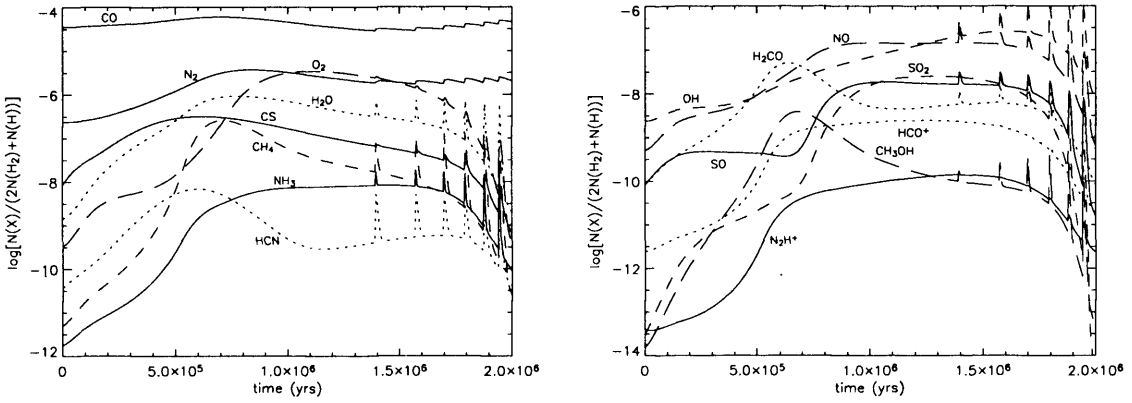

a: Species set 1 b: Species set 2

case. Because of these higher levels, depth points 11 & 12 start within the freeze-out zone. I invoke the same argument in justification of this as for model G-A2. Six depth points in total reach $A_{V,crit}$. The larger visual extinctions across the core mean earlier passage into the freeze-out zone. The size scale of the core starts around twice as large as the standard value. By peak time it collapses down to the standard size.

Figures 3.17 & 3.18 show column densities and fractional abundances for model G-K1. CO levels start higher than standard due to the greater visual extinctions and larger size providing more effective self-shielding. Because these high levels are established in stage 1, where the chemistry is run to equilibrium, there is less free C/C^+, which means less charge transfer to sulphur. Since the main mechanism for sulphur depletion is via S^+-grain sticking, there is more free sulphur in the gas phase during this run at inner depth points. This produces higher CS levels at the centre of the core at peak time, but the longer period the outer freeze-out points spend in the freeze-out zone means more CS depletion at those points.

CO column density, as for model G-A2, relaxes steadily compared to the standard case, due to the continual re-injection of mantle-bound CO, and the greater level of protection from the ISRF.

As peak time approaches, most species tend to assume the same levels as the standard run. This is because the difference in the rate of change of A_V slows as t_m approaches, and with the same density profile all through, this means that at the higher densities where the chemistry around peak time mostly takes place, there is little physical difference between

Figure 3.17: Column densities as functions of time, calculated through the core – $k = 1.2$ run

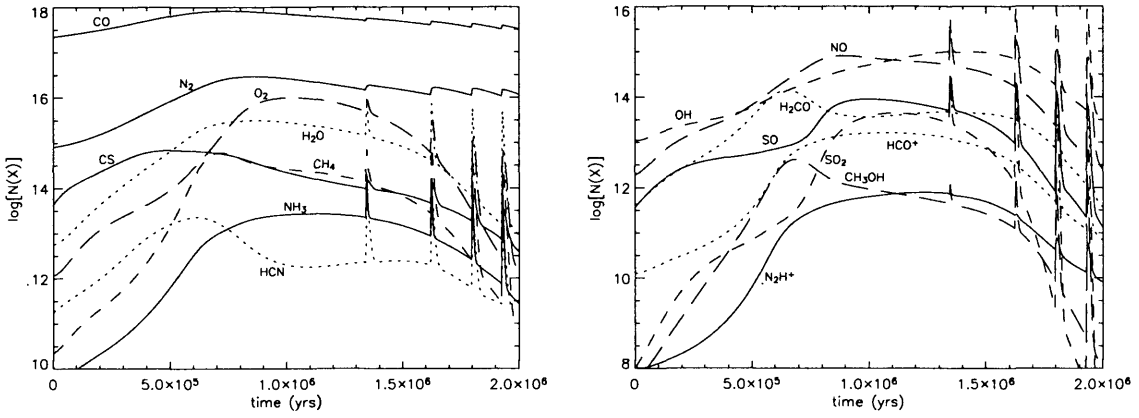

a: Species set 1 b: Species set 2

the models.

The pre-peak time shoulder is again present, although hydrocarbon abundances here are marginally lower, due to the conversion of some carbon into CO during stage 1.

CS levels are again fairly stable throughout the evolution, varying little from the standard profile or standard levels, even near beginning and end times.

The lower k value allows the re-expanded core more protection from the interstellar radiation field, allowing longer survival of species formed at peak time densities. Peak time column density-derived abundances remain higher for longer. Final abundances are also more significant for G-K1 than the standard run. For example, here, N_2H^+ levels are potentially observable at end time, taking a value around 10^{-12}, while the standard run takes a value more than an order of magnitude lower.

Figures 3.19 & 3.20 show column densities and fractional abundances for model G-K2, for which $k = 1.8$. The initial level of visual extinction is lower than for the standard case. All six freeze-out depth points begin outside the freeze-out zone, due to their lower visual extinctions. The size scale of the core starts around half as large as the standard value. By peak time it collapses down to the standard size, as for model G-K1.

Chemical abundances for G-K2 are almost identical to the standard values, depth point for depth point, excepting the initial and very end times, at which abundances are somewhat lower. However, the lower initial visual extinctions (and size scale) make the column density evolution much more dramatic than for G-K1 or the standard run. Again,

Figure 3.18: Fractional abundances with respect to total hydrogen as functions of time, calculated from column densities through the core – $k = 1.2$ run

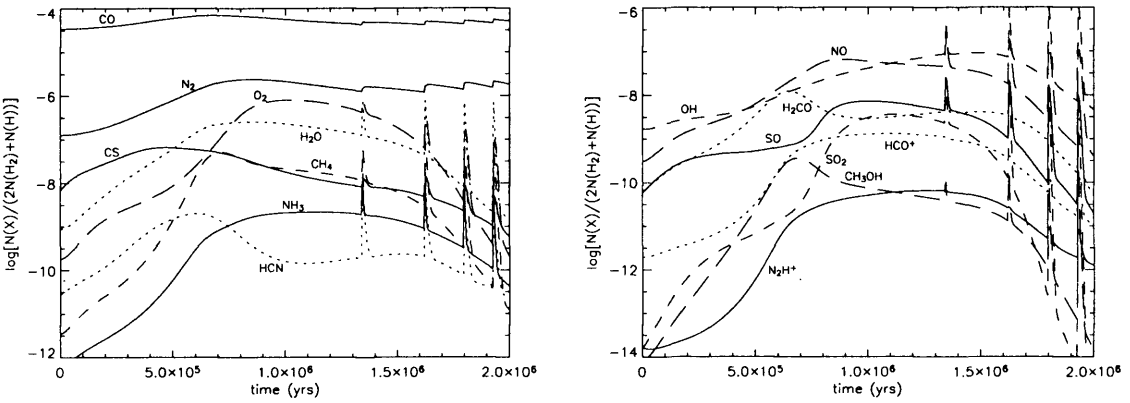

a: Species set 1 b: Species set 2

the peak time values tend to be very similar to standard, since at this time the physical parameters are the same, and are increasingly similar in the approach to peak time.

Pre-peak time shoulder abundances are virtually the same as the standard run values.

Again CS column density and associated fractional abundance is very robust in comparison with other observables.

At the very early and late times, the major reason for lower column densities in most observable species, besides the smaller scale, is the loss of higher A_V points at the core centre.

3.3.5 Run G-S

This run uses all the same physical parameters as for the standard run. Only the level of freeze-out is brought down, by approximately 90%, to represent a sticking coefficient of $S = 0.1$.

Initial and final column density and fractional abundance levels are the same as for the standard case, indicating that for the sort of timescales and densities employed in this study, with other parameters taking standard values, a change in the level of freeze-out has no effect on end time column densities and fractional abundances. This is indeed true for the individual depth points as well.

However, at all other times in between, column densities are very different from the standard case. The low level of freeze-out means that C/C^+ is converted into CO much more strongly than it is frozen out. Also, as a consequence of lower ionic freeze-out, the

Figure 3.19: Column densities as functions of time, calculated through the core – $k = 1.8$ run

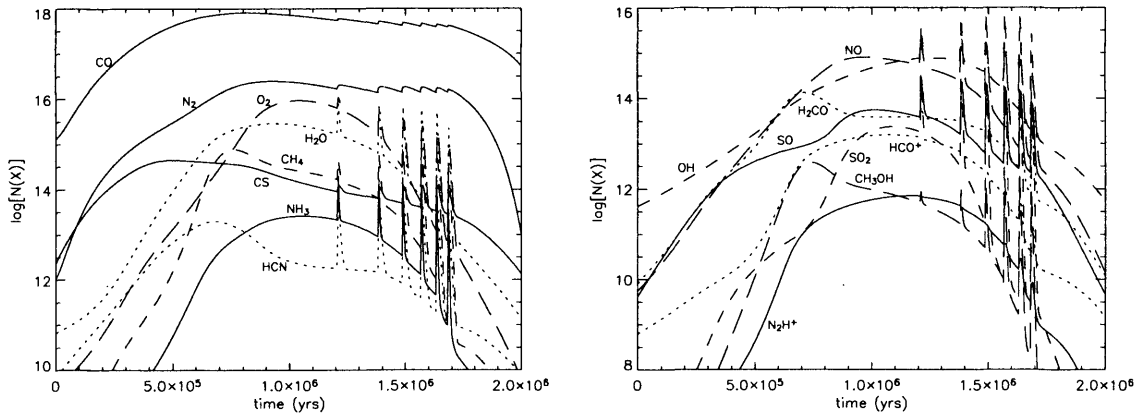

a: Species set 1 b: Species set 2

electron abundance is higher than for the standard case – by ~25 times at peak time for the central depth point, much more than the ratio of freeze-out levels. This means that hydrocarbon formation is very much suppressed, as can be seen in figures 3.21 & 3.22, at all times.

CO remains high throughout the high density period, and bears no obvious signatures of re-injection. N_2 is also minimally affected.

The CS profile is very much altered by the lower freeze-out level; it continues to grow beyond its standard run peak level, finally peaking at around the peak density time, t_m. Meanwhile, NH_3, N_2H^+, O_2, and HCO^+ are dramatically reduced. O_2 requires the strong removal of atomic carbon in the freeze-out zone to reach as high as the standard case, otherwise it may be destroyed via:

$$C + O_2 \longrightarrow CO + O$$

At peak time, C is around an order of magnitude larger at the central depth point for model G-S than for the standard run.

SO and SO_2 benefit from the later peaking of O_2, since there is still a lot of sulphur left in the gas phase at this point, whilst there is again much less destructive atomic carbon around, allowing them to reach higher levels than for the standard case.

H_2O, singularly of the selected observable species, is mostly unaffected by the change in sticking coefficient, aside from a slightly later peaking. This is not just a column density effect – it stems from the strong similarity of the point by point abundances. This is

Figure 3.20: Fractional abundances with respect to total hydrogen as functions of time, calculated from column densities through the core – $k = 1.8$ run

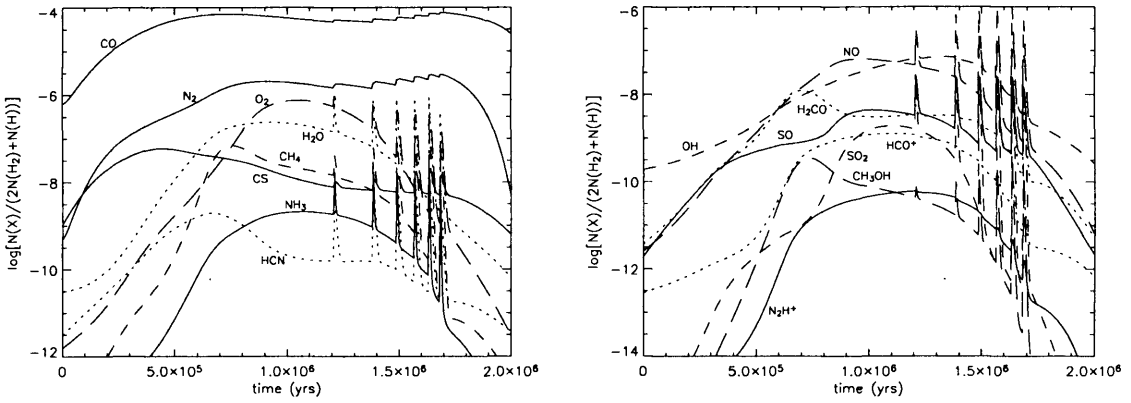

a: Species set 1 b: Species set 2

mainly as a result of a balance between O and H_3^+ which may form OH^+, which is a necessary link in the H_2O-formation chain. This balance is effected by on one hand the larger electron abundance in model G-S, which limits H_3^+, and on the other the freeze-out of O onto dust grains in the standard model. Since these happen to approximately cancel out, and since the two effects are closely coupled to the freeze-out rate, this relationship is more or less maintained throughout the evolution of the core, and OH^+ levels are therefore not strongly affected by the change in sticking coefficient. This carries through to H_2O through the chain:

$$OH^+ \xrightarrow{H_2} H_2O^+ \xrightarrow{H_2} H_3O^+ \xrightarrow{e^-} H_2O$$

The larger electron abundance of model G-S also acts in the last stage of H_2O formation, above, to stabilise levels between the two runs.

3.3.6 Run G-D

Model G-D takes a peak central density of 5×10^5 cm^{-3}. As it is restricted to the same peak central visual extinction as the standard run, visual extinctions at times $t \neq t_m$ are lower than the standard levels, gradually converging towards peak time. Visual extinction profiles are also shallower across the core than their corresponding standard profiles at times $t \neq t_m$. This model requires a smaller size scale to fix its peak central A_V to 5. At peak time, the core is ten times smaller than the standard size; at time $t = 0$ it is roughly half as large as the standard initial size. Model G-D therefore requires its own stage one.

Figure 3.21: Column densities as functions of time, calculated through the core – $S = 0.1$ run

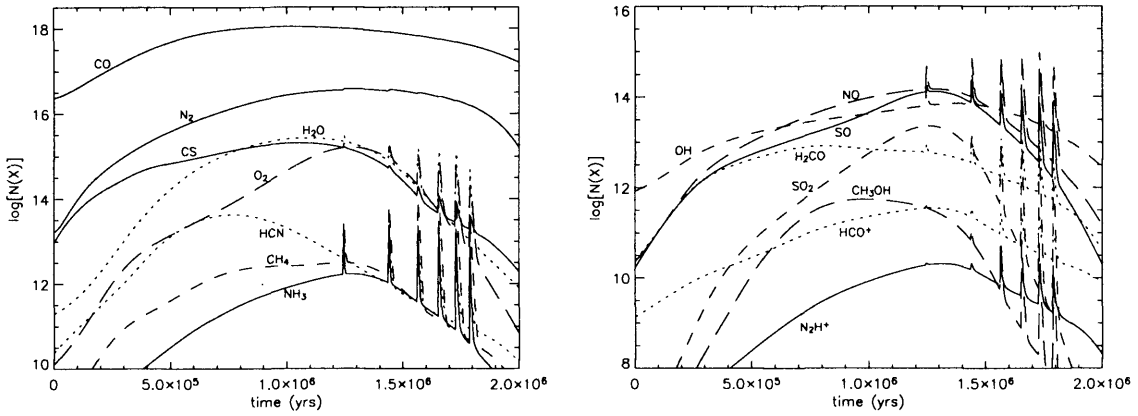

a: Species set 1 b: Species set 2

Note that while peak density is ten times higher than standard, the initial density profile is the same as for the standard run.

Due to the shallower A_V profiles, $A_{V,crit}$ is reached later on for those points which reach it, compared to the standard run.

Figures 3.23 & 3.24 show column densities and fractional abundances for model G-D. CO can be seen to peak both higher and slightly earlier than standard. Enhancement from initial levels is very strong, as is the level of hysteresis by the end time, which is close to two orders of magnitude and leaves CO fractional abundance at around 10^{-5} in the diffuse conditions of end time. The sharp increase in density early on in the core's evolution allows much carbon to be converted quickly into CO, when visual extinctions reach levels which allow it to survive.

CS takes a similar profile to the standard run, except for two features. Firstly, column density drops at around the time CO peaks, rising to around the same level again just before peak time. This drop is because of a sharp fall in C_2 levels at certain depth points. This itself comes about because of fast CO conversion, and a fast drop in electron abundance because of the loss of C/C^+, which otherwise effectively transfers charge to other species. As C_2 formation relies heavily on both atomic carbon levels and on electron abundance for the final stage in its formation (recombination of $C_2H_2^+$), it sharply falls, removing a major contributor to CS formation for medium range depth points. CS gradually rises again at these points, as SO levels begin to peak. Sulphur is still abundant as the fast removal of carbon leaves large amounts of S charge-neutral, so that it is present

Figure 3.22: Fractional abundances with respect to total hydrogen as functions of time, calculated from column densities through the core – $S = 0.1$ run

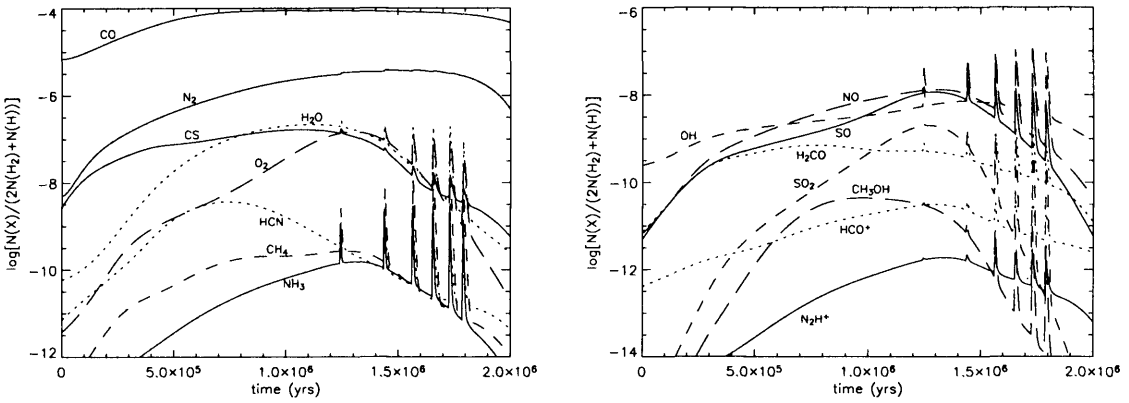

a: Species set 1 b: Species set 2

to react with O_2 as *its* levels rise. CS is formed again when the large abundances of SO react with small amounts (relative to CO) of atomic carbon which arise from He^+ breaking down carbon monoxide to leave C^+, which quickly transfers the charge to the abundant atomic sulphur.

The other feature in the CS profile is the late bump after the last freeze-out point has re-injected its grain mantles into the gas phase. This is caused by the core's descent into low visual extinction. When A_V starts to approach its initial/final levels, density is still comparatively high. This drives a chemistry which quickly feeds off the products of newly photo-destroyed species, of which CS is a beneficiary.

The pre-peak time hydrocarbon shoulder is not present here, due to the fast removal of C/C^+.

In this model, H_2O column densities and point by point fractional abundances do not vary strongly from standard levels. This is due to the same mechanism as for model G-S, except that here it is the electron abundance that plays the most important part; within the freeze-out zone, higher electron abundances limit H_3^+, whilst enhancing the level of H_3O^+ recombination.

The high SO levels discussed above should be noted; SO peaks more than an order of magnitude higher in column density than in the standard run.

Generally, column densities are less broad about time $t = t_m$, and rise and fall more sharply, than the standard case. This is because visual extinctions start lower, but when they reach a point where species are reasonably protected from the interstellar radiation

Figure 3.23: Column densities as functions of time, calculated through the core – $\rho(0, t_m) = 5 \times 10^5$ cm^{-3} run

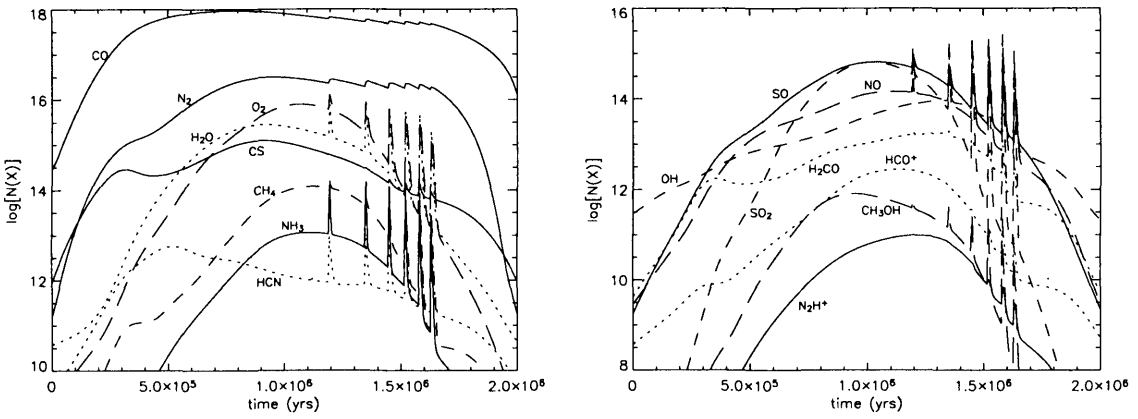

a: Species set 1 b: Species set 2

field, the high density allows them to be produced more quickly. Likewise, they may be destroyed more quickly when visual extinctions are no longer very large.

There are certain similarities between model G-D and model G-A1, since their relationships between density and visual extinction are similar. There are some major differences though – the abundances of CH_4 and NH_3 at peak time are larger in model G-D, both species assuming levels an order of magnitude higher than in the model G-A1. Also, peak SO levels in model G-D are the highest of any of the runs, making this high density model quite unmistakeable (excluding the uncertain levels after peak time, due to re-injection of grain mantles).

It is noteworthy that neither NH_3 nor N_2H^+ reach such high levels as are achieved in the standard run. This reveals a divide in species according to the two freeze-out categories mentioned earlier; because sulphur depletion is dominated by ionic freeze-out processes, and carbon, the important carrier of charge, is converted quickly to CO, S is not frozen out as strongly as C and N which are affected more strongly by neutral species freeze-out.

3.4 Discussion

Clearly, the chemical behaviour of the models displays a strong dependence on freeze-out; the rate, the period of time over which it is active, its physical extent, and the level of chemical processing before it begins all play their part in determining abundances through the core's evolution, whilst the re-injection of frozen-out species exerts an influence

Figure 3.24: Fractional abundances with respect to total hydrogen as functions of time, calculated from column densities through the core – $\rho(0, t_m) = 5 \times 10^5$ cm^{-3} run

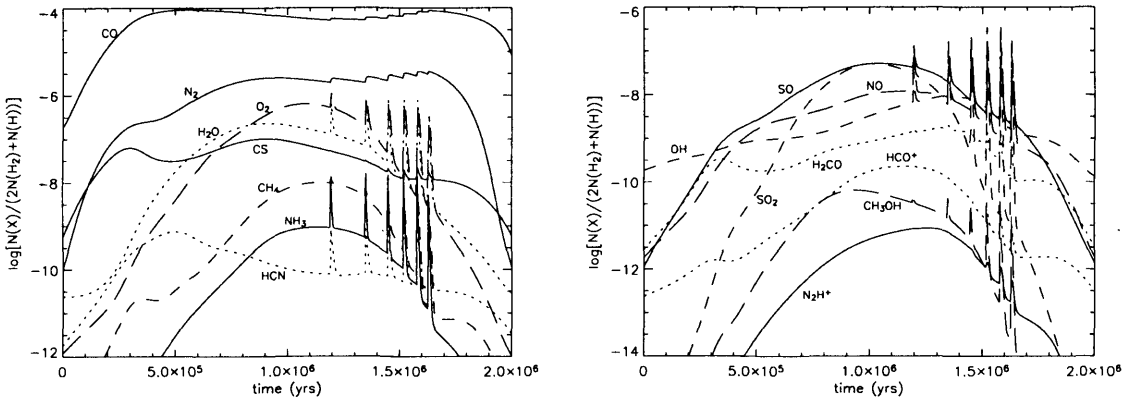

a: Species set 1 b: Species set 2

over the post-peak time chemistry. These elements are controlled by the interplay of parameter choices. The multi-point modelling of this study emphasises how important these parameter choices are, since they affect an entire set of chemical reference points which react in their own way to the changes.

The value of the peak time parameter, t_m, makes only a small difference to column densities for most of the core's evolution (models G-T1 & G-T2). Levels for most species are not drastically affected, although what might normally be labelled late-time species, like NH_3, show some enhancement with longer evolution times, as might be expected. The behaviours of HCO^+ and N_2H^+, contrary to those of many other molecules, are unaffected by the time scale, either in the levels reached or in their overall profiles. These two molecules follow the density and visual extinction evolution, hence they remain good tracers of these parameters in the regime of this model.

The main variation in chemical behaviour around peak time is the larger growth of the hydrocarbon "shoulder" for shorter time scales, although its brief period of prominence would make it difficult to detect individual cores. Its contribution in statistically large samples might be noticeable.

The effect of changing the peak central visual extinction (models G-A1 & G-A2) is drastic; the lower value of 3 produces a chemistry where little appreciable molecular material is formed, and little survives the return to diffuse conditions. The re-injection spikes are very large, however this is a result of the standardisation of freeze-out levels through-

out the grid. The higher value of 10 produces rather larger abundances of many observable species, however its high initial visual extinction values (up to $A_V = 3$) may in reality be unlikely to pertain in the diffuse background conditions which I cite as a starting point, especially considering the initial size required to achieve this particular example: ~ 1.5 pc. Such a large-scale fluctuation in density in a medium of a nominal background gas density of $n_H = 300$ cm^{-3} is inconsistent with our picture of a cloud consisting of small unresolved cores; the large column density of CO over such a potentially large size scale should be resolved by single-dish telescopes, and would be something more akin to the traditional dark cloud core (*i.e.* Myers core). The fact that such cores tend to have density estimates of $n_H = 10^5$ cm^{-3} or higher (as opposed to the initial 10^3 cm^{-3} of this model) leaves model G-A2 inconsistent with either regime. Since the large column densities of this model are to a large degree dependent on the initial (high A_V) conditions, we should not expect to see this kind of chemical behaviour in transient dense cores, at least without commensurately higher densities to provide the large visual extinctions instead of large size scales.

Aside from these points, the trends displayed by these models are such that chemical hysteresis should scale in the same sense as visual extinction.

The same argument may be made against model G-K1, for which $k = 1.2$, as against model G-A2. This model has a similar initial size and central visual extinction to model G-A2. We should therefore expect that a real core of value $k = 1.2$ should achieve a putative visual extinction of $A_V = 5$ through a larger central density. Model G-K2, for which $k = 1.8$, assumes more reasonable initial sizes and visual extinctions. However, regardless of the individual merits of the models, the chemical trends resulting from the variation of this parameter are of stronger chemical hysteresis in cores of lower values of k. This is not only due to the higher initial and final visual extinctions but to the less vigorous change in A_V throughout the core's evolution. This also means that large column densities, formed more strongly around the peak time when densities are high, are stretched out over time, providing a longer "memory" of a high density era in the core.

The model with sticking coefficient of $S = 0.1$, model G-S, shows how important a large level of freeze-out is to the formation of certain observable molecules. This means that observations of such large CO column densities as are achieved with this model combined with high levels of H_2O ($\sim 10^{-7}$) and very low NH_3 and hydrocarbon levels would imply a low sticking coefficient.

Model G-D does not display much chemical hysteresis, apart from carbon monoxide, and peaking in density-tracing molecules is low and comparatively sharp. The locking-up of carbon into CO before freeze-out begins to act seriously curtails the formation of carbon-bearing species. A high density run like this using a lower value of k would give higher initial and final visual extinctions, and therefore might allow a more interesting chemistry to develop.

3.5 Conclusions

This study of a number of parameter variations in the transient dense core model shows firstly how substantially column densities may vary due to the behaviour of the chemistry at individual points within a core. This lends more weight to the argument that a multi-point approach to chemical modelling of such environments is crucial to our understanding of their chemistry and the interpretation of observational results.

The testing also gives more confidence as to the robustness of the standard model in broadly representing the chemical and physical behaviour of a transient dense core. The representative time scale of 1 million years is a safe value, and in the case of real cores, variations in the timescale of a factor of 2 either way should not dramatically affect the chemistry or hence the detected column densities.

Whilst the chemical variations and levels of hysteresis seen in the k-runs and the A_V-runs seem strongly dependent on those variables, the underlying influence is the initial visual extinctions of those runs, and the time taken for points to reach the critical visual extinction. Those runs with larger peak time molecular abundances and/or stronger chemical hysteresis are those which have initially higher visual extinctions.

Also, those runs with less overall freeze-out, either through the sticking coefficient or through the time taken to reach $A_{V,crit}$, through k or $A_{V,max}$, show less molecular enhancement at any time over the core's evolution. We should therefore expect that the cores observed in Morata *et al.* (2003) would have higher rather than lower peak visual extinctions, and lower rather than higher values of the collapse dimensionality parameter, k, so that more points (*i.e.* a larger fraction of the core) reached the critical visual extinction. This arrangement should produce cores which do not contribute highly extended emission in their early stages. Also, we should expect that the sticking coefficient would be closer to $S = 1.0$ than to 0.1 so that substantial levels of molecular species could be

achieved at all, to be subsequently detected.

All this means that the initial physical conditions of the transient dense cores are all-important for their resultant chemistries. It also leaves our standard run as being fairly representative of the sort of cases that we are trying to model. This study shows that the results of the parameter variations can be entirely understood from the chemical network. This gives great confidence in both the physical and chemical aspects of the model, and its robustness relative to parameter changes, providing a sound basis for further applications of the model.

CHAPTER 4

Cyclical Dense Cores in Dark Clouds

4.1 Introduction

In the work of previous chapters, the timescale for formation and destruction of cores is assumed to be on the order of 1 Myr. This leaves the opportunity for a number of core cycles to take place within the lifetime of a dark cloud, determined to be on the order of a few Gyrs (see *e.g.* Bash *et al.* 1977, Leisawitz *et al.* 1989). On this basis, we might expect that some material which had previously resided in one core might be recycled into another, newly-forming core. The evidence of the previous chapters shows that definite chemical hysteresis results from the core evolution process, and so this could in turn affect the chemistry throughout the evolution of a subsequent core.

In order to test this hypothesis, I here investigate the chemistry of a core cycled through a number of contractions and expansions governed by the standard run parameters of the transient dense core model used in the previous chapter. On completion of an entire cycle of core evolution, the same material immediately embarks on an identical cycle of physical evolution, with the chemical state at each depth point preserved over the transition between cycles. Previous studies of cycling in dark clouds such as Charnley *et al.* (1988a), Charnley *et al.* (1988b), Nejad *et al.* (1990) and Nejad & Williams (1992) have adopted a different mechanism for the formation and destruction of dense clumps from that used here, resulting in a different chemistry. This makes the work of this chapter unique from those studies. However, some of their general results are preserved in this work.

The processing of the diffuse background gas that results from the formation and dissipation of a dense core, in the regime of the transient dense core model, will by definition influence the chemistry of the subsequent core cycle. This cycling model assumes that cycles immediately follow one-another, however this may not be strictly necessary for approximately similar values between the end of one cycle and the next to obtain. This depends on the time period over which the enhanced chemistry of the post-evolution core degenerates back to the pre-evolution equilibrium levels. Hence in this chapter I take a deeper look at the post-evolution chemistry of the background gas, and relate it to the chemical evolution which may take place in a regime where cyclical core formation takes place.

4.2 Cyclical Cores

The only other studies of cycling in dark clouds used a model of clump/core formation very different from this one. Charnley *et al.* (1988a) investigated a mechanism by which winds from young low-mass stars cause cycling of material between dense clumps and tenuous interclump gas, following the suggestion of Norman & Silk (1980) and Goldsmith *et al.* (1986). Their model involved an initial collapse of diffuse material to form a dense clump, which after a period of quiescense is then ablated by wind moving around the clump. At this point the density drops quickly, and mixing of the wind and dense core gas takes place. When the clump reaches the edge of the wind-blown bubble, it passes through a shock, the density increases sharply, and frozen grain mantles are re-injected immediately into the gas phase. Over a period, the gas cools, and the density rises to pre-collapse values. The total evolution time of this mechanism is on the order of a few million years. The subsequent studies of Charnley *et al.* (1988b), Nejad *et al.* (1990) and Nejad & Williams (1992) used this ("slow cycle") or similar models to run a single-point chemistry through a number of cycles. The broad conclusions of these studies that are pertinent to this one were that the resultant chemistry was characteristically young, that a limit cycle was achieved after only a small number of cycles, and that the re-injection of grain mantles would strongly affect abundances. Also, fractional abundances were predicted to vary a great deal between points in a dark cloud.

The cycling model to be investigated in this chapter does not involve mixing at boundaries, hence no injection of ionised material. It includes no shock chemistry, hence no sharp

changes in density, visual extinction or temperature, and generally the transitions in density and visual extinction are smooth. It does involve the instantaneous re-injection of grain mantle-bound species into the gas phase; however, for the central depth point of the core in this study (which corresponds to the single point modelled in the other works), re-injection does not take place until a relatively low visual extinction and density are achieved. In the Charnley *et al.* (1988a) and subsequent models, there is no photoionising radiation, and ignoring the mixing of wind-borne ions, the sole source of ionisation is cosmic rays. It should also be noted that those models were single-point simulations, whilst this one uses an array of 12 depth points. On the evidence of previous chapters, the range of chemistries across the width of a core is quite broad, and warrants a multi-point treatment.

These differences highlight the necessity for a consideration of the Falle & Hartquist mechanism, in the context of this transient dense core model, as a cyclical process potentially capable of enhancing dark cloud chemistry more than might be indicated by a single cycle. It would also be instructive to consider what observable differences might be apparent to discern the level of chemical processing in dark clouds due to this mechanism, and the sensitivity of these observables to the timescale between one core cycle and the next.

4.2.1 The Cyclical Core Model

The chemical and physical parameters adopted for this model are exactly the same as those used in the standard run of chapter 3, and indeed the first cycle is that very run. I have made subsequent cycles of the model, taking the final fractional abundance values at each depth point as the starting values of the following run. Hence this model assumes that the same parcels of gas are being modified in the same way for each cycle, *i.e.* there is no intercore mixing or core-background mixing between cycles, and the physical evolution of the core proceeds in the same way for each point as it did in the previous cycle. The multi-point approach of this model demands that these limitations be explicitly stipulated. A more complex model of the cycling process (such that subsequent cycles might process the material in different ways, according to larger or smaller changes to physical parameters, or might be physically displaced from the original site) is beyond the scope of this study, and would be of questionable value before a straight-forward study of this kind has been carried out and more supporting observational data are obtained to further constrain

Figure 4.1: Column densities as functions of time, calculated through the core – cycle 2

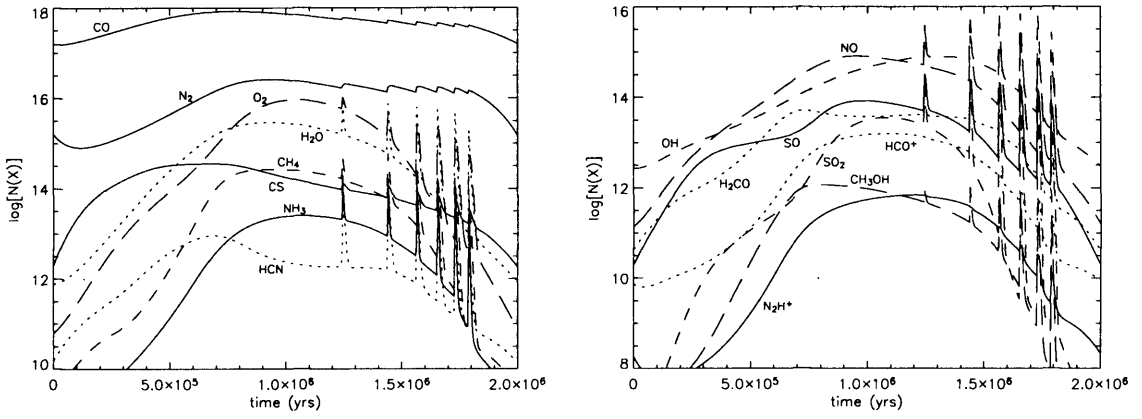

a: Species set 1 b: Species set 2

model parameters (or ranges thereof).

The freeze-out *rate* was maintained for all subsequent cycles at the same level as the first (the standard run), which in fact leads to slightly larger values of freeze-out in later cycles (~62% for the second cycle, compared to 60%). This however maintains a consistency between cycles in a way appropriate to the model, that fixing the *level* of freeze-out would not.

Five cycles (including the initial, standard model) have been run, the results of which are displayed and explored in the next section.

4.2.2 Results

I present time-dependent column densities and resultant fractional abundances for cycle 2 of the standard core model, obtained in the usual way, in figures 4.1 & 4.2. I compare these figures with those obtained for the standard run of chapter 3, see figures 3.3 & 3.4.

The first obvious difference between this and the standard run is the dip in some column densities and fractional abundances, and rises in others, just after time $t = 0$. This is due to the low visual extinctions at these times, which still act to break down molecular material, and it takes the gradual return to higher visual extinctions for this trend to turn around.

The other main difference is the diminution of the hydrocarbon "shoulder" – this is due to the retention of carbon in the form of CO following the first cycle, producing a lower initial C/C^+ level, so leaving less available for the formation of CH_4, etc. Thus the

Figure 4.2: Fractional abundances with respect to total hydrogen as functions of time, calculated from column densities through the core – cycle 2

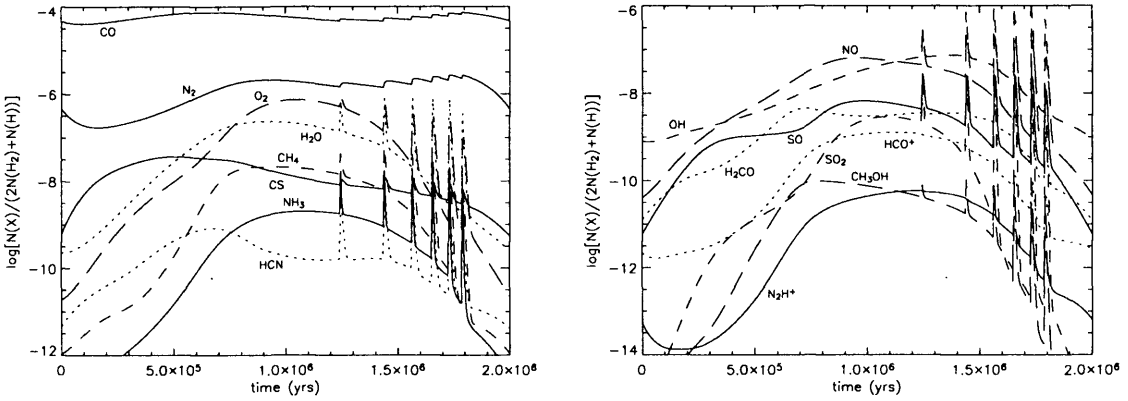

a: Species set 1 b: Species set 2

chemical hysteresis resulting from the first cycle limits the chemistry of the second.

The column densities and fractional abundances of further cycles of the model are in fact very little different from the second, and almost all molecules show no difference after this cycle. Tables 4.1, 4.2 & 4.3 show column densities and fractional abundances at beginning/end time, at the hydrocarbon "shoulder" ($t = 7.2 \times 10^5$ yrs), and at peak time for the first, second and third cycles. Values which are different from the previous cycle are highlighted in bold face. By the third cycle, a limit cycle is quite definitely reached and almost all point by point fractional abundances are identical at equal times through the cycle. Calculated column densities and resultant fractional abundances are identical for all molecules. I therefore omit results for cycles 4 and 5.

It may easily be seen by the highlighting of values in the tables that levels at the "shoulder" vary the most between the cycles, and that variations persist for longer (in terms of cycles) at this time than for the other two. The time at which the shoulder peaks in various molecules is the same for each cycle, although individual molecules peak at slightly different times from each other; I choose $t = 7.2 \times 10^5$ yrs as a representative time value for the shoulder. As mentioned above, the strength of the shoulder in the initial run is not subsequently replicated, due to the chemical hysteresis, which leads to lower levels in the later runs. Levels of CH_4, CH_3OH and H_2CO are approximately 4 times, 4 times and 3 times lower, respectively, in the second cycle than the first. Meanwhile SO_2 is 5 times higher, and SO is twice as high. All this may provide criteria for the determination of the frequency between putative cycles in dark clouds. If observed levels in cores which

Table 4.1: Selected column densities through the core and fractional abundances computed from column densities, for three cycles at start/end time †

	Standard	(start)	Standard	(end)	Cycle 2	(end)	Cycle 3	(end)
Species i	$N[i]$ (cm^{-2})	$X_N[i]$ ‡	$N[i]$	$X_N[i]$	$N[i]$	$X_N[i]$	$N[i]$	$X_N[i]$
H_2	**1.6(21)**	**4.9(-1)**	**1.7(21)**	4.9(-1)	1.7(21)	4.9(-1)	1.7(21)	4.9(-1)
CO	**2.3(16)**	**6.9(-6)**	**1.6(17)**	**4.7(-5)**	1.6(17)	4.7(-5)	1.6(17)	4.7(-5)
O_2	**1.3(10)**	**3.8(-12)**	**6.3(10)**	**1.9(-11)**	**7.5(10)**	**2.2(-11)**	7.5(10)	2.2(-11)
H_2O	**2.0(11)**	**5.9(-11)**	**7.7(11)**	**2.3(-10)**	**8.7(11)**	**2.6(-10)**	**8.8(11)**	2.6(-10)
CH_4	**4.6(8)**	**1.4(-13)**	**3.5(8)**	**1.1(-12)**	**3.6(8)**	1.1(-12)	3.6(8)	1.1(-12)
OH	**8.4(11)**	**2.5(-10)**	**2.7(12)**	**8.1(-10)**	**3.1(12)**	**9.2(-10)**	3.1(12)	9.2(-10)
CH	**1.9(14)**	**5.7(-8)**	**1.1(14)**	**3.3(-8)**	1.1(14)	**3.2(-8)**	1.1(14)	3.2(-8)
HCO^+	**1.4(9)**	**4.1(-13)**	**7.4(9)**	**2.2(-12)**	**9.2(9)**	**2.7(-12)**	**9.3(9)**	**2.8(-12)**
H_2CO	**2.5(10)**	**7.4(-12)**	**4.3(10)**	**1.3(-11)**	**4.1(10)**	**1.2(-11)**	4.1(10)	1.2(-11)
CH_3OH	**3.1(5)**	**9.2(-17)**	**1.9(6)**	**5.7(-16)**	**2.0(6)**	**5.9(-16)**	2.0(6)	5.9(-16)
NH_3	**3.8(7)**	**1.1(-14)**	**9.6(8)**	**2.9(-13)**	**1.1(9)**	**3.2(-13)**	1.1(9)	3.2(-13)
N_2H^+	**9.8(5)**	**2.9(-16)**	**1.8(8)**	**5.4(-14)**	**2.2(8)**	**6.5(-14)**	2.2(8)	6.5(-14)
CN	**2.1(12)**	**6.3(-10)**	**4.1(11)**	**1.2(-10)**	**3.7(11)**	**1.1(-10)**	3.7(11)	1.1(-10)
NO	**2.3(10)**	**6.9(-12)**	**1.4(11)**	**4.1(-11)**	**1.6(11)**	**4.7(-11)**	1.6(11)	4.7(-11)
CS	**9.3(12)**	**2.7(-9)**	**2.0(12)**	**6.0(-10)**	**1.8(12)**	**5.5(-10)**	1.8(12)	5.5(-10)
SO	**1.7(10)**	**5.0(-12)**	**2.0(10)**	**5.9(-12)**	2.0(10)	5.9(-12)	2.0(10)	5.9(-12)
SO_2	**7.2(5)**	**2.1(-16)**	**9.3(5)**	**2.8(-16)**	**9.5(5)**	2.8(-16)	9.5(5)	5.9(-12)

† $a(b) = a \times 10^b$

‡ $X_N[i] = N[i]/(2N[H_2] + N[H])$

happen to be at this stage of their evolution (*i.e.* at the hydrocarbon shoulder) are of a type consistent with a later cycle, we may infer that cycling is sufficiently frequent that core chemistry does not have the time to degenerate substantially before the onset of further cycles. If observed cores display abundances in line with first cycle core chemistry, we may infer that cycles are "infrequent" and that core chemistry has time to return to equilibrium values between cycles. Such a determination would also allow inferences to be made about the chemical state of the diffuse background gas (when not dynamically involved in core evolution). The state of this gas would not be uniformly determinable by direct observation due to the low densities (and column densities) involved. We should not expect to be able to detect cores at the beginning or end of their cycles, so the shoulder chemistry may provide a useful tool, if it is detectable.

Peak time molecular column densities show very little variation between cycles, and by the second cycle the limit is very nearly reached already. Because the variations are so small between the first and second cycles, it should not be possible to distinguish them from observations of cores at such a stage of evolution.

Looking at end time values, it may be seen that after the first cycle there is little further hysteresis in the chemistry of the gas by the time it returns to diffuse conditions. Hence the immediate chemical effects on the diffuse background gas of multiple cycles

Table 4.2: Selected column densities through the core and fractional abundances computed from column densities, for three cycles at hydrocarbon "shoulder" †

	Standard		Cycle 2		Cycle 3	
Species i	$N[i]$ (cm^{-2})	$X_N[i]$ ‡	$N[i]$	$X_N[i]$	$N[i]$	$X_N[i]$
H_2	**5.6(21)**	**5.0(-1)**	5.6(21)	5.0(-1)	5.6(21)	5.0(-1)
CO	**7.9(17)**	**7.0(-5)**	**8.3(17)**	**7.4(-5)**	8.3(17)	7.4(-5)
O_2	**6.1(14)**	**5.4(-8)**	**1.2(15)**	**1.1(-7)**	1.2(15)	1.1(-7)
H_2O	**2.1(15)**	**1.9(-7)**	**1.8(15)**	**1.6(-7)**	1.8(15)	1.6(-7)
CH_4	**7.3(14)**	**6.5(-8)**	**1.3(14)**	**1.2(-8)**	**1.2(14)**	**1.1(-8)**
OH	**1.4(14)**	**1.2(-8)**	**1.2(14)**	**1.1(-8)**	1.2(14)	1.1(-8)
CH	**1.3(14)**	**1.2(-8)**	**1.2(14)**	**1.1(-8)**	1.2(14)	1.1(-8)
HCO^+	**6.0(12)**	**5.3(-10)**	**3.7(12)**	**3.3(-10)**	**3.6(12)**	3.3(-10)
H_2CO	**1.4(14)**	**1.2(-8)**	**5.1(13)**	**4.5(-9)**	**5.0(13)**	**4.4(-9)**
CH_3OH	**4.1(12)**	**3.6(-10)**	**9.6(11)**	**8.5(-11)**	**9.1(11)**	**8.1(-11)**
NH_3	**7.2(12)**	**6.4(-10)**	**5.2(12)**	**4.6(-10)**	**5.1(12)**	**4.5(-10)**
N_2H^+	**1.6(11)**	**1.4(-11)**	**1.0(11)**	**9.0(-12)**	**9.8(10)**	**8.7(-12)**
CN	**3.2(13)**	**2.8(-9)**	**1.2(13)**	**1.1(-9)**	1.2(13)	1.1(-9)
NO	**2.3(14)**	**2.1(-8)**	**3.2(14)**	**2.8(-8)**	3.2(14)	2.8(-8)
CS	**4.5(14)**	**4.0(-8)**	**3.5(14)**	**3.1(-8)**	3.5(14)	3.1(-8)
SO	**9.3(12)**	**8.2(-10)**	**1.9(13)**	**1.7(-9)**	**2.0(13)**	**1.8(-9)**
SO_2	**1.9(11)**	**1.7(-11)**	**9.7(11)**	**8.6(-11)**	**1.1(12)**	**9.4(-11)**

† $a(b) = a \times 10^b$

‡ $X_N[i] = N[i]/(2N[H_2] + N[H])$

taking place would be little different from just single cycles taking place. The important difference would be in the time period between cycles.

So, in order to distinguish observationally between cores in one cycle or another, the ratios of CH_3OH, H_2CO and CH_4 to SO and SO_2 might be used, in conjuction with levels of CS and CO to determine which cores are in their "shoulder" phase. As mentioned above, detections of only cores with first cycle chemistry would indicate some period of time between cycles of the same material, such that something close to equilibrium were attained in between, implying such an equilibrium state for the background gas in general. In the following section, I examine the degeneration over time of post-cycle chemistry back to pre-cycle equilibrium values.

4.3 Processing of Diffuse Background Gas

I take the output values of fractional abundances from all depth points at the end time of the first cycle (*i.e.* standard run) as a starting point for a further simulation. Using these values, I maintain the physical state of the core at the end of the standard run (*i.e.* diffuse conditions) and run the chemical code until complete equilibrium has been achieved. Obviously no freeze-out onto dust grains takes place, since visual extinctions at

Table 4.3: Selected column densities through the core and fractional abundances computed from column densities, for three cycles at peak time †

	Standard		Cycle 2		Cycle 3	
Species i	$N[i]$ (cm^{-2})	$X_N[i]$ ‡	$N[i]$	$X_N[i]$	$N[i]$	$X_N[i]$
H_2	**6.2(21)**	**5.0(-1)**	6.2(21)	5.0(-1)	6.2(21)	5.0(-1)
CO	**7.2(17)**	**5.8(-5)**	**7.3(17)**	**5.9(-5)**	7.3(17)	5.9(-5)
O_2	**9.7(15)**	**7.7(-7)**	**9.0(15)**	**7.2(-7)**	9.0(15)	7.2(-7)
H_2O	**2.9(15)**	**2.3(-7)**	**2.8(15)**	**2.2(-7)**	2.8(15)	2.2(-7)
CH_4	**2.8(14)**	**2.2(-8)**	**2.6(14)**	**2.1(-8)**	2.6(14)	2.1(-8)
OH	**4.7(14)**	**3.8(-8)**	**4.6(14)**	**3.7(-8)**	4.6(14)	**3.6(-8)**
CH	**6.5(13)**	**5.2(-9)**	6.5(13)	5.2(-9)	6.5(13)	5.2(-9)
HCO^+	**1.5(13)**	**1.2(-9)**	1.5(13)	1.2(-9)	1.5(13)	1.2(-9)
H_2CO	**3.7(13)**	**2.9(-9)**	3.7(13)	3.0(-9)	3.7(13)	3.0(-9)
CH_3OH	**9.5(11)**	**7.6(-11)**	9.5(11)	7.6(-11)	9.5(11)	7.6(-11)
NH_3	**2.6(13)**	**2.1(-9)**	**2.4(13)**	**1.9(-9)**	2.4(13)	1.9(-9)
N_2H^+	**5.9(11)**	**4.7(-11)**	**5.5(11)**	**4.4(-11)**	5.5(11)	4.4(-11)
CN	**5.6(12)**	**4.5(-10)**	**5.7(12)**	4.5(-10)	5.7(12)	4.5(-10)
NO	**7.7(14)**	**6.2(-8)**	**7.9(14)**	**6.3(-8)**	7.9(14)	6.3(-8)
CS	**1.9(14)**	**1.5(-8)**	**1.8(14)**	**1.4(-8)**	1.8(14)	1.4(-8)
SO	**6.6(13)**	**5.2(-9)**	**8.3(13)**	**6.6(-9)**	8.3(13)	**6.8(-9)**
SO_2	**2.5(13)**	**2.0(-9)**	**3.2(13)**	**2.5(-9)**	**3.3(13)**	**2.6(-9)**

† $a(b) = a \times 10^b$

‡ $X_N[i] = N[i]/(2N[H_2] + N[H])$

all points are below $A_{V,crit}$.

4.3.1 Results

Figures 4.3 & 4.4 show column densities and resultant fractional abundances through the core up to 1 Myr after the core's physical evolution has come to a halt.

By a time of approximately 200,000 years into this run, those species which are enhanced after the standard run are still more than an order of magnitude greater than their pre-cycle equilibrium values. After half a million years, values are close to equilibrium.

It should again be stressed however that the longevity of molecular material this long after the cycle's end is a result of the multi-point approach of the model, and the density and visual extinction structure which we adopted. Figures 4.5a – e show point by point fractional abundances at six times in this post-standard cycle run. We may see more easily from these plots that the calculated column densities are strongly dependent on the penetration of the interstellar radiation field into the post-cycle core. As time goes on, the chemistries at individual depth points are affected at different rates according to the static visual extinction profile. Whilst the inner depth points have higher visual extinctions which protect molecular species from photodestruction, the higher densities at these points expedite ion-molecule reactions which are fed by photoionisation. Hence the

Figure 4.3: Column densities as functions of time, calculated through the core, up to 1 Myr after standard run

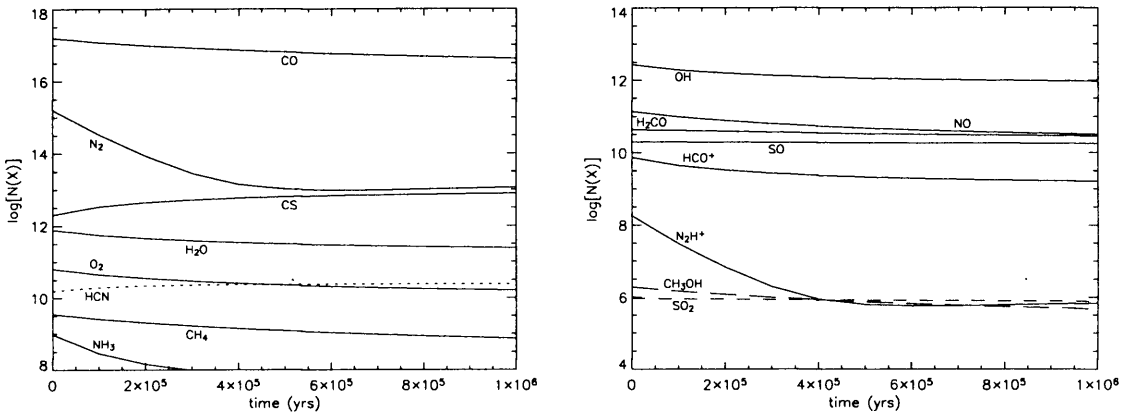

a: Species set 1 b: Species set 2

combination of these two static profiles governs the gradient of molecular degeneration across the core.

A minor feature of the run is the kink in N_2 abundance - this arises from the later breakdown of CO, compared to N_2, due to its self-shielding. Until CO has been sufficiently broken down to allow for large abundances of C^+, a major route for N_2 formation is suppressed. When CO is broken down enough and C^+ levels rise, this allows larger abundances of CH and C_2 to be formed, with which atomic nitrogen may react to form CN, and again to form N_2.

The level of enhancement at various times after core cycling implied by the column densities and fractional abundances produced in figures 4.3 & 4.4 should not just be taken at face value but also understood in the context of the chemistry at individual depth points across the core. The level of chemical enhancement at any one point will follow its own evolution, and we can see that it is only the inner points of the cores which retain significant amounts of molecular material formed at high density/A_V times. However, the outer points will generally have lost most of their molecular material before the end of a cycle is reached, so levels at these points should not affect the behaviour of any subsequent core cycles, whatever the intervening period.

The most important effect of the core cycle on the diffuse background gas may be its expansion phase, which carries material out to large distances such that (by way of processes which are not treated in this model) mixing of material within dark clouds, or formation of cores whose positions do not coincide with a previous one may further

Figure 4.4: Fractional abundances with respect to total hydrogen as functions of time, calculated from column densities through the core, up to 1 Myr after standard run

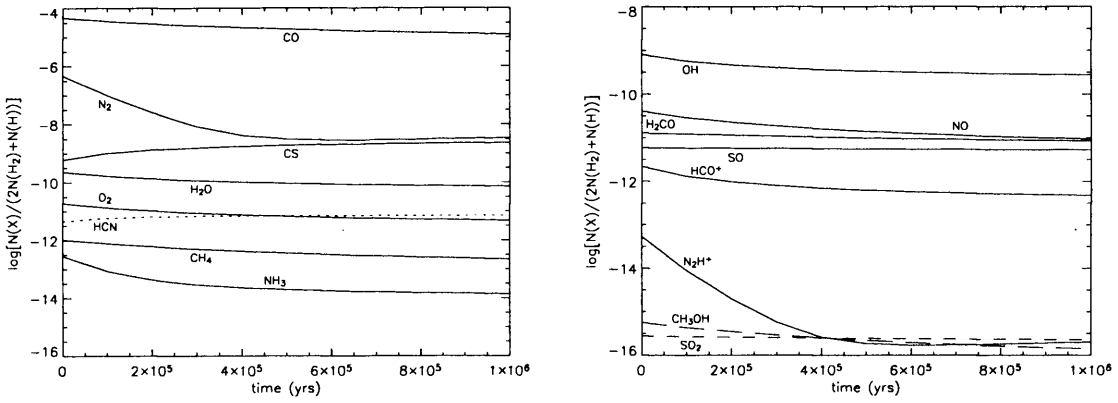

a: Species set 1 b: Species set 2

move, cycle and/or chemically process the already enhanced molecular gas. Since the Falle & Hartquist MHD mechanism, upon which this core formation model is based, is so far only treated in one dimension, and since the observational library of data at high enough resolution to pick out small dense cores is so far very sparse, it is difficult to speculate on how far-reaching may be the effects of chemical enhancement within dark clouds by this mechanism. We may still confidently say, however, that the extent and lifetime of molecular material after core dissipation is significant. Figure 4.5a shows the extent of molecular material at end time of the standard run. Figure 4.5b shows its extent after another 200,000 years. At this point, although the extent of CO has fallen by approximately half, from 0.3 pc to 0.15, this extent represents an unattenuated fractional abundance of about 10^{-4}. Material with $X(\mathrm{CO}) \geq 10^{-5}$ still extends out to $\sim$0.25 pc at this time, and to $\sim$0.20 pc at 0.5 Myrs, compared to $\sim$0.35 pc at the end of the standard run. This effect is more pronounced for CO, due to its self-shielding at visual extinctions greater than about 1, however the same effect is seen in all of the enhanced species; long-lived abundances significantly higher than the usual diffuse levels, far extended into the surrounding dark cloud.

The fact that the degeneration of column densities results from the reduction of the extent of molecular material, by the action of the interstellar radiation field, means that observed column densities obtained along lines of sight which do not coincide with the principal axis of collapse may not degenerate as quickly as those shown here (which should

Figure 4.5: Fractional abundances across the core – up to 10 Myr after standard run

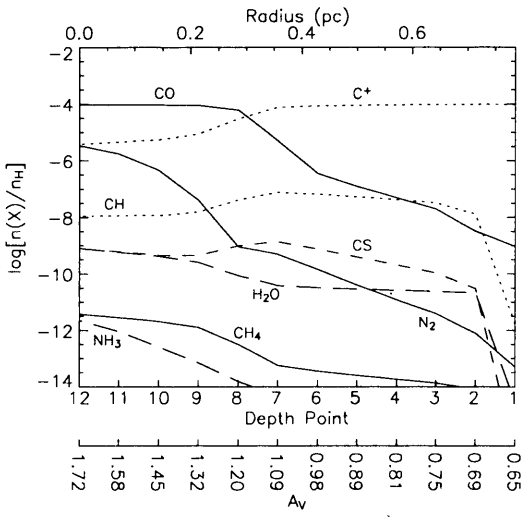

a: $t = 0$ Myr

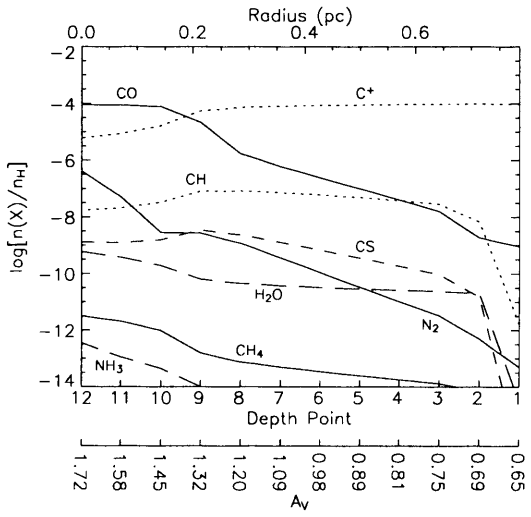

b: $t = 0.2$ Myr

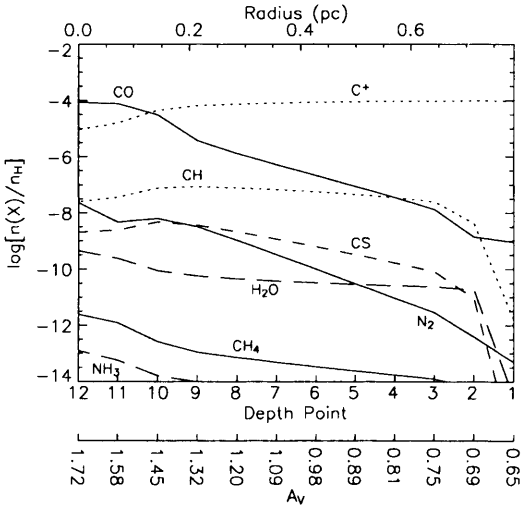

c: $t = 0.5$ Myr

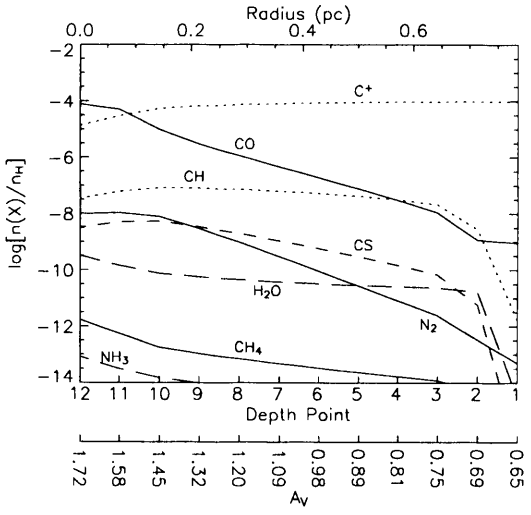

d: $t = 1$ Myr

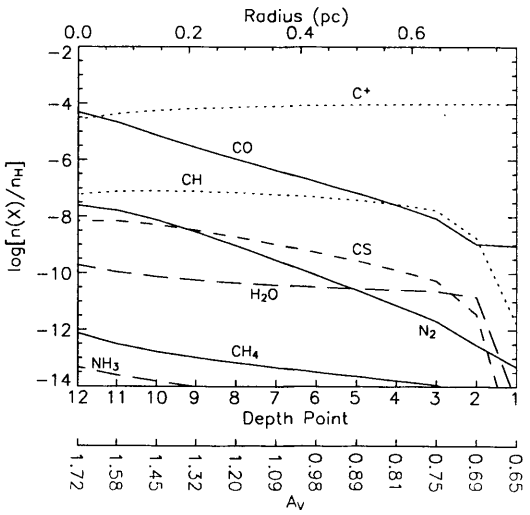

e: $t = 10$ Myr

in a sense be the most drastically affected since they take in the full spectrum of densities and visual extinctions and the resultant chemical differentiation), although we might not expect that levels would be as high.

4.4 Discussion

These results suggest that there are *not* great differences, either in the local chemistries or in the observed column densities, between cores in different cycles. However, we should expect that two extremes in the abundances of observable species would arise for cores in the stage of evolution at which the hydrocarbon "shoulder" becomes prominent. In the first cycle, the ratio of hydrocarbon levels to sulphur-bearing species' levels should be higher, whereas in all subsequent cycles it should be much lower. A search for molecules such as H_2CO or CH_4, which are singularly abundant at this point in core evolution, might indicate those cores which were in one or other state. Ratios of column densities of these molecules with those of SO or SO_2 might then provide a strong enough contrast between the two cases to permit their distinction. Using table 4.2 we obtain ratios between cycles 1 and 2, at the "shoulder", of: $(H_2CO/SO)_1 : (H_2CO/SO)_2 = 5.6$, $(H_2CO/SO_2)_1 : (H_2CO/SO_2)_2 = 14.2$, and $(CH_4/SO)_1 : (CH_4/SO)_2 = 11.5$, $(CH_4/SO_2)_1 : (CH_4/SO_2)_2 = 28.7$.

The attainment of either first cycle or later cycle chemistry would be dependent on the period of time between the end of one cycle and the onset of another. We might attribute a grace period of $\sim$0.5 Myrs before re-cycling had to take place for the subsequent chemistry to show appreciable signs of previous enhancement. This is the point (after end time) at which the innermost depth points begin to return to their equilibrium values – these points contribute the most to column densities at the hydrocarbon "shoulder", and so when their carbon monoxide is broken down they may produce more hydrocarbons from the free carbon, in their subsequent cycle of evolution. Observationally, detected levels which were solely representative of first cycle chemistry would indicate that cycling was not achieved within this 0.5 Myr period. Conversely, a later cycle chemistry would indicate only that such cycling took place within that time-frame; the chemistry is not sensitive enough in later cycles to distinguish between them.

The level of post-cycle enhancement of the diffuse background gas is not strongly dependent on the number of cycles the material has been through, even though this is not the case for the "shoulder" phase chemistry. Therefore the level of chemical enhancement

of background material as a result of cycling would be dependent only on the period of time between the cycles. (Obviously, the precise time scale is dependent on the model parameters which were chosen for the standard model). Therefore, detection of later cycle chemistries would inherently imply that the intercore background gas should be strongly chemically enhanced. This model implies such levels to be on the order of: $X(\mathrm{CO}) \simeq 10^{-5} - 10^{-4}$; $X(\mathrm{CS}) \simeq 10^{-10}$; $X(\mathrm{CH_4}) \simeq 10^{-12}$; $X(\mathrm{H_2CO}) \simeq 10^{-11}$; $X(\mathrm{H_2O}) \simeq 10^{-10}$; $X(\mathrm{O_2}) \simeq 10^{-11}$. Other important species are not enhanced, or are at negligible levels.

In fact, the observations of Morata *et al.* (2003) could indicate just such a case of background chemical enhancement. The separations between cores in that paper are generally less than 1 arcmin for the CS cores. Those seen in $\mathrm{HCO^+}$ and $\mathrm{N_2H^+}$, which do not generally coincide with each other or those in CS, show similar separations. Using the quoted distance to L673 of 300 pc, this corresponds to separations of less than 0.09 pc, *if the cores are all in the same plane.* This is not suggested to be the case, but leaves open the possibility that the cores are separated by less than ~0.2 pc, meaning there could be some level of mixing of enhanced molecular material between subsequent generations of cores (albeit in a way not examined in this model, *i.e.* material from core centres being cycled into later cores' edge regions). Line centre measurements of cores in Morata *et al.* (2003) were on the limit of the resolution of the instruments used, but were "compatible with being originated in the same bulk of gas". However, it is not clear from the transitions mapped in that study as to whether this is the case.

4.5 Conclusions

Firstly, the main conclusions of the previous cycling work are preserved; as noted in the last two chapters, the chemistry of cores is characteristically young (and stays that way in subsequent cycles), and the re-injection of grain mantle-bound molecular material strongly affects abundances. As with those studies, a limit cycle is reached after a small number of cycles, although perhaps even fewer in this case - 2 - 3. This means that limit cycles could easily be achieved within the dynamical lifetime of a dark cloud.

The chemistries of secondary, tertiary and subsequent cycles are not significantly different to be observationally distinguishable, but the differences between primary and later cycles should be. This is only true, however, for the hydrocarbon "shoulder" column density feature, so it would require statistically large samples of cores to be able to distinguish

between these alternative chemistries. This could be achieved by comparison of H_2CO or CH_4 to SO or SO_2 ratios, with the higher values signifying a first cycle chemistry.

We should expect that first cycle chemistries would obtain in regions where core cycling was infrequent enough that a period of $\geq$0.5 Myr would pass before the same material were re-cycled. In regions where later cycles are detected we should expect the diffuse background gas to be significantly enhanced. In regions where first cycle chemistry is detected we should expect that the background gas is not *generally* enhanced, but in localised areas (where cores have dispersed recently) it may be so.

I test the above hypotheses in later chapters using synthetically constructed molecular line maps.

CHAPTER 5

Core Ensembles — A Statistical Approach to Producing Synthetic Molecular Line Maps

5.1 Introduction

The work of previous chapters on the chemistry of small, transient, dense cores in dark clouds is partially based on the observational evidence of Morata *et al.* (2003), who looked at the region L673. The approximate sizes of the cores in that work were used to guide parameter choices in the chemical models of previous chapters of this study. Here I attempt to use the results of the standard transient dense core model for whole ensembles of cores, to produce synthetic molecular line maps of dark clouds which may be qualitatively (and to a degree, quantitatively) compared with those of Morata *et al.* (2003). I use a simple statistical approach to place cores at random positions in space, each at a randomly selected stage of its evolution. I then convolve the computed column densities of the cores into a map. I take approximate values of the size of a region and the number of cores within it from Morata *et al.* (2003) to produce maps at small and large angular resolution, to be compared with that work and the study of Morata *et al.* (1997), who examined the same region at lower angular resolutions. I *do not* attempt to explicitly model or reproduce the molecular line maps of those works, only their characteristic molecular morphologies.

5.2 Producing Synthetic Molecular Line Maps

5.2.1 Methodology

In this work I expand the idea that dark clouds are composed of small, transient, dense cores, surrounded by a diffuse medium, by constructing a map of such a region. I attempt to model a region with physical conditions the same as those of L673, a region studied in the molecular line maps of Morata *et al.* (2003), so that the characteristic molecular morphologies of that region may be compared with those of the synthetic maps which I produce. I assume that the synthetic dark cloud region is made up entirely of cores with the chemical and physical parameters of the standard run of chapter 3.

To produce the synthetic molecular line maps, I first require a region to map, made up of cores positioned in space. To construct this region I adopt the following approach:

- Designate a map size, and the number of cores within it
- Assign each core a randomly determined position within the map
- Assign each core a randomly determined stage of evolution

This results in a purely random ensemble of cores, with no inherent bias towards any particular structure other than that the region is composed of discrete cores of gas, and that a uniform core number density has been adopted for the whole region. We might expect that different regions in space should assume somewhat different local core number densities, however in this work I do not attempt to study such larger-scale structure. There will, however, be an effect on the resultant local morphologies displayed within the maps from groupings resulting from the random distribution of the cores – I do not, after all, simply place all cores at equal separations from one another so as to achieve a uniform core number density at every point in the map. But such deviations from strict uniformity may in any case be necessary to produce realistic morphologies, and the imposition of a strictly uniform core number density structure would be just as restrictive as of any other artificial regime.

The cores are positioned only in two dimensions, since the observational evidence in Morata *et al.* (2003) gives no indication of the depth into the line of sight of the region of gas in which the cores are situated, and in fact the position of a core in this third dimension has no impact on the way the maps of this study are constructed, or the way the molecular levels are calculated.

To designate each core with a position, first the x-coordinate is assigned a random value (from a uniform distribution) of between 0 and 2 pc. This step is then repeated for the y-coordinate. To designate each core with a particular stage of evolution, it is assigned a random (integer) index of value between 0 and 401, each of which corresponds to one of the equally spaced points in time for which outputs are produced from the chemical model.

The random determination of the stage of evolution of each core is necessary since there is no indication of any particular bias generally in the L673 region. Nor is there an indication that small groups of localised cores should necessarily influence one another's evolution such that the stage of evolution of cores within that group should obey any particular relationship (indeed, those cores which are localised in the plane of the map may not in fact be close neighbours in three dimensions). The cores' true proximity to each other does not affect the chemistry of the cores, as this has already been computed; therefore the cores are chemically and physically non-interacting.

With the basic map constructed, I then convolve the integrated column densities of each core into a set of molecular line maps for various tracers, one at a time, thus:

- Divide map into a grid of "detection points"
- Designate a beam resolution/beam width
- For each detection point, calculate contribution of "detected column density" from each core which lies within the detection radius
- Plot contour map of data at detection points

I here assume each core to behave as the standard run core of chapter 3, hence each core has the same chemical and physical/dynamical parameters. To each core I therefore the assign column densities calculated for all the molecules modelled in the standard run, which vary depending on the designated stage of evolution of each core.

In order ultimately to produce a contour map, I require a grid of reference points on the main map to which to assign "detected" levels for any particular molecule. I choose a resolution for this grid that is smaller than the beam resolution, so that the entire map is well covered by the simulated beam.

To convolve the cores' emissions, I choose a beam resolution to simulate the resolution effects of using a real telescope. I assume a Gaussian diffraction profile for the beam, and

treat each core as a *point source*; therefore I define the beam resolution as the minimum angle of separation for which two point sources (of equal intensity) may be individually resolved, and so the beam resolution is twice the angle for which the Gaussian diffraction profile falls to half its peak value. I therefore identify this definition of beam resolution with FWHM beam width. The point source approximation I deem to be valid on the basis that the column densities employed in the convolution method are calculated for the centre of a core, and that the outer regions will contribute less than this point. The degree to which the "wings" contribute levels of emission significant enough to render this approximation invalid should become clear in this comparison of the synthetically produced maps with the observational evidence.

For each detection point, all the surrounding cores add a contribution to the "detected emission level" – a contribution which is equal to the value of the diffraction profile (normalised to unity) for the distance between core and detection point, multiplied by the calculated column density of the molecule in question, as determined by the stage of evolution of the core. Cores which are more than a few beam resolution radii away from the detection point will not contribute significantly to the total level of detection, and so are not included in the sum. In this way, simulated detection levels are attributed to each detection point in the map. From these levels contour maps are plotted for a number of molecular tracers.

Clearly, in this analysis I make no attempt to model radiative transfer, and this treatment ignores both optical depth and excitation effects. The map contours represent the column densities underlying the "detected" emission, rather than the emission itself. Implicit in the mapping procedure is the non-interaction between cores, either physically or chemically, since the chemical data are computed individually for a generic core. Also implicit in this method is that all cores contract and expand along the line of sight, since all column densities are calculated in this direction.

5.2.2 The Map Parameters

I use a map size of 2 pc × 2 pc. The CS maps of L673 shown in Morata *et al.* (1997) are approximately of this size.

I obtain a core number density for the map by counting the number of cores observed in the CS (J=2→1) line in Morata *et al.* (2003). This gives a figure of around 40. I count on the basis that cores are essentially circular in the plane of observation, in order to

distinguish apparently merged cores. The cores observed in the HCO^+ (J=1→0) and N_2H^+ (J=1→0) lines do not generally coincide with those of CS or with each other; however, this may partially be a result of chemical differentiation within the cores (as might be expected on the evidence of previous chapters), which could therefore imply falsely high numbers of cores if all cores in all three molecules were deemed independent. Also, with some cores taking sizes approximately equal to the resolution limit of the observations, some contributions from individual cores may be convolved together. Taking these points into account, and remembering that cores modelled using the standard run of chapter 3 may at their beginning and end times not produce column densities which are sufficient for their detection, I assume a value of ~60 cores. The maps of Morata *et al.* are of a size $\sim(0.5\text{ pc})^2$, and so I adopt a core number density value of 250 pc^{-2}. Therefore, for the map of size $(2\text{ pc})^2$, I use a total of 1000 cores.

I take this basic map and produce two sets of molecular line maps:

- Large-scale, low resolution maps
- Small-scale, high resolution maps zoomed-in on a region chosen for its CS and NH_3 peaks

This approach mimics that taken in the two Morata *et al.* papers.

I adopt a low-resolution beam width of just under 2 arcmin to agree approximately with Morata *et al.* (1997). This corresponds to a beam radius of 0.085 pc, calculated at a distance to L673 of 300 pc.

From the large-scale maps I ignore "emission" from the outer 0.1 pc bounding them. This is because levels at the edges are influenced by the lack of any cores outside of the map, producing an unnatural drop in "detection". To avoid this artifact, I remove a strip around the edge of the maps of size approximately equal to the beam radius. The cores in this bounding strip are still contributing to "emission" within the rest of the map – only the final convolved emission within the strip is ignored.

When plotting contour maps, I set contour levels according only to those levels "detected" within the region that I plot, rather than the levels calculated for the entire map. This means that peaks (or troughs) that might exist *outside* the area displayed in the map do not influence the displayed levels (and hence morphologies), ensuring that maps are consistent with real molecular line surveys (since contour maps of real regions are not normalised to molecular peaks outside of the detected region). In that sense we might

identify the basic unconvolved maps (which consist only of core positions and stages of evolution) as the "sky", with the convolved contour maps comparable to observations of it.

The region examined in Morata *et al.* (2003), of size $\sim$ 0.5 pc $\times$ 0.5 pc, was chosen from within the detection map of Morata *et al.* (1997) to coincide with peaks in CS emission, and in NH_3 detected by Sepúlveda Cerrada (2001).

For my high resolution maps, I zoom in on a region of the low resolution maps of size $\sim$ 0.6 pc $\times$ 0.6 pc (– slightly larger, to accomodate better both the CS and NH_3 peaks), chosen according to local CS and NH_3 peaks, to allow for meaningful comparison. However, the beamwidths employed in Morata *et al.* (2003) are $\sim$20 arcsec, corresponding to a beam radius $\sim$0.015 pc. Since the physical size of the cores detected in that paper were generally larger than this (*i.e.* $\leq$ 0.08 pc), my treatment of the cores as point-sources would produce mapped cores all with sizes of $\leq$0.03 pc, if a 20" resolution were adopted. This would not produce morphologies comparable to the Morata paper. Hence, to allow for such qualitative comparison, I adopt a high-resolution beam width of $\sim$ 40", corresponding to a beam radius of 0.03 pc, and mapped core sizes of $\leq$0.06 pc.

Because in this analysis the cores are treated as point sources and are therefore not given an intrinsic width, we should not expect the *absolute* "detected" levels of column density to accurately represent observed *absolute* levels. This is because the convolved column density values at each detection point would need to be normalised in order to average the emission over the area of the simulated beam. This is not possible because the cores have no intrinsic emitting area (only a point position), and so they occupy a zero fraction of the area of the beam. Hence I do not attempt to compare the calculated absolute values at molecular line peaks with those levels detected in the Morata papers. I treat this issue in the following chapter. However, this in no way affects the reliability of the contour maps, since the normalisation is not required to obtain relative levels across the map in any particular molecular line. Whilst ratios of absolute levels of *different* molecules at specific points in the synthetic maps are also not reliable, the relative physical extents of molecules are, since their contour maps are consistent when adopting the same beam width. The low resolution and high resolution maps are each self-consistent in the adoption of a single beam width for all molecules, therefore they are consistent with each other. We require the same beam resolution for all molecules, for either set of high or low resolution maps, so that detected core sizes are consistent; this is because core size and beam resolution are

directly linked when the point source approximation is made. It is not so important for the low resolution maps, since the beam width is much larger than the maximum size of the standard run core, and therefore resolved structure is much more dependent on core distribution in the map than on the core size.

5.3 Results

5.3.1 Low resolution, large-scale maps

Figure 5.1 shows the basic map of core positions, the synthetic "sky". By way of the symbol used for each core, I denote the approximate stage of evolution: Plusses (+) indicate cores that have not yet reached peak time, and are therefore not yet at maximal density; crosses (×) indicate cores which have evolved past the peak time. The relative sizes of the symbols also indicate approximately how far into the cycle the cores are: larger symbols indicate larger densities (or proximity to peak time). Hence a large cross indicates a core that is only just past peak time; a small plus indicates a core that is some time away from reaching peak density.

Figure 5.2 shows a low resolution map of the L673 data presented in Morata *et al.* (1997), taken from figure 6 of Morata *et al.* (2003).

Figures 5.3a – f show low resolution (~2' FWHM) *column density* convolved molecular line maps for five density tracers, plus molecular hydrogen, which I include only as a measure of the underlying density structure. I overlay the basic map of core positions for ease of comparison. The contours represent fractions of the peak value calculated for the map, for any particular molecule. The fractions of peak "emission" represented by the contours are chosen to correspond with those of the low resolution observations shown in Morata *et al.* (2003) (see figure 5.2). The outermost (thick) contour line represents the half-maximum (0.5), with the levels rising by ~0.05. The overlaid boxes represent the portion of the map which is zoomed-in on in the high resolution maps.

It should be remembered that the map has no bias towards a large-scale structuring of cores, so large-scale structure in real dark clouds should not be accurately replicated. However, we might reasonably treat local dense regions within the maps as being self-consistent.

The basic "sky" map is clearly not uniform in the positioning or stages of evolution of cores, and we can see that the grouping of cores in this basic map produces certain

Figure 5.1: Core positions in the basic "sky" map

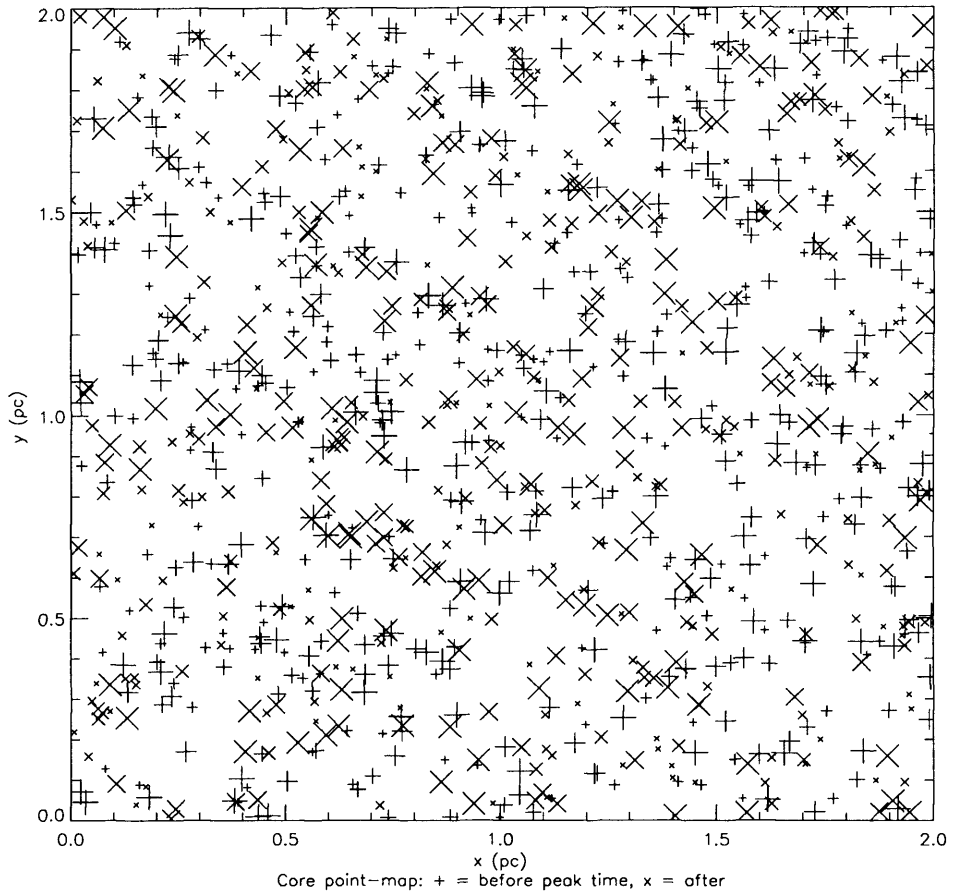

structures in the molecular line maps. Using the H_2 map as a "true" indicator of density structure we can see that not all of the cores in the "sky" map sit within even the half maximum contour. This shows how close groupings of cores produce the strongest peaks, and that individual cores are *not* responsible for density peaks.

As is generally observed in dark clouds (see *e.g.* Myers *et al.* 1991) the morphologies of different molecular tracers in figures 5.3a – e are not the same, do not trace the same regions, and have different spatial extents. Indeed we see here that, broadly, the characteristic features exhibited in molecular line maps of CO, CS and NH_3 in Myers *et al.* (1991) are re-produced here, without recourse to critical density arguments, or appeals to differences in the sticking coefficients or grain surface chemistries of carbon-, sulphur- and nitrogen-bearing species (*e.g.* Tafalla *et al.* 2002). CO and CS here are not significantly different in spatial extent (although in fact, here the CS extent is larger), judging by the half-maximum contour, and local peaks in either do not generally coincide or necessarily correspond. Meanwhile, the "detection" of NH_3 is comparatively compact, and there are

Figure 5.2: Low resolution contour map of L673 showing CS (J=1→0) (solid line) and NH_3 (1,1), from figure 6, Morata *et al.* (2003)

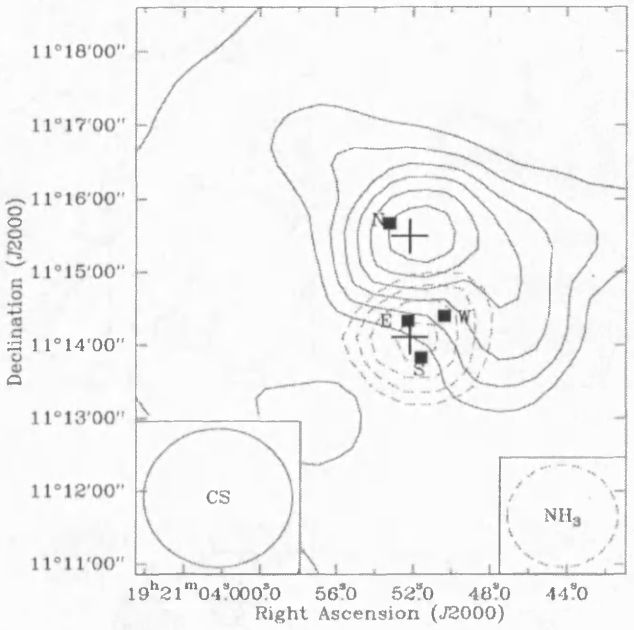

only three peaks in this map, hence not every peak in CS or CO has a corresponding peak in NH_3. Those few CO or CS peaks which do have an NH_3 peak in their vicinity do not coincide with it, although the NH_3 peaks *are* mostly contained within the half-maximum contours of those two molecules. The extent of NH_3 especially, in comparison to CO and CS, agrees well with the evidence of Myers *et al.* (1991).

HCO^+ and N_2H^+ both seem to track the same regions of gas, taking very similar morphologies and extents; this is due to the similar column density profiles that they display in figure 3.3 (in chapter 3) of the standard model run. These molecules display smaller extents than CO or CS, however they tend to trace the same regions as CO. Both their column densities in the standard core rise to their highest around peak time. All of their contour map peaks correspond to peaks in H_2 and CO. This means that they tend to trace higher densities, as is often assumed for N_2H^+ in observational studies.

5.3.2 High resolution, small-scale maps

For the zoomed-in high resolution synthetic molecular line maps, I choose a region from the bottom-left section of the map of approximately the same size as the region of L673 examined in Morata *et al.* (2003). I choose it for the same reasons as did Morata *et al.*,

Figure 5.3: Trimmed map – low resolution

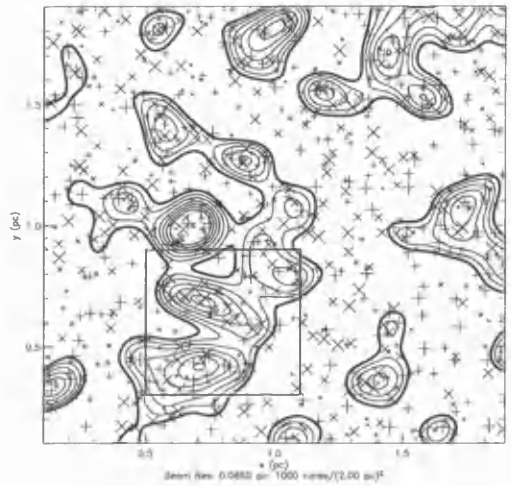

a: CO

b: CS

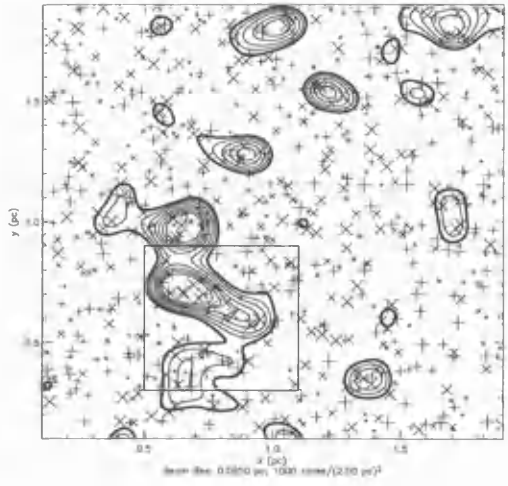

c: HCO^+

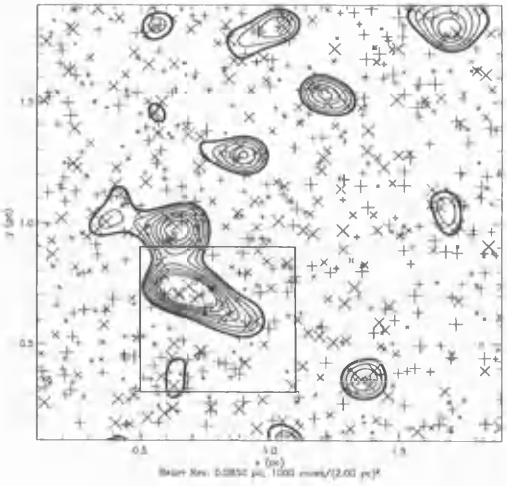

d: N_2H^+

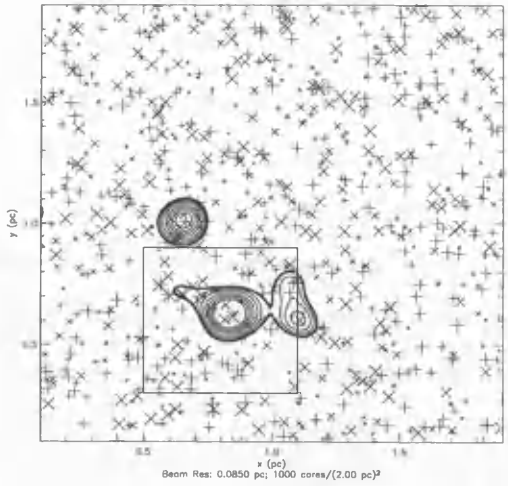

e: NH_3

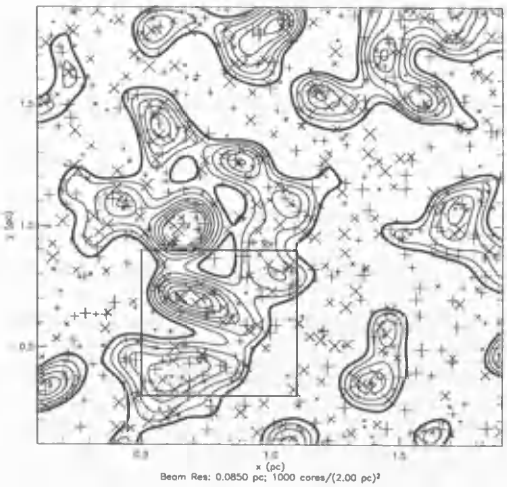

f: H_2

Figure 5.4: High resolution contour map of L673 showing CS (J=2→1), from figure 1, Morata *et al.* (2003)

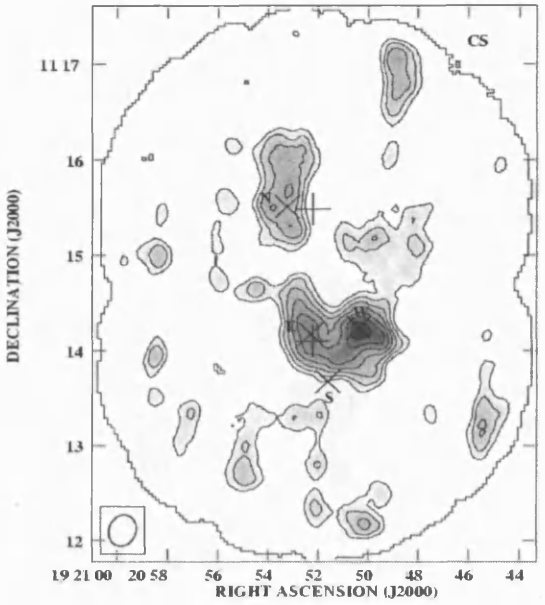

i.e. CS and NH_3 peaks in that area.

Figures 5.4, 5.5 and 5.6 show maps of the high resolution L673 CS (J=2→1), N_2H^+ (J=1→0) and HCO^+ (J=1→0) data respectively, taken from figures 1 – 3 of Morata *et al.* (2003).

Figures 5.7a – d show maps for the same three molecules as were observed in that paper, plus CO. I also include NH_3 and H_2 for comparison with the previous section. Contour levels are set to correspond to those used in Morata *et al.* (2003): the lowest is 0.36 of maximum, the others increasing by 0.07. The distance scales are preserved from figures 5.3.

This time, although the two do not correspond exactly, there is much greater correlation between CO and CS peaks and extents.

We see here that there are still cores which are not within any areas of emission, although in CO it is really only the low density cores which do not register. The "emission" is still not purely centred around individual cores but around small groupings. Clumps of emission out on their own which reach only two or three contour levels (0.43 – 0.50 of maximum) tend to be the result of individual cores or loose associations of two or three.

The long region of CO in the centre of the high resolution map is not strongly represented in CS. It may be seen that where CS is present, it corresponds to pre-peak time

Figure 5.5: High resolution contour map of L673 showing N_2H^+ (J=1→0) from figure 2, Morata *et al.* (2003)

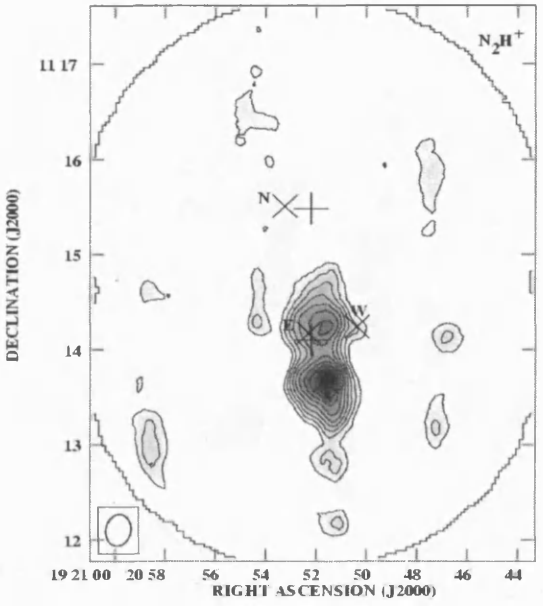

cores, or close combinations of these with high density post-peak time cores. Whereas CO tends to map everything that CS maps plus some more that it does not, HCO^+ and N_2H^+ seem to map mainly those regions in the CO map which CS does not. N_2H^+, in particular, maps regions which are post-peak time. HCO^+ maps mainly the cores which are just around the peak time. It is a subtle difference, however. Although the regions that HCO^+ and N_2H^+ map are broadly the same as are mapped in CO, closer inspection shows that not all of the peaks in CO are represented in these molecules. The NH_3 map again shows a small extent; it is apparent that only one core is responsible for this peak, rather than a grouping of them.

In comparison with Morata *et al.* (2003), CS morphologies are generally similar, although we do not see so many resolved cores in the synthetic map; the same is true for HCO^+. We do not see the *comparative* sparsity of weaker cores in N_2H^+ to those in other molecules in the synthetic maps as we might expect, although again, since the weaker cores are not so numerous in any of the maps this is not inconsistent with the former point. Indeed, ignoring the comparative morphologies of the other maps, N_2H^+ actually reproduces the morphology displayed in Morata *et al.* (2003) rather well. The relative numbers of strong and weak detections and their groupings seem consistent – the smaller cores are scattered, and distant from each other and from the stronger peaks; the larger

Figure 5.6: High resolution contour map of L673 showing HCO^+ (J=1→0), from figure 3, Morata *et al.* (2003)

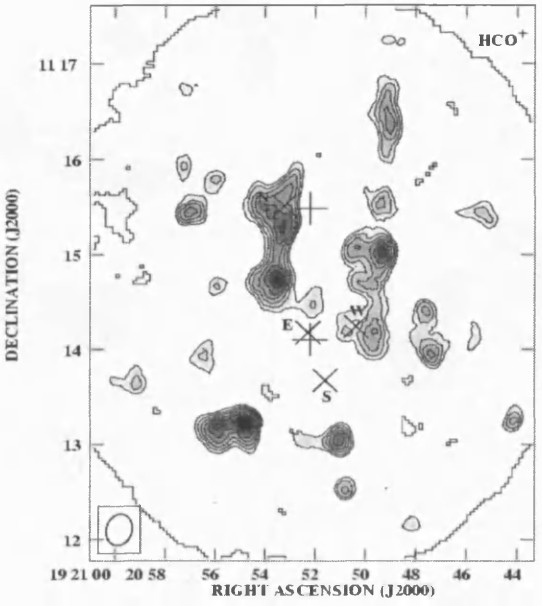

peaks are spatially associated with each other.

Some of the morphological information given in Morata *et al.* (2003) may be specific to the region L673, and may not necessarily be borne out in any particular simulation of such regions, however I bring it to the reader's attention. The two greatest peaks in CS emission in that study were contained well within the contours of the single-dish (*i.e.* low resolution) NH_3 peak. That is not the case in this study. Also, the Morata work showed no N_2H^+ detections close to the single-dish CS peak, whereas in this work there are some small detections. But, to re-state, the most striking point is that in Morata *et al.* (2003), N_2H^+ and HCO^+ appeared to map completely different material, and that is quite clearly not the case here.

However, aside from the similarity in HCO^+ and N_2H^+ maps, these molecules clearly map different material from the CS and, in that comparison, peaks generally do not coincide or correspond, which is in agreement with Morata *et al.* (2003). Both the larger- and smaller-sized cores are reproduced, whether or not in the same ratios, and N_2H^+ morphologies match particularly well with the detected emission. We may say that morphologically, the synthetic maps compare favorably with the observations, within the obvious limits presented.

Figure 5.7: Close-up map – high resolution

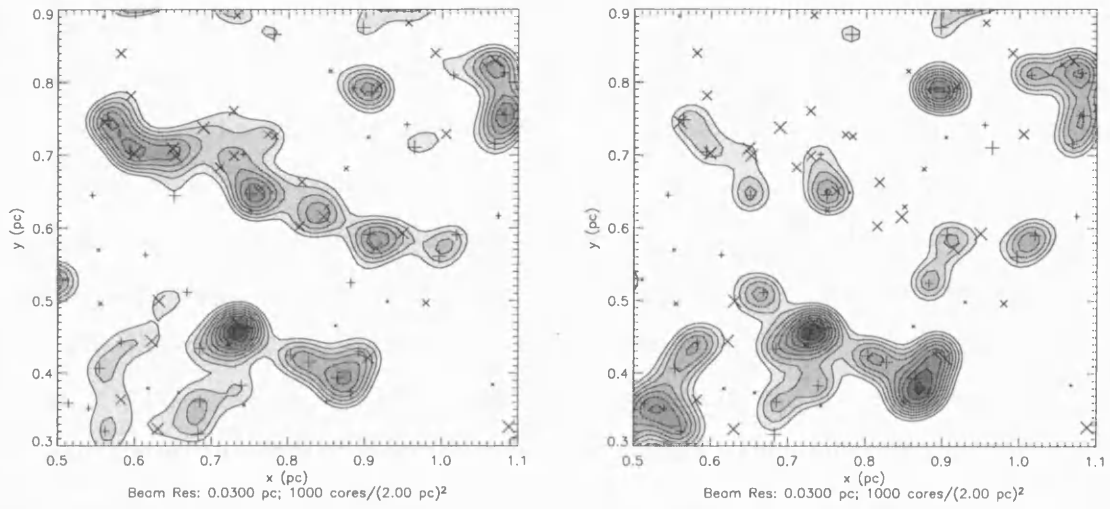

a: CO

b: CS

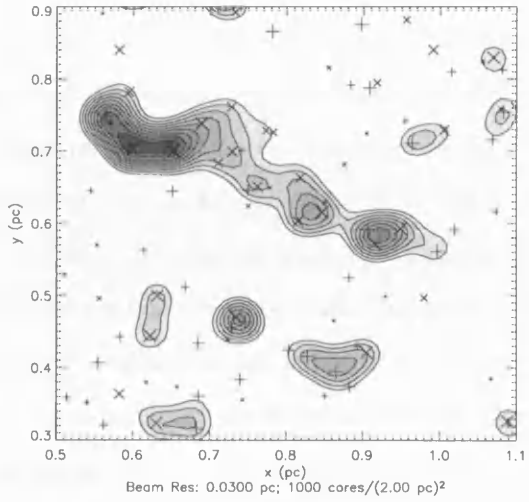

c: HCO^+

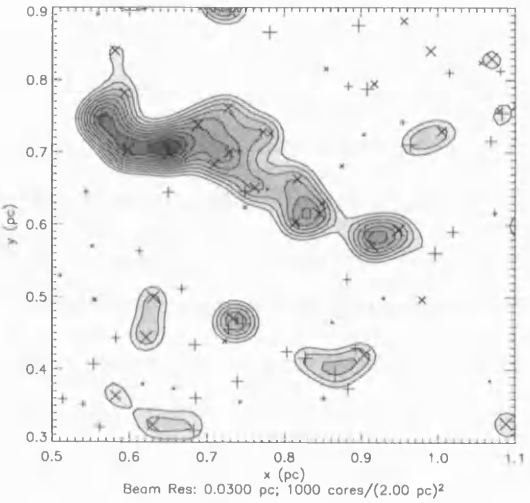

d: N_2H^+

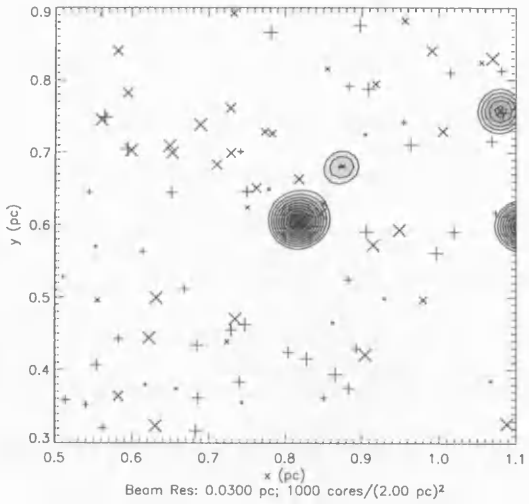

e: NH_3

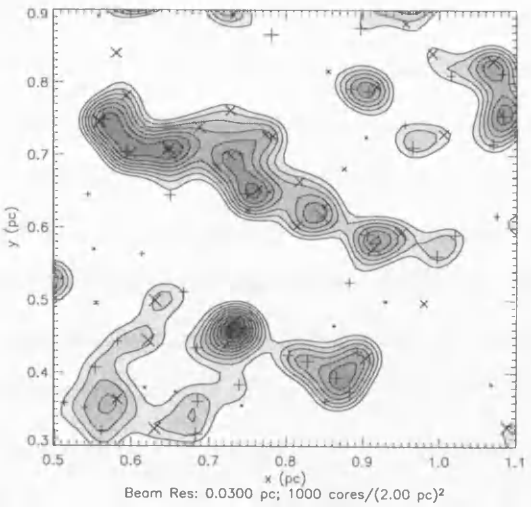

f: H_2

5.4 Discussion

The good agreement of comparative CS and NH_3 peak positions and extents in the low resolution maps of this chapter with the observational evidence of Morata *et al.* (1997) is encouraging. The main NH_3 peaks are contained within the half-maximum contours of CS, and sit at about the second or third contour lines of the CS peaks, which is also in agreement. Aside from this, the general morphologies of these molecules match those of dark cloud cores examined in Myers *et al.* (1991). Those authors calculated mean FWHM extents in 16 dark cloud cores to be 0.15 pc (NH_3), 0.27 pc (CS) and 0.36 pc ($C^{18}O$). The extents of CS and NH_3 in figures 5.7b & e are arguably larger than this, but appear to preserve the correct relative extents. This indicates that the sort of small transient dense cores of this model may also exist within at least some of the low resolution Myers cores, and that this is the reason for their consistently smaller extent in NH_3. The ratios of CS and NH_3 extents in such observed cores are of particular interest since they do not agree with the critical densities required for emission from either molecule (see *e.g.* Rawlings 1996) when applied to a model which assumes a single coherent core to be the cause of emission. A number of arguments have been put forward to explain this discrepancy; for example, Tafalla *et al.* (2002), the most recent, invokes a greater central CS depletion compared to NH_3, which they attribute to differences in the relative sticking probabilities of carbon- and sulphur-bearing species on the one hand and nitrogen-bearing species on the other (Bergin & Langer 1997). This analysis is based on the assumption that the observational data represent one single core (modelled as being spherically symmetric). Hence at least in the case where small cores, unresolved by single-dish telescopes, are present, this is not a viable explanation. Other explanations also depend on the assumption of the Myers cores being single entities. It should also be noted that the critical density analysis is a simplistic one, and that a number of factors can act to suppress the densities required to observe any particular molecular line (Evans 1999).

Taylor *et al.* (1996) first suggested that the CS/NH_3 discrepancy could be a result of the clumpy nature of molecular clouds. Their chemical models used the modified free-fall collapse mechanism of Rawlings *et al.* (1992), and did not include subsequent dispersal. They conjectured that most clumps would disperse before significant NH_3 levels could build up, whilst CS should peak before this time arrived. The adoption of the mechanism proposed by Falle & Hartquist (2002) in *this* work allows for the (controlled) dispersal of

a core. However it is for similar reasons as those suggested by Taylor *et al.* (1996) that the CS/NH_3 discrepancy is reproduced in figures 5.3b & e. Consider figure 3.3a of chapter 3, showing the calculated column densities through the standard run core which are used in the mappings of this chapter. Ignoring for a moment the re-injection peaks, it may be seen that as in Taylor *et al.* (1996) the NH_3 peaks later than CS; but crucially, its peak level is sharper with respect to time. I suggest that this factor determines the relative extents of molecules in dark clouds. The sharpness of the peaking produces a contrast in the statistical weight of mapped cores, between those which have comparatively high CS levels and those which have high NH_3 levels.

Unfortunately, the re-injection peaks in the column density profiles complicate matters. The high resolution NH_3 map again shows a very small extent, however here we may see more clearly what is contributing to it – it seems that it is one core which is responsible for the peak. That core is contributing strongly because it is at a stage where re-injection of icy grain mantles is at its peak. The very tight contours of NH_3 in the synthetic maps may therefore be an artifact of the discrete re-injection mechanism discussed in chapter 3. This does not preclude column density behaviour from being the cause of the CS/NH_3 discrepancy, but it does require for its vindication a chemical treatment which produces smooth column density profiles consistent with continuous re-injection. However, the CS is probably less peaked than the NH_3 whether strong (continuous) re-injection peaking is present or not. I look further into this problem in the following chapter. Looking at the column density profiles does however give a conclusive explanation for the displacement of the peaks of different molecules (as also suggested in Taylor *et al.* 1996); the CS and NH_3 profiles peak at different times through core evolution, resulting in different cores contributing the strongest emission in either molecule, which will inevitably lead to different morphologies and peak positions in studies which do not resolve the small cores modelled in this work.

The good morphological agreement of the high resolution maps, especially for N_2H^+, with those of Morata *et al.* (2003) indicates that the Falle & Hartquist (2002) mechanism produces data consistent with observations of small, transient, dense cores. Whilst the simulated low resolution maps should not be expected to correspond closely with the particular example of region L673, as regards relative positions of molecular peaks (although in fact they do correspond reasonably well), we might expect that the high resolution maps should share certain properties – that the emission from CS, HCO^+ and N_2H^+ should not

generally represent the same cores, that regions of stronger emission should overlap or correspond somewhat, and that we should observe broadly similar ratios of strongly and weakly emitting cores, or large and small cores. These expections are partially borne out in these simulations. The CS does map different cores from HCO^+/N_2H^+, but the latter two molecules do not differentiate from each other. The strongest regions of emission in CS do not coincide with those of HCO^+/N_2H^+. Since the CS and HCO^+/N_2H^+ map different stages of core evolution, we might infer that the region of L673 mapped in Morata *et al.* (2003) has a mixture of cores of different ages in the strongest regions of emission. We might derive from the fact that HCO^+ and N_2H^+ map different regions from each other in L673 in the Morata *et al.* (2003) work that either the column density profiles of HCO^+ and N_2H^+ shown in figure 3.3 should not in fact behave so similarly to each other, indicating an at least slightly different set of core parameters, or that the region is composed not only of a mixture of cores of different ages, but also of cores of different intrinsic physical properties whose chemistries therefore follow different time-dependencies. Finally, we do not generally see so many smaller, weaker cores as we do in L673, however in N_2H^+ the ratio appears correct.

There are a number a factors involved in the construction of the maps and the computation of convolved molecular emission levels which could be producing some of these discrepancies. Firstly, the physical sizes of the cores on the convolved maps and the angular resolution of the simulated observations are bound together. This has meant choosing a beam width for the high resolution maps which is roughly twice as large as it should be for comparison with Morata *et al.* (2003), in order to produce appropriate core widths. This is likely to be at least part of the cause of the non-detection of many smaller cores in CS and HCO^+, since to achieve the right overall size scales, the resolution may be too large to be able to pick out the smaller ones. In the high resolution maps, the size of the cores is smaller than the beam radius, and so the detections should be picking out features in individual cores, not just the convolution of the emission from a group of them, as in the low resolution case.

The critical densities for emission from particular molecules will also affect their relative extents, especially since column densities are computed by summing over a number of points in a core which assume different densities both from each other and over time. We might also expect that the simplistic modelling of the cores as point sources (and the avoidance of a radiative transfer analysis) would inhibit the morphological effects

of critical densities on the relative extents of the molecules, and not just in the line-of-sight contributions to column density calculations. The inclusion of critical density considerations such as this might resolve the inconsistency of CO extent being slightly smaller than CS extent in the low resolution simulated maps.

With the above two paragraphs taken into account in subsequent attempts to model core ensembles, an appropriate value of beam width might be chosen for the high resolution case.

The one-dimensional approach to the chemistry and the fact that column densities are evaluated along the line of sight may also affect the appearance of the synthetic molecular line maps, and may contribute to "non-detection" of smaller cores. However, these limitations are inherent to the whole approach of the work, and can therefore not be improved upon within the scope of this study. The chemical differentiation within the cores presented in chapters 2 – 4 is also not brought out in the physical morphologies of the synthetic maps. Additionally, the fact that only one model run (using one set of parameter choices) has been used in this study means that, for example, a mix of smaller or larger cores could alter the detected molecular levels and/or contribute larger or smaller cores to the maps. But we should recognise that with only this one model as a representative core, some of the broad morphologies presented in the Morata papers have been very well reproduced. This could indicate that the range of model parameters of cores needed to closely represent such a region as L673 may be fairly narrow.

Finally, the level of uniformity of core distribution in the basic "sky" map may be very important to the observed molecular levels (via the overlap or convolution of closely spaced cores), to the relative numbers of smaller and larger cores which are resolved (due to the contrast in emission levels), and to the morphologies. The level of uniformity needs to be quantified and, on that basis, investigated.

In the following chapter I incorporate some of those variables mentioned above into the mapping procedure, and investigate their effects.

5.5 Conclusions

A synthesised map of a dark cloud region has been constructed by placing a number of cores randomly in space and attributing each with a randomly determined stage of evolution. The column density data from the standard chemical model examined in chapter 3 have

been applied to each core in the map, and convolved together to simulate molecular line maps of real dark cloud regions. In particular, observational evidence of the region L673 from Morata *et al.* (1997) and Morata *et al.* (2003) has been used to guide the choice of map parameters, such as size, core number density and angular resolution, to compare the characteristic morphologies of molecular line maps at both low and high angular resolution. The cores are approximated as point sources for the purposes of the convolution.

Low resolution morphologies of NH_3 and CS in the synthetic maps are found to agree well with general observational evidence of the spatial extent of the two molecules, and the relative positions of peaks and contours in those molecules agree well with general morphologies in the specific case of L673. CO assumes a slightly smaller extent than is evidenced by the survey by Myers *et al.* (1991) of 16 dark cloud cores (at resolutions approximately the same as the low resolution case of this work). This may in fact be remedied by consideration of critical density arguments. This result shows that the concept of dark clouds generally being made up of small, transient, dense cores unresolved at low angular resolutions is quite plausible, and shows that the discrepancy in NH_3 and CS spatial extents may be explained in terms of the time-dependent (and multi-point) chemistry of such unresolved cores.

The high resolution maps show further that the general approach of this chapter produces morphologies and peak positions which are not unlike those observed in the example of L673. The comparison of general characteristics of the synthetic maps with the observations suggests that the cores of L673 are in various stages of evolution with no particular bias within local groupings. Also, some of the resolved cores may in fact consist of groups of cores which contribute cumulatively, without being directly resolved themselves. The small, weak cores of the observations may indeed be individual cores, or a loose association of two. This conclusion may however be dependent on the tying together of beam resolution and true core size in this simulation.

In spite of the success of the method, HCO^+ and N_2H^+ are not spatially differentiated as they should be. This indicates a deviation from the standard run column density profile adopted from chapter 3. This may be the result of using only a single core to represent the chemistry and dynamics of all cores within a dark cloud region.

In order to map the cores more realistically, at appropriate angular resolutions, it will be necessary to assign each core with an intrinsic width. I also suggest a number of other alterations to the mapping procedure to improve applicability to Morata *et al.* (2003): to

use critical density data to constrain the "emission" from various molecules; to smooth over the re-injection peaks in the applied column density profiles; to test the influence of the level of uniformity of core distribution within the basic "sky" maps. The use of intrinsic widths would also allow comparison of absolute column density values from the convolved maps, providing another measure by which to test and constrain the theory. These considerations will be explored in the next chapter.

CHAPTER 6

Core Ensembles — A More Detailed Approach to Mapping

6.1 Introduction

I here build on the approach, developed in the previous chapter, of producing synthetic molecular line maps. Firstly, I introduce an intrinsic width to each core, dependent on the physical time-evolution of the core as determined in chapter 2, and divorced from the entirely separate quantity of resolution beam width. This in turn lends each core a physical area in the "sky", thereby enabling absolute values of molecular column densities to be calculated. This allows further comparison with the observational work of Morata *et al.* (1997) and Morata *et al.* (2003), who studied the region L673. This improvement to the basic convolution mechanism employed previously should allow appropriate beam widths to be adopted, so that the characteristic molecular morphologies produced in the high resolution synthetic maps may be assumed to represent "true" morphologies, rather than ones which depend implicitly on the convolution mechanism itself.

Further to this, I make two adjustments to the calculation of the molecular column densities of the representative standard core. The first limits the contribution to the calculation of column densities to gas which has a density greater than an effective critical density for emission in a particular molecular line. Therefore, the column density "detected" in the maps represents "emission" due to a particular transition for any one molecule, whereas previously the "emission" in the maps might have been considered to represent the total amount of a molecule present in the core, at whatever gas density. The

effective critical density for emission is determined by a number of factors, and I *do not* attempt to model the radiative transfer through the cores; I merely adopt a single critical density for each molecular transition, obtained from Evans (1999).

The second adjustment to column density calculation acts to smooth the column density profiles between re-injection peaks. These are approximations to the expected profiles which would be obtained if the chemical model of chapter 3 were run using a large number of chemical reference points, to provide continuous coverage of the freeze-out/non-freeze-out boundary. Because, as discussed in chapter 3, the mechanism for re-injection is unknown and could therefore take place over a range of timescales, I approximate the profiles for two scenarios: where re-injection is fast compared to gas phase chemistry (producing highly peaked profiles), and where it is slow (producing un-peaked profiles). I initially assume that that the maximal re-injection feature obtains.

Having modified the mapping procedure thus, I first test it on the basic map of the previous chapter. I then apply the technique in three different ways: to investigate the effects of different spatial distributions of cores on high resolution morphologies, to investigate the effects of a minimal re-injection feature, and to investigate the effects on the convolved maps of adopting the column density profiles obtained for a "limit cycle" core, whose chemistry was investigated in chapter 4.

6.2 A Modified Convolution Mechanism

The convolution of previously calculated (chapter 3) column densities examined in the last chapter utilised an approximation to the "emission" from a core. Each core was approximated to a point source, and a Gaussian beam profile was assumed, so that the contributions from each core to the "detected" molecular emission at each detection point could easily be calculated. This presented two main problems: firstly, because the cores had no intrinsic size of their own, their detected spatial widths were entirely dependent on the beam width adopted for the convolution. Consequently, in order to compare the synthetic maps with real maps obtained from Morata *et al.* (2003), much larger beam widths had to be chosen to provide appropriate core sizes. This was necessary since the resolution of the Morata *et al.* (2003) observations was such that the cores were of approximately the same size as the FWHM beam. The second problem was that because the simulated cores took up an infinitesimally small area, the beam could not be

normalised. Normalisation requires that we know what the detected level of "emission" would be for a uniform column density profile throughout the area of the beam. This level is impossible to calculate when a potentially infinite number of emitters (of infinitesimal size) could be present within the beam.

These problems may be solved by assuming an intrinsic radius for each core. However, so that the emission from the cores is smooth between its centre and its nominal edge, I adopt a Gaussian profile, and define a scale width as the intrinsic radius. Since the models of Falle & Hartquist (2002) (on which this study is partially based) are only one-dimensional, we cannot say with any certainty how the density profiles along other axes may vary. However, the adoption of a Gaussian profile is in line with the density profile approximations of chapter 2 (onwards) along the axis of core collapse, and satisfies the physical requirement that the density of a core should be continuous (*i.e.* not a step-function). I make one further constraint on the intrinsic radius of the core: that it obeys the conservation of mass requirement as laid out in chapter 2. This means that where the scale width of a core along the principal axis varies with $1/k$ (see equation 2.6, chapter 2), the other axes must vary in the correct proportion. Because all of the column density calculations obtained for the standard core run are made along the principal collapse axis, for the sake of consistency I assume that each core is aligned with its principal collapse axis along the line of sight. Therefore, I allow the observed radius of each core to vary only in a way consistent with this alignment.

If $\Delta z(t)$ represents the scale width of the core along the principal axis of collapse, and assuming that collapse along the other two axes takes place at equal rates (in the absence of other information), we may assign a core with a time-dependent radius in the plane of observation (representing scale width for a Gaussian function) of $\Delta r(t)$. We may relate these quantities to the total mass of a core via:

$$M_{tot} \propto \rho V \propto \rho.\Delta z(t).[\Delta r(t)]^2$$

Since the total mass is conserved, we have that:

$$\Delta z(t).[\Delta r(t)]^2 \propto \rho^{-1}$$

And therefore, eliminating $\Delta z(t)$ via equation (2.6):

$$\Delta r(t) \propto \rho^{(\frac{1}{k}-1)/2} \tag{6.1}$$

Or, eliminating ρ:

$$\Delta r(t) \propto [\Delta z(t)]^{(k-1)/2} \tag{6.2}$$

For the standard run case which I use to construct the maps, $k = 1.5$, hence:

$$\Delta r(t) \propto [\Delta z(t)]^{1/4} \tag{6.3}$$

So the observed physical widths of the cores in this model display a weak time dependence. I use the width $\Delta z(t)$ calculated for each time point in the chemical runs directly in the convolution program to give values of $\Delta r(t)$. The dependence of equation (6.3) still leaves $\Delta r(t)$ at its smallest at the core's peak density time, t_m. However, when the core is not at this peak density (and therefore is not "emitting" so strongly along the principal collapse axis), it takes a slightly larger radius, which will tend to counteract somewhat the weaker emission at lower densities. I fix $\Delta r(t_m)$ so that it assumes a value of some (substantial) fraction of $\Delta z(t_m)$, to be determined according to comparisons with Morata *et al.* (2003).

Having attributed each core with an intrinsic width dependent on its stage of evolution, I require a method by which to take into account "emission" from all parts of a core, at any distance from a particular detection point. I therefore assume that each infinitesimal part of the core emits as a point source, emitting the same level as at the core centre, but limited by the Gaussian profile defined by $\Delta r(t)$. Its contribution to the sum of all emission at the detection point is then reduced according to the Gaussian beam profile, which is dependent on the distance between the element and the detection point. I sum all contributions from the core elements over the entire core.

So, taking an element of area within the circular face presented by the core, the emission from that element, in units of the underlying column density of molecular material which emits it, is:

$$\mathrm{d}N_{emit} = N.\exp\left[-\frac{r^2}{[\Delta r(t)]^2}\right]\exp\left[-\frac{l^2}{\Delta l^2}\right] r.\mathrm{d}r.\mathrm{d}\theta$$

where N is the column density of a molecule calculated for the standard model run (see chapter 3) which represents the level through the centre of the core, l is the distance from the element to the detection point and Δl is the half width half maximum beam radius. Hence total emission from the core is:

$$N_{emit} = N \int_0^{2\pi} \int_0^R \exp\left[-\frac{r^2}{[\Delta r(t)]^2}\right] \exp\left[-\frac{l^2}{\Delta l^2}\right] r.\mathrm{d}r.\mathrm{d}\theta \tag{6.4}$$

where R is an arbitrary integration edge, chosen such that material outside of R makes no significant contribution due to the small value of the Gaussian. Using the cosine rule, l can be substituted for terms in r and d (the distance between the core centre and the detection point). Hence:

$$N_{emit} = N \int_0^{2\pi} \int_0^R \exp\left[-r^2\left(\frac{1}{[\Delta r(t)]^2} + \frac{1}{\Delta l^2}\right) - \left(\frac{d^2 - 2rd.\cos\theta}{\Delta l^2}\right)\right] r.\mathrm{d}r.\mathrm{d}\theta \tag{6.5}$$

This function integrates to a single integral in r, dependent on the Bessel I-function of zero order, $I_0(x)$:

$$N_{emit} = 2\pi N \int_0^R \exp\left[-r^2\left(\frac{1}{[\Delta r(t)]^2} + \frac{1}{\Delta l^2}\right) - \left(\frac{d^2}{\Delta l^2}\right)\right] .r.I_0\left(\frac{2.d.r}{\Delta l^2}\right) .\mathrm{d}r \tag{6.6}$$

The solution of equation (6.6) requires numerical integration, which I achieve using the Simpson's Rule ("QSIMP") routine on the IDLDE platform. (QSIMP is based on the *qsimp* routine in section 4.2 of *Numerical Recipes, The Art of Scientific Computing* (Second Edition), Press *et al.* 1992).

The integration of equation (6.6) produces a value which must be added to the contributions from all other cores. Cores whose centres lie approximately 1 core scale width plus a few beam resolution radii from the detection point in question do not make a significant contribution to the "detection", and are ignored. Once contributions from all cores have been summed, the overall detected level at that detection point must be averaged over the beam. The beam profile of a telescope would be known, and I normalise with respect to a beam taking in a hypothetical region of uniform emission. The absolute level of (uniform) emission is unimportant, since the purpose is to determine a "weighted area" for the beam – weighted according to the beam profile, so that the centre of the beam accounts for most of the detection. Hence, to obtain the beam area with which to normalise the contributions from the cores, I begin with equation (6.5), without the factor N. For a uniform level of emission, $\Delta r(t) \rightarrow \infty$, and the value of d becomes unimportant, so to simplify the integration we set $d = 0$. This leaves:

$$\begin{aligned}\int_0^{2\pi}\int_0^{R}\exp\left(-\frac{r^2}{\Delta l^2}\right)r.\mathrm{d}r.\mathrm{d}\theta &= 2\pi\left[-\frac{\Delta l^2}{2}\exp\left(-\frac{r^2}{\Delta l^2}\right)\right]_0^R \\ &= \pi\Delta l^2\left[1-\exp\left(-\frac{R^2}{\Delta l^2}\right)\right] \\ &\simeq \pi\Delta l^2\end{aligned}$$

The final approximated value is valid, and accurate, since a value of R is chosen which is large in comparison to Δl, as stated above. Hence the normalised "detected" column density of a molecule for any detection point is:

$$N_{beam} = \frac{2}{\Delta l^2}\sum_i^I N_i \int_0^{R_i}\exp\left[-r^2\left(\frac{1}{[\Delta r_i(t)]^2}+\frac{1}{\Delta l^2}\right)-\left(\frac{d_i^2}{\Delta l^2}\right)\right].r.I_0\left(\frac{2.d_i.r}{\Delta l^2}\right).\mathrm{d}r \quad (6.7)$$

Where I is the total number of cores which are close enough to the detection point to contribute significantly.

As already mentioned, this method produces normalised column density values which may be used in comparison with observed levels. Since the column densities calculated for the standard run model only account for the centre of the core, along the line of sight, we should treat the "detected" morphologies as being representative of the extents of the *core centres* rather than the entire region for which the density is enhanced with respect to the background value of 300 cm^{-3}. The core centres will produce the strongest emission in this case, so the loss of the extremities of the cores should not drastically affect the results.

6.3 Column Density Profiles Constrained by Critical Emission Densities

A major drawback in the comparison of real observations with levels obtained through this method of synthesised mapping is that the radiative transfer through the objects is not modelled in any way. This means that the synthesised levels represent "true" column densities – that is to say that the simulated "emission" corresponds directly with the amount of material deemed to reside in the cores. There is no intermediate mechanism, and therefore the particular molecular transitions responsible for emission, and their optical depths, have no bearing on the resultant maps or levels. However, it is observationally well established that different transitions within the same molecular species should trace

regions of different density and temperature (see *e.g.* Evans 1989). We may simplistically argue that for emission in a molecular line to be detectable, the gas density must be above a critical density value, defined by:

$$n_c(jk) = A_{jk}/\gamma_{jk} \tag{6.8}$$

where A_{jk} is the Einstein coefficient for spontaneous emission between upper molecular level j and lower level k, and where γ_{jk} is the coefficient for collisional de-excitation of the line. n_c represents the density at which radiative and collisional de-excitation compete equally, and above which the transition is (approximately) thermalised; that is T_{ex}, the excitation temperature of the line, equals the gas kinetic temperature, T_K. However, as explained in Evans (1989), the ratio of n_H/n_c (where n_H is gas density) required for thermalisation depends on the energy interval, ΔE_{jk}, between levels. The relationship is such that, although transitions with larger ΔE_{jk} generally have larger A_{jk} and therefore larger n_c, the ratio n_H/n_c required for thermalisation is smaller. This means that the differences between densities required for thermalisation of particular transitions are not as stark as might be suggested by the critical densities alone.

The picture is further complicated by other features of the radiative transfer: multi-level excitation effects, and trapping of line photons, where lines are optically thick, act to lower the density required for detection of a line.

Evans (1999) provides results of an LVG (large velocity gradient) radiative transfer code (which includes trapping considerations) for some commonly observed molecular transitions, for a kinetic temperature of $T_K = 10$ K. Calculated in the code are values of n_{eff}, an effective critical density (taking into account those issues raised above) for the emission of a line of 1 K, deemed to be easily detectable in most cases. The obtained values are expected to be accurate to within a factor of $\sim$3.

I adopt these threshold values and employ them in the calculation of column densities for the standard run model of chapter 3. In those calculations, I merely use the value of n_{eff} as an integration edge, so that material in the core for which $n_H \geq n_{eff}$ contributes as usual, whilst material of $n_H < n_{eff}$ does not contribute at all. This approach is therefore still quite simplistic, but acts to limit contributions from highly extended regions of gas which may not be of sufficient density to emit. This will mostly affect CS morphologies in the synthetic maps, since the CS (J=2$\rightarrow$1) line, used in Morata *et al.* (2003), has a high critical density and n_{eff}. This molecule is abundant in relatively low density cores,

Table 6.1: Properties of Line Transitions Utilised in Column Density Calculations for Standard Run Model

Molecule	Transition	ν (GHz)	n_c(10 K) (cm^{-3})	n_{eff}(10 K) (cm^{-3})
CS	$J = 1 \rightarrow 0$	49.0	4.6×10^4	7.0×10^3
CS	$J = 2 \rightarrow 1$	98.0	3.0×10^5	1.8×10^4
HCO^+	$J = 1 \rightarrow 0$	89.2	1.7×10^5	2.4×10^3
NH_3	(1,1)inv	23.7	1.8×10^3	1.2×10^3
CO †	—	—	—	1.0×10^3

All values taken from Evans (1999), except † taken from Ungerechts *et al.* (1997)

at around their start and end times (as defined in chapter 2); the effect should heavily subdue contributions from these cores in the CS (J=2→1) line, and should cut down the calculated levels even in cores at peak time.

The critical densities and other line transition information obtained from Evans (1999) are shown in table 6.1. Transitions chosen are relevant to those used in the Morata *et al.* papers. Note that N_2H^+ transitions were not available. Although carbon monoxide transitions were also not available, I assume that a gas density of 1000 cm^{-3} is sufficient to produce a detection (Ungerechts *et al.* 1997), since the small dipole moment of the CO molecule produces lines that are usually very well thermalised.

The resultant calculated column densities for the standard run model are employed in equation (6.7) for the construction of the synthetic maps.

6.4 Smoothed Column Density Profiles

A problem with the approach of the previous chapter was that the discrete distribution of chemical reference points led to discontinuities in the column density profiles when grain mantle-bound material was instantaneously re-injected into the gas phase. Here I remedy this problem by integrating the profiles between the peaks, to eliminate the artificial peak structure. Later in this work, I examine the effects of removing the peak structure altogether.

This integration between peaks is not entirely consistent with the chemistry, since with

a continuous distribution of reference points throughout the core, we should expect the levels at each point to combine with the others, producing larger overall levels. However, as discussed in chapter 3, the rate of re-injection and the range of visual extinctions over which it may take place is not known, since the mechanism itself is not understood. Also, since one depth point represents one twelfth of the width of the core in the column density calculations, and considering the quite large difference in visual extinction across such a distance, we should not expect that absolute levels produced by a model with a continuous chemical reference point distribution would exceed the levels attained at the peaks in the 12 point model, for the same times. (For example, note the width of the re-injection peaks in figure 2.6b of chapter 2). Therefore, the smoothed column density profiles should reasonably represent a maximal re-injection peak effect. Conversely, by smoothing over the peaks by integrating between the levels obtained before the peaks occur and after they have relaxed, we may obtain profiles for a minimal level of re-injection. This approximates the case where re-injection is slow compared to gas phase reactions, such that there is no obvious enhancement in fractional abundances nor, therefore, in column densities. I investigate this case later in the chapter.

The integration between these peaks is conducted after the main calculations of column densities discussed in the previous section have been completed.

6.5 Application to the Previous Basic Map

Here I use this modified approach to produce molecular line maps of the same basic "sky" map as was employed in the previous chapter, and contrast the two.

Figure 6.1a shows the unsmoothed column density profiles obtained using the effective critical densities of table 6.1. Figure 6.1b shows the smoothed profiles. Note that CS and NH_3 are by far the most strongly affected by re-injection. These smoothed profiles are used for the convolution of the basic "sky" map of figure 5.1, chapter 5. The CS (J=2→1) transition may be seen to trace the cores at closer to the peak density than the CS (J=1→0) transition, although the column densities produced are a little lower. The figures show clearly at what stage in a (standard run) core's evolution that densities are too low to produce detectable emission in the CS transitions.

Figures 6.2a–e show low resolution convolved maps using a beam resolution of $\sim 2'$, as used in chapter 5. In this comparison, both for the low and high resolution maps, the

Figure 6.1: Column densities of selected transitions as functions of time, with n_{eff} considerations, calculated through the standard run core – unsmoothed and smoothed

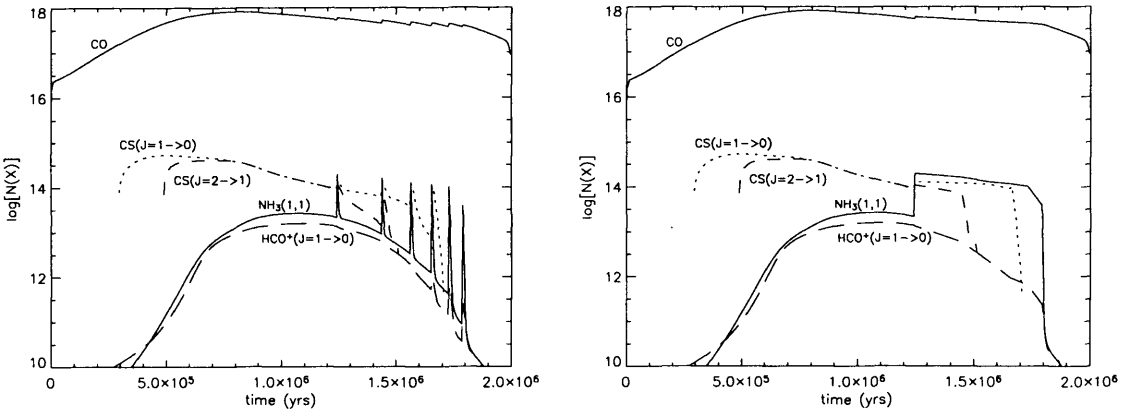

a: Unsmoothed re-injection b: Smoothed re-injection

core sizes are set such that $\Delta r(t_m)/\Delta z(t_m) = 1/4$. This achieves approximately the right sizes for the cores in the high resolution maps.

Comparing with figure 5.3a, we can see that CO emission peaks are present in all the same places, only they are now much wider. Also, CO is now no smaller in extent than CS (J=1→0), and perhaps a little larger. Morata *et al.* (1997) mapped CS in the J=1→0 line. The new CS (J=1→0) map of figure 6.2b perhaps matches the spatial extent of the observations better than figure 5.3b did, but morphologies are more drastically widened in the new CO map. The CS (J=2→1) map of figure 6.2c shows far fewer detected regions than the CS (J=1→0) map, although the spatial extents of regions which show emission in both maps are similar. The slightly smaller extents and lower coverage of the CS (J=2→1) transition demonstrate the effect of differentiating between the different molecular trasitions by the limiting of emission to critical densities.

In figure 6.2d, for HCO^+ (J=1→0), again spatial extents are broadened, but the same regions are being traced as in figure 5.3c. All of these broadening effects on the spatial extents, compared to the maps of the previous chapter, evidence the intrinsic widths adopted for the underlying cores in this modified approach.

Finally, NH_3 coverage in figure 6.2e is dramatically increased in comparison with figure 5.3f. This, most clearly of all, demonstrates the effect of column density profile smoothing to produce continuous levels over the re-injection stage of a core's evolution. Crucially, the column density profile smoothing leaves NH_3 with a much larger spatial extent. However,

Figure 6.2: Trimmed map – low resolution, modified approach

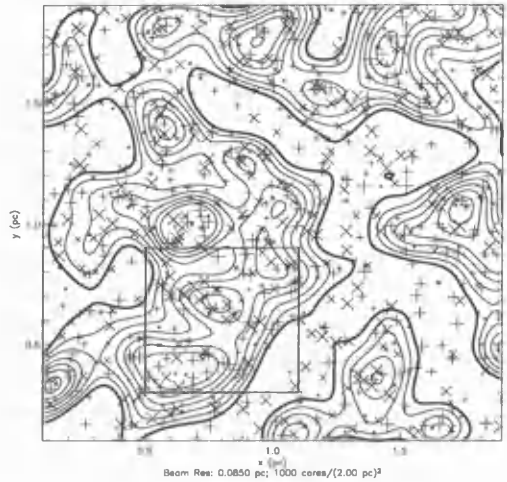

a: CO

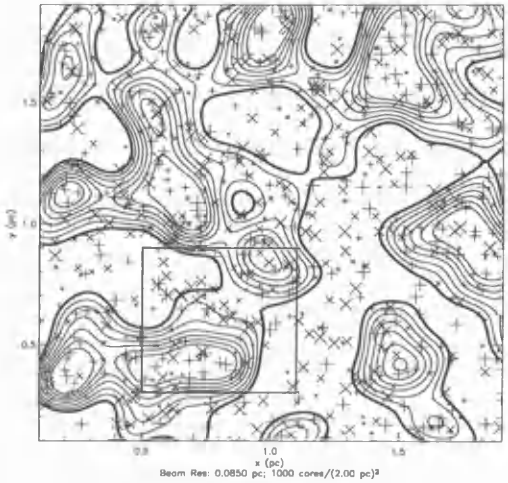

b: CS (J=1→0)

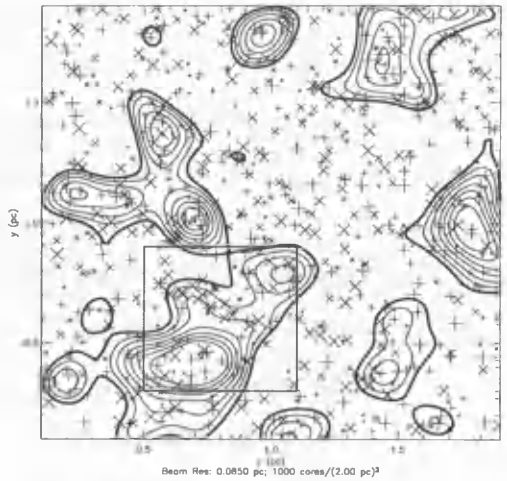

c: CS (J=2→1)

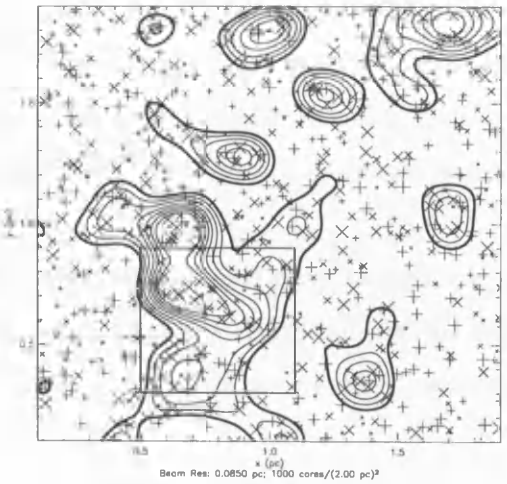

d: HCO^+ (J=1→0)

e: NH_3 (1,1)inv

the total coverage of NH_3 in the map is arguably still smaller than CS or CO coverage.

The high resolution maps of figures 6.3a – e again correspond to the boxed section of figures 6.2, as chosen in the previous chapter for its coincidence of molecular line peaks. Comparing figure 6.3a with figure 5.7a, the CO peaks in the new map are more defined, and a little smaller (as a result of imperfect agreement of sizing between the mapping procedures). The same regions are mapped, as expected from the small difference between column density profiles in either case. The contour morphologies in all of the new maps appear less regular, due to the differences in sizes between various mapped cores, which were not present when using the point source approximation of the previous chapter. The CS emission of figures 6.3b & c generally map the same material as each other, although there are some cores which do not appear in both figures. The CS (J=2→1) map shows slightly smaller spatial extent than the CS (J=1→0), and does not exhibit so many strong emission peaks. The CS (J=2→1) map has more individually resolved, low emission regions, which is in keeping with the characteristic morphologies of the observations, although the number of such regions is lower than observations might demand. This may imply the presence of other, probably smaller, cores which contribute these small, isolated emissions in L673.

The HCO^+ extents of figure 6.3d are somewhat smaller than in the last chapter's map, but the same regions are detected. Figure 6.3e shows that the smoothing of the NH_3 column density profile permits the detection of many more cores at the high resolution scale than previously.

The normalisation of molecular levels using the modified approach allows the determination of absolute column densities (and ratios) for any point in a synthesised map. Hence I present these quantities as determined by the model, for the low resolution and high resolution maps, and compare with levels detected in Morata *et al.* (1997) and Morata *et al.* (2003). Taking a similar approach to the latter work, I select the peak position for each transition in the high resolution maps, and provide column density values for *each* molecule at *each* point – in order to compare values at the same spatial positions. These points are represented by *diamond*-shaped markers in figures 6.3b–e. I also give column density values calculated from the low resolution data, at the low resolution molecular line maxima within the high resolution map domain. These are represented by *square*-shaped markers. In agreement with Morata *et al.* (1997), for each low resolution peak I present the column density only of the molecule whose peak it is.

Figure 6.3: Close-up map – high resolution, modified approach

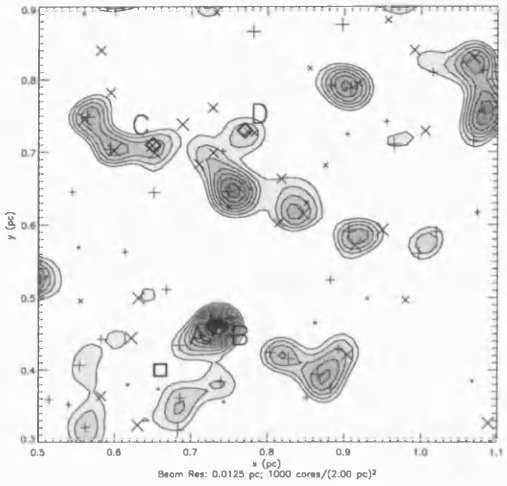

a: CO

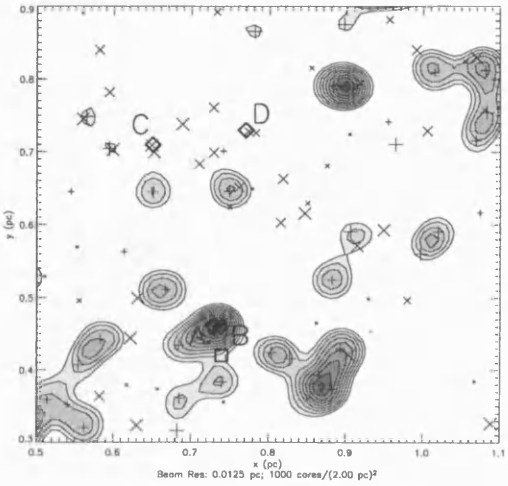

b: CS (J=1→0)

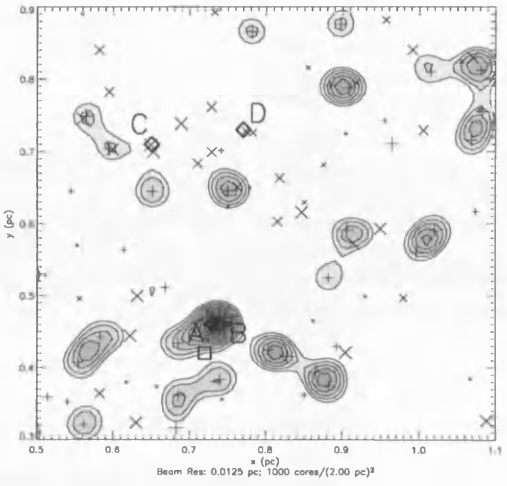

c: CS (J=2→1)

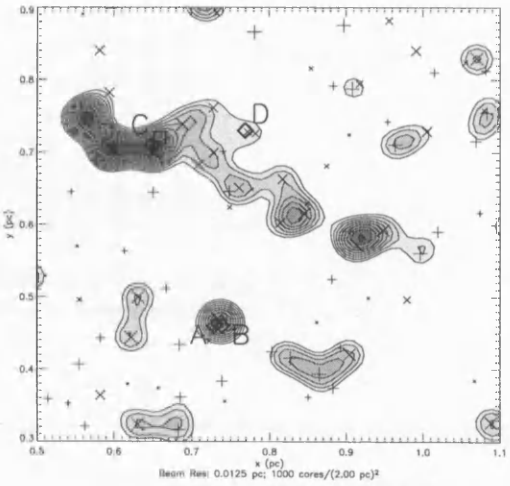

d: HCO^+ (J=1→0)

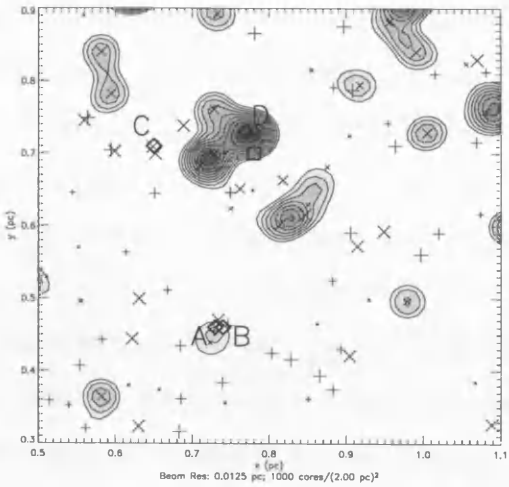

e: NH_3 (1,1)inv

Table 6.2: Peak Column Densities for Synthetic Maps

Molecule	Transition	x (pc)	y (pc)	$N[i]$ † (cm^{-2})	Peak ‡
CO	—	0.66	0.40	6.0(17)	Low Res
		0.73	0.46	2.2(18)	**Hi – A**
		0.74	0.46	2.2(18)	Hi – B
		0.65	0.71	1.2(18)	Hi – C
		0.77	0.73	1.0(18)	Hi – D
CS	J=1→0	0.74	0.42	2.4(14)	Low Res
		0.73	0.46	9.2(14)	**Hi – A**
		0.74	0.46	9.1(14)	Hi – B
		0.65	0.71	2.4(14)	Hi – C
		0.77	0.73	2.3(14)	Hi – D
CS	J=2→1	0.72	0.42	1.8(14)	Low Res
		0.73	0.46	7.5(14)	Hi – A
		0.74	0.46	7.6(14)	**Hi – B**
		0.65	0.71	2.4(14)	Hi – C
		0.77	0.73	1.1(14)	Hi – D
HCO^+	J=1→0	0.66	0.72	7.5(12)	Low Res
		0.73	0.46	2.4(13)	Hi – A
		0.74	0.46	2.5(13)	Hi – B
		0.65	0.71	2.8(13)	**Hi – C**
		0.77	0.73	1.2(13)	Hi – D
NH_3	(1,1)inv	0.78	0.70	7.9(13)	Low Res
		0.73	0.46	1.4(14)	Hi – A
		0.74	0.46	1.2(14)	Hi – B
		0.65	0.71	4.7(13)	Hi – C
		0.77	0.73	3.1(14)	**Hi – D**

† $a(b) = a \times 10^b$

‡ Low resolution peak positions are different for each transition. High resolution peaks in bold correspond to the peak in the given transition.

All these column density data are presented in table 6.2. Peak A corresponds to the shared high resolution peak in CO and CS (J=1→0). Peaks B, C, and D correspond to the high resolution peaks in CS (J=2→1), HCO^+ (J=1→0) and NH_3 (1,1), respectively.

In table 6.3 I present the equivalent column density data obtained from the low resolution observations of Morata *et al.* (1997) (their table 4) and the high resolution observations of Morata *et al.* (2003) (their table 3). Peaks E and W correspond to CS (J=2→1) peaks, whilst peak N corresponds to HCO^+ (J=1→0) and peak S to N_2H^+ (J=1→0). Although I do not model N_2H^+ in this section, I include the values for completeness.

Firstly, consider the low resolution peaks in table 6.2. The CS (J=2→1) maximum (B) is close to in value, though a little lower than, the CS (J=1→0) peak level (A), and they are located very close together. The low resolution HCO^+ value is more than an order of magnitude lower than either CS transition's peak. NH_3 is a factor of 2 – 3 lower than the CS peak levels. The distance between the NH_3 and CS (J=1→0) low resolution peaks

Table 6.3: Peak Column Densities from Low and High Resolution Morata *et al.* Observations

Molecule	Transition	$N[i]$ † (cm^{-2})	Peak ‡
CS	J=1→0	2.5(13)	M97 – Low Res
CS	J=2→1	1.20(12) – 2.69(12)	M03 – S
		2.53(12) – 8.48(12)	**M03 – E**
		3.72(12) – 9.96(12)	**M03 – W**
		2.71(12) – 7.22(12)	M03 – N
HCO^+	J=1→0	<4.73(11)	M03 – S
		<3.60(11)	M03 – E
		4.7(11) – 7.7(11)	M03 – W
		7.7(11) – 1.91(12)	**M03 – N**
NH_3	(1,1)inv	≥2.2(14)	M97 – Low Res
N_2H^+	J=1→0	2.2(11) – 3.1(11)	**M03 – S**
		1.7(11) – 2.4(11)	M03 – E
		<2.0(11)	M03 – W
		<1.6(11)	M03 – N

† $a(b) = a \times 10^b$

‡ Values are taken from Morata *et al.* (1997) and Morata *et al.* (2003). Low resolution peak positions are different for each transition. High resolution peaks in bold correspond to the peak in the given transition.

is 0.31 pc, which agrees reasonably well with the $\sim$ 0.2 pc quoted for the specific case of L673 in Morata *et al.* (1997). However, the actual levels and ratios detected do not agree well with that paper. Whilst the synthesised NH_3 peak level may be as low as half the observed value, the synthesised CS (J=1→0) peak level is about an order of magnitude too high. This leaves a ratio of $[CS/NH_3]$=3.0, rather than the quoted value of ≤ 0.11.

For the high resolution synthetic values, at the CS (J=2→1) peak (B), HCO^+ (J=1→0) column density is little changed from its peak value (C). However, CS (J=2→1) column density at peak C is a factor of three lower than at B. This difference is due to peak B being an unresolved combination of three strongly emitting cores – one slightly post-peak density, another slightly pre-peak density, and the other a little younger again. This combination acts to give high values for each of the molecules except NH_3 (which is so strongly weighted towards later times in the column density profile of figure 6.1). The close proximity of the three cores, which are approximately 1 high resolution FWHM beamwidth apart, allows them to reinforce each other effectively.

The high resolution synthesised CS (J=2→1) and HCO^+ (J=1→0) column densities are even larger again than the observed values – peak CS levels are as much as two orders of magnitude larger than observed, and HCO^+ levels more than one order of magnitude larger. This therefore indicates that the discrepancies are more than just some kind of

scaling error.

6.5.1 Discussion

The morphologies produced by this more detailed method of synthesised mapping are not drastically different from those produced in the previous chapter. However the effects of each individual modification of the method are well exhibited in one or another of the maps. The introduction of effective critical densities for molecular transitions to produce detectable emission tends to subdue or remove contributions from very young and very old (within the framework of this model) cores, in particular for CS transitions. At the same time, the young and old cores assume greater sizes in accordance with equation (6.1), the cores at the peak time in their evolution being the smallest. This tends to mitigate the former critical density effect for those cores which *do* emit, not in the column density level contributed at a core's centre, but by the extent of the emitting area. The detected level within the finite beam is then increased as a result. The time-dependent widening of the cores is important for CS transitions, where the peak emission level is not attained at the peak density. The individual cores of the basic map at coordinates (0.65, 0.65) and (0.88, 0.53) show up quite strongly in the two CS maps, with no major contributions from other nearby cores, as these cores are at the period of evolution at which CS column density is highest. These, however, are rare exceptions – in these maps, most detected contributions come from associations of cores which are not generally individually resolved. To apply this to the observational results of Morata *et al.* (2003), we note that the detected transition line widths at each of peak N, E and S are about the same as were measured for the single dish observations of Morata *et al.* (1997). If the cause of line broadening is primarily the combination of the different velocities of individual cores which are convolved together, we should expect that points N, E and S each represent associations of cores which are too close together to be individually resolved, and which are large enough that the strongest emission emanates from their geometric centre (weighted by the levels of emission of each core). Point W has yet a higher line width, making it an even more likely candidate for such an association.

Clearly, the smoothing of the re-injection peaks makes the mapping procedure far more consistent. It also acts to enlarge the very small spatial extents for NH_3 that were obtained in the previous chapter. The extent of CO is also increased somewhat with the modified approach, such that it is a little larger than that of CS, which is at least qualitatively in

agreement with the Myers *et al.* (1991) work.

It can be seen that the synthesised column densities are higher at the high resolution peaks than for the low resolution peaks, whereas this situation is reversed for the Morata *et al.* papers. They explained that a large fraction of their expected emission may not have been detected by the interferometer (perhaps as much as 80%) if the observed medium were composed of a small number of strongly emitting (*i.e.* large) cores/clumps, with many more weakly emitting cores/clumps contributing little detected emission. This hypothesis of a clumpy, heterogeneous medium was tested (modelled) against a scenario adopting an extended, homogeneous medium, and was found to suit the observations more satisfactorily. The synthetic maps, however, take no account of such instrumental effects (no special treatment is made to mimic the performance of an interferometer), so the effect is absent in this work; however, this does not affect the validity of the synthesised values.

The overall column density levels obtained from the synthetic mapping technique of this chapter are generally too high, even at low resolution. Four factors may explain this: firstly, the level of uniformity of core distribution may have an effect such that the peaks observed in the synthetic maps represent close associations of cores (as mentioned above), in particular those close associations of cores at similar stages of evolution. Secondly, the chemical (and/or physical) evolution of individual cores may vary from that adopted here – in particular, initial elemental fractional abundances may be responsible for the discrepancies in peak column densities. Thirdly, this approach uses only one core chemistry to model the entire region. In reality, we might expect to see a spectrum of cores within the same cloud, all exhibiting somewhat different chemical and physical properties. As chapter 3 effectively showed, the resultant chemistry can vary strongly with visual extinction. If a large number of cores took maximum central visual extinctions of 3, as in model G-A1 in chapter 3, we might expect many of them to show smaller CS column densities than in the standard run. Meanwhile, the low visual extinctions would additionally mean that freeze-out had only a short period to operate, producing quite sharp re-injection peaks (even with smoothing taken into account). Therefore, NH_3 could take on smaller spatial extents, which would be in line with the evidence of Myers *et al.* (1991). With a spectrum of such variations in the cores' displayed chemistries, with the standard run representing the more strongly emitting, sparsely distributed cores, the column densities of the Morata *et al.* observations might be reproduced. Within the spectrum, a core with a lower peak central density would have lower CS (J=2→1) emission (and over a shorter period of its

evolution), since the strongest part of the column density profile for this transition is near to its limit of emission. The NH_3 (1,1)inv transition has a very low n_{eff}, so it would not be affected to anywhere near the degree that the CS transitions would. Hence, smaller central peak densities could act to rectify the CS/NH_3 column density discrepancy seen in tables 6.2 & 6.3, notwithstanding the resultant chemical effects of the density changes. Finally, smaller core widths (in the plane) should produce smaller column densities. The Morata *et al.* (2003) HCO^+ emission is less extended and more defined than the CS in particular, and this may be due to only smaller regions near the core centre being able to produce it.

The amount of what might be called "lobing" of the emission (that is, large areas of fairly continuous emission) in figure 6.3c is not so great in the synthetic maps as is observed in L673 for the CS (J=2→1) transition. Compare with figure 6.3d, where HCO^+ cores take an apparently larger extent than is seen in the observations. This may be a result of the one-dimensional approach to the chemical modelling, which leads to the approximation where all regions of a core assume the column density ratios of the core centre. The larger lobes in CS (J=2→1) in the observations may be due to a much larger extent of CS, compared to say HCO^+, in individual cores, *away from the line-of-sight core centre* — the examination of the standard model in chapter 3 (and its pre-cursor in chapter 2) shows that the large levels of HCO^+ rely on freeze-out effects, whilst CS is diminished in those parts. In regions of a core where visual extinction is not high enough to reach the threshold level for freeze-out, we might therefore still expect large amounts of CS. However, it is difficult to quantify the effects of this hypothesis, since at present there is little observational or theoretical evidence with which to constrain a >1-dimensional chemical/physical model of a core. It should also be remembered that this analysis uses regular core shapes (circular in the plane of the map), whereas this may not strictly be the case.

6.5.2 Conclusions

The modified approach of this section compares favourably with the more simplistic approach of the previous chapter, against the Morata *et al.* observations. Each of the modifications is justifiable, either by extension of the logic of the physical model into three dimensions (as in the case of the time-dependent intrinsic width), on the grounds of self-consistency (as for the re-injection smoothing), or on the basis of broad observational

and theoretical evidence (as for the implementation of critical emission densities in the column density calculations). Each has a noticeable and comprehensible effect on the map morphologies and peak column densities.

The calculation of convolved column densities at any point within the map is also very useful on its own, and allows a more rigorous comparison with observational data. Indeed, the consideration of such information leads to a number of possible explanations of the discrepancies. Whilst two of these would involve drastic re-modelling of certain features of the pre-mapping stage chemical evolution of a standard core, or the construction of a representative, coherent spectrum of core chemistries, the first and last explanations given in the discussion section above may be tested with this model. The uniformity of core distribution may be controlled, making the distribution adhere more rigorously to the mean core frequency. The impact of smaller emission regions within cores (in particular for HCO^+) could be studied by a simple variation in the ratio $\Delta r(t_m)/\Delta z(t_m) = 1/4$ for certain molecules. This should have an effect not only on morphologies but also on the resultant peak column densities which are "detected", however, the adopted widths would have to be fitted using approximate observed values taken from Morata *et al.* (2003).

6.6 Testing the Effects of the Variation of Core Distribution

In this section I investigate the importance of the level of uniformity of the core distribution on the morphologies and peak column density values produced, looking at the effects of greater or smaller mean core separations. I restrict the analysis to the high resolution maps. This ensures that the level of uniformity as measured for a map is locally valid, and not just an averaged value over a region of which only a small part is examined at high resolution.

In order to test the variable, I require the level of core distribution uniformity in a map to be quantified in some way, and to be able to vary it. I start by defining a mean separation between cores. This distance is related to the core number density in a basic "sky" map, however, that quantity does not carry much meaning when applied to small regions which contain very few cores, and is difficult to calculate locally for the purpose of determining local variations. Hence, for each core, I calculate the separation between it and its nearest neighbour. In the locality of a single core, this quantity is very important for the relative influences of either core on the convolved map. This is because for two cores to be resolved

Figure 6.4: Core positions in the basic "sky" map

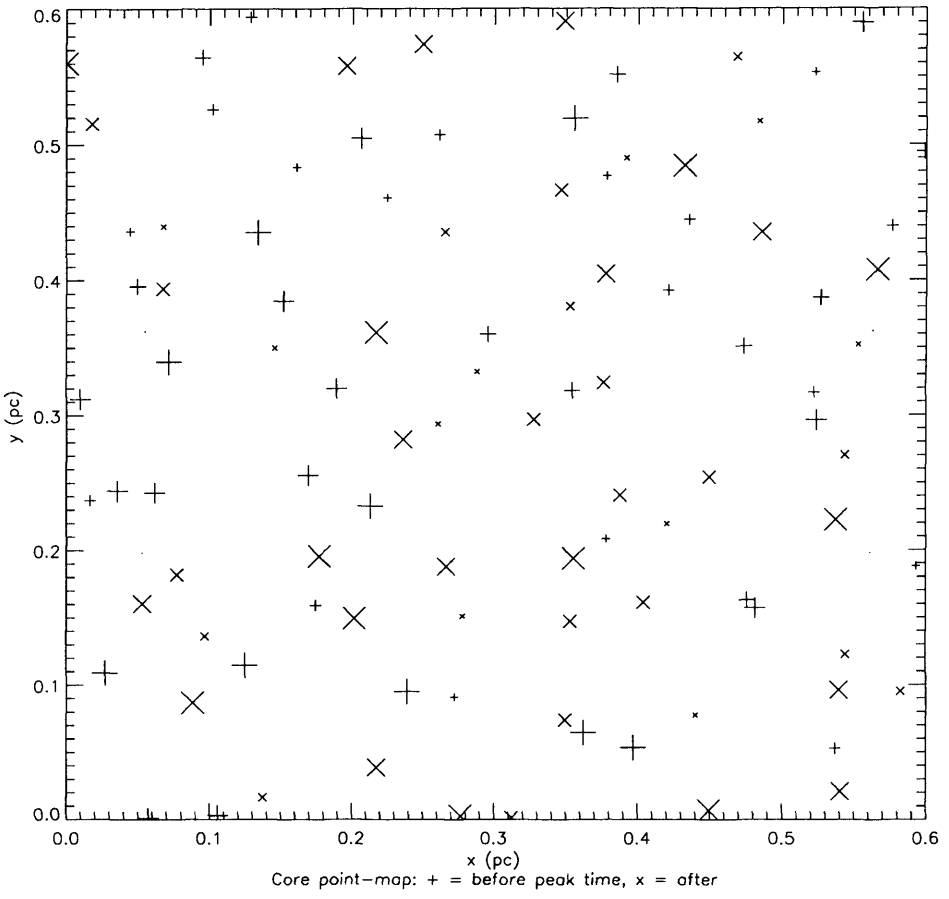

individually, the distance between them (in relation to beam resolution) is all important. This quantity is therefore also important for the determination of detected levels calculated via the convolution process. By then calculating the *mean* shortest inter-core distance, a "global" variable is obtained. From this point, it is then easy to quantify the level of uniformity within a map using the standard error on the mean: with a zero SEM, the basic map is a grid of equally spaced cores (with maximal uniformity of distribution, according to this regime), whilst increasingly large error values indicate more (random) variation from this extreme. By quantifying the level of uniformity of distribution with respect to *cores* rather than to regions of the spatial area of the map, which may or may not contain cores, the variable is more sensitive to the elements of the mapping process which I wish to investigate: the effect of the relative spatial arrangement of cores.

With this definition in hand, I investigate the two variables: the mean shortest inter-core distance (analogous to core number density) and the standard error on the mean

Table 6.4: Parameters of basic "sky" maps

Core Distribution	Mean Shortest Inter-Core Distance (pc)	SEM
1 (standard)	0.524	4.21%
2	0.520	4.85%
3	0.529	5.19%

(uniformity of distribution). To do this, I first construct a basic "sky" map of a high level of uniformity. For this, instead of assigning cores to random x- and y- positions within one map "unit", I divide the map into 100 map units, and designate one core to each. Each of these cores is then assigned random positions within its designated map unit. This starting map is shown in figure 6.4. The size of the basic map is set to 0.6 $\times$ 0.6 pc, the same as the high resolution maps of the previous chapter.

To produce maps of varying uniformity, I move each core in a random direction by a randomly determined distance of up to 0.03 pc, half the map unit size. I then modify the resultant map again in the same way. The advantages of this particular method are that firstly the same distribution of cores in terms of their stages of evolution is preserved, elimimating any resultant differences in the relative weighting of column densities; secondly that the associated spatial positions of these cores are approximately preserved, such that the same associations of core chemistries are compared between maps. The convolved molecular line maps of the three basic maps are shown in figures 6.5, 6.6 and 6.7. From a range of resultant randomly modified maps which were produced, these were chosen so that their mean shortest inter-core distances were approximately the same, in order to isolate their varying levels of uniformity.

The molecular line maps show CO, CS (J=2$\rightarrow$1), HCO^+ (J=1$\rightarrow$0), and NH_3 (1,1)inv. Each is trimmed to avoid edge effects, as explained in the previous chapter.

6.6.1 Results and Discussion

I display the parameters of the basic "sky" maps of varying uniformity of core distribution in table 6.4. Here, I address the broad morphological differences between the maps.

Firstly, we see that even with the much greater level of uniformity of core distribution in the "standard" map (distribution 1), seen in figure 6.4, than in the basic "sky" map of

Figure 6.5: Core distribution 1 (standard) – high resolution, modified approach

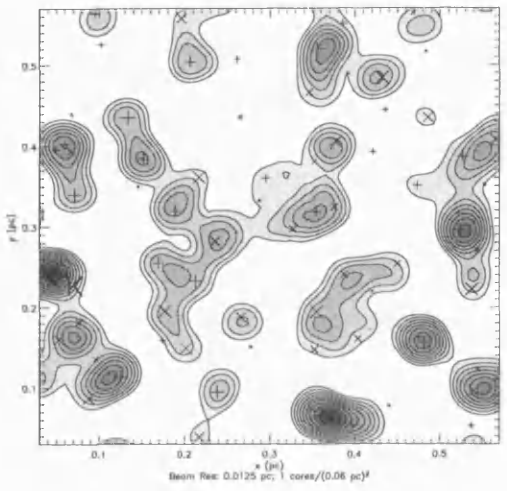

a: CO

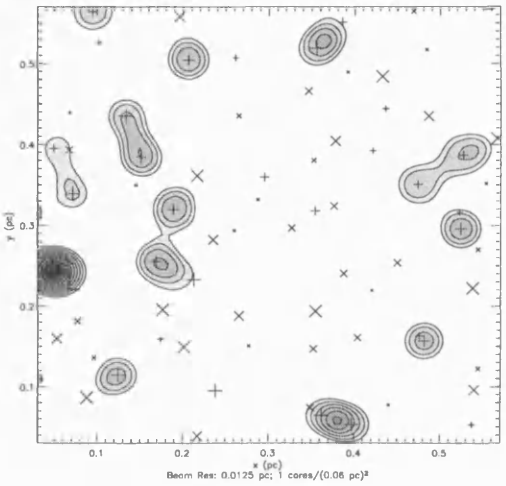

b: CS (J=2→1)

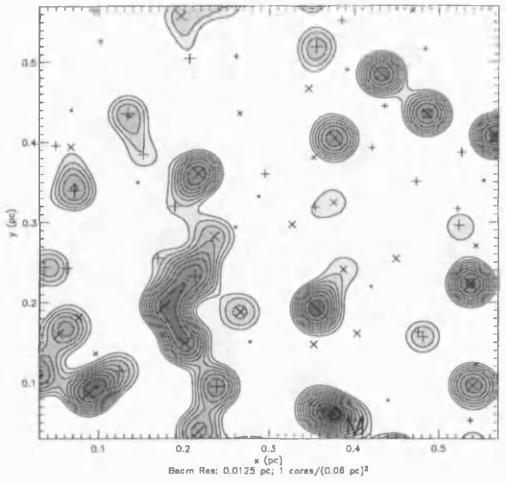

c: HCO^+ (J=1→0)

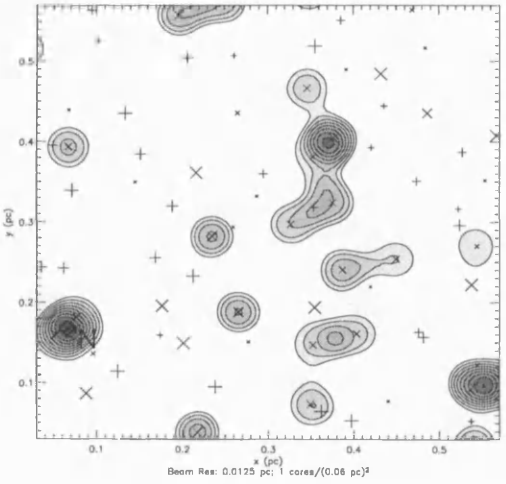

d: NH_3 (1,1)inv

the previous section, we do not resolve many cores individually. We may discern, however, that for CO (which is well represented in coverage) those peaks whose contours are very tight tend to be the result of core associations, whereas peaks whose contours are broad and fairly regular tend to be single cores, close to their peak densities. These peaks do not tend to be as strong as those for which core associations are responsible. For the other molecules, most peaks tend to be the result of the resolution of single, fairly isolated cores.

In general we find that the amount of lobing in the maps is reduced as uniformity decreases and the peak levels detected in each map broadly increase, raising the contour levels and effectively sharpening all contrasts. The ratio of the numbers of strong to weak

Figure 6.6: Core distribution 2 – high resolution, modified approach

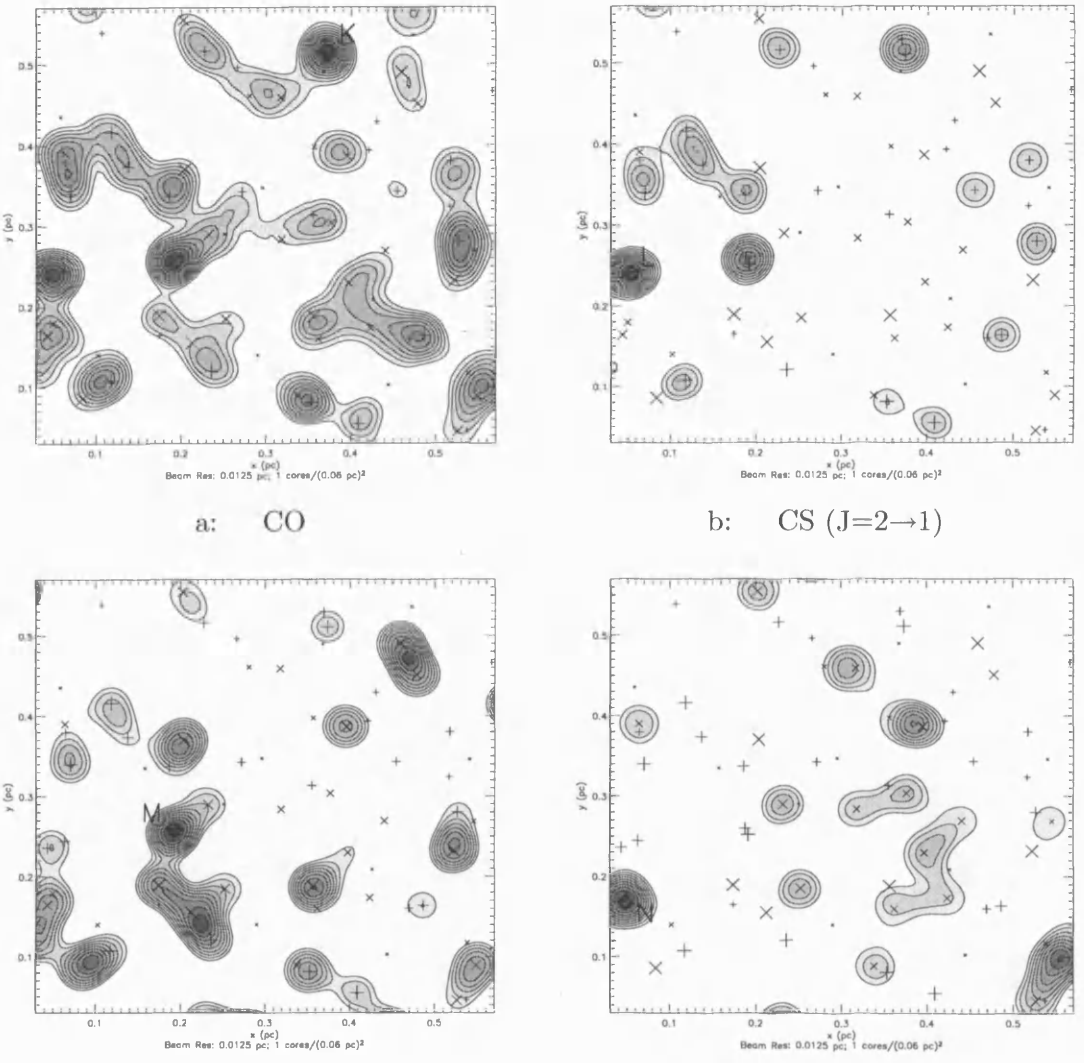

a: CO

b: CS (J=2→1)

c: HCO^+ (J=1→0)

d: NH_3 (1,1)inv

peaks in the CS (J=2→1) map tends to increase, whilst in the others it does not.

It is worth while to point out that, regardless of the molecular tracer or core chemistry involved in producing the "detected" emission, it is the spacing between emitting cores which determines the morphologies of the maps. The spacing is dependent not only on core number density and uniformity of distribution, but also on whether or not a core emits enough in the molecular line in question to be registered, which is then dependent on the column density profile for the standard core. Using the different molecular tracers as test cases for these variables, we see that as in the case of the CS (J=2→1) maps, widely spaced emitting cores produce quite tight peaks, and more strong peaks tend to

Figure 6.7: Core distribution 3 – high resolution, modified approach

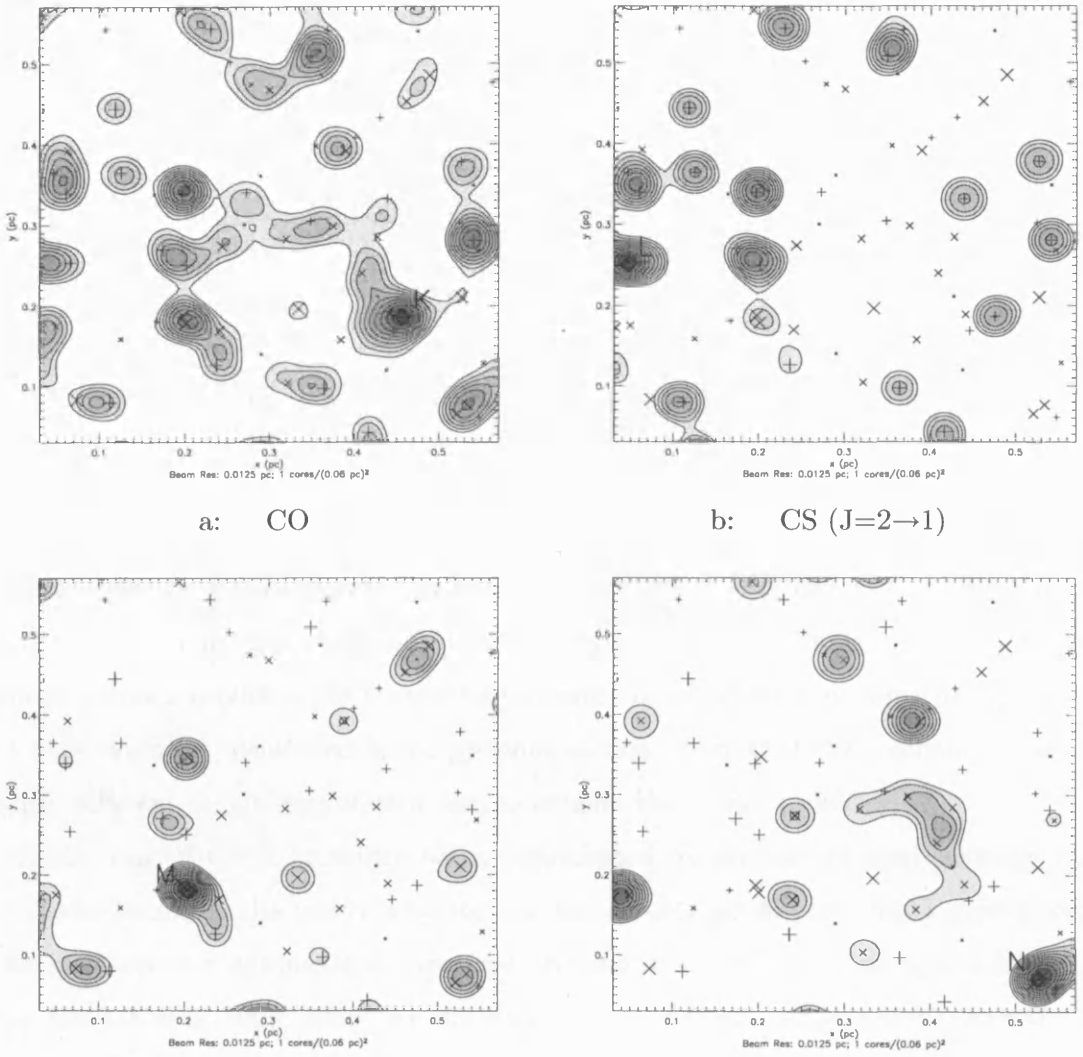

a: CO

b: CS (J=2→1)

c: HCO^+ (J=1→0)

d: NH_3 (1,1)inv

be present with decreasing uniformity of general core distribution. The CO maps show that for closely spaced emitting cores, the large structures, though less lobed, are still "connected" for those contour levels shown (as adopted from Morata *et al.* 2003) when lower levels of uniformity are taken. However, the CS (J=2→1) maps of this section do not look so much like the Morata *et al.* (2003) maps for that transition. This suggests firstly that where the large connected structures seen in that paper are present, the number of "emitting" cores responsible must be greater than are suggested in figure 6.5, etc – in other words, the true distribution of cores registering CS (J=2→1) emission may be more like that shown by CO (particularly that in figure 6.5). Since Morata *et al.* (2003) ruled out

Table 6.5: Peak Column Densities for Maps of Various Levels of Uniformity of Core Distribution

Molecule	Transition	Distribution	x (pc)	y (pc)	$N[i]$ † (cm^{-2})
CO (Peak K)	—	1	0.048	0.240	1.4(18)
		2	0.186	0.456	1.5(18)
		3	0.390	0.210	2.0(18)
CS (Peak L)	J=2→1	1	0.048	0.246	6.8(14)
		2	0.090	0.030	6.1(14)
		3	0.390	0.210	1.0(15)
HCO^+ (Peak M)	J=1→0	1	0.378	0.060	1.7(13)
		2	0.384	0.480	2.5(13)
		3	0.066	0.486	2.0(13)
NH_3 (Peak N)	(1,1)inv	1	0.066	0.168	2.9(14)
		2	0.384	0.474	3.2(14)
		3	0.480	0.294	3.0(14)

† $a(b) = a \times 10^b$

large extended regions of emission, it is likely to be caused by a different *average* column density profile. This may either be due to a different chemistry giving different CS levels through a core's evolution, or it may be the effect of a spectrum of cores being present in a dark cloud (as mentioned in the previous section), such that the combination of the slightly different chemistries of each core re-weights the overall profile.

Either way, if CS is in reality better represented by the sort of map coverage that CO shows thanks to its gently evolving column density profile, we might expect that, judging by contour morphologies, the east (E) and west (W) peaks of figures 5.4 – 5.6 (from Morata *et al.* 2003) which are the strongest in CS (J=2→1), should be the result of core associations, whereas the emission around the north (N) peak should be perhaps two individually strong cores, convolved together in CS (J=2→1) emission. This should also be the case with the region of emission in the NW corner of the map. The lobed areas could be the result of larger, less strongly emitting associations of cores. Judging from the synthesised CO maps, these associations might also be aided by the emission from the edges of the strong cores at the central peaks. The CS emission map of Morata *et al.* (2003) appears to match best with the high level of uniformity shown in the CO map of figure 6.5. Meanwhile, the observed HCO^+ (J=1→0) emission of that paper is characterised well by that of HCO^+ in figure 6.5. Most peaks are sharp, and do not deviate strongly from regular (*i.e.* circular) shapes, whilst there are some regions where the peaks are "connected". This should indicate that the cores which register in HCO^+ are well spaced, and regularly spaced. These characteristics may be more achievable because of a smaller

emitting region within each core for HCO^+ (as suggested in the previous section), which would make those emissions more easily resolved individually.

The NH_3 maps of this section do not appear to vary much with the level of uniformity of core distribution, as the NH_3 column density profile of the standard core is quite sharp, leaving the few strong emitters quite sparsely distributed.

Table 6.5 shows column densities at the peak positions for each molecule. We might say that there is a slight trend for levels to be higher for lower uniformity of core distributions, but this is only consistently true for CO. However, this does suggest firstly that the levels obtained from observations are quite robust with respect to the pattern of core distribution, and secondly that the discrepancy of CS/NH_3 column densities (described in the previous section of this chapter) compared to observations is not likely to be resolved by consideration of such effects. It should be noted, however, that the table gives details of the strongest peak in each map, which is not always the same one as for other distributions. Hence the levels really represent more of an upper limit. Because each of these peak levels represents an association of cores, these levels should also not necessarily be relied upon to provide accurate column density estimates for individual cores.

6.6.2 Conclusions

The level of uniformity of core distribution, and in general the way cores are distributed in a dark cloud, is clearly a crucial element in producing the morphologies seen in observational work. This factor acts in combination with the physical sizes of the cores, and the beam resolution, to determine the way and the extent to which emission from individual cores overlaps and convolves together.

Although this variable is difficult to treat in such a way that we may meaningfully compare different arrangements of cores, we may draw some conclusions which obviously are to some degree dependent on the specific cases modelled here. (We might, for example, achieve slightly different results by using a different distribution of core evolution times, or a different permutation of their arrangement in each spatial position, so that spatial core associations were composed of cores in different stages of evolution from those in another permutation).

We find that for CO, and by extension, for transitions whose contributors are generally quite closely spaced, that emission peaks with tightly spaced contours tend to be caused by close associations of cores, whereas those with weaker, more broadly spaced contours

usually represent one core, or perhaps one strong emitter and one weak.

For transitions whose emitters are widely spaced, peak contours tend to be quite tight, and morphologically, the ratio of stronger to weaker peaks tends to increase with decreasing uniformity of distribution.

We find that the morphologies observed in Morata *et al.* (2003) for CS (J=2→1) most closely resemble the morphologies of CO, particularly for the most uniform distribution, meaning that CS cores are not excessively clustered in L673, and that the contributing cores in that region are probably more numerous than is assumed in this model. The most probable explanation for this is that there are a number of inherently more weakly emitting cores in this region, which have different physical conditions from those modelled in the standard model run, such that at peak density they contribute slightly less CS emission than the standard run, but far less of other molecular lines.

From the above-mentioned similarity between CO in this study and CS in Morata *et al.* (2003), and the trends as to which emission peaks are caused by associations or individual cores, may infer that the E and W CS (J=2→1) peaks of Morata *et al.* (2003) are more likely to be the result of core associations, whilst the emission at N may come from two underlying cores.

More generally we find, from the column densities obtained at the peaks of the synthetic maps, that the absolute levels obtained from observations are quite robust with respect to the pattern of core distribution, and that the CS/NH_3 discrepancy in column densities compared with the Morata *et al.* papers is unlikely to be resolved by such considerations.

6.7 Molecular Line Maps with Different Grain Mantle Re-injection Characteristics

In this section I briefly contrast the results of section 6.5, in which the modified convolution approach was applied to the basic "sky" map of chapter 5, with those which are obtained here by using column density profiles with a minimal contribution from the re-injection of dust grain mantles. As mentioned in section 6.4, this is achieved merely by integrating the raw column density profiles between the points immediately before and after each re-injection peak. Figure 6.8 shows the resultant column density profiles for molecules in the five transitions previously studied. I apply these profiles to the same basic "sky" map.

Figure 6.8: Column densities of selected transitions as functions of time, with n_{eff} considerations, calculated through the standard run core – minimal re-injection

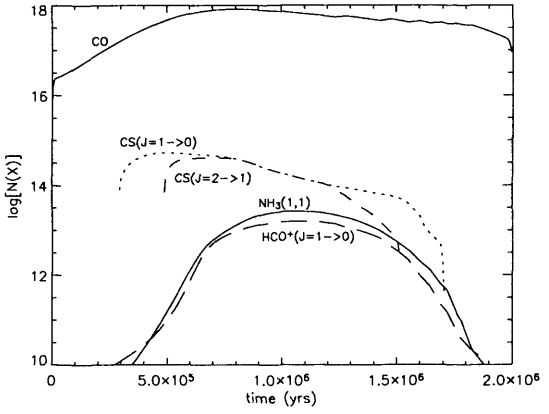

6.7.1 Results and Discussion

Figure 6.9 shows the low resolution maps obtained using the column density profiles with minimal re-injection. CO is very little changed, since its profile is largely unaffected. All other molecular transitions assume smaller spatial morphologies; most strongly affected is the NH_3 morphology. It not only assumes a smaller spatial extent but maps different material from the maximal re-injection case. The regions it now maps are very similar to those traced by HCO^+ (J=1→0). The shrinking of NH_3 (1,1) extent relative to CO and CS (J=1→0), and the shrinking of both NH_3 (1,1) and CS (J=1→0) extents relative to CO makes the behaviour of the minimal re-injection maps more in keeping with Myers *et al.* (1991) than the maximal re-injection case. The regions mapped by transitions other than NH_3 (1,1) are essentially unchanged.

Figure 6.10 shows the high resolution maps zoomed-in on the same region as used previously. As before, the diamond-shaped markers represent high resolution peaks (for transitions indicated in table 6.6), whilst the square-shaped markers indicate the low resolution peak *local within the zoomed-in region* for the transition surveyed in each map. Again, the differences are slight compared to the maximal re-injection case for all species but NH_3; for example the CS (J=1→0) and CS (J=2→1) peaks now exactly coincide, and the regions mapped and their spatial extents are almost identical to their high re-injection counterparts. Now, rather than mapping its own distinct regions, NH_3 maps very similar regions to HCO^+ (J=1→0) as at low resolution. Therefore, a test of this extreme of

Table 6.6: Peak Column Densities for Low Re-injection Synthetic Maps

Molecule	Transition	x (pc)	y (pc)	$N[i]$ † (cm^{-2})	Peak ‡
CO	—	0.68	0.40	5.9(17)	Lo Res
		0.74	0.46	2.2(18)	**Hi – Q**
		0.87	0.38	1.4(18)	Hi – R
		0.65	0.71	1.2(18)	Hi – S
		0.60	0.70	1.3(18)	Hi – T
CS	J=1→0	0.76	0.42	2.3(14)	Lo Res
		0.74	0.46	8.5(14)	Hi – Q
		0.87	0.38	8.7(14)	**Hi – R**
		0.65	0.71	2.4(14)	Hi – S
		0.60	0.70	3.3(14)	Hi – T
CS	J=2→1	0.72	0.42	1.8(14)	Low Res
		0.74	0.46	7.6(14)	**Hi – Q**
		0.87	0.38	5.1(14)	Hi – R
		0.65	0.71	2.4(14)	Hi – S
		0.60	0.70	3.3(14)	Hi – T
HCO^+	J=1→0	0.66	0.72	7.5(12)	Low Res
		0.74	0.46	2.5(13)	Hi – Q
		0.87	0.38	1.4(13)	Hi – R
		0.65	0.71	2.8(13)	**Hi – S**
		0.60	0.70	2.8(13)	Hi – T
NH_3	(1,1)inv	0.66	0.72	1.2(13)	Low Res
		0.74	0.46	4.1(13)	Hi – Q
		0.87	0.38	2.3(13)	Hi – R
		0.65	0.71	4.7(13)	Hi – S
		0.60	0.70	4.8(13)	**Hi – T**

† $a(b) = a \times 10^b$

‡ Low resolution peak positions are different for each transition. High resolution peaks in bold correspond to the peak in the given transition.

re-injection would be whether or not HCO^+ and NH_3 appear to map the same regions.

Table 6.6 shows peak column densities measured at the (local) low resolution peaks and the high resolution peaks labelled Q,R,S,T. Of the low resolution peak levels, only that of NH_3 is significantly different, down by a factor of almost 7. The high resolution NH_3 peak level is also down by a similar amount. Both these differences are easily explained by the lower peak level in the NH_3 (1,1) column density profile. The lower levels of NH_3 are evidence against the minimal re-injection case, since they further lower the ratio with CS, which was determined to take a value of around 10 by Morata *et al.* (1997) and Morata *et al.* (2003).

Comparing high resolution peaks with their equivalents in the maximal re-injection case for the same transitions, there is little else of note. However, differences between the two cases are slightly more apparent when comparing levels in one transition at the peak positions of another; for example, CS (J=2→1) levels are 3 times higher for the low

Figure 6.9: Trimmed map – low resolution, modified approach, minimal re-injection

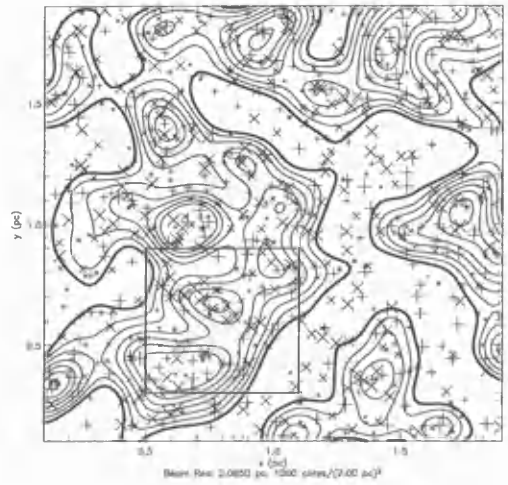

a: CO

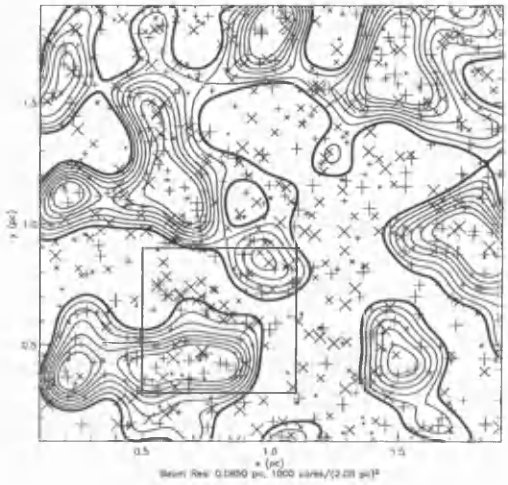

b: CS (J=1→0)

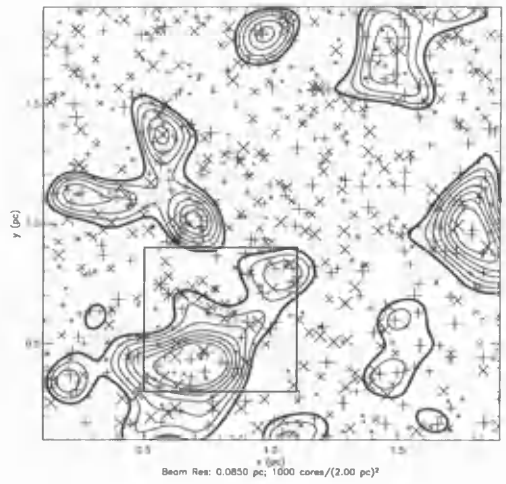

c: CS (J=2→1)

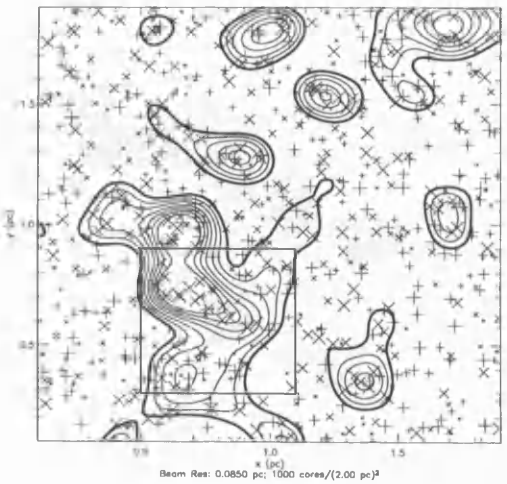

d: HCO^+ (J=1→0)

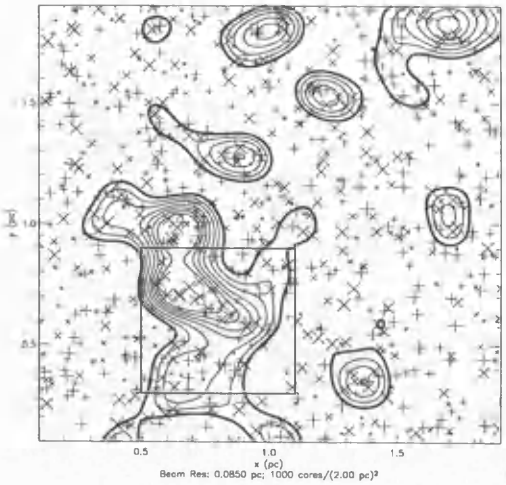

e: NH_3 (1,1)inv

Figure 6.10: Close-up map – high resolution, modified approach, minimal re-injection

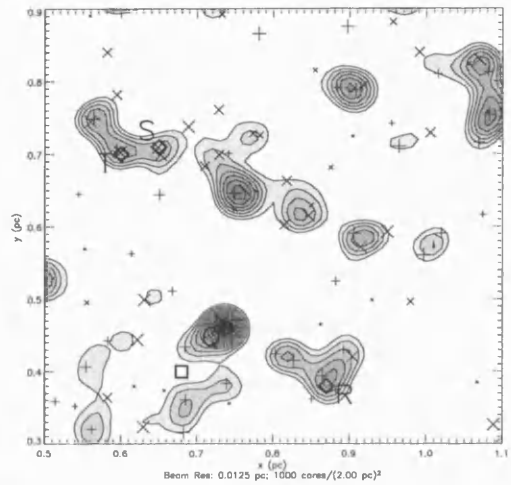

a: CO

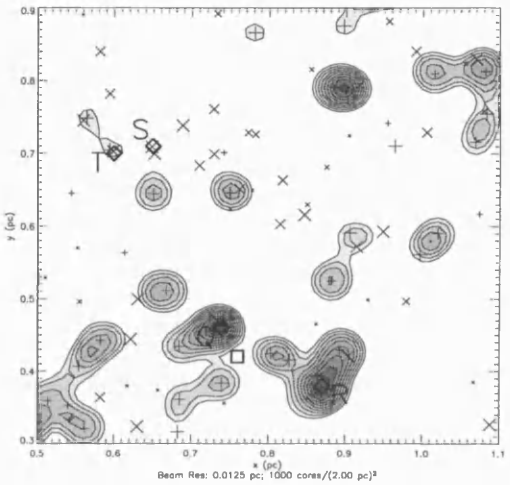

b: CS (J=1→0)

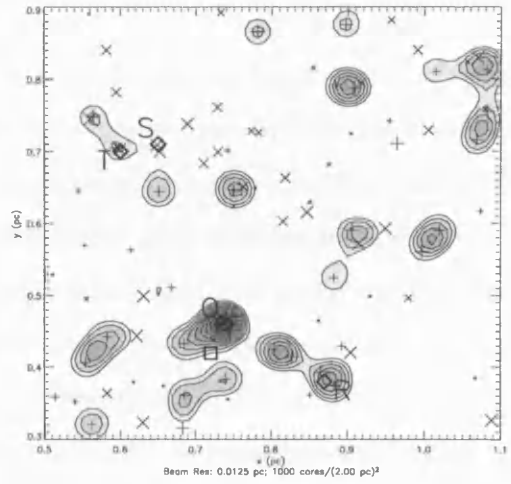

c: CS (J=2→1)

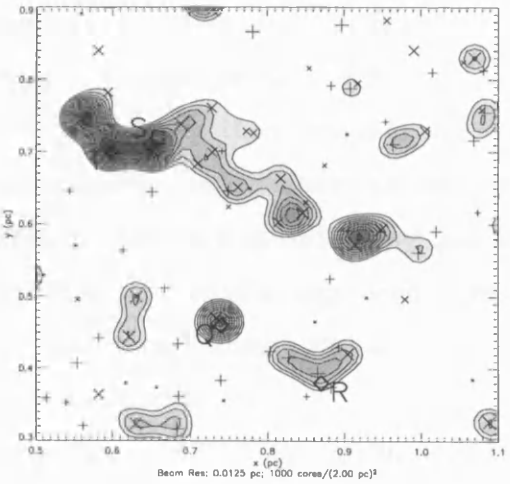

d: HCO^+ (J=1→0)

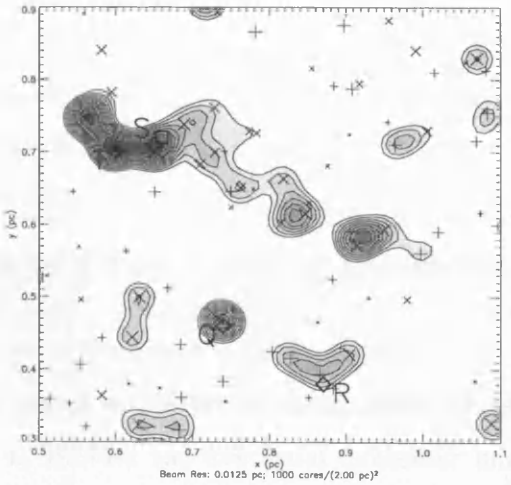

e: NH_3 (1,1)inv

re-injection case, measured at peaks T and D – the respective NH_3 high resolution peaks for low and high re-injection features. This difference is due to NH_3 (1,1) now assuming a column density profile whose peak is closer in time to that of CS (J=2→1).

6.7.2 Conclusions

As mentioned previously, the minimal re-injection case is a representation of the situation where the rate of deposition of grain mantle-bound species is so slow compared to the rate of destruction of injected species by the gas phase chemistry that there is no discernible difference in the resultant column density measured through the core. Conversely, the maximal case represents a situation where deposition is so fast that gas phase destruction cannot keep up, such that there is a local spike in fractional abundances which manifests itself in the calculated column densities.

All of the evidence of this section confirms what may be seen from the column density profiles of figures 6.1b and 6.8: namely that NH_3 is by far the most strongly affected of the molecular transitions for the minimal re-injection case. The morphological differences seen in the maps are more in line with observations than are those for the maximal re-injection case, however, the absolute NH_3 peak levels are less consistent with measured values. Since the absolute NH_3 column densities are a more robust measure, it is more likely that the morphologies exhibited in Myers *et al.* (1991) *etc* are the product of a range of chemistries engendered by a spectrum of cores in dark clouds, as already discussed, rather than being explained purely by the adoption of the minimal re-injection profile.

The level of morphological coincidence between NH_3 and HCO^+ in particular would be a useful test of the level of coupling of their chemistries, with different re-injection levels being one possible cause for discrepancies. The inclusion of more molecular transitions in the convolution model could help to constrain both the way in which re-injection takes place (its rates and critical visual extinction) and the relative time-dependent chemical behaviours of cores within any re-injection regime.

6.8 The Effects of Core Cycling on Molecular Line Maps

Finally, in this section I contrast the results of section 6.5, which used the standard core model, with those which are obtained using "limit cycle" column density profiles obtained from chapter 4. Besides the five usual molecular line transitions, I map three

Figure 6.11: Column densities of selected transitions as functions of time, with n_{eff} considerations, calculated through the standard run core – limit cycle chemistry

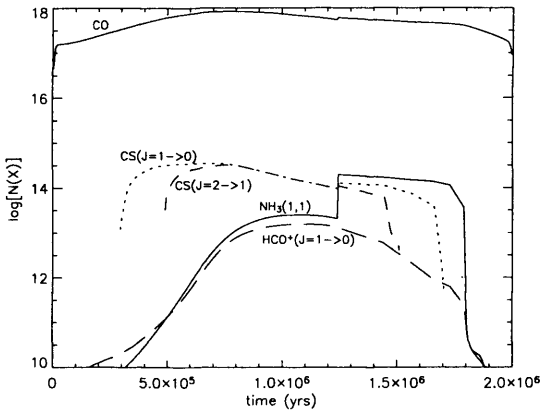

other molecules: SO, SO_2 and CH_4. These were three of a small number of molecules which the results of chapter 4 suggested could be used to distinguish a cloud with significant cycling, versus a cloud without. However, since effective critical density information is only forthcoming for those transitions already shown in table 6.1, I merely assume the same critical density as for CO of 1000 cm^{-3} for these three other molecules (which represents an absolute minimum level). It may be remembered that $N(H_2CO)$ also showed significant differences between the standard and limit cycle cases, however the value of $n_{eff}(H_2CO) = 6 \times 10^4$ cm^{-3} for the $2_{12} \rightarrow 1_{11}$ transition quoted in Evans (1999), the lowest n_{eff} value listed for H_2CO, is too low to contribute any detectable emission using the peak density of 5×10^4 cm^{-3} adopted for the two models (where detectable emission is deemed to constitute a line of 1 K or more). I initially return to the maximal re-injection column density profiles for this analysis, a case which is more likely to obtain according to the evidence of section 6.7. I then look at the case of a minimal re-injection feature.

6.8.1 Results and Discussion

Figure 6.11 shows the column density profiles of the five main transitions previously mapped, for the "limit cycle" case (which is effectively reached by cycle number three; for certainty I use cycle number five, the fourth after the standard run). See chapter 4 for details of the dynamics and chemistry of the limit cycle. Notably, here CO starts higher than in the standard run, and the peak column densities for the CS transitions are a little lower. NH_3 and HCO^+ profiles are not strongly affected.

Figure 6.12: Trimmed map – low resolution, modified approach, limit cycle chemistry

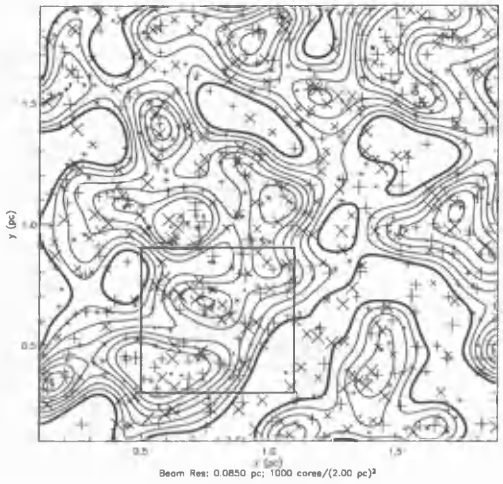

a: CO

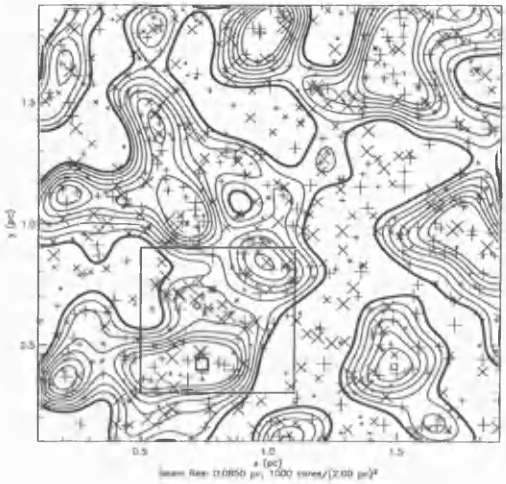

b: CS (J=1→0)

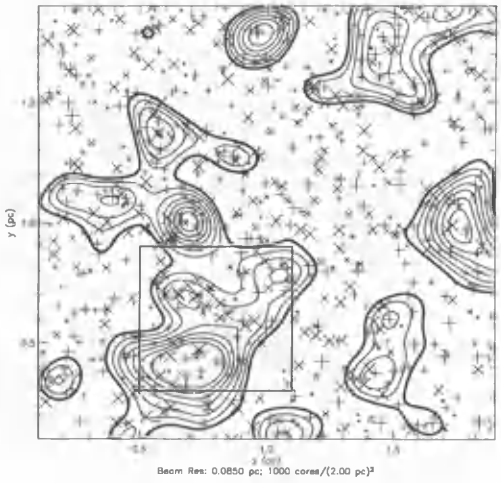

c: CS (J=2→1)

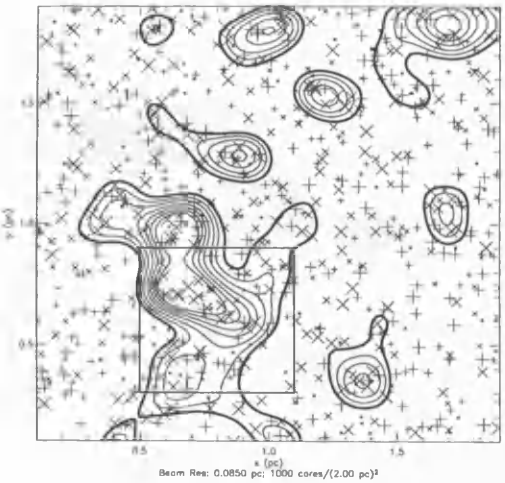

d: HCO^+ (J=1→0)

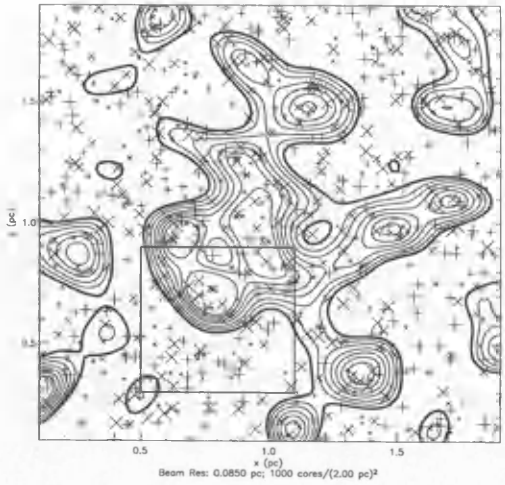

e: NH_3 (1,1)inv

Figure 6.13: Close-up map – high resolution, modified approach, limit cycle chemistry

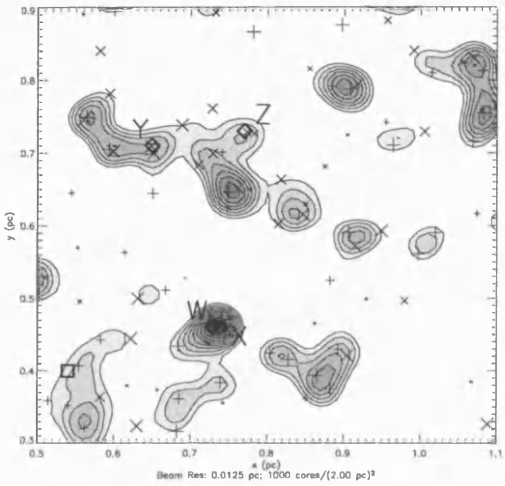

a: CO

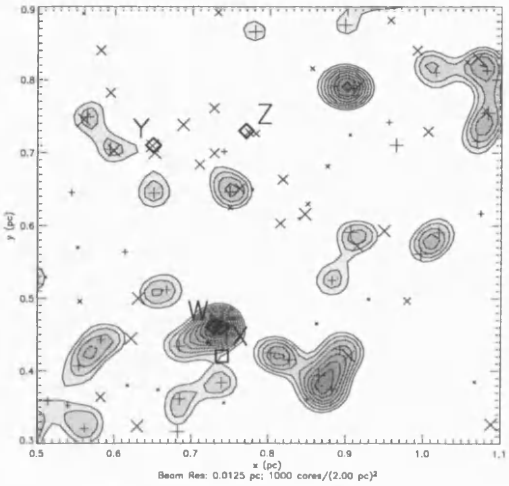

b: CS (J=1→0)

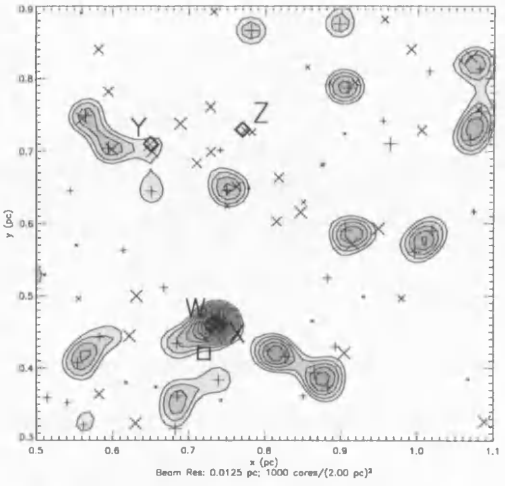

c: CS (J=2→1)

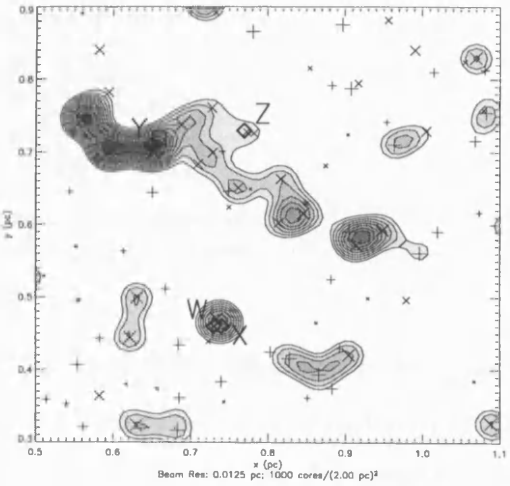

d: HCO^+ (J=1→0)

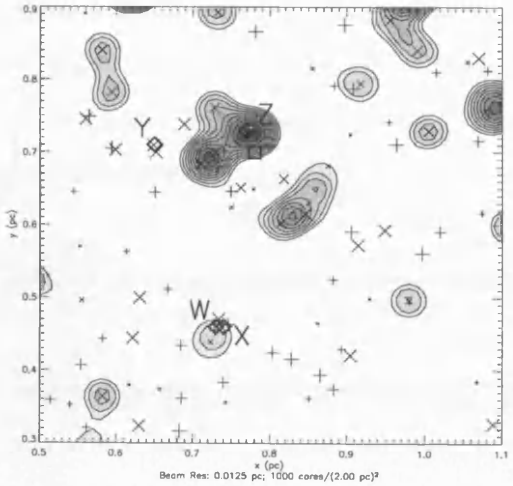

e: NH_3 (1,1)inv

Table 6.7: Peak Column Densities for Limit Cycle Maps

Molecule	Transition	x (pc)	y (pc)	$N[i]$ † (cm^{-2})	Peak ‡
CO	—	0.54	0.40	6.9(17)	Lo Res
		0.73	0.46	2.3(18)	**Hi – Q**
		0.74	0.46	2.3(18)	Hi – R
		0.65	0.71	1.3(18)	Hi – S
		0.77	0.73	1.1(18)	Hi – T
CS	J=1→0	0.74	0.42	1.8(14)	Lo Res
		0.73	0.46	7.1(14)	Hi – Q
		0.74	0.46	7.1(14)	**Hi – R**
		0.65	0.71	2.4(14)	Hi – S
		0.77	0.73	2.1(14)	Hi – T
CS	J=2→1	0.72	0.42	1.4(14)	Low Res
		0.73	0.46	5.8(14)	Hi – Q
		0.74	0.46	6.0(14)	**Hi – R**
		0.65	0.71	2.4(14)	Hi – S
		0.77	0.73	1.0(14)	Hi – T
HCO^+	J=1→0	0.66	0.72	7.3(12)	Low Res
		0.73	0.46	2.3(13)	Hi – Q
		0.74	0.46	2.4(13)	Hi – R
		0.65	0.71	2.8(13)	**Hi – S**
		0.77	0.73	1.1(13)	Hi – T
NH_3	(1,1)inv	0.78	0.70	8.2(13)	Low Res
		0.73	0.46	1.5(14)	Hi – Q
		0.74	0.46	1.4(14)	Hi – R
		0.65	0.71	4.5(13)	Hi – S
		0.77	0.73	3.2(14)	**Hi – T**

† $a(b) = a \times 10^b$

‡ Low resolution peak positions are different for each transition. High resolution peaks in bold correspond to the peak in the given transition.

The low resolution maps of figure 6.12 are therefore little affected by the change, except for CO, which assumes broader profiles and achieves greater map coverage due to the higher levels for cores at the start of their evolution. Whilst the extents of the other molecules change slightly on a local level, throughout each map they are on average unaltered. All the transitions still map the same regions as for the standard run case.

The same may be said of the high resolution maps of figure 6.13; the CO map is more extended, and lobing between peaks is marginally more pronounced. However, none of the maps show any drastic differences and certainly do not map different regions from the standard case.

Hence there are no obvious morphological differences which may be exploited to distinguish the two cases.

Table 6.7 shows the column density values obtained for the low and high resolution peaks indicated in the high resolution maps. Again, there are few differences between these

Figure 6.14: Column densities of selected transitions as functions of time – standard chemistry and limit cycle chemistry

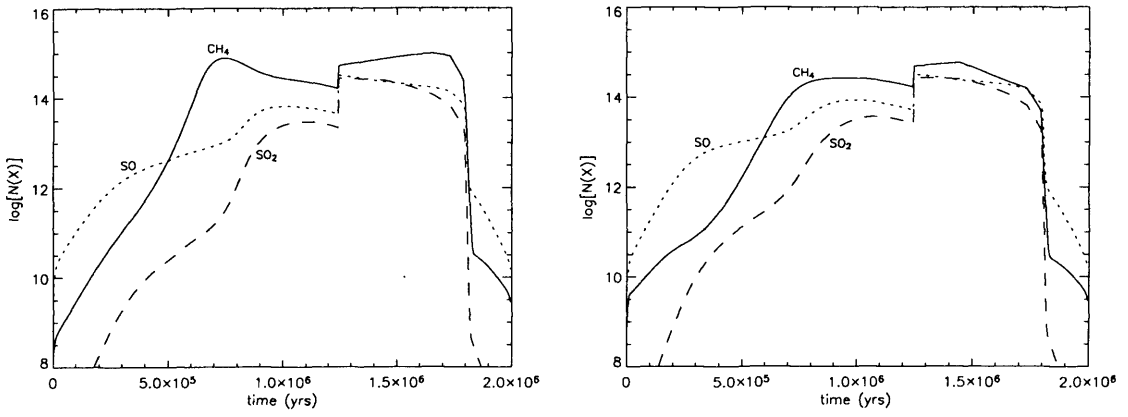

a: Standard Run b: Limit Cycle Run

and the standard case values. CO and NH_3 show small increases in the low resolution peak values; the other molecules show slight decreases. The CS transitions generally show the greatest variation for the high resolution values. However, none of the differences in high or low resolution peaks is significant enough to distinguish observationally the standard case from the limit cycle case. Therefore, we should not expect to gain any information on this issue from the Morata *et al.* observations.

I now investigate any differences between the models for the molecules SO, SO_2 and CH_4, in particular to test whether the ratios suggested for these molecules at the "shoulder" feature discussed in chapter 4 propagate effectively enough through the convolution process to distinguish the two cases. It should be noted that since CH_4 has no dipole moment, observing it is made very difficult. However, I treat the CH_4 as more of a representative species – a hydrocarbon to represent the hydrocarbon shoulder. In future work, with more effective critical density information, I should be able to investigate more easily observed molecules.

Figure 6.14 shows the column density profiles for the three molecules, for both the standard run and the limit cycle. The major difference between the two runs for these molecules is the greater contrast between CH_4 levels with the other two molecules, at the time CH_4 peaks in the standard core's evolution. The other notable difference is the higher level of late-time re-injection in the standard run, for CH_4.

Figure 6.15 shows the standard run high resolution maps, figure 6.16 the limit cycle maps. For SO and SO_2 there are no notable morphological differences, due to the similarity

Figure 6.15: Close-up map – high resolution, modified approach, standard chemistry

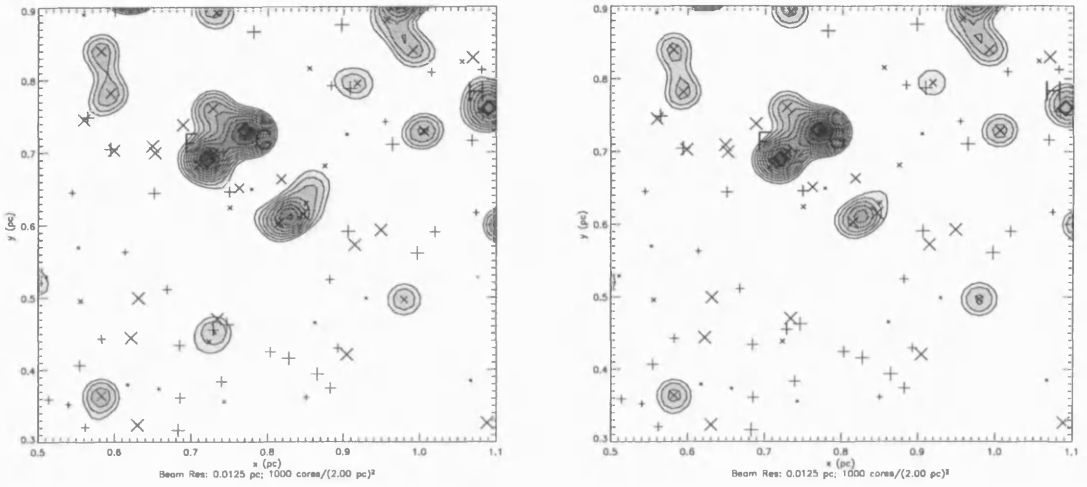

a: SO b: SO_2

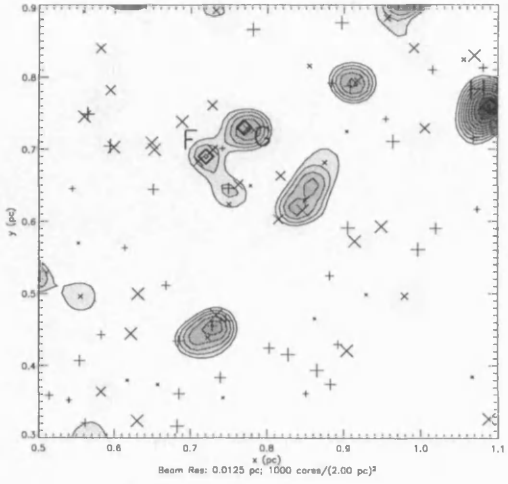

c: CH_4

of the profile shapes, regardless of their absolute levels.

The CH_4 morphologies differ drastically. Whilst in the limit cycle case, CH_4 maps mostly the same regions as SO and SO_2, for the standard run, CH_4 maps somewhat different regions, though a lot of the same peaks are present. This differentiation may be a practical tool to determine which regime obtains in real dark cloud regions.

Tables 6.8 and 6.9 show SO, SO_2 and CH_4 levels determined for the peaks indicated in the standard and limit cycle maps respectively. Note that the CH_4 peaks in one case do not correspond to the peaks in the other.

It is only the CH_4 values which vary in any significant way, by a factor of two at most.

Figure 6.16: Close-up map – high resolution, modified approach, limit cycle chemistry

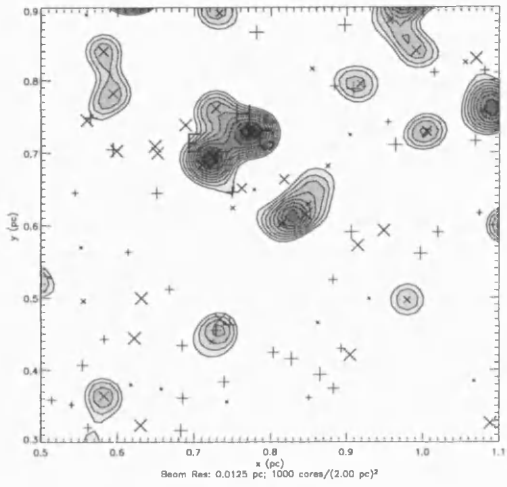

a: SO

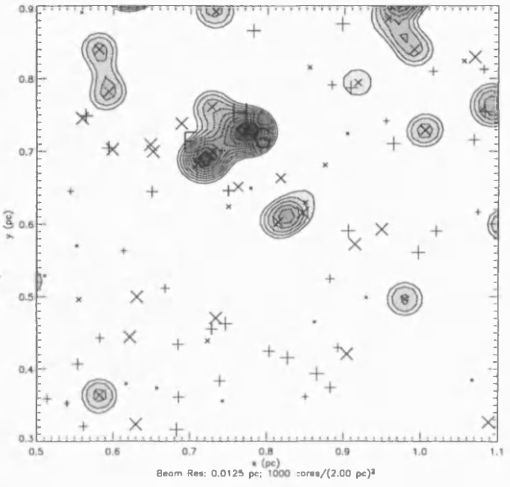

b: SO_2

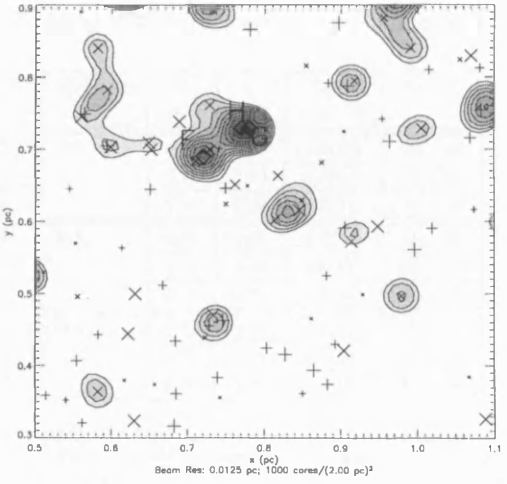

c: CH_4

There is one interesting feature that may just be significant enough for detection, however: The ratio of CH_4 at the CH_4 peak to CH_4 at the SO peak is almost a factor of two larger for the standard run. This might provide stronger evidence than absolute CH_4 peak values alone. However, the observational errors would have to be small to distinguish these cases, and would more likely be swamped by the effects of departures from the precise physical and chemical parameters chosen for this study. The relative influences of cores across any putative spectrum of cores would also affect the measurement of this ratio.

Table 6.10 shows molecular ratios at each peak, and the ratios of these between the standard and limit cycle cases. Unfortunately, the large ratios forecast in chapter 4 do

Table 6.8: Peak Column Densities for Standard Maps

Molecule	x (pc)	y (pc)	$N[i]$ † (cm^{-2})	Peak ‡
SO	0.72	0.69	4.7(14)	**Hi – F**
	0.77	0.73	4.4(14)	Hi – G
	1.09	0.76	3.8(14)	Hi – H
SO_2	0.72	0.69	4.5(14)	Hi – F
	0.77	0.73	4.7(14)	**Hi – G**
	1.09	0.76	2.9(14)	Hi – H
CH_4	0.72	0.69	1.1(15)	Hi – F
	0.77	0.73	1.4(15)	Hi – G
	1.09	0.76	2.2(15)	**Hi – H**

† $a(b) = a \times 10^b$

‡ Peaks in bold correspond to the peak in the given transition.

Table 6.9: Peak Column Densities for Limit Cycle Maps

Molecule	x (pc)	y (pc)	$N[i]$ † (cm^{-2})	Peak ‡
SO	0.72	0.69	4.8(14)	**Hi – F**
	0.77	0.73	4.6(14)	Hi – G
	0.78	0.73	4.6(14)	Hi – H
SO_2	0.72	0.69	4.6(14)	Hi – F
	0.77	0.73	4.7(14)	**Hi – G**
	0.78	0.73	4.7(14)	Hi – H
CH_4	0.72	0.69	9.5(14)	Hi – F
	0.77	0.73	1.1(15)	Hi – G
	0.78	0.73	1.1(15)	**Hi – H**

† $a(b) = a \times 10^b$

‡ Peaks in bold correspond to the peak in the given transition.

Table 6.10: Ratios of Peak Column Densities

Molecular Ratio	R_{stan} †	R_{lim} †	R_{stan}/R_{lim}	Peak
CH_4:SO	2.34	1.98	1.18	Hi – F
	3.18	2.39	1.33	Hi – G
	5.79	2.39	2.42	Hi – H
CH_4:SO_2	2.44	2.07	1.18	Hi – F
	2.98	2.34	1.27	Hi – G
	7.59	2.34	3.24	Hi – H

† $R = N[i]/N[j]$

Figure 6.17: Column densities of selected transitions as functions of time – standard chemistry and limit cycle chemistry, minimal re-injection

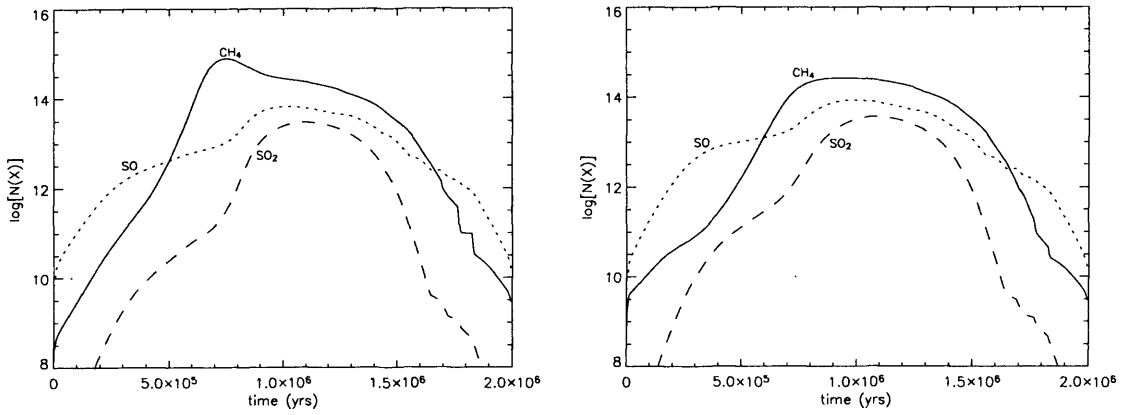

a: Standard Run b: Limit Cycle Run

not propagate through to the convolved maps. The greatest ratio between the standard and limit cycle cases is a little over 3 for CH_4:SO_2, at the CH_4 peak. Although better than the CH_4 ratios between CH_4 and SO peaks, this would still make it very difficult to distinguish the two cases observationally. Since the ratios predicted in chapter 4 are for cores at the pre-peak density CH_4 peak (the "shoulder"), choosing points in the map other than the CH_4 peak at which to determine "detected" column densities would not produce better results.

We may observe, however, that the CH_4 peak takes a different position for the limit cycle case compared to the standard run case. This is because in the limit cycle case, the "shoulder" CH_4 column density value is lower than that at the re-injection peak, so that re-injection enhanced cores are favoured. Hence the CH_4 limit cycle peak also assumes different, high, SO and SO_2 levels, skewing the ratio between the two. We could always compare the same map positions in each case, to try to produce the correct CH_4:SO and CH_4:SO_2 ratios, however this rather defeats the object, which is to provide an observational means of distinguishing the two cases. For the approach to be consistent when dealing only with one set of real observational data, we must look at the levels at the CH_4 peak. So, in the situation where the re-injection feature of the column density profiles is maximal (or at least fairly high), we should not expect to be able to ascertain whether core cycling is taking place or not.

With this limitation in mind, I now investigate whether the two cases may be distinguished in the situation where the re-injection feature is minimal. Figure 6.17 shows the

Figure 6.18: Close-up map – high resolution, modified approach, standard chemistry, minimal re-injection

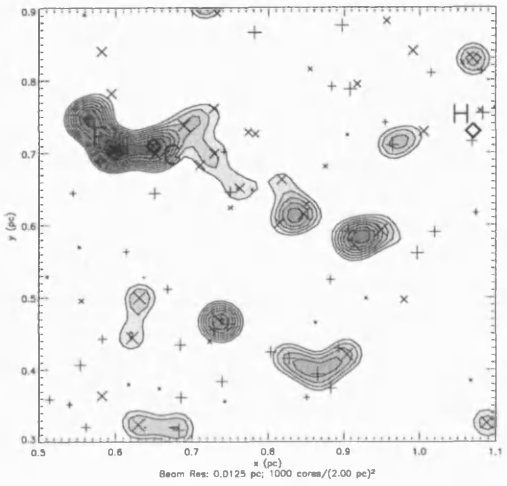

a: SO

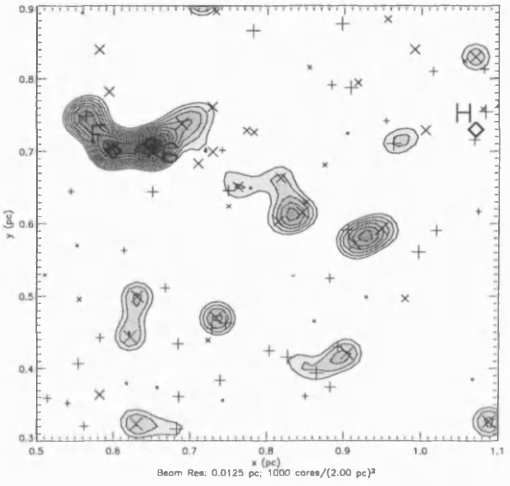

b: SO_2

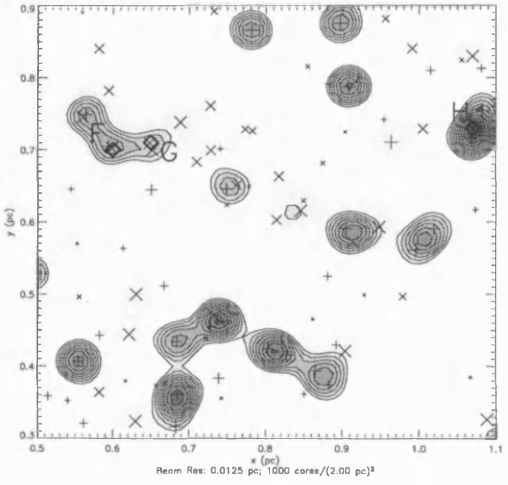

c: CH_4

resultant column density profiles for SO, SO_2 and CH_4 for each case. I do not show the CO, CS, HCO^+ or NH_3 maps, as they do not vary significantly between the standard and limit cycle cases. The slight kinks at late times in the CH_4 column density profiles are smoothing errors, but are at low enough levels to be wholly insignificant. We see from the profiles that the pre-peak density "shoulder" chemistry should now dominate for the standard run case. In the limit cycle case, all three molecules now peak at approximately the same stage of core evolution, around the peak density time, t_m.

Figures 6.18 and 6.19 show high resolution standard run and limit cycle maps, respectively. For maximal re-injection, standard run CH_4 mapped somewhat different regions

Figure 6.19: Close-up map – high resolution, modified approach, limit cycle chemistry, minimal re-injection

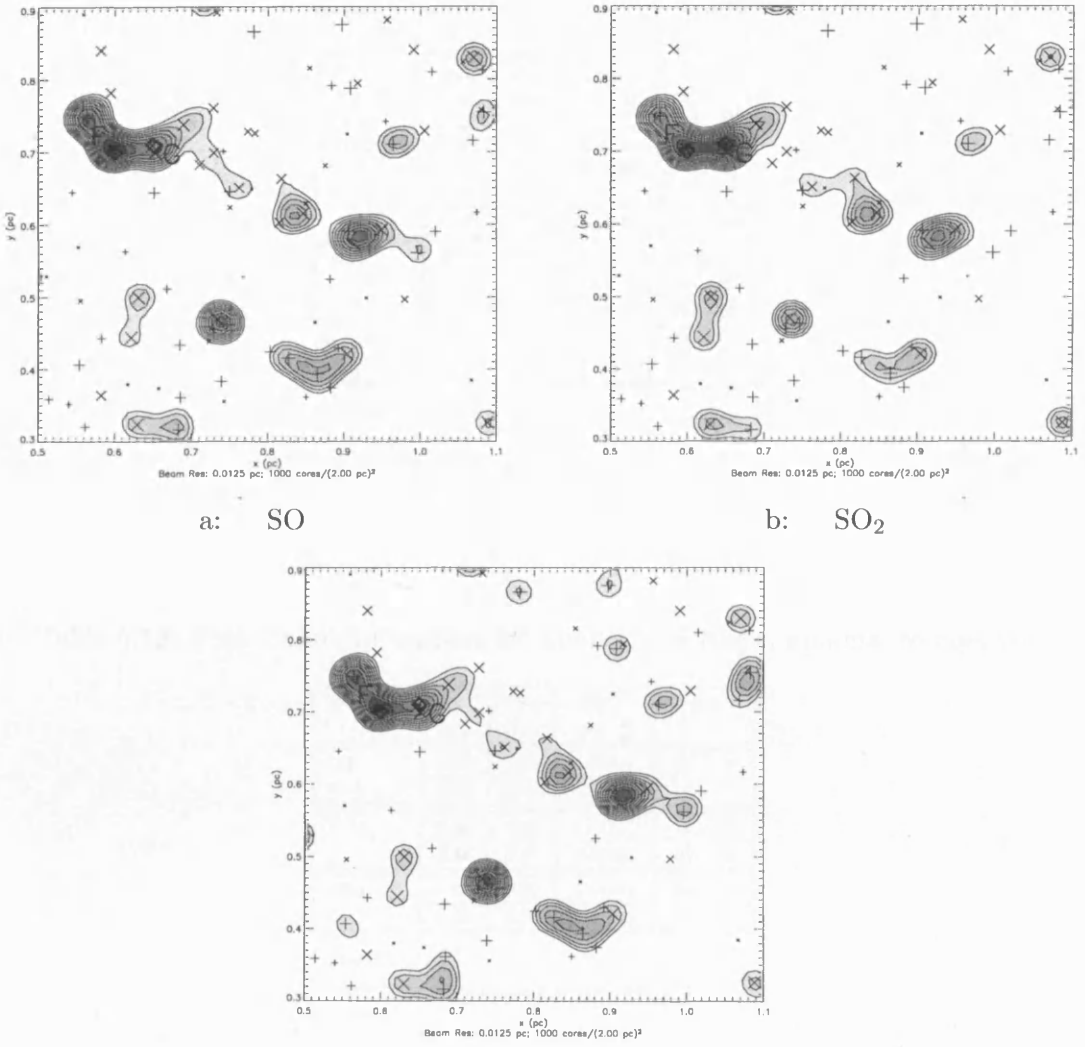

a: SO b: SO_2

c: CH_4

to the other two molecules. For the minimal re-injection case this is also true. As was seen previously, in the case of the limit cycle, all three molecules map the same regions as each other (but not the same regions as were mapped for the maximal re-injection case), although CH_4 does pick up a few weaker cores which SO and SO_2 do not.

Tables 6.11 and 6.12 show column densities obtained at the peaks, for the standard run and limit cycle cases, respectively. Note that SO and CH_4 share their peak positions at point F for the limit cycle case. In the standard run case, the CH_4 peak, point H, is far from the SO and SO_2 peaks. The obtained column density values show clearly the impact of the standard run CH_4 "shoulder". Whilst the values at the SO and SO_2 peaks vary by

Table 6.11: Peak Column Densities for Standard Maps, minimal re-injection

Molecule	x (pc)	y (pc)	$N[i]$ † (cm^{-2})	Peak ‡
SO	0.60	0.70	1.2(14)	**Hi – F**
	0.65	0.71	1.1(14)	Hi – G
	1.07	0.73	2.8(13)	Hi – H
SO_2	0.60	0.70	4.7(13)	Hi – F
	0.65	0.71	5.2(13)	**Hi – G**
	1.07	0.73	2.6(12)	Hi – H
CH_4	0.60	0.70	5.0(14)	Hi – F
	0.65	0.71	4.0(14)	Hi – G
	1.07	0.73	8.1(14)	**Hi – H**

† $a(b) = a \times 10^b$

‡ Peaks in bold correspond to the peak in the given transition.

Table 6.12: Peak Column Densities for Limit Cycle Maps, minimal re-injection

Molecule	x (pc)	y (pc)	$N[i]$ † (cm^{-2})	Peak ‡
SO	0.60	0.70	1.6(14)	**Hi – F**
	0.65	0.71	1.3(14)	Hi – G
SO_2	0.60	0.70	6.2(13)	Hi – F
	0.65	0.71	6.3(13)	**Hi – G**
CH_4	0.60	0.70	4.8(14)	**Hi – F**
	0.65	0.71	4.1(14)	Hi – G

† $a(b) = a \times 10^b$

‡ Peaks in bold correspond to the peak in the given transition.

Table 6.13: Ratios of Peak Column Densities, minimal re-injection

Molecular Ratio	R_{stan} †	R_{lim} †	R_{stan}/R_{lim}	Peak
CH_4:SO	4.15	3.07	1.35	Hi – F
	3.78	3.17	1.19	Hi – G
	29.2	3.07	9.51	Hi – H, F
CH_4:SO_2	10.7	7.77	1.38	Hi – F
	7.78	6.53	1.19	Hi – G
	309	7.77	39.7	Hi – H, F

† $R = N[i]/N[j]$

small amounts between the two cases, the differences at the CH_4 peaks are very significant. Table 6.13 shows the molecular ratios obtained at each indicated peak for either case, and their ratios between the two cases. CH_4:SO is almost an order of magnitude greater at the standard run CH_4 peak than at its SO or SO_2 peaks. The standard run CH_4:SO peak level is an order of magnitude greater than for the limit cycle case. This large a difference should be observationally determinable. Meanwhile, CH_4:SO_2 for the standard run is immense compared to other values, at approximately 300. When measuring this ratio with real data, the R_{stan}/R_{lim} ratio for CH_4:SO_2 of about 40 should be determinable one way or the other.

Hence, when the re-injection feature of column density profiles is minimal, we should expect that the relative column densities of CH_4 and SO/SO_2 should be quite precise enough to determine whether core cycling is taking place as defined in chapter 4. We might expect, however, that any scenario where the re-injection feature is significantly less than the maximum value, leaving the pre-peak density CH_4 peak ("shoulder") dominant, would allow for the spatial differentiation of CH_4 and SO/SO_2, and would make a survey of molecular line stregths at CH_4 peaks an effective way of determining the frequency of cycling in the gas.

6.8.2 Conclusions

In keeping with the purely chemical analysis of the limit cycle of chapter 4, we find that the five transitions listed in table 6.1 are little affected by the implementation of such column density profiles into the same map as was examined using the standard run profiles. Hence there should be no useful information on this topic to be gained from the Morata *et al.* papers.

We find that in a maximal re-injection scenario, the limit cycle is not easily distinguishable from the standard run case. The extents of the molecular morphologies do not provide evidence for one or other case, although in the limit cycle case, CH_4 maps the same regions as SO and SO_2, whereas in the standard run case it does not. The peak column density values show perhaps marginally detectable differences between the two cases.

Conversely, in the minimal re-injection scenario the peak column density levels, particularly of CH_4, vary greatly between the standard run and limit cycle cases. The ratio of CH_4:SO_2 at the CH_4 peak is a factor of $\sim$40 greater in the standard run case, a difference

which should certainly be observable. This difference is greater even than was predicted in the chemical analysis of chapter 4. This is probably because the cores which are responsible for producing the CH_4 peaks in either case are not quite in the same stage of evolution, since the ratios predicted in chapter 4 were calculated for a time $t = 7.2 \times 10^5$ years into a single core's evolution. Again, morphological differences in CH_4 are apparent between the standard run and limit cycle cases.

We should expect that even if minimal re-injection features are not attained, if those features are weak enough then the CH_4 "shoulder" peak (see chapter 4) in the column density profile could take a higher value than the re-injection peak, such that it would be favoured as the most likely to register emission peaks in a map. As this balance shifts towards the "shoulder", then the difference between the CH_4:SO_2 ratios at the standard run and limit cycle CH_4 peaks would increase towards the extreme values shown in this study.

In a real dark cloud we should not necessarily expect to see such stark evidence of one case over the other, since the situations modelled here represent extremes (and in the case of CH_4, due to the lack of a dipole moment for that molecule, the explicit features shown here would be hard to observe). Either all material in the cores has been recently cycled in another core, or it has not been recently cycled at all, such that there is no observable evidence of previous cycling. In reality, the time scale between recycling of material by core formation and destruction should vary, so that cores may begin with a possible range of chemical starting points, dependent on the level of destruction of the chemical hysteresis in the intervening period. Also, core formation subsequent to destruction of a local core may not occur in the same spatial position, leading to regions of the previous core being brought into different regions of the subsequent core, affecting the way the material is re-processed.

Although CH_4 is difficult to observe, the behaviour highlighted in this section might be observed in other molecules (or ratios thereof), like H_2CO, CH_3OH, or other hydrocarbon molecules which show similar behaviour.

6.9 Overall Conclusions

The modifications made to the convolution and mapping method of the previous chapter have improved the model in a number of ways. Firstly, they have made the entire approach more appropriate to the physical situation, by allocating each core with an intrinsic width. Whilst this has in a way introduced a new parameter to the model, the previous approach of tailoring the beam resolution to the observed size of cores did this anyway. By divorcing the two quantities, and then using appropriate values of beam resolution, the change has in reality only simplified the parameter, framing it in terms of the fundamental quantity which it represents: the physical extents of the cores. Crucially, this modification has allowed absolute "detected" column density values to be obtained, providing another measure by which to compare with observations. Secondly, the smoothing of re-injection peaks has provided a simple way of eliminating the effects of the discrete chemical reference point distribution in the chemical model (which became important when considering the *instantaneous* re-injection of dust grain mantle-bound material), and of providing a means to approximate both extremes of re-injection rate, and then to explore the effects on observed column densities and morphologies. Finally, the use of effective critical emission densities has allowed the discrimination of different molecular line transitions in the simulated observations. The absence of proper radiative transfer modelling in the code was a necessary compromise in this model. However, the convolution of data obtained from chemical modelling to produce maps with morphologies so similar to observations is quite unique. The level of agreement of absolute column densities also suggests, taking into account the inevitable discrepancies caused by the adoption of such a simple means of dark cloud construction from an ensemble of identical cores, that the idea is sound and does not produce results which deviate wildly from observations.

This method produces results which fit well with the observational evidence of the Morata *et al.* papers. Also, the broad low resolution morphologies which result are in qualitative agreement with the observational evidence of Myers *et al.* (1991). In future, the mean core sizes of CO, CS and NH_3 could be calculated from the synthesised data, in order to compare more meaningfully with this observational evidence.

The method allows the presentation of the results of the chemical models in a synthesised observational framework, and permits constraints to be placed on observable physical and chemical quantities, like the relative molecular extents, at both high and low resolu-

tions. It has also allowed for the testing of various hypotheses derived from the chemical studies of previous chapters. It may be seen that in the case where the re-injection of grain mantles is slow enough to present no observable effects on column densities, the morphologies and absolute column density values of a selection of molecules may be used to determine the level (*i.e.* the approximate time scale) of re-cycling of core material in a dark cloud.

A recurrent, though not explicitly tested hypothesis for the deficiencies and/or inaccuracies of this method of synthesised molecular line mapping regards not the process itself, but the construction of the synthetic basic "sky" maps. Certain features of the observational evidence, and the evidence produced in this chapter, appear to be most easily explicable in the context of a spectrum of core types and sizes acting together to produce the morphologies and column densities observed across regions of dark clouds (and in fact this spectrum could be relevant to star formation, if larger cores became gravitationally unstable as briefly explored in chapter 2 – this spectrum could therefore be related to the initial mass function). Such a spectrum of cores would determine the relative and absolute levels of molecular emission. In future work I should explore this idea, however it would require an amount of chemical modelling which would have made it difficult to examine simply in this work.

Besides the variation in physical parameters which might exist between individual cores, the results of the mapping procedure ought to be affected by variations in chemistry in different regions within a core. It is impossible as yet to investigate this phenomenon and will remain so until further work is carried out into the formation mechanisms of cores (*cf* Falle & Hartquist 2002) which examines more than one dimension.

Whilst the smoothing of column density re-injection features is an adequate means of obtaining continuous and reasonably self-consistent profiles, in future work these features might be treated at the level of the chemical models which produce them. Firstly, greater chemical reference point resolution might be employed around the freeze-out/non-freeze-out boundary to avoid the need for smoothing. Secondly, by employing a specific mechanism for the re-injection of the grain mantles, realistic desorption rates might be adopted, and in such a way that an artificially imposed threshold visual extinction might not be necessary, and also that the re-injection feature profiles might be more reliable.

The artificial convolution method provides a unique testing-ground for theories regarding both the dynamics and chemistry of core formation and dissipation.

BIBLIOGRAPHY

Arons, J. & Max, C. E., 1975, *ApJ*, **196**, L77

Balsara, D., Ward-Thompson, D. & Crutcher, R. M., 2001, *MNRAS*, **327**, 715

Bash, F. N., Green, E. & Peters, W. L., 1977, *ApJ*, **217**, 464

Bergin, E. A. & Langer, W. D., 1997, *ApJ*, **486**, 316

Charnley, S. B., Dyson, J. E., Hartquist, T. W. & Williams, D. A., 1988, *MNRAS*, **231**, 269

Charnley, S. B., Dyson, J. E., Hartquist, T. W. & Williams, D. A., 1988, *MNRAS*, **235**, 1257

Ciolek, G. E. & Mouschovias, T. C., 1995, *ApJ*, **454**, 194

Duley, W. W. & Williams, D. A., 1984, *Interstellar Chemistry* (Academic Press, London, UK)

Evans, N. J., 1989, *RMxAA*, **18**, 21

Evans, N. J., 1999, *ARA&A*, **37**, 311

Falle, S. A. E. G., 2002, *ApJ*, **577**, L123

Falle, S. A. E. G. & Hartquist, T. W., 2002, *MNRAS*, **329**, 195

Farebrother, A. J., Meijer, A. J. H. M., Clary, D. C. & Fisher, A. J., 2000, *Chem Phys Letters*, **319**, 303

Fiedler, R. A. & Mouschovias, T. C., 1992, *ApJ*, **391**, 199

Frisch, P. C. & Jura, M., 1980, *ApJ*, **242**, 560

Gammie, C. F., Lin, Y. T., Stone, J. M. & Ostriker, E. C., 2003, *ApJ*, **592**, 203

Garrod, R. T., Rawlings, J. M. C. & Williams, D. A., 2003, *Ap&SS*, **286**, 487

Garrod, R. T., Wiiliams, D. A., Hartquist, T. W., Rawlings, J. M. C. & Viti, S., 2005, *MNRAS*, **356**, 654

Girart, J. M., Viti, S., Williams, D. A., Estalella, R. & Ho, P. T. P., 2002, *A&A*, **388**, 1004

Goldsmith, P. F., Langer, W. D. & Wilson, R. W., 1986, *ApJ*, **303**, L11

Gredel, R., Lepp, S. & Dalgarno, A., 1987, *ApJ*, **323**, L137

Habing, H. J., 1968, *Bull. Astron. Inst. Netherlands*, **19**, 421

Lambert, D. L. & Danks, A. C., 1986, *ApJ*, **303**, 401

Leisawitz, D., Bash, F. N. & Thaddeus, P., 1989, *ApJS*, **70**, 731

Lepp, S. & Tiné, S., 1998, *The Molecular Astrophysics of Stars and Galaxies (Eds. Hartquist, T. W. and Williams, D. A.)* (Clarendon Press, Oxford, UK)

Linsky, J. L., Diplas, A., Wood, B. E., Brown, A., Ayres, T. R. & Savage, B. D., 1995, *ApJ*, **451**, 335

McKee, C. F., 1989, *ApJ*, **345**, 782

Meijer, A. J. H. M., Farebrother, A. J., Clary, D. C. & Fisher, A. J., 2001, *J. Phys. Chem. A*, **105**, 2173

Millar, T. J., Bennett, A., Rawlings, J. M. C., Brown, P. D. & Charnley, S. B., 1991, *A&AS*, **87**, 585

Millar, T. J., Farquhar, P. R. A. & Willacy, K., 1997, *A&AS*, **121**, 139

Morata, O., Estalella, R., López, R. & Planesas, P., 1997, *MNRAS*, **292**, 120

Morata, O., Girart, J. M. & Estalella, R., 2003, *A&A*, **397**, 181

Myers, P. C., Fuller, G. A., Goodman, A. A. & Benson, P. J., 1991, *ApJ*, **376**, 561

Nejad, L. A. M. & Williams, D. A., 1992, *MNRAS*, **255**, 441

Nejad, L. A. M., Williams, D. A. & Charnley, S. B., 1990, *MNRAS*, **246**, 183

Norman, C. & Silk, J., 1980, *ApJ*, **238**, 138

Perry, J. S. A., Gingell, J. M., Newson, K. M., To, J., Watanabe, N. & Price, S. D., 2002, *Measurement Science and Technology*, **13**, 1414

Pravdo, S. H., Feigelson, E. D., Garmire, G., Maeda, Y., Tsuboi, Y. & Bally, J., 2001, *Nature*, **413**, 708

Press, W. H., Teukolsky, S. A., Vetterling, W. T. & Flannery, B. P., 1992, *Numerical Recipes, The Art of Scientific Computing (Second Edition)* (Cambridge University Press)

Rawlings, J. M. C., 1996, *QJRAS*, **37**, 503

Rawlings, J. M. C., Hartquist, T. W., Menten, K. M. & Williams, D. A., 1992, *MNRAS*, **255**, 471

Rawlings, J. M. C., Hartquist, T. W., Williams, D. A. & Falle, S. A. E. G., 2002, *A&A*, **391**, 681

Rawlings, J. M. C. & Yates, J. A., 2001, *MNRAS*, **326**, 1423

Ruffle, D. P., Hartquist, T. W., Caselli, P. & Williams, D. A., 1999, *MNRAS*, **306**, 691

Sepúlveda Cerrada, I., 2001, *PhD Thesis* (Universitat de Barcelona)

Stecher, T. & Williams, D. A., 1972, *ApJ*, **177**, L141

Tafalla, M., Myers, P. C., Caselli, P., Walmsley, C. M. & Comito, C., 2002, *ApJ*, **569**, 815

Taylor, S. D., Morata, O. & Williams, D. A., 1996, *A&A*, **313**, 269

Tiné, S., Williams, D. A., Clary, D. C., Farebrother, A. J., Fisher, A. J., Meijer, A. J. H. M., Rawlings, J. M. C. & Davis, C. J., 2003, *Ap&SS*, **288**, 377

Umebayashi, T. & Nakano, T., 1980, *PASJ*, **32**, 405

Ungerechts, H., Bergin, E. A., Goldsmith, P. F., Irvine, W. M., Schloerb, F. P. & Snell, R. L., 1997, *ApJ*, **482**, 245

Viti, S., Girart, J. M., Garrod, R., Williams, D. A. & Estalella, R., 2003, *A&A*, **399**, 187

Viti, S. & Williams, D. A., 1999, *MNRAS*, **310**, 517

Whittet, D. C. B., 2003, *Dust in the galactic environment, second edition* (Institute of Physics publishing, Bristol and Philadelphia)

Williams, D. A., Clary, D. C., Farebrother, A., Fisher, A., Gingell, J. M., Jackman, R., Mason, N., Meijer, A., Perry, J., Price, S. D., Rawlings, J. M. C. & Williams, D. E., 1999, *H_2 in Space, in: F. Combes (ed.), Pineau des Forêts, G.* (Cambridge University Press, Astrophysics Series)

Williams, D. A., Hartquist, T. W. & Whittet, D. C. B., 1992, *MNRAS*, **258**, 599